Title
Strategies for the Precision Targeting of Nucleotide Metabolism in Cancer

Author
Abt, Evan Robert

Publication Date
2019

Peer reviewed|Thesis/dissertation

UNIVERSITY OF CALIFORNIA

Los Angeles

Strategies for the Precision Targeting of Nucleotide Metabolism in Cancer

A dissertation submitted in partial satisfaction of the requirements for the degree

Doctor of Philosophy in Molecular and Medical Pharmacology

by

Evan Robert Abt

2019

ABSTRACT OF THE DISSERTATION

Strategies for the Precision Targeting of
Nucleotide Metabolism in Cancer

by

Evan Robert Abt
Doctor of Philosophy in Molecular and Medical Pharmacology
University of California, Los Angeles, 2019
Professor Caius Gabriel Radu, Chair

Cancer cell proliferation and survival are dependent upon on a sufficient supply of deoxyribonucleotide triphosphates (dNTPs), the substrates for DNA replication. dNTPs are produced by convergent intracellular metabolic pathways, either by the *de novo* pathway which utilizes glucose and amino acid precursors or by the salvage pathway which allows for the scavenging of preformed nucleosides from the environment. Despite its fundamental nature, the regulation of nucleotide biosynthesis by intracellular signaling networks in cancer cells is poorly defined and the implications this control are unclear. Here we systematically evaluate the regulation of cancer cell nucleotide metabolism by two signaling networks, the replication stress response pathway and signaling elicited by the cytokine interferon. Armed with new insights into the regulation of nucleotide metabolism in cancer we develop new, rationally designed therapeutic strategies to be translated for the treatment of precisely defined patient populations.

Chapter 1 provides an introduction to nucleotide metabolism function and regulation in cancer.

Chapter 2 concerns the investigation of nucleotide metabolism regulation by the replication stress response signaling pathway. Here we define a link between the proximal replication

stress response kinase ataxia telangiectasia and Rad3-related protein (ATR) and rate-limiting enzymes in *de novo* and salvage nucleotide biosynthetic pathways: ribonucleotide reductase (RNR) and deoxycytidine kinase (dCK). In cancer cells, ATR inhibition produces a collateral dependency on RNR and dCK activity. We demonstrate that simultaneously targeting ATR, RNR and dCK using small molecule inhibitors effectively eradicates acute lymphoblastic leukemia cells *in vitro* and *in vivo*.

In Chapter 3 we report an investigation of nucleotide metabolism regulation by the pleiotropic cytokine type I interferon. We determine that interferon signaling is constitutive in pancreatic ductal adenocarcinoma (PDAC) patient tumors and xenograft models and is driven by the cGAS/STING pathway. In PDAC cells, interferon signaling triggers a decrease in dNTP pool abundance and up-regulates dNTP phosphohydrolysis mediated by sterile alpha-motif and histidine-aspartate domain-containing protein 1 (SAMHD1). Activation of ATR is a compensatory response to this stress and we find that interferon signaling triggers a dependency on ATR activity in a subset of PDAC models.

Chapter 4 concerns the identification of a cancer cell metabolic vulnerability that results from impaired dNTP catabolism. Here we show that inhibition of purine nucleoside phosphorylase (PNP) selectively induces dNTP pool imbalance and cell death in cancer cells lacking the phosphohydrolase SAMHD1. In this chapter we define a new synthetic lethal interaction in cancer and demonstrate that SAMHD1 deficiency is a requisite biomarker for PNP inhibitor activity.

In Chapter 5 we present the development and application of a cell-based metabolic modifier screening platform that leverages the redundancy in pyrimidine metabolism for the discovery of specific modulators of convergent nucleotide biosynthetic pathways. Here we report the identification and characterization of selective small molecule inhibitors of the pyrimidine *de novo* pathway enzyme dihydroorotate dehydrogenase and of nucleoside transporters which are essential for nucleoside salvage pathway activity.

The dissertation of Evan Robert Abt is approved.

Timothy R. Donahue

Harvey R. Herschman

Antoni Ribas

Patrick G. Harran

Caius G. Radu, Committee Chair

University of California, Los Angeles

2019

DEDICATION

This dissertation is dedicated to my parents, Carol and Robert Abt, and to my wife, Ariel Abt.

Thank you for your unending patience, love and support.

TABLE OF CONTENTS

LIST OF FIGURES

CHAPTER 1

CHAPTER 2

ACKNOWLEDGMENTS

First, I must thank Dr. Caius Radu for his outstanding mentorship and support. Caius gave me an opportunity for which I will always be grateful. He is a brilliant scientist, an incredibly hard worker and a very thoughtful, tremendously supportive mentor. I am thankful that Caius always pushed me to be the best scientist possible. Together, Caius and I shaped each of the projects described in this thesis and it is because of his support and guidance that I am able to write this dissertation. I hope that our collaboration will continue for years to come.

I thank Dr. Timothy Donahue for his mentorship, invaluable clinical perspective and for always encouraging me to consider the translational significance of my work. Without fail, he would ask the most insightful, most important and the most difficult questions in our weekly lab meetings which helped sharpen my presentation and critical thinking skills.

I thank Dr. Johannes Czernin for always supporting my work, for always seeking innovative ways to translate basic discoveries to patients, and for creating an outstanding environment, filled with the best people and best equipment, on the A-level.

I would also like to thank the members my doctoral committee, Dr. Antoni Ribas, for his critical and particularly helpful feedback; Dr. Harvey Herschman, for his incredible insight into fundamental biology; and Dr. Patrick Harran for his encouragement.

I thank Dr. Robert Damoiseaux, Director of the UCLA Molecular Shared Screening Resource, for teaching me the nuances of high throughput screening. Learning how to apply this powerful approach profoundly impacted my training as a scientist and granted me exposure to new, exciting areas of biology. Most importantly, Robert taught me to always think big.

I thank Dr. Thuc Le for his mentorship and for teaching me the power of mass spectrometry. I thank Dr. Shili Xu for his guidance and invaluable insight. I thank my fellow graduate students in the Radu lab, Soumya Poddar, Woosuk Kim and Joe Capri, for sharing this journey and for

always being willing to provide either excellent technical assistance or advice. I thank Dr. Amanda Dann for her support, hard work and for her help in shaping this thesis.

I am indebted to the many current and former members of the Radu, Donahue and Czernin groups, including Liu Wei, Arthur Cho, Nanping Wu, Luyi Li, Joel Almajano, Kyle Current, Ethan Rosser and Larry Pang for their outstanding technical skill, their dedication, and their willingness to help unconditionally.

I am grateful to have had the opportunity to mentor Chloe Cheng, Juna Yi and Vincent Lok alongside a number of other extremely intelligent and hardworking undergraduate students. I am very proud that several of my students decided to pursue careers in research themselves and I wish them the best of luck.

Finally, I must thank for my wonderful wife Ariel. She is my inspiration and I will forever be grateful for her unending love and support during my time as a graduate student.

Chapter 2 is a version of Le TM, Poddar S, Capri JR, Abt ER, Kim W, Wei L, Uong NT, Cheng CM, Braas D, Nikanjam M, Rix P, Merkurjev D, Zaretsky J, Kornblum HI, Ribas A, Herschman HR, Whitelegge J, Faull KF, Donahue TR, Czernin J, Radu CG. ATR inhibition facilitates targeting of leukemia dependence on convergent nucleotide biosynthetic pathways. Nat Commun (2017).

Chapter 5 is a version of Abt ER, Rosser EW, Durst MA, Poddar S, Lok V, Cho, A, Kim W, Song J, Capri JR, Le TM, Slavik R, Jung ME, Damoiseaux R, Czernin J, Donahue TR, Lavie A and Radu CG. Metabolic modifier screen reveals secondary targets of protein kinase inhibitors within nucleotide metabolism. Submitted to Cell Chem Biol. Available at SSRN: https://ssrn.com/abstract=3389530 (2019).

VITA

2010	Bachelor of Science, Molecular, Cell and Developmental Biology University of California, Santa Cruz Santa Cruz, CA
2011-2013	Staff Research Associate - Lab of Dr. David Shackelford Department of Pulmonary and Critical Care Medicine University of California, Los Angeles Los Angeles, CA
2013-2019	Graduate Student Researcher - Lab of Dr. Caius Radu Department of Molecular and Medical Pharmacology University of California, Los Angeles Los Angeles, CA

PUBLICATIONS

Abt ER, Rosser EW, Durst MA, Poddar S, Lok V, Cho, A, Kim W, Song J, Capri JR, Le TM, Slavik R, Jung ME, Damoiseaux R, Czernin J, Donahue TR, Lavie A and Radu CG. Metabolic modifier screen reveals secondary targets of protein kinase inhibitors within nucleotide metabolism. Submitted to Cell Chem Biol. Available at SSRN: https://ssrn.com/abstract=3389530 (2019).

Sun DL, Poddar S, Pan RD, Valkenburgh JV, Rosser EW, **Abt ER**, Lok V, Capri J, Hernandez SP, Song J, Li J, Vergnes L, Cabebe A, Armstrong WR, Plamthottam S, Steele D, Osto C, Stuparu A, Le TM, Reue K, Damoiseaux R, Czernin J and Radu CG. Evaluation of potent isoquinoline-based thiosemicarbazone antiproliferatives against solid tumor models. Submitted to J Med Chem. Available at: https://doi.org/10.26434/chemrxiv.7877987.v1 (2019).

Elliott IA, Dann AM, Kim SS, **Abt ER**, Kim W, Poddar S, Moore A, Zhou L, Williams JL, Capri JR, Ghukasyan R, Matsumura C, Tucker DA, Armstrong WR, Cabebe AE, Wu N, Li L, Le TM, Radu CG and Donahue TR. Lysosome inhibition sensitizes pancreatic cancer to replication stress by aspartate depletion. Proc Natl Acad Sci U S A (2019).

Le TM, Poddar S, Capri JR, **Abt ER**, Kim W, Wei L, Uong NT, Cheng CM, Braas D, Nikanjam M, Rix P, Merkurjev D, Zaretsky J, Kornblum HI, Ribas A, Herschman HR, Whitelegge J, Faull KF, Donahue TR, Czernin J, Radu CG. ATR inhibition facilitates targeting of leukemia dependence on convergent nucleotide biosynthetic pathways. Nat Commun (2017).

Kim W, Le TM, Wei L, Poddar S, Bazzy J, Wang X, Uong NT, **Abt ER**, Capri JR, Austin WR, Van Valkenburgh JS, Steele D, Gipson RM, Slavik R, Cabebe AE, Taechariyakul T, Yaghoubi SS, Lee JT, Sadeghi S, Lavie A, Faull KF, Witte ON, Donahue TR, Phelps ME, Herschman HR, Herrmann K, Czernin J, Radu CG. [18F]CFA as a clinically translatable probe for PET imaging of deoxycytidine kinase activity. Proc Natl Acad Sci U S A (2016).

PATENTS

Caius G. Radu, **Evan R. Abt**, Ethan W. Rosser, Amon Lavie, Matthew A. Durst.
"MODULATORS OF PYRIMIDINE NUCLEOTIDE BIOSYNTHETIC PATHWAYS".
US Provisional Patent No. 62/848,728 filed 5/16/2019.

Caius G. Radu, **Evan R. Abt**, Thuc M. Le.
"COMPOSITIONS AND METHODS FOR TREATING CANCER WITH NUCLEOSIDE-METABOLISM MODULATORS".
US Provisional Patent No. 62/881,058 filed 7/31/2019.

PRESENTATIONS

Abt ER. "Abstract GA613: STING-driven inflammatory cytokine signaling triggers metabolic alterations detected by [^{18}F]FLT PET in mouse models of pancreas cancer". World Molecular Imaging Congress (WMIC) hosted in Montreal, QC. September, 2019. *Oral Presentation*.

Abt ER. "Abstract 4971: Identification of new modulators of nucleotide metabolism and replication stress in PDAC". American Association of Cancer Research (AACR) Annual Meeting hosted in Chicago, IL. March, 2018. *Oral Presentation*.

Abt ER. "Interferons regulate nucleotide metabolism and sensitivity to replication stress response inhibition in PDAC". University of California Pancreas Cancer Consortium Meeting hosted in San Diego, CA. February, 2018. *Oral Presentation*.

Abt ER. "Defining the effects of interferon on nucleotide metabolism and replication stress in pancreatic cancer". UCLA Department of Molecular and Medical Pharmacology Annual Retreat hosted in Huntington Beach, CA. November, 2017. *Oral Presentation*.

Abt ER. "Identification of new modulators of nucleotide metabolism". UCLA Metabolism Interest Group Monthly Meeting hosted in Los Angeles, CA. June, 2017. *Oral Presentation*.

CHAPTER 1

Introduction

Function and Regulation of Nucleotide Metabolism in Cancer

A sufficient, balanced supply of nucleotides is essential for cancer cell proliferation

Nucleotides are perhaps the oldest molecules of life and thus participate in many cellular processes. These processes include: nucleic acid biosynthesis, DNA repair, energy transfer, signal transduction, carbohydrate metabolism and lipid metabolism (**Figure 1.1**)[1].

Cancer cells require an adequate, balanced supply of nucleotides for proliferation and survival. Deoxyribonucleotide triphosphates (dNTPs), the substrates for DNA replication and repair, are produced *de novo* from glucose and amino acids or by salvage of preformed nucleosides and nucleobases from the environment[1]. dNTP pool sizes are tightly regulated by the coordinated activity of a network of biochemical pathways controlled by over 200 proteins (**Figure 1.2**)[1,2]. The functions of these pathways within nucleotide metabolism encompass:

(i) ***nucleotide biosynthesis*** mediated by the rate-limiting enzyme complex ribonucleotide reductase (RNR) that converts ribonucleotides (NDPs) to deoxyribonucleotides (dNDPs). Nucleotide diphosphate kinases add a terminal phosphate to complete dNTP synthesis.

(ii) ***nucleotide utilization*** for DNA replication and repair.

(iii) ***nucleotide phosphohydrolysis*** mediated by sterile alpha-motif and histidine-aspartate domain-containing protein 1 (SAMHD1) which hydrolyzes dNTPs to corresponding deoxyribonucleosides (dNs) and triphosphate[3].

(iv) ***nucleoside recycling*** of phosphohydrolysis-produced dNs by nucleoside kinases deoxycytidine kinase (dCK), which accepts dC, dA and dG; and thymidine kinase 1 (TK1) which accepts dT.

(v) ***nucleoside salvage*** of preformed dNs from the environment via the action of nucleoside transporters and kinases.

(vi) ***nucleoside breakdown*** of nucleosides by phosphorylases thymidine phosphorylase (TYMP) and purine nucleoside phosphorylase (PNP).

A hallmark characteristic of nucleotide metabolism, and of cellular metabolic networks in general, is the presence of convergent metabolic nodes: metabolites which are supplied by parallel biochemical pathways[4]. This redundancy grants metabolic plasticity and allows for adaption to alterations in environmental nutrient availability. Uridine monophosphate (UMP), the precursor to all pyrimidine nucleotides, is one such metabolic node and is produced redundantly by parallel *de novo* and salvage pathways. The *de novo* pathway utilizes glucose, glutamine and aspartate precursors in a six-step biochemical process mediated by tri-functional CAD, dihydroorotate dehydrogenase (DHODH), which is located on the other surface of the inner mitochondrial membrane and contributes electrons to the mitochondrial electron transport chain, and bi-functional UMP synthase (UMPS; **Figure 1.3A**)[5]. A parallel salvage pathway allows for utilization of preformed uridine from the environment via the combined actions of nucleoside transporters and the uridine-cytidine kinases (UCKs)[6]. Nucleoside membrane translocation is regulated by two major classes of nucleoside transporters: (i) concentrative nucleoside transporters (CNTs) which are obligatory inward transporters that co-import Na^+, and (ii) equilibrative nucleoside transporters (ENTs) which are bidirectional, energy independent and responsive to nucleoside concentration gradients[7]. Similar convergent *de novo* and salvage pathways exist for the biosynthesis of pyrimidine deoxyribonucleotides dCMP and dTMP (**Figure 1.3B**).

The first evidence of a cellular deoxyribonucleoside salvage pathway was obtained in the 1951 by Reichard and colleagues who elegantly demonstrated that ^{15}N-labeled dNs are incorporated into nucleic acids in cells[8]. It has been decades since the process of nucleoside salvage was biochemically mapped however its biological significance, particularly in the context of cancer, remains unclear. This metabolic pathway has been exploited in the treatment of cancer by the development of antimetabolite chemotherapies, such as gemcitabine and cytarabine, which are toxic analogs of natural nucleosides that rely on the salvage kinase dCK for their activation. dN salvage is perhaps most well studied for its role as a resistance mechanism in the context of therapeutic inhibition of *de novo* nucleotide biosynthetic pathways[9].

The development of deoxycytidine and thymidine analogs labeled with a positron-emitter, including [^{18}F]FAC, [^{18}F]CFA and [^{18}F]FLT, allowed for the measurement of endogenous nucleoside kinase activity in mice and humans using non-invasive positron emission tomography (PET)[10–12]. These studies indicated that dCK activity is enriched at sites of hematopoiesis, including the thymus, spleen and bone marrow. Consistently, defects in T- and B-cell development were found to be consequences of genetic dCK inactivation in mice, a finding which prompted the development of small molecule dCK inhibitors for the treatment of hyper-proliferative hematological malignancies[2,13]. dCK inhibitors have been deployed for treatment of acute lymphoblastic leukemia in preclinical models and found to potently enhance response to the pyrimidine *de novo* pathway inhibitors thymidine and triapine[14,15].

An increasing body of evidence indicates that the nucleoside salvage kinases dCK, TK1 and uridine-cytidine kinase 2 (UCK2) are active in cancer cells and that their substrates are abundantly produced by tumor-supporting cells in the microenvironment, including fibroblasts and immune cells[16]. A role for nucleosides in cancer cell fate is further supported by an association between elevated nucleoside kinase expression and poor prognosis in multiple cancers including pancreatic ductal adenocarcinoma[17]. One challenge in the study of nucleoside salvage lies in traditional *in vitro* cell culture systems where *de novo* pathway substrates (glucose and glutamine) are supplied in abundance in hyperoxic (20% O_2) environments. In contrast, this *de novo* pathway may be limited in some tumors as a consequence of poor vasculature, nutrient starvation or hypoxia thereby increasing the relevance of salvage. Additionally, pyrimidine nucleosides are detected in human and rodent plasma but are generally omitted from cell culture media[11]. Thus, experimental artifacts resulting *in vitro* model systems could confound the investigation of the interplay between d*e novo* and salvage nucleotide biosynthetic pathways. Furthermore, the end product of uridine salvage, UTP, is a potent allosteric inhibitor of the proximal *de novo* pathway enzyme CAD, suggesting that pyrimidine biosynthesis by the energetically economical salvage pathway is “preferred” (the *de novo* pathway requires expenditure of 1 glucose, 1 glutamine, 1 aspartate, and 2 ATP molecules to

produce UMP whereas the salvage pathway requires only preformed uridine scavenged from the environment and 1 molecule of ATP)[4].

Whether nucleoside kinase inhibitors can be effectively applied in cancer treatment with acceptable tolerability remains to be determined. This translation may require identification of optimal companion therapies (small molecule inhibitors and/or immunotherapy) and the stratification of patients using genomic (identification of tumors in which mutational inactivation of *de novo* pathway genes is observed) or transcriptional signatures. The first-in-class dCK inhibitor TRE-515 is currently progressing towards clinical trials for the treatment of cancer and the findings of these studies will undoubtably enhance our understanding of nucleoside salvage in humans.

The replication stress response allows cancer cells to sense and respond to nucleotide insufficiency

dNTP pool insufficiency, excesses or imbalances impair DNA replication fidelity and genome stability (**Figure 1.4**)[18,19]. Importantly, imbalances amongst dNTP pools have been implicated as a cause of the human pathologies severe combined immunodeficiency (SCID) and mitochondrial neurogastrointestinal encephalomyopathy (MNGIE)[20,21]. Thus, in mammalian cells, dNTPs pools are tightly regulated and maintained in limited supply. Consequently, even small reductions in dNTP biosynthesis could limit DNA replication and induce DNA damage in actively proliferating tumor cells.

Nucleotide biosynthesis is regulated by both biochemical (allosteric feedback control) and signaling mechanisms (transcriptional and post-translational control of nucleotide metabolism enzymes)[22–24]. The KRAS oncogene has been shown to induce the expression of rate-limiting nucleotide biosynthetic enzymes in cancer cells via impairment of Retinoblastoma protein function and subsequent activation of E2F transcription factors[25]. The KRAS effector MYC has

also been shown to positively regulate nucleotide biosynthesis in pancreas cancer cells via induction of the pentose phosphate pathway gene RPIA[26].

More recently, the replication stress response pathway was identified as a key modulator of dNTP consumption, biosynthesis and salvage[23,26]. Initiated by replication stress, which is in turn triggered by any obstacle to DNA replication that causes stalling of replication forks, the replication stress response pathway is an extensive (over 700 component) signaling cascade[27]. This pathway is coordinated by the serine threonine kinase ataxia telangiectasia and Rad3-related protein (ATR) and its downstream effectors, the checkpoint kinases CHEK1 and WEE1 (**Figure 1.5A**)[28]. ATR senses replication stress by binding RPA-coated single-strand DNA (ssDNA) at stalled replication forks and functions to prevent their collapse into lethal DNA double-strand breaks. The replication stress response functions to stabilize stalled replication forks, inhibit new DNA synthesis, promote DNA repair, initiate nucleotide biosynthesis and restart DNA replication[27]. If unresolved, replication stress is an important source of DNA damage.

An established cause of replication stress is an insufficient or imbalanced supply of dNTP precursors for DNA replication in S-phase. In addition to sensing nucleotide insufficiency, ATR directly promotes nucleotide biosynthesis by phosphorylating and activating dCK, and indirectly by stabilizing the E2F1 transcription factor which regulates the expression of genes required for *de novo* nucleotide biosynthesis, including RRM2, TYMS and DHFR, or by preventing untimely RRM2 proteasomal degradation initiated by CDK1 phosphorylation and mediated by the $SCF^{Cyclin\ F}$ ubiquitin ligase complex[23,29,30].

Small molecule inhibitors of ATR, including M6620 (EMD Serano; also known as VE-822) and AZD6738 (AstraZeneca) have demonstrated anti-tumor activity in pre-clinical models and are being investigated in over 60 active clinical trials (**Figure 1.5B**)[31]. However, it has become evident that this class of drugs must be administered as a component of rationally designed

combination therapies for the treatment of tumors characterized by high basal levels of replication stress.

In this context, the replication stress response pathway may be particularly important for the survival of tumor cells with oncogenic signaling driven by activating KRAS mutations and mutant TP53[32,33]. Specifically, mutant RAS has been shown to cooperate with ATR suppression to induce DNA damage in tumor cells[32]. Additionally, mitogenic oncogenic signaling in KRAS mutant tumor leads to an increased number of active replication origins during S-phase[34]. If this is not accompanied by a proportional upregulation of nucleotide biosynthesis, the increased number of replicons may lead to dNTP insufficiency, a known cause of oncogene-induced replication stress and senescence[35,36]. Collectively, these observations indicate that the replication stress response pathway, and consequently ATR activity, is a collateral dependency of transformed cells and is an example of non-oncogene addiction[37].

While the replication stress response pathway is a well-established regulator of nucleotide biosynthesis significant gaps remain in our understanding of the therapeutic significance of this link. Furthermore, the mechanisms and implications of the link between nucleotide metabolism and other signaling networks, such as cytokine signaling, remain to be investigated.

Targeting nucleotide metabolism in pancreas cancer

Pancreatic adenocarcinoma (PDAC) is a devastating disease with a median overall survival of less than one year and is expected to become the second most common cause of cancer related death in the United States by 2020[38,39]. In addition to an aggressive tumor biology and late stage at diagnosis, the dismal prognosis is a result of high resistance to current tumor cell-directed cytotoxic chemotherapies and immune checkpoint blockade[40,41]. Additionally, the majority of PDAC patients are not candidates for treatment with oncogene targeted kinase inhibitors as most tumors are driven by mutations in “un-druggable” KRAS. However, this

dogma is currently being challenged with the translation of KRAS G12C-mutant inhibitors to the clinic[42].

While surgery provides the only chance of cure, patients with metastatic disease are not candidates for resection. Chemotherapy is administered in adjuvant and advanced disease settings and approved regimens include: gemcitabine/abraxane combinations, or FOLFIRINOX a combination consisting of folinic acid, 5-fluorouracil (5-FU), irinotecan and oxaliplatin[43,44]. Both of these regimens contain either a nucleoside or nucleobase toxic antimetabolite, either the dCK-dependent deoxycytidine analog gemcitabine or the modified pyrimidine nucleobase 5-FU[43,44]. While a subset of patients respond to chemotherapy, the 5-year overall survival rate of PDAC patients is <10%[38].

Thus, the development of new effective therapies for PDAC patients is an urgent need. One approach taken to improve outcomes has been to define genomic and transcriptional signatures to stratify patients[45,46]. Mutational inactivation of the DNA repair genes BRCA1/2 occurs in 4-7% of PDAC patients and is associated with improved responses to pharmacological PARP inhibition[47]. Furthermore, two transcriptional subtypes, epithelial/progenitor and mesenchymal/ squamous, have been recurrently identified in PDAC patient specimens and cells of the squamous subtype have been shown to exhibit elevated levels replication stress and enhanced sensitivity to ATR and WEE1 inhibitors[41].

The defining characteristics of PDAC tumors are mutations in KRAS and TP53 (which occur in 90% and 78% of patients respectively), a heterotypic cellular microenvironment with a dense stromal compartment, and extensive inflammatory cytokine signaling (**Figure 1.6**)[40,41]. Recently, rewired cellular metabolism has emerged as an additional hallmark of PDAC and is driven by both cell autonomous mechanisms (i.e. oncogenic KRAS signaling) and by heterotypic cellular interactions within the tumor microenvironment[48]. Mutant KRAS is a critical driver of PDAC cell proliferation and survival and has been shown to orchestrate the up-regulation of multiple anabolic pathways including, glycolysis (the Warburg effect)[49], glutamine metabolism[50], the

pentose phosphate pathway[26], nutrient scavenging via macropinocytosis[51] and recycling by autophagy[52]. These metabolic alterations fuel the unrestrained proliferation of PDAC cells and allow for their survival in nutrient-poor, hypoxic microenvironment. Consistently, PDAC cells are particularly dependent on the activity of nutrient scavenging mechanisms, including autophagy, for survival.

While nucleotide metabolism has been a target in PDAC for decades (by means of the antimetabolite chemotherapies gemcitabine and 5-FU) it has recently been rediscovered as a critical regulator of cancer cell growth and survival. The pyrimidine biosynthetic enzyme DHODH has been identified as a collateral dependency of KRAS driven PDAC and DHODH inhibitors effectively prevent PDAC cell proliferation *in vitro* and *in vivo*[26]. In PDAC cells, lysosomes have been identified as a contributor to cellular aspartate pools which are essential for *de novo* pyrimidine and purine biosynthesis[53]. Recent work has revealed that dN substrates for nucleoside kinases are abundantly produced by fibroblasts and tumor-promoting macrophages in PDAC tumors and competitively inhibit the activation and phosphorylation of gemcitabine by dCK[16]. However, the endogenous roles of these environmental nucleosides remain unclear and whether they are serve as a nutrient source for PDAC cells remains to be determined.

The study of PDAC cell metabolism *in vivo* is confounded by the characteristic heterotypic cellular microenvironment of PDAC tumors. Cancer cells represent only a fraction of the cellular composition of these tumors the bulk of which consists of tumor supporting stromal cells including specialized fibroblasts termed stellate cells. Stellate cells directly contribute to PDAC cell metabolism by secreting the amino acid alanine which is scavenged by tumor cells[51]. Interestingly, this process has been shown to be orchestrated by PDAC cells indicating that they are capable of hijacking the metabolism of neighboring cells to fuel their own proliferation and promote their survival. It is clear that heterotypic cellular interactions profoundly influence PDAC cell metabolism and must be considered in the context of metabolism-targeted therapy.

A significant challenge in the targeting of cellular metabolism is the lack of tumor cell selectivity

as cancer cells utilize the same “hard-wired” metabolic pathways present in non-transformed cells. However, the rewiring of metabolism in PDAC cells driven by environmental factors and mutant KRAS may provide unique, actionable metabolic dependencies and a sufficient therapeutic window for selective small molecule metabolism modifiers. Furthermore, pharmacological inhibition KRAS or its downstream effectors may reprogram metabolite production, salvage and utilization in PDAC cells and unlock new metabolic targets.

While the links between mutant KRAS and altered metabolism are well documented in PDAC the regulation of cellular metabolism by other signaling networks, induced by either cell autonomous and environmental factors, is poorly characterized. Significant gaps remain in our understanding of how microenvironmental factors such as cytokines, which are abundant in the PDAC tumor microenvironment, influence metabolism and therapy response. A more complete understanding of this interaction may lead to the identification of new vulnerabilities that can be leveraged by targeted therapies in precisely defined patient populations.

Goals of this work

This thesis describes a search for new regulators of nucleotide metabolism in cancer. Broadly, the goals of the work are to expand the understanding of the molecular links between signaling and metabolic networks and to use this information to define new therapeutic strategies.

Specifically, the goals of this work are:

(i) To evaluate the regulation of nucleotide metabolism by the replication stress response signaling network.

(ii) To investigate the mechanisms by which the a hallmark characteristics of pancreatic ductal adenocarcinoma, cytokine signaling, regulates tumor cell nucleotide metabolism and to identify associated targetable vulnerabilities.

(iii) To identify of new synthetic-lethal interactions arising from impaired dNTP phosphohydrolase activity in cancer cells.

(iv) To identify new small molecule tools to modulate convergent pyrimidine biosynthetic pathways.

Translational significance

Armed with new insight into this fundamental biochemical network we developed new, rationally designed therapeutic approaches to be translated for the treatment of precisely defined patient populations.

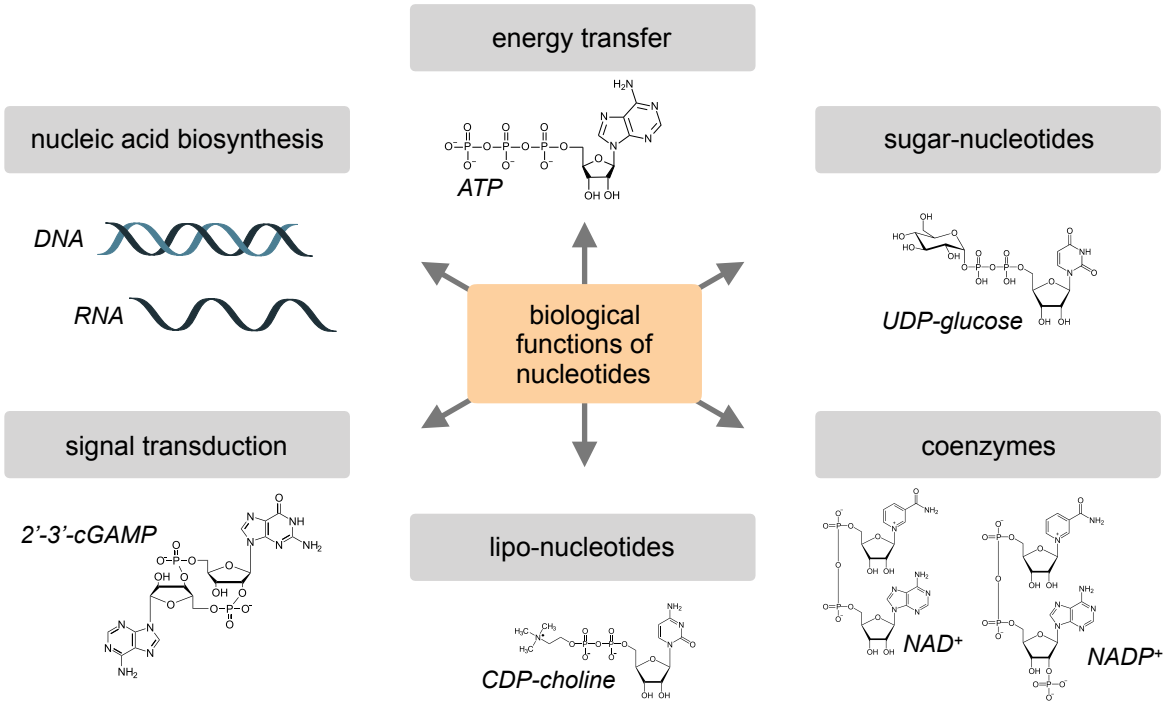

Figure 1.1 | Summary of the biological functions of nucleotides. cGAMP: cyclic guanosine monophosphate–adenosine monophosphate; NAD: nicotinamide adenine dinucleotide; NADP: nicotinamide adenine dinucleotide phosphate.

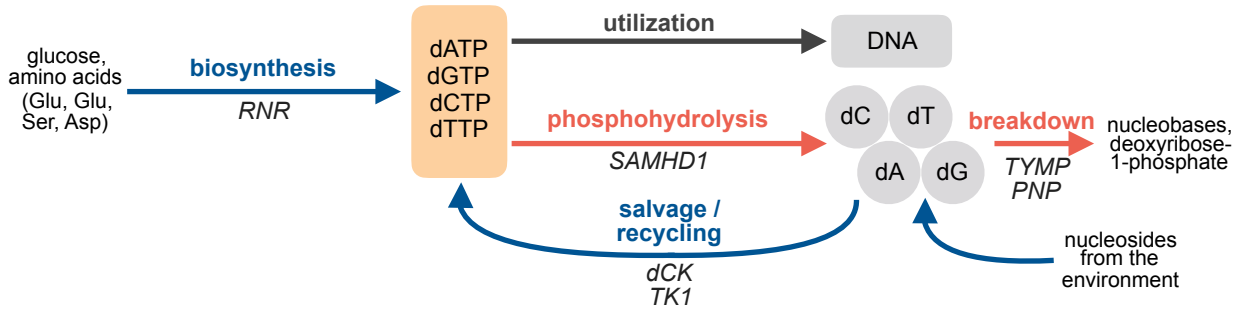

Figure 1.2 | Overview of nucleotide biosynthesis, recycling and catabolism. Schematic overview of key metabolic processes that regulate deoxyribonucleoside triphosphate (dNTP) pool sizes: (i) **biosynthesis** from glucose and amino acids in which a key rate-limiting step is the reduction of ribonucleotide diphosphate (NDPs) to deoxyribonucleotide diphosphates (dNDPs) by RNR; (ii) **utilization** for DNA replication and repair; (iii) **phosphohydrolysis** to deoxyribonucleosides (dNs), which can be (iv) recycled back to dNTPs by deoxyribonucleoside kinases, (v) **nucleoside salvage** from the environment or (vi) **nucleoside breakdown** of nucleosides by catabolic enzymes such as PNP (in the case of dG) or TYMP (in the case of dT). dCTP: deoxycytidine triphosphate; dTTP: thymidine triphosphate; dGTP: deoxyguanosine triphosphate; dATP: deoxyadenosine triphosphate; RNR: ribonucleotide reductase; SAMHD1: sterile alpha-motif and histidine-aspartate domain-containing protein 1; dCK: deoxycytidine kinase; TK1: thymidine kinase-1; PNP: purine nucleoside phosphorylase; TYMP: thymidine phosphorylase.

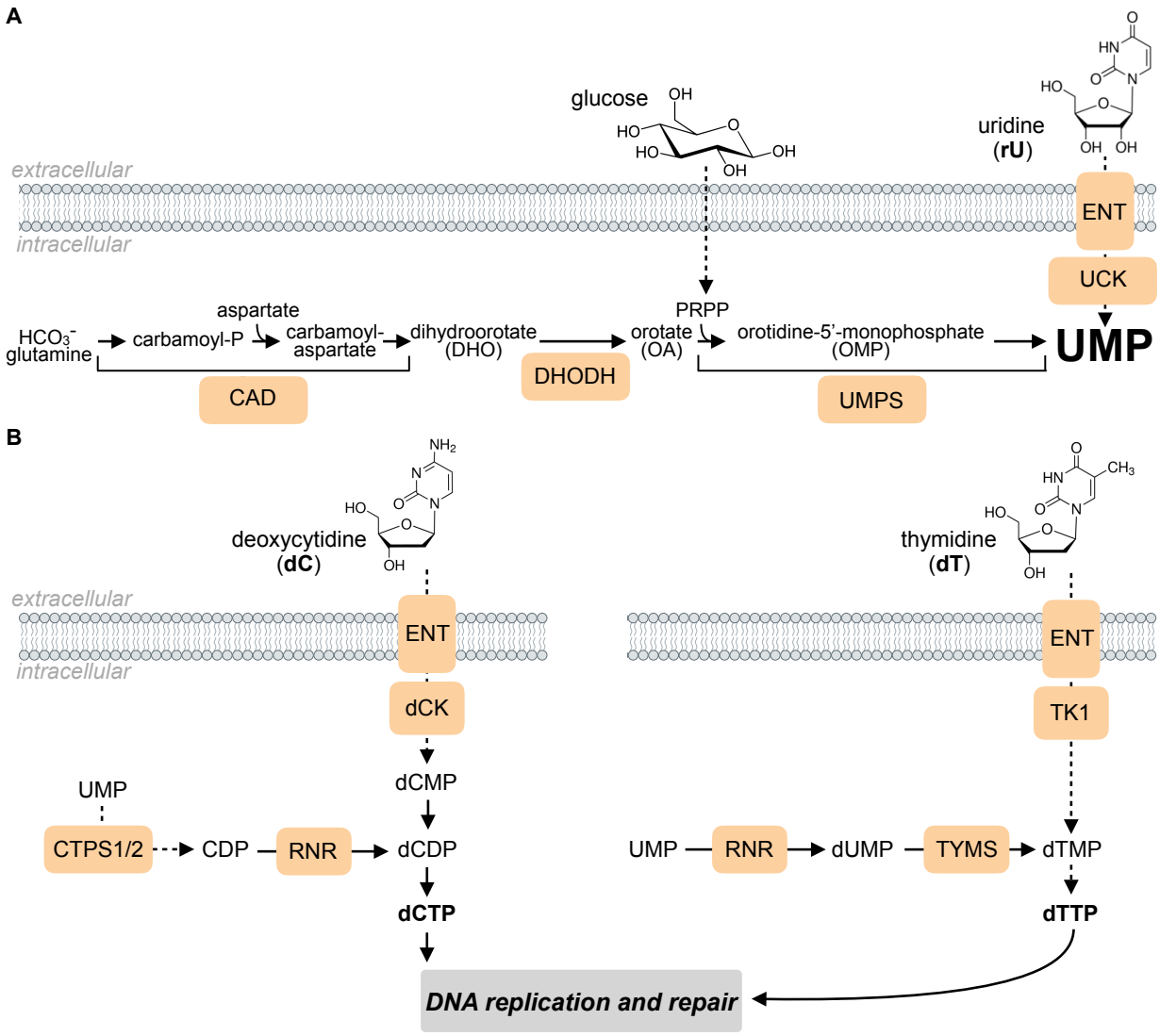

Figure 1.3 | Pyrimidine nucleotides are produced by convergent *de novo* and salvage pathways. DHODH: dihydroorotate dehydrogenase; UMPS: UMP synthase; UCK: uridine/ cytidine kinase; dCK: deoxycytidine kinase; TK1: thymidine kinase 1; RNR: ribonucleotide reductase; PRPP: phosphoribosyl pyrophosphate; TYMS: thymidylate synthase; ENT: equilibrative nucleoside transporter.

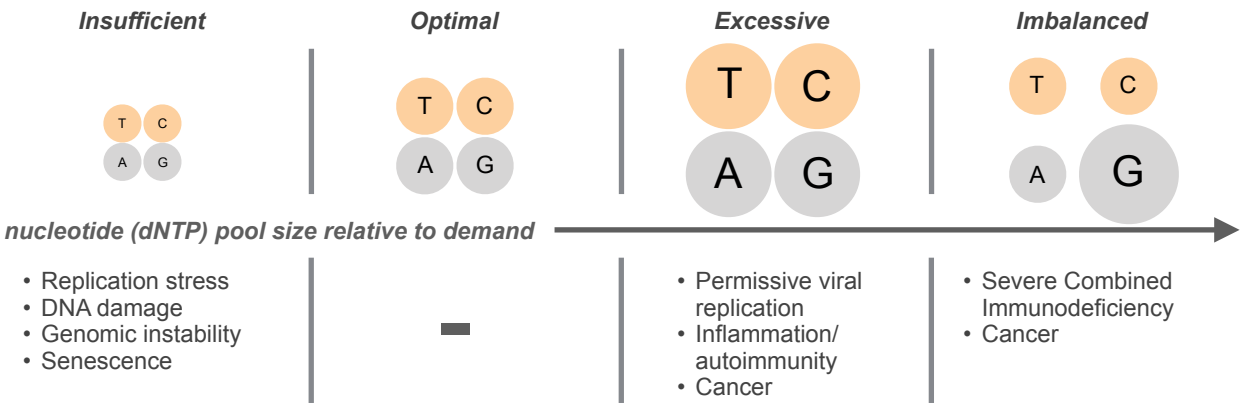

Figure 1.4 | Consequences of nucleotide insufficiency or imbalance. A sufficient, balanced supply of nucleotides (dNTP) is required for cancer cell growth and survival. An insufficient supply of nucleotides results in activation of the replication stress response signaling pathway which restricts proliferation.

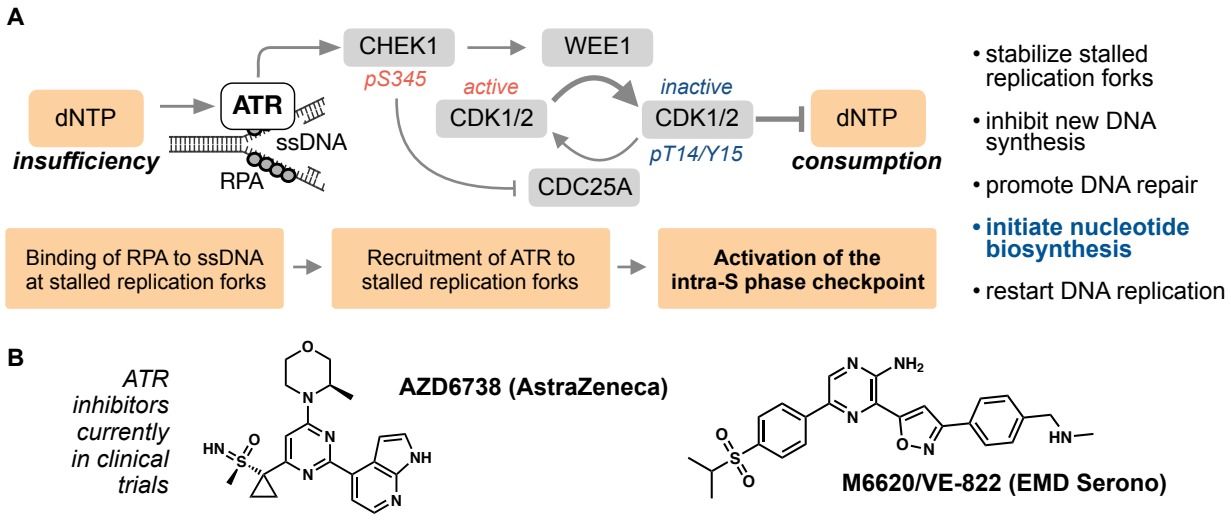

Figure 1.5 | Nucleotide insufficiency triggers activation of the replication stress response signaling pathway. (**A**) Schematic overview of the replication stress response signaling pathway. dNTP insufficiency results in stalling of replication forks and accumulation of RPA-coated single stranded DNA (ssDNA) that recruits and activates ATR, the proximal kinase in the replication stress response pathway. Activated ATR phosphorylates CHEK1 and its downstream target WEE1. WEE1 inactivates CDK1/2 by phosphorylation, restricting new origin firing thereby reducing dNTP consumption. CHEK1 additionally inhibits CDC25A, preventing reactivation of CDK1/2. ATR increases dNTP production and recycling by promoting transcription and preventing degradation of RNR and by directly phosphorylating dCK. (**B**) M6620 (also known as VE-822) and AZD6738 are currently being evaluated in phase I/II clinical trials in combination with chemotherapy, PARP inhibitors or immunotherapy for treatment of various advanced solid tumors. ATR: ataxia-telangiectasia-mutated and Rad3-related kinase; CHEK1: serine/threonine-protein kinase; WEE1: Wee1-like protein kinase; CDK1: cyclin-dependent kinase-1; CDK2: cyclin-dependent kinase-2; CDC25A: cell division cycle 25A.

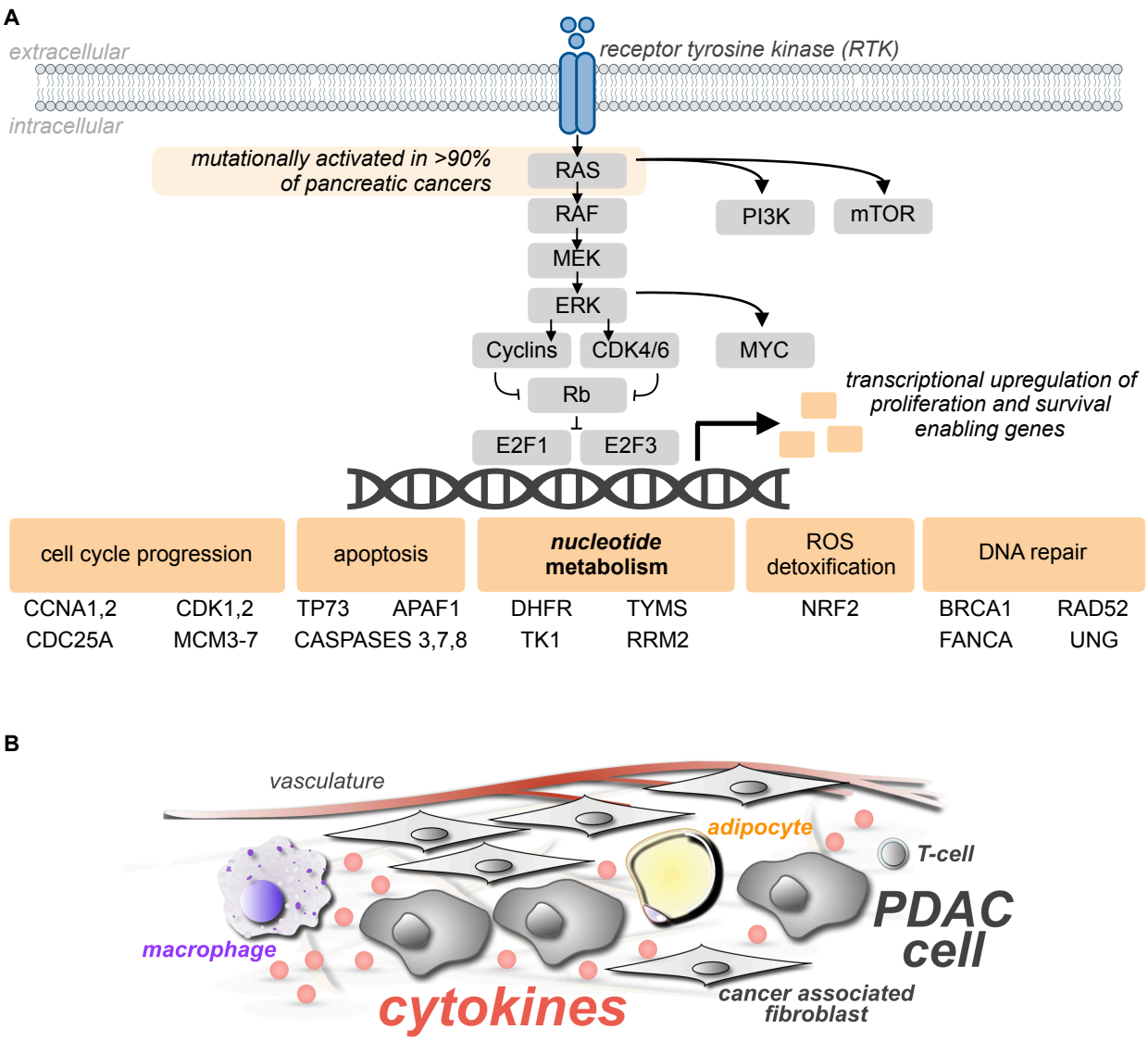

Figure 1.6 | Hallmarks of pancreatic ductal adenocarcinoma (PDAC). (**A**) Schematic overview of the RAS signaling pathway. Mutant RAS controls nucleotide metabolism via transcriptional up-regulation of rate-limiting biosynthetic enzymes DHFR, TYMS, TK1 and RRM2. This up-regulation is achieved by the E2F1 and E2F3 transcription factors which are controlled by Rb. (**B**) Schematic of the PDAC tumor microenvironment.

REFERENCES

1. Reichard, P. Interactions between deoxyribonucleotide and DNA synthesis. Annu Rev Biochem 57, 349-374 (1988).
2. Austin, W. R. et al. Nucleoside salvage pathway kinases regulate hematopoiesis by linking nucleotide metabolism with replication stress. J Exp Med 209, 2215-2228 (2012).
3. Goldstone, D. C. et al. HIV-1 restriction factor SAMHD1 is a deoxynucleoside triphosphate triphosphohydrolase. Nature 480, 379-382 (2011).
4. Evans, D. R. & Guy, H. I. Mammalian pyrimidine biosynthesis: fresh insights into an ancient pathway. J Biol Chem 279, 33035-33038 (2004).
5. Jones, M. E. Pyrimidine nucleotide biosynthesis in animals: genes, enzymes, and regulation of UMP biosynthesis. Annu Rev Biochem 49, 253-279 (1980).
6. Van Rompay, A. R., Norda, A., Lindén, K., Johansson, M. & Karlsson, A. Phosphorylation of uridine and cytidine nucleoside analogs by two human uridine-cytidine kinases. Mol Pharmacol 59, 1181-1186 (2001).
7. Baldwin, S. A., Mackey, J. R., Cass, C. E. & Young, J. D. Nucleoside transporters: molecular biology and implications for therapeutic development. Mol Med Today 5, 216-224 (1999).
8. Reichard, P. & Estborn, B. Utilization of desoxyribosides in the synthesis of polynucleotides. J Biol Chem 188, 839-846 (1951).
9. Mathews, C. K. DNA synthesis as a therapeutic target: the first 65 years. FASEB J 26, 2231-2237 (2012).
10. Radu, C. G. et al. Molecular imaging of lymphoid organs and immune activation by positron emission tomography with a new [18F]-labeled 2'-deoxycytidine analog. Nat Med 14, 783-788 (2008).
11. Kim, W. et al. [18F]CFA as a clinically translatable probe for PET imaging of deoxycytidine kinase activity. Proc Natl Acad Sci U S A 113, 4027-4032 (2016).

12. Shields, A. F. et al. Imaging proliferation in vivo with [F-18]FLT and positron emission tomography. Nat Med 4, 1334-1336 (1998).
13. Toy, G. et al. Requirement for deoxycytidine kinase in T and B lymphocyte development. Proc Natl Acad Sci U S A 107, 5551-5556 (2010).
14. Murphy, J. M. et al. Development of new deoxycytidine kinase inhibitors and noninvasive in vivo evaluation using positron emission tomography. J Med Chem 56, 6696-6708 (2013).
15. Nathanson, D. A. et al. Co-targeting of convergent nucleotide biosynthetic pathways for leukemia eradication. J Exp Med 211, 473-486 (2014).
16. Le, T. M. et al. ATR inhibition facilitates targeting of leukemia dependence on convergent nucleotide biosynthetic pathways. Nat Commun 8, 241 (2017).
17. Halbrook, C. J. et al. Macrophage-Released Pyrimidines Inhibit Gemcitabine Therapy in Pancreatic Cancer. Cell Metab 29, 1390-1399.e6 (2019).
18. Tang, Z. et al. GEPIA: a web server for cancer and normal gene expression profiling and interactive analyses. Nucleic Acids Res 45, W98-W102 (2017).
19. Kumar, D., Viberg, J., Nilsson, A. K. & Chabes, A. Highly mutagenic and severely imbalanced dNTP pools can escape detection by the S-phase checkpoint. Nucleic Acids Res 38, 3975-3983 (2010).
20. Kunz, B. A. et al. International Commission for Protection Against Environmental Mutagens and Carcinogens. Deoxyribonucleoside triphosphate levels: a critical factor in the maintenance of genetic stability. Mutat Res 318, 1-64 (1994).
21. Buckley, R. H. The multiple causes of human SCID. J Clin Invest 114, 1409-1411 (2004).
22. Filosto, M. et al. Mitochondrial Neurogastrointestinal Encephalomyopathy (MNGIE-MTDPS1). J Clin Med 7, (2018).
23. Lane, A. N. & Fan, T. W. Regulation of mammalian nucleotide metabolism and biosynthesis. Nucleic Acids Res 43, 2466-2485 (2015).

24. Beyaert, M., Starczewska, E., Van Den Neste, E. & Bontemps, F. A crucial role for ATR in the regulation of deoxycytidine kinase activity. Biochem Pharmacol 100, 40-50 (2016).
25. Pfister, S. X. et al. Inhibiting WEE1 Selectively Kills Histone H3K36me3-Deficient Cancers by dNTP Starvation. Cancer Cell 28, 557-568 (2015).
26. Harbour, J. W. & Dean, D. C. The Rb/E2F pathway: expanding roles and emerging paradigms. Genes Dev 14, 2393-2409 (2000).
27. Santana-Codina, N. et al. Oncogenic KRAS supports pancreatic cancer through regulation of nucleotide synthesis. Nat Commun 9, 4945 (2018).
28. Zeman, M. K. & Cimprich, K. A. Causes and consequences of replication stress. Nat Cell Biol 16, 2-9 (2014).
29. Dobbelstein, M. & Sørensen, C. S. Exploiting replicative stress to treat cancer. Nat Rev Drug Discov 14, 405-423 (2015).
30. Lin, W. C., Lin, F. T. & Nevins, J. R. Selective induction of E2F1 in response to DNA damage, mediated by ATM-dependent phosphorylation. Genes Dev 15, 1833-1844 (2001).
31. D'Angiolella, V. et al. Cyclin F-mediated degradation of ribonucleotide reductase M2 controls genome integrity and DNA repair. Cell 149, 1023-1034 (2012).
32. Brown, J. S., O'Carrigan, B., Jackson, S. P. & Yap, T. A. Targeting DNA Repair in Cancer: Beyond PARP Inhibitors. Cancer Discov 7, 20-37 (2017).
33. Gilad, O. et al. Combining ATR suppression with oncogenic Ras synergistically increases genomic instability, causing synthetic lethality or tumorigenesis in a dosage-dependent manner. Cancer Res 70, 9693-9702 (2010).
34. Nghiem, P., Park, P. K., Kim Ys, Y. S., Desai, B. N. & Schreiber, S. L. ATR is not required for p53 activation but synergizes with p53 in the replication checkpoint. J Biol Chem 277, 4428-4434 (2002).
35. Di Micco, R. et al. Oncogene-induced senescence is a DNA damage response triggered by DNA hyper-replication. Nature 444, 638-642 (2006).

36. Aird, K. M. & Zhang, R. Nucleotide metabolism, oncogene-induced senescence and cancer. Cancer Lett 356, 204-210 (2015).
37. Bester, A. C. et al. Nucleotide deficiency promotes genomic instability in early stages of cancer development. Cell 145, 435-446 (2011).
38. Luo, J., Solimini, N. L. & Elledge, S. J. Principles of cancer therapy: oncogene and non-oncogene addiction. Cell 136, 823-837 (2009).
39. Siegel, R. L., Miller, K. D. & Jemal, A. Cancer statistics, 2019. CA Cancer J Clin 69, 7-34 (2019).
40. Rahib, L. et al. Projecting cancer incidence and deaths to 2030: the unexpected burden of thyroid, liver, and pancreas cancers in the United States. Cancer Res 74, 2913-2921 (2014).
41. Ryan, D. P., Hong, T. S. & Bardeesy, N. Pancreatic adenocarcinoma. N Engl J Med 371, 1039-1049 (2014).
42. Bailey, P. et al. Genomic analyses identify molecular subtypes of pancreatic cancer. Nature 531, 47-52 (2016).
43. Ni, D. et al. Drugging K-Ras. Pharmacol Ther (2019).
44. Von Hoff, D. D. et al. Increased survival in pancreatic cancer with nab-paclitaxel plus gemcitabine. N Engl J Med 369, 1691-1703 (2013).
45. Conroy, T. et al. FOLFIRINOX or Gemcitabine as Adjuvant Therapy for Pancreatic Cancer. N Engl J Med 379, 2395-2406 (2018).
46. Collisson, E. A. et al. Subtypes of pancreatic ductal adenocarcinoma and their differing responses to therapy. Nat Med 17, 500-503 (2011).
47. Cancer, G. A. R. N. E. A. A. & Cancer, G. A. R. N. Integrated Genomic Characterization of Pancreatic Ductal Adenocarcinoma. Cancer Cell 32, 185-203.e13 (2017).
48. Golan, T. et al. Maintenance Olaparib for Germline. N Engl J Med 381, 317-327 (2019).

49. Biancur, D. E. & Kimmelman, A. C. The plasticity of pancreatic cancer metabolism in tumor progression and therapeutic resistance. Biochim Biophys Acta Rev Cancer 1870, 67-75 (2018).
50. Ying, H. et al. Oncogenic Kras maintains pancreatic tumors through regulation of anabolic glucose metabolism. Cell 149, 656-670 (2012).
51. Son, J. et al. Glutamine supports pancreatic cancer growth through a KRAS-regulated metabolic pathway. Nature 496, 101-105 (2013).
52. Sousa, C. M. et al. Pancreatic stellate cells support tumour metabolism through autophagic alanine secretion. Nature 536, 479-483 (2016).
53. Yang, A. et al. Autophagy is critical for pancreatic tumor growth and progression in tumors with p53 alterations. Cancer Discov 4, 905-913 (2014).
54. Elliott, I. A. et al. Lysosome inhibition sensitizes pancreatic cancer to replication stress by aspartate depletion. Proc Natl Acad Sci U S A 116, 6842-6847 (2019).

CHAPTER 2

Targetable Dependence on Convergent Nucleotide Biosynthetic Pathways in Leukemia is Facilitated by ATR Inhibition

ABSTRACT

Leukemia cells rely on two nucleotide biosynthetic pathways, *de novo* and salvage, to produce dNTPs for DNA replication. Using metabolomic, proteomic, and phosphoproteomic approaches, we show that inhibition of the replication stress sensing kinase ataxia telangiectasia and Rad3-related protein (ATR) reduced the output of both *de novo* and salvage pathways by regulating the activity of their respective rate-limiting enzymes, ribonucleotide reductase (RNR) and deoxycytidine kinase (dCK), via distinct molecular mechanisms. Quantification of nucleotide biosynthesis in ATR-inhibited acute lymphoblastic leukemia (ALL) cells revealed substantial remaining *de novo* and salvage activities, and could not eliminate the disease *in vivo*. However, targeting these remaining activities with RNR and dCK inhibitors triggered lethal replication stress *in vitro* and long-term disease-free survival in mice with B-ALL, without detectable toxicity. The functional interplay between alternative nucleotide biosynthetic routes and ATR provides new therapeutic opportunities in leukemia and potentially other cancers.

INTRODUCTION

Unabated proliferation is a hallmark of cancer which requires new DNA synthesis from deoxyribonucleotide triphosphates (dNTPs). However, cellular dNTP levels only suffice to sustain a few minutes of DNA replication indicating that dNTP pools are produced "on demand" via tightly regulated biosynthetic pathways[1]. These deoxynucleotide biosynthetic pathways, termed *de novo* and salvage, rely on distinct carbon and nitrogen sources[2]. *De novo* pathways use glucose and amino acids to produce ribonucleotide diphosphates (rNDPs) which are converted into deoxyribonucleotide diphosphates (dNDPs) by ribonucleotide reductase (RNR), a two-subunit enzyme complex[3] upregulated in most cancers[4]. Salvage pathways convert preformed ribonucleosides, deoxyribonucleosides, and nucleobases into nucleotides through the actions of metabolic kinases and phosphoribosyltransferases[2]. Amongst nucleoside salvage kinases, deoxycytidine kinase (dCK) has the broadest substrate specificity, encompassing both purine and pyrimidine nucleosides[5]. While tumors are thought to predominantly rely on *de novo* pathways to produce nucleotides[6], scavenging of preformed nucleosides via dCK and other salvage kinases may also play important roles in the economy of nucleotide metabolism in cancer cells. Many of the cell lines included in the Cancer Cell Line Encyclopedia (CCLE)[7,8] express dCK at higher levels than the corresponding normal tissues. Increased tumor dCK expression relative to matched normal tissues also occurs in patient samples, as evidenced by RNASeq data from The Cancer Genome Atlas (TCGA, http://cancergenome.nih.gov)[9,10]. Moreover, *in vivo*, cancer cells often encounter limited supplies of essential *de novo* pathway substrates, e.g. glucose, glutamine and aspartate, because of their avid consumption of these nutrients and inadequate vascularization[11]. An insufficient *de novo* biosynthetic capacity, coupled with an increased demand for dNTPs due to unabated proliferation driven by oncogenic signaling, might increase the dependency of certain tumors on salvage pathways for nucleotide production.

Consistent with this hypothesis, we previously demonstrated that acute lymphoblastic leukemia (ALL) cells display nucleotide biosynthetic plasticity[12], defined as the ability to compensate for the inhibition of either *de novo* or salvage pathways by upregulating the alternate pathway. These metabolic transitions occurred both *in vitro* and *in vivo*; moreover partial inhibition of both *de novo* and salvage biosynthetic routes was required for therapeutic activity in animal models of T and B-ALL[12].

Collectively, these results described above suggest that, in acute leukemia, and potentially in other cancers, nucleoside salvage biosynthetic pathways may be metabolic non-oncogene addictions[13] targetable by specific inhibitors. However, since both *de novo* and salvage biosynthetic pathways also operate in normal cells[14,15], a better understanding of the signaling mechanisms that regulate their activity in cancer cells may lead to the development of more effective targeted therapies. In this context, the mTOR[16–18], Myc[19,20] and Ras[21] pathways have been shown to regulate nucleotide biosynthesis. The replication stress response pathway, constitutively upregulated in many tumors, also plays important roles in regulating nucleotide metabolism, given its unique ability to 'sense' dNTP insufficiency[22]. The most proximal enzyme in the cellular response to replication stress is ataxia telangiectasia and Rad3-related protein (ATR), a serine threonine kinase activated at stalled replication forks[23] in response to nucleotide insufficiency and other replication defects. In addition to its well-established role in regulating origin firing and promoting fork stability[24], ATR has been recently linked to nucleotide metabolism. Inhibition of ATR, or its downstream effector kinases CHEK1 and WEE1, reduces dNTP levels in multiple cancer cell lines[25]. This effect of ATR inhibition was proposed to involve the downregulation of the small RNR subunit RRM2, particularly at the G1/S transition[26], when cells are most susceptible to nucleotide insufficiency[27]. Intriguingly, ATR also regulates dCK activity in several solid tumor and myeloid leukemia cells by phosphorylation at serine 74[28]. This post-translational modification (PTM) modulates dCK's catalytic properties and substrate specificity[29,30]. While collectively these findings support a connection between ATR signaling and dNTP production, the metabolic consequences of ATR inhibition in malignancies with

nucleotide biosynthetic plasticity are yet to be defined. Here, we examined ATR modulation of dNTP synthesis and utilization for DNA synthesis, and the consequences for tumor cell viability in culture and *in vivo* in ALL models, using quantitative approaches. A targeted multiplexed mass spectrometric (MS) assay was developed to measure the differential contributions of the *de novo* and salvage pathways both to nucleotide pools and newly replicated DNA. This assay was used in conjunction with proteomic and phosphoproteomic MS approaches to investigate the mechanisms responsible for alterations in nucleotide biosynthesis induced by ATR inhibition. In addition, we compared direct targeting of *de novo* and salvage rate-limiting enzymes, using specific inhibitors versus indirect inhibition of these enzymes via interference with ATR signaling. These studies identified a synthetically lethal interaction between inhibition of convergent nucleotide biosynthetic routes and ATR in ALL. This combination is therapeutically exploitable *in vivo*, resulting in long-term, disease-free survival in a systemic p185$^{BCR\text{-}ABL}$*Arf*$^{-/-}$ pre-B-ALL mouse model representative of the human disease[31–33]. Overall, our findings suggest that nucleotide biosynthetic plasticity in lymphoblastic leukemia cells, and potentially in other malignancies, is mediated by both ATR signaling and nucleotide metabolic adaptive mechanisms which may be targetable without overt toxicity to normal tissues, using existing small molecule inhibitors.

RESULTS

Inhibition of ATR and dCK impairs G1/S transition in T-ALL cells and alters substrate utilization for dCTP biosynthesis.

Human T-ALL cells CCRF-CEM (subsequently referred to as “CEM”) express dCK and exhibit constitutive phosphorylation of the ATR effector kinase CHEK1 on Serine 345 (pS345; **Figure S2.2A**), a marker of replication stress[34]. CHEK1 pS345 levels are reduced following exposure to VE-822, a specific ATR inhibitor[35] (**Figure S2.2A**). To investigate whether ATR inhibition increases the dependence of T-ALL cells on dCK activity at the G1/S transition, CEM cells were synchronized in G1 using Palbociclib, a CDK4/6 inhibitor[36,37], and then released from G1 arrest into media containing VE-822 and/or DI-82, a high affinity competitive dCK inhibitor (dCKi) developed by our group[38]. At various time points following G1 release, cells were pulsed for 1 h with 5’-ethynyl-2’-deoxyuridine (EdU) to analyze cell cycle kinetics by flow cytometry. Six hours after release from G1, ~25% of cells in the untreated and single drug treated groups advanced into early S-phase (designated as S1, in blue, **Figure 2.1A**). In contrast, only 16% of cells treated with both VE-822 and dCKi entered S1. Twelve hours after release from G1 arrest, 16% fewer VE-822-treated cells entered the later part of S-phase (designated as S2, in red, **Figure 2.1B**) compared to untreated cells. While at this time point dCK inhibition alone did not affect the number of cells that progressed beyond early S phase, progression to late S-phase was significantly impeded (**Figure S2.2B**). Co-inhibition of ATR and dCK decreased the percentage of cells that reached S2 by five-fold relative to untreated cells (**Figure 2.1B**). The effects of ATR inhibition on cell cycle kinetics were partially rescued by nucleotide supplementation, in a dCK-dependent manner (**Figures S2.2C, S2.2D**).

To further investigate the functions of dCK and ATR at the G1/S transition in CEM cells, a non-targeted liquid chromatography mass spectrometry (LC-MS) assay was used to determine the utilization of labeled [$^{13}C_6$]glucose and [$^{13}C_9$,$^{15}N_3$]deoxycytidine, the main substrates for *de novo* and salvage nucleotide biosynthesis, respectively. Of the 166 metabolites identified in CEM cells

treated with VE-822 and/or dCKi, 105 metabolites found in all four treatment groups contained glucose-derived ^{13}C atoms. While ATR inhibition did not decrease glucose uptake and labeling of glycolytic intermediates (**Figure S2.3**), it significantly decreased glucose utilization for 29 other metabolites (**Figure 2.1C**). These metabolites included intermediates such as rUTP, rCTP, and rCDP in the *de novo* dCTP biosynthesis (**Figure S2.1D**). These data indicate that ATR inhibition impacts glucose utilization for *de novo* nucleotide biosynthesis. However, several deoxyribonucleotides, including dCTP, were below the limit of detection of the non-targeted LC-MS approach, raising the concern that the sensitivity of this assay is not sufficient to measure the contribution of the salvage pathway or the ratio of *de novo* and salvage biosynthesis to these pools. To address this problem, a newly developed targeted mass spectrometric assay was developed (**Figures 2.1E, S2.4**). In this assay, samples containing either extracted dNTPs or hydrolyzed DNA from labeled cells are separated by liquid chromatography for detection by a triple quadrupole mass spectrometer (QQQ) using multiple reaction monitoring (LC-MS/MS-MRM). The first (Q1) and third (Q3) quadrupoles function as mass filters, while the second (Q2) quadrupole serves as a collision chamber (**Figure 2.1E**). For instance, to profile the biosynthetic composition of deoxycytidine (dC) derived from hydrolyzed DNA or dCTP, an intact, protonated dC ion is selected in Q1, followed by fragmentation of the glycosidic bond, which releases in Q2 a protonated nucleobase, cytosine, that is filtered in Q3 and detected to generate an ion chromatogram. The peak areas for the ion chromatograms of salvage [$^{13}C_9$,$^{15}N_3$]dC (red trace), *de novo* [$^{13}C_5$]dC (black trace, from [$^{13}C_6$]glucose) and unlabeled dC (gray trace) (**Figure 2.1E**) are used to determine the relative contributions of the *de novo* and salvage routes both to dCTP pools and to dCTP incorporated into DNA.

Since dCK phosphorylates not only dC but also dA and dG[5], the targeted LC-MS/MS-MRM assay was first used to determine whether, in T-ALL cells, dCK mediates the salvage of multiple deoxyribonucleosides (dNs). However, salvaging of purine dNs via dCK occurred only if the catabolic enzymes which degrade these dNs, adenosine deaminase (ADA) and purine nucleoside phosphorylase (PNP), were inhibited pharmacologically (**Figure S2.5, S2.6**). Since

inactivating mutations in ADA and PNP have been associated with severe combined immunodeficiency[39], but not with cancer, we focused on examining the metabolic fate of dC as the most relevant dCK substrate in ATR-inhibited T-ALL cells for salvage biosynthesis. CEM cells were collected at multiple points after release from Palbociclib-induced G1 arrest into media containing VE-822 and/or dCKi, as well as substrates for the *de novo* and salvage pathways, [$^{13}C_6$]glucose and [$^{13}C_9$, $^{15}N_3$]dC, respectively. At each of the examined time points, free dCTP pools in untreated cells were predominantly synthesized by the salvage pathway from [$^{13}C_9$,$^{15}N_3$]dC via dCK, with only a small contribution from [$^{13}C_6$]glucose via the *de novo* pathway (**Figure 2.1F**). While ATR inhibition alone did not alter free dCTP levels or their biosynthetic origins (e.g. *de novo vs*. salvage), dCKi either alone or in combination with VE-822, nearly eliminated the contribution of the salvage pathway and reduced the amount of free dCTP by ~50% at the 12 h time point.

In contrast to the free dCTP pool, which was predominantly derived from the salvage pathway, dCTP incorporated into newly replicated DNA of CEM cells was produced in equal proportions by the *de novo* and salvage pathways (**Figure 2.1G**). This observation is consistent with previous findings that *de novo* synthesized dCTP is more readily incorporated in DNA than is dCTP synthesized by the salvage pathway[12]. ATR inhibition reduced the DNA incorporation of both *de novo* and salvage produced dCTP, yielding a combined 30% reduction in overall DNA labeling compared to untreated cells at the 12 h time point (**Figure 2.1G**). This reduction is consistent with the literature showing replication fork collapse and delays in restarting DNA replication following ATR inhibition in other cell types[40–43]. dCK inhibition abolished the incorporation of salvage produced dCTP into newly replicated DNA and triggered a compensatory increase in the DNA incorporation of *de novo* generated dCTP. This compensatory response was suppressed in cells treated with both VE-822 and dCKi (**Figure 2.1G**).

ATR inhibition alters protein and phosphorylation levels of *de novo* and salvage nucleotide biosynthetic enzymes.

To investigate the molecular mechanisms underlying the metabolic consequences of ATR and dCK inhibition, global changes in protein expression were assessed in CEM cells using quantitative nano-liquid chromatography tandem mass spectrometry (nLC-MS/MS) (**Figure 2.2A**). Chemical isotope coding following reductive dimethylation of peptide N-termini and lysine primary amines with differential stable isotopes (light:medium:heavy) was used to compare expression of experimental (VE-822, dCKi, and VE-822 + dCKi) samples to controls (untreated, NT) by mixing equal proportions for triplex nLC-MS/MS quantitative analyses. The proteomics dataset was filtered for proteins identified in all treatment groups in three independent experiments with coefficients of variation <20%. This yielded 1757 proteins with relative fold changes in treated *vs*. untreated cells ranging from 0.45 to 1.83. Of these, about 3% (46 proteins) displayed statistically significant (as determined by one-way ANOVA and false discovery rate cut-offs) fold changes in expression (>20%) in at least one treatment group (**Figure 2B**). Protein levels of both RNR subunits, RRM1 and RRM2, as well as thymidylate synthase (TYMS) decreased by more than 20% following ATR inhibition (**Figure 2.2C**). Changes in the expression of *de novo* enzymes observed in synchronous cells also occurred with ATR inhibition in asynchronous CEM cells (**Figure 2.2D**), thereby arguing against the possibility of experimental artifacts introduced by Palbociclib-mediated cell cycle synchronization. The reduction in RRM2 protein levels induced by ATR inhibition was accompanied by an ~50% decrease in the phosphorylation of RRM2 on threonine 33 (pT33) (**Figure 2.2E**), a phosphosite previously linked to the stability of the RRM2 subunit[44].

ATR inhibition decreased dNTP levels in several solid tumor-derived cell lines and has been linked to reduced RRM2 levels[26,45]. However, it remains unclear to what degree RRM2 protein levels are rate-limiting for *de novo* dCTP biosynthesis. To further investigate the relationship between RRM2 protein levels and dCTP biosynthesis, we knocked down RRM2 in CEM cells using shRNA (**Figure S2.7A**). RRM2 levels in the CEM shRNA^{RRM2} cells were reduced by 35–

50%, as determined by quantitative nLC-MS/MS and intracellular flow cytometry analyses (**Figures S2.7A, S2.7B**). The CEM shRNA^{RRM2} cells exhibited approximately 30% lower incorporation of *de novo* synthesized dCTP into newly replicated DNA compared to control cells (**Figure S2.7C**); a response comparable with the effects of pharmacological ATR inhibition (**Figure 2.1G**). These findings suggest that the RRM2 regulation by ATR is an important determinant of *de novo* dCTP biosynthesis in T-ALL cells. Since ATR inhibition reduced RRM2 levels by only 20%, it is likely that there are other mechanisms by which ATR regulates *de novo* dCTP biosynthesis. These additional mechanisms could include reduced levels of the large RNR subunit, RRM1 (**Figures 2.2C, 2.2D**), and/or changes in yet to be identified regulatory PTMs in RRM1 and RRM2 that are modulated directly or indirectly by ATR signaling.

In contrast to the reduced RRM1 and RRM2 levels in response to ATR inhibition, dCK protein levels were not affected (**Figures 2.2C, 2.2D**). A recent study showed that ATR directly phosphorylates dCK on serine 74 (dCK pS74) to control its activity under replication stress[28]. We therefore quantified the effects of ATR inhibition on the biosynthetic output and phosphorylation status of dCK. Used as a positive control, the dCKi reduced dCK activity, as defined by contribution of labeled [$^{13}C_9$,$^{15}N_3$]dC to intracellular dCMP, by almost 90% (**Figure 2.2F, left panel**). ATR inhibition in CEM cells reduced the dCK-labeled [$^{13}C_9$,$^{15}N_3$]dCMP pool by ~33% compared to untreated cells (**Figure 2.2F, left panel**). The reduction in dCMP biosynthesis following ATR inhibition correlated with a ~36% decrease in dCK pS74 levels (**Figure 2.2F, right panel**). Collectively, these data (**summarized in Figure 2.2G**) show that, in T-ALL cells, ATR regulates *de novo* and salvage nucleotide biosynthetic pathways by diverse mechanisms involving alterations in total protein (ATR) and protein phosphorylation (dCK) levels. Nonetheless, both *de novo* and salvage pathways retain significant activity in ATR inhibited CEM cells and therefore, may allow these cells to survive therapeutic interventions that interfere with ATR signaling.

Effects of the RNR inhibitor 3-AP on *de novo* and salvage dCTP biosynthesis in CEM cells.

To identify the most potent clinically relevant RNR inhibitors that could be used to target the remaining *de novo* nucleotide biosynthetic activity in ATR inhibited CEM cells we evaluated four compounds, each with a distinct mechanism of action: (3-AP)[46,47], hydroxyurea (HU)[48], gallium maltolate (GaM)[49], and thymidine (dT)[50] (**Figure 2.3A**). Amongst these, 3-AP was the most potent, as indicated by its ability to induce S-phase arrest at concentrations as low as 0.5 μM **(Figures 2.3B, S2.8**). In contrast, 60 to 100-fold higher concentrations of HU, GaM, and dT were required to induce S-phase arrest. The effects of 3-AP on the utilization of [$^{13}C_6$]glucose and [$^{13}C_5$, $^{15}N_3$]dC for nucleotide biosynthesis in CEM cells were investigated (**Figure 2.3C**), using the targeted LC-MS/MS-MRM assay. 3-AP doubled the rCTP and rCDP pools, likely reflecting an inefficient conversion of these pools to dCDP via RNR. However, the most significant change in 3-AP treated cells occurred downstream of RNR and involved a ~19-fold reduction in the incorporation of *de novo* produced dCTP into newly replicated DNA. Along with its effects on *de novo* biosynthesis, 3-AP triggered a compensatory upregulation of the salvage pathway. Salvage dC nucleotide pools doubled in size following 3-AP treatment, and the incorporation of salvage-produced dCTP into DNA increased by >1.5-fold, thereby providing a potential mechanism of resistance to RNR inhibition by 3-AP (**Figure 2.3C**).

Co-targeting ATR, RNR and dCK in CEM cells induces significant alterations in nucleotide metabolism followed by replication stress overload and caspase-8 mediated apoptosis.

Having identified 3-AP as a clinically relevant and potent RNR inhibitor that can be used to directly target the remaining *de novo* activity in ATR treated T-ALL cells, we next quantified the impact of combined ATR, dCK and RNR inhibition on the *de novo* and salvage dCTP biosynthesis in asynchronous CEM cells (**Figure 2.4A**). ATR inhibition decreased the

[$^{13}C_6$]glucose labeling of the rCDP pool by 40% (**Figure 2.4A, rCDP panel**), an effect similar to that observed in the synchronous model (**Figure 2.1D**). In contrast, RNR inhibition increased the size of the rCDP pool (**Figure 2.4A, rCDP panel, 3-AP**). While neither ATR nor RNR inhibition alone had a statistically significant impact on the *de novo* contributions to the dCDP, dCMP and dCTP pools, these pools were nearly abolished when both ATR and RNR were inhibited simultaneously. However, the salvage biosynthetic contributions to the dCMP, dCDP and dCTP pools remained substantial in the absence of the dCKi. In fact, RNR inhibition, alone or combined with ATR inhibition, increased the salvage contributions to the dCMP, dCDP, and dCTP pools by approximately two-fold, indicative of a compensatory mechanism. dCK inhibition abolished this adaptive mechanism to augment these deoxyribonucleotide pools. Consequently, the rate of dCTP incorporation into newly replicated DNA was lowest when all three enzymes were inhibited (**Figure 2.4A, DNA panel**).

Persistent nucleotide insufficiency triggers replication stress characterized by the accumulation of single-stranded DNA (ssDNA) at stalled replication forks, which progresses to DNA double stranded breaks (DSBs)[51]. To investigate these events following ATR, dCK, and RNR inhibition, we used flow cytometry and antibodies against ssDNA[52] as an indicator of replication stress, and phosphorylated histone H2A.X on serine 139 (pH2A.X) as an indicator of DNA damage (**Figure 2.4B**). RNR inhibition by 3-AP increased the percentage of ssDNA$^+$ cells by more than two-fold as early as 0.5 h after treatment, and by greater than three-fold at the 4 h time point. Combined inhibition of ATR and dCK also increased the ssDNA$^+$ and ssDNA$^+$;pH2A.X$^+$ cell populations at the 0.5 and 4 h time points. Addition of an RNR inhibitor resulted in a rapid and massive (>12-fold) expansion of ssDNA$^+$ population at the 0.5 h time point compared to untreated cells, an effect which was further amplified at the later time point (**Figure 2.4B**). Along with these changes, RNR inhibition triggered rapid induction of CHEK1 pS345, a direct downstream target of ATR (**Figure 2.4C**). This PTM was abrogated by VE-822 treatment at the 0.5 h time point and partially inhibited at the 4 h time point. The rebound in CHEK1 pS345 expression at the 4 h time point was likely mediated by the ATR related kinase, ataxia

telangiectasia mutated (ATM), which also phosphorylates CHEK1 on serine 345[53]. ATM was activated in cells treated with the triple combination therapy, as indicated by an increase in phosphorylation of CHEK2 on threonine 68 (pT68, **Figure 2.4C**); a direct target of activated ATM. The induction of CHEK2 pT68 in cells treated with the triple combination therapy coincided with an increase in the pH2A.X-positive population (**Figure 2.4B**) and with cleavage of the apoptotic markers caspase 8 (but not caspase 9), caspase 3, and Poly (ADP-ribose) polymerase (PARP) (**Figure 2.4C**). Consistent with these observations, co-targeting ATR, dCK, and RNR resulted in the highest percentage of apoptotic cells, as measured by Annexin V staining (**Figure S2.9A**). The cytotoxic effect of ATR inhibitors has been attributed to the induction of premature mitotic entry of cells undergoing DNA replication, an event that exacerbates the level of replication stress and DNA damage[54,55]. Consistent with this model, ATR inhibition increased the percentage of S-phase CEM cells with phosphorylation of histone 3 on serine 10 (H3 pS10), a marker for mitotic kinase activation. This effect was significantly amplified in the triple combination therapy and correlated with the induction of apoptosis (**Figure S2.9B**).

ATR inhibition alone is marginally effective in a systemic primary B-ALL mouse model.

To investigate the *in vivo* efficacy and tolerability of co-targeting alternative nucleotide biosynthetic pathways and ATR, we used a previously described primary *BCR-ABL*-expressing *Arf*-null pre-B ($p185^{BCR\text{-}ABL}Arf^{-/-}$) model which is difficult-to-treat and thought to be representative of the human disease[31,33]. When compared with 31 cancer cell lines of different origins, $p185^{BCR\text{-}ABL}Arf^{-/-}$ cells were amongst the most sensitive to ATR inhibition by VE-822, with an IC_{50} value of ~300 nM (**Figure 2.5A**). However, despite its high potency in culture against pre-B-ALL cells, VE-822 alone was only marginally efficacious *in vivo*. C57BL/6 mice inoculated with luciferase expressing $p185^{BCR\text{-}ABL}Arf^{-/-}$ cells succumbed to disease within 17 days; all VE-822 treated mice died of leukemia within 38 days after inoculation (**Figures 2.5B–D**). We then

investigated whether targeting the activities of *de novo* and salvage pathways can improve the efficacy of ATR inhibition in p185$^{BCR\text{-}ABL}$*Arf*$^{-/-}$ cells. Similar to the findings in the human T-ALL cells, targeting these biosynthetic pathways along with ATR was necessary to achieve maximal induction of cell death (**Figure 2.5E**) and complete inhibition of cell growth (**Figures S2.10A, S2.10B**).

Co-targeting ATR, dCK, and RNR is well-tolerated and promotes long-term survival in a systemic primary B-ALL mouse model.

To translate the above cell culture findings into an *in vivo* setting, we first developed a new drug formulation consisting of PEG-200, Transcutol, Labrasol, and Tween-80 blended in a ratio of 5:3:1:1 to solubilize three different drugs (3-AP, VE-822, and dCKi) and achieve therapeutically relevant plasma concentrations via oral delivery (**Figure 2.6A**). Based on the observed plasma pharmacokinetic parameters, 3-AP and dCKi were administered twice/day while VE-822 was administered once/day (**Figure 2.6B**). Treatment was initiated on day 7 post-inoculation of pre-B-ALL when all mice showed evidence of systemic disease, as indicated by whole body bioluminescence imaging (BLI, **Figure 2.6C**, top row, right panel). While mice in the control group succumbed to disease within 17 days, mice in the combination treatment group had significantly lower disease burden on day 17 (**Figure 2.6C, 2.6D**). All treated mice remained disease-free for 442 days after treatment withdrawal, 42 days post-inoculation of pre-B-ALL (**Figure 2.6E**). The combination therapy was well-tolerated, as indicated by maintenance of body weight during treatment (**Figure 2.6F**) and long term survival (over 1 year and currently ongoing) without any detectable pathology. We also assessed the efficacy of the combination therapy when all 3 components were administered once daily. Although this therapeutic scheme appeared to be slightly less efficacious than the twice/day schedule for 3-AP and dCKi, it was well tolerated and four out of five mice had no detectable disease 313 days after treatment withdrawal (**Figure S2.11**). Importantly, removing the dCKi from the combination therapy

significantly reduced the therapeutic efficacy *in vivo* (**Figure S2.12**), a result consistent with cell culture findings (**Figures 2.4, 2.5E, S2.9, S2.10**).

While BCR-ABL tyrosine kinase inhibitors are becoming standard care for patients with Philadelphia chromosome positive ALL[56], therapeutic resistance in pre-B-ALL is common and is caused by the rapid emergence of the T315I BCR-ABL kinase domain ("gatekeeper") mutation which renders this class of kinase inhibitors ineffective[32,56]. To test the combination of VE-822, dCKi, and 3-AP against kinase inhibitor resistant ALL we generated p185$^{BCR\text{-}ABL}$*Arf*$^{-/-}$ T315I mutant cells by exposing the leukemia bearing mice to dasatinib and harvesting drug-resistant cells from bone marrow (**Figures S2.13A–C**). Mice were inoculated with the T315I-positive cells and treated with the combination therapy (**Figures S2.13D–G**). The combination therapy was effective against the highly aggressive dasatinib resistant *in vivo* pre-B-ALL model with 13 of 20 mice being disease-free over 365 days post-inoculation of leukemia cells (**Figure S2.13**). To determine whether mice that did not achieve complete remissions harbor ALL cells that have acquired resistance to the triple combination, we harvested leukemia cells from the bone marrow of the moribund mice. These cells were then used to test the efficacy of the combination treatment in cell culture, and compare it with the original dasatinib-resistant p185$^{BCR\text{-}ABL}$*Arf*$^{-/-}$ pre-B-ALL cells. The harvested leukemia cells responded to the combination treatment as well as did the parental cells (**Figure 2.14**). One potential reason for the incomplete response in some of the treated mice is the rapid engraftment of p185$^{BCR\text{-}ABL}$*Arf*$^{-/-}$ T315I+ pre-B-ALL cells in the brain coupled with the suboptimal penetrability of 3-AP and potentially, dCKi across the blood-brain-barrier.

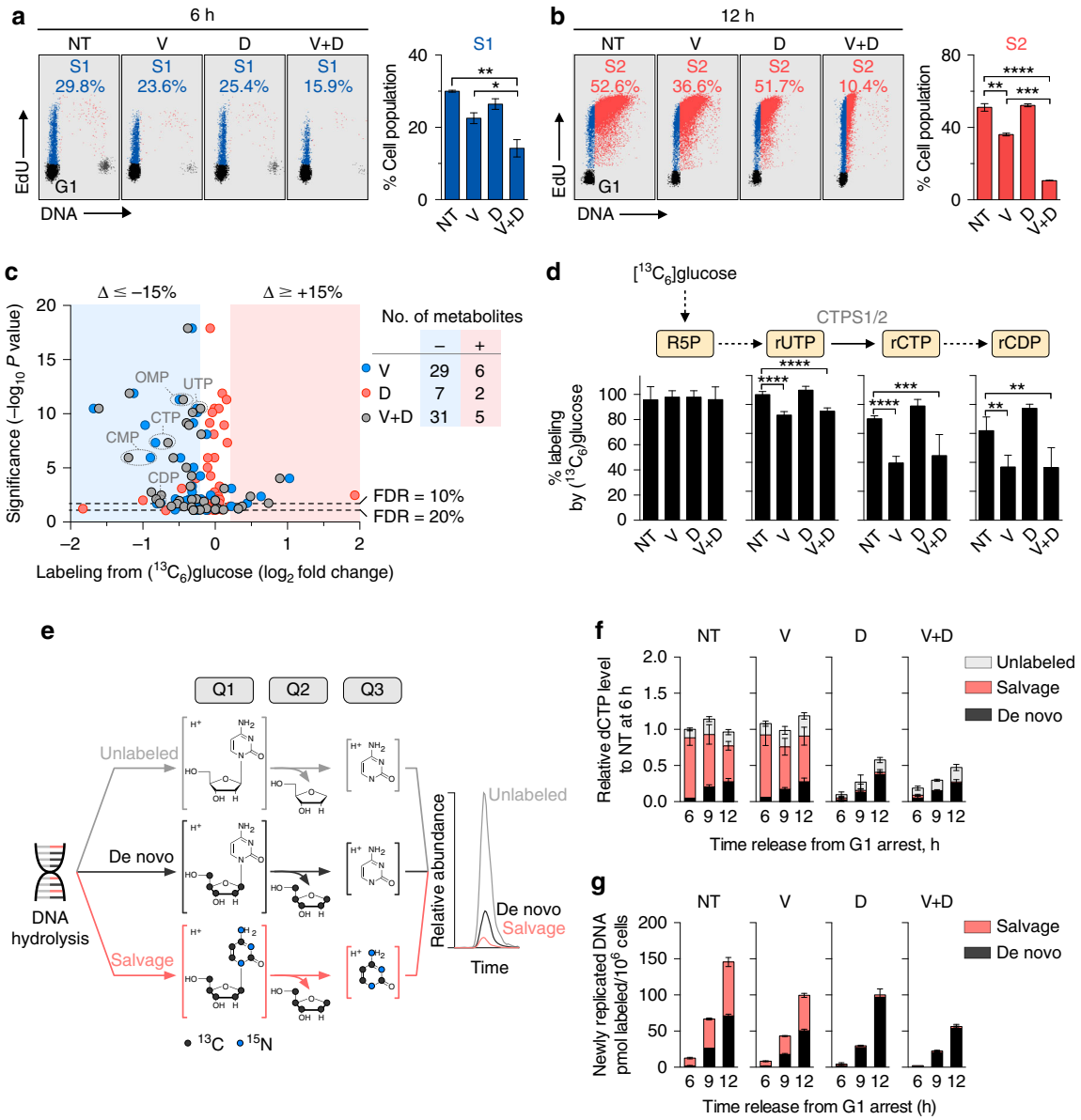

Figure 2.1 | Effects of ATR and dCK inhibition on G1-S transition and substrate utilization for dCTP biosynthesis. (**A and B**) Flow cytometry analysis of EdU incorporation in CEM T-ALL cells treated with VE-822 (1 μM) and/or dCKi (DI-82,1 μM) for 6 (**A**) and 12 h (**B**) following release from G1 arrest, respectively. Bar graphs summarize the percentage of cell populations in S1 (early S-phase) and S2 (mid to late S-phase) at 6 and 12 h (mean ± s.d., n = 2, one-way ANOVA, Bonferroni corrected). Plots are representative of two independent experiments. (**C**) Comparison of metabolite labeling by [$^{13}C_6$]glucose in CEM T-ALL cells treated with VE-822 and/or dCKi for 12 h following release from G1 arrest. Number of metabolites exhibiting

alterations in [$^{13}C_6$]glucose labeling greater than 15% with significance at a false discovery rate (FDR) ≤ 20% are indicated. (**D**) Percent glucose labeling of ribonucleotides intermediates in the *de novo* dCTP biosynthesis (mean ± s.d., n = 6, one-way ANOVA, Bonferroni corrected). (**E**) Workflow for targeted LC-MS/MS-MRM analysis of dCTP incorporated into newly replicated DNA using a triple quadrupole mass spectrometer (QQQ). See text for details and **Figure S2.4** for the LC-MS/MS-MRM analysis of dCTP pools. (**F and G**) Contributions of the *de novo* and salvage pathways to dCTP pools (**F**) and dCTP incorporated into newly synthesized DNA (**G**) in CEM cells treated with VE-822 and/or dCKi after release from G1 arrest (mean ± s.d., n = 3). Results are representative of two independent experiments.

NT = Not treated, V = VE-822, D = dCKi, V+D = VE-822 + dCKi.

* $P < 0.05$; ** $P < 0.01$; *** $P < 0.001$; **** $P < 0.0001$.

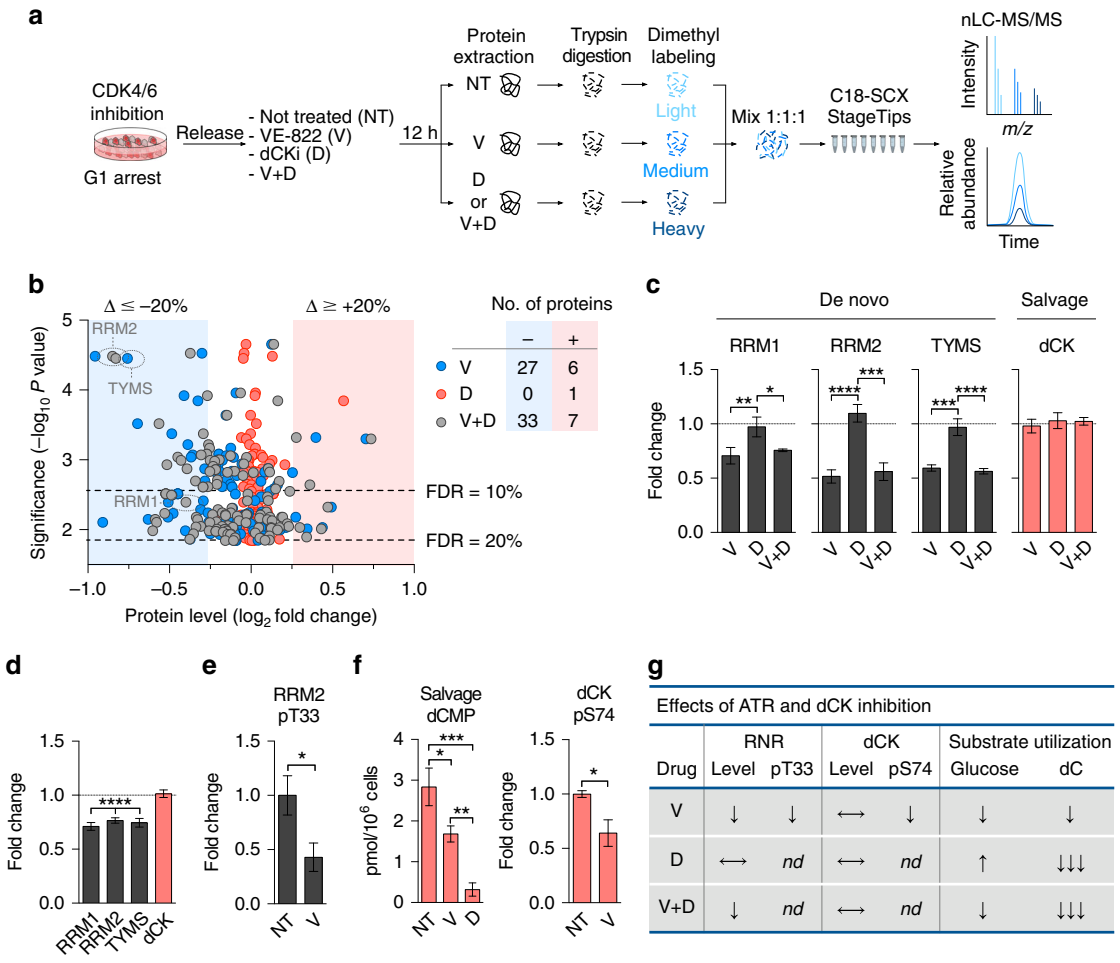

Figure 2.2 | Alterations in total protein and phosphoprotein levels following ATR and dCK inhibition. (**A**) Workflow for quantitative global proteomics using nLC-MS/MS. See text for details. (**B**) Comparison of protein levels in CEM cells treated with VE-822 and/or dCKi for 12 h following release from G1 arrest. Number of proteins exhibiting fold changes greater than 15% changes with significance at a false discovery rate (FDR) ≤ 20% are indicated. (**C**) Protein levels of nucleotide biosynthetic enzymes (mean ± s.d., n = 3, one-way ANOVA, Bonferroni corrected). (**D**) Protein levels in asynchronous CEM cells treated with VE-822 (1 μM) for 12 h (mean ± s.d., n = 3, one sample t-test to assess if the mean of the protein level normalized to untreated control is equal to one). (**E**) Relative level of RRM2 pT33 normalized to RRM2 protein level from (**D**), in asynchronous CEM cells treated with VE-822 (1 μM) for 12 h (mean ± s.d., n = 3, unpaired two-tailed Student's t-test). (**F, left panel**) Salvage produced [$^{13}C_9$,$^{15}N_3$]dCMP in asynchronous CEM cells treated with VE-822 or dCKi for 12 h (mean ± s.d., n = 3, one-way

ANOVA, Bonferroni corrected). (**F, right panel**) Relative levels of dCK pS74, after normalized to dCK protein level from (**D**), in asynchronous CEM cells treated with VE-822 (1 μM) for 12 h (mean ± s.d., n = 3, unpaired two-tailed Student's t-test). (**G**) Summary of the observed effects of ATR and dCK inhibition in CEM cells. ↓ partial decrease/inhibition, ↓↓↓ nearly complete inhibition, ↑ increase, ⟷ no change, *nd* not determined.

NT = Not treated, V = VE-822, D = dCKi, V+D = VE-822 + dCKi.

* $P < 0.05$; ** $P < 0.01$; *** $P < 0.001$; **** $P < 0.0001$.

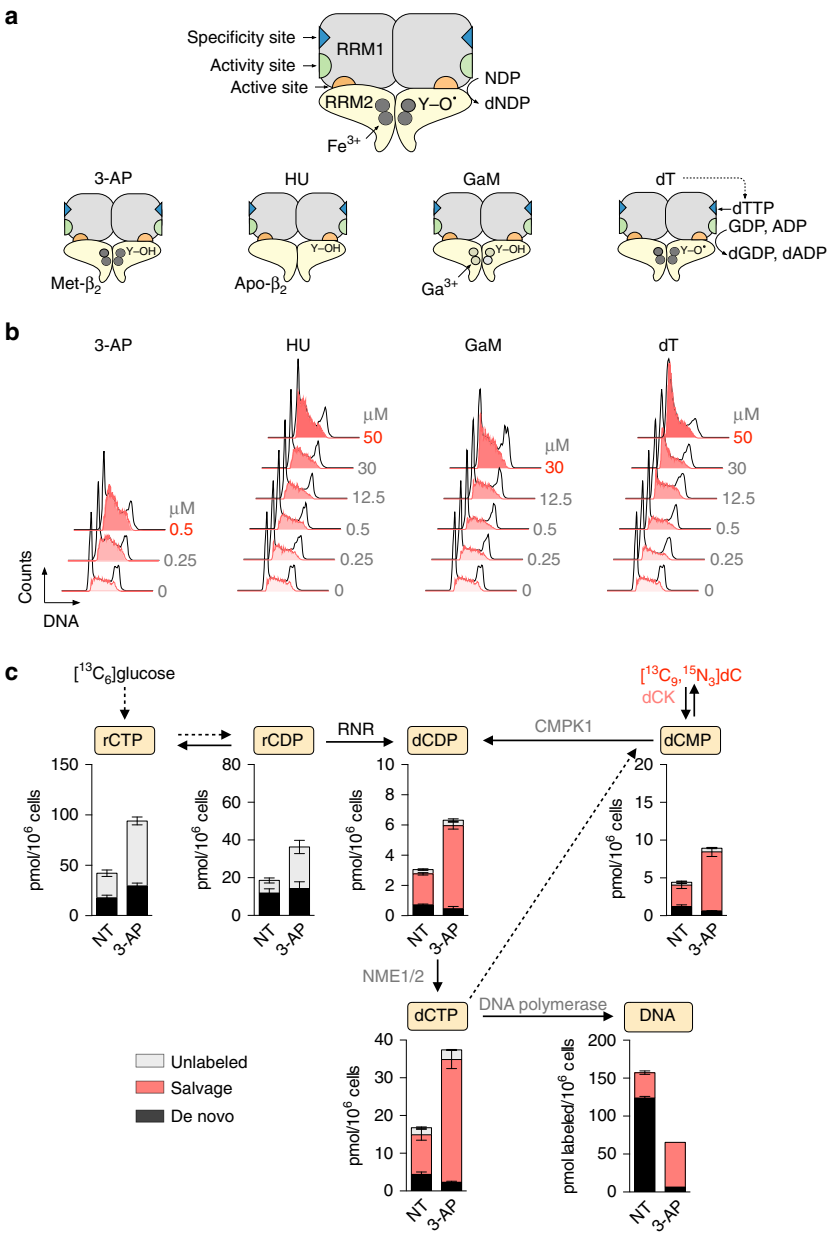

Figure 2.3 | 3-AP potently inhibits RNR and enhances salvage nucleotide biosynthesis.

(**A**) Mechanisms of action of four RNR inhibitors. The two RNR subunits, RRM1 (α) and RRM2 (β) form a catalytically active $\alpha_2\beta_2$ complex. Each RRM1 subunit contains two allosteric regulatory sites (the specificity and activity sites), as well as the active site, where nucleotide reduction occurs. The active form of the RRM2 dimer (holo-β_2) houses the di-iron cofactor and the tyrosyl radical (Y-O•). 3-AP forms a complex with Fe^{2+} which interferes with the regeneration

of the tyrosyl radical in RRM2 therefore promoting the formation of an inactive met-β small subunit which retains its di-iron center[7]. Hydroxyurea (HU) scavenges the RRM2 tyrosyl radical and depletes the di-iron center to form an inactive apo-β form. Gallium maltolate (GaM) releases Ga^{3+} which mimics Fe^{3+} and disrupts the RRM2 di-iron center. Thymidine (dT) is converted via the salvage pathway to thymidine triphosphate (dTTP) which binds to the allosteric specificity site on RRM1 to favor GDP reduction over pyrimidine (CDP and UDP) reduction, thereby resulting in dCTP insufficiency. (**B**) Effects of RNR inhibitors on cell cycle progression. CEM cells were incubated for 24 h with indicated concentrations of RNR inhibitors followed by cell cycle analyses using flow cytometry. Shown in bold red are the concentrations of each RNR inhibitor required to induce a greater than 45% increase in the S-phase population, indicative of S-phase arrest due to nucleotide insufficiency. Cell cycle plots are representative of two independent experiments. See **Figure S2.8** for quantification. (**C**) LC-MS/MS-MRM analysis of dCTP biosynthesis in CEM cells treated with 500 nM 3-AP for 12 h (mean ± s.d., n = 3). NT: not treated.

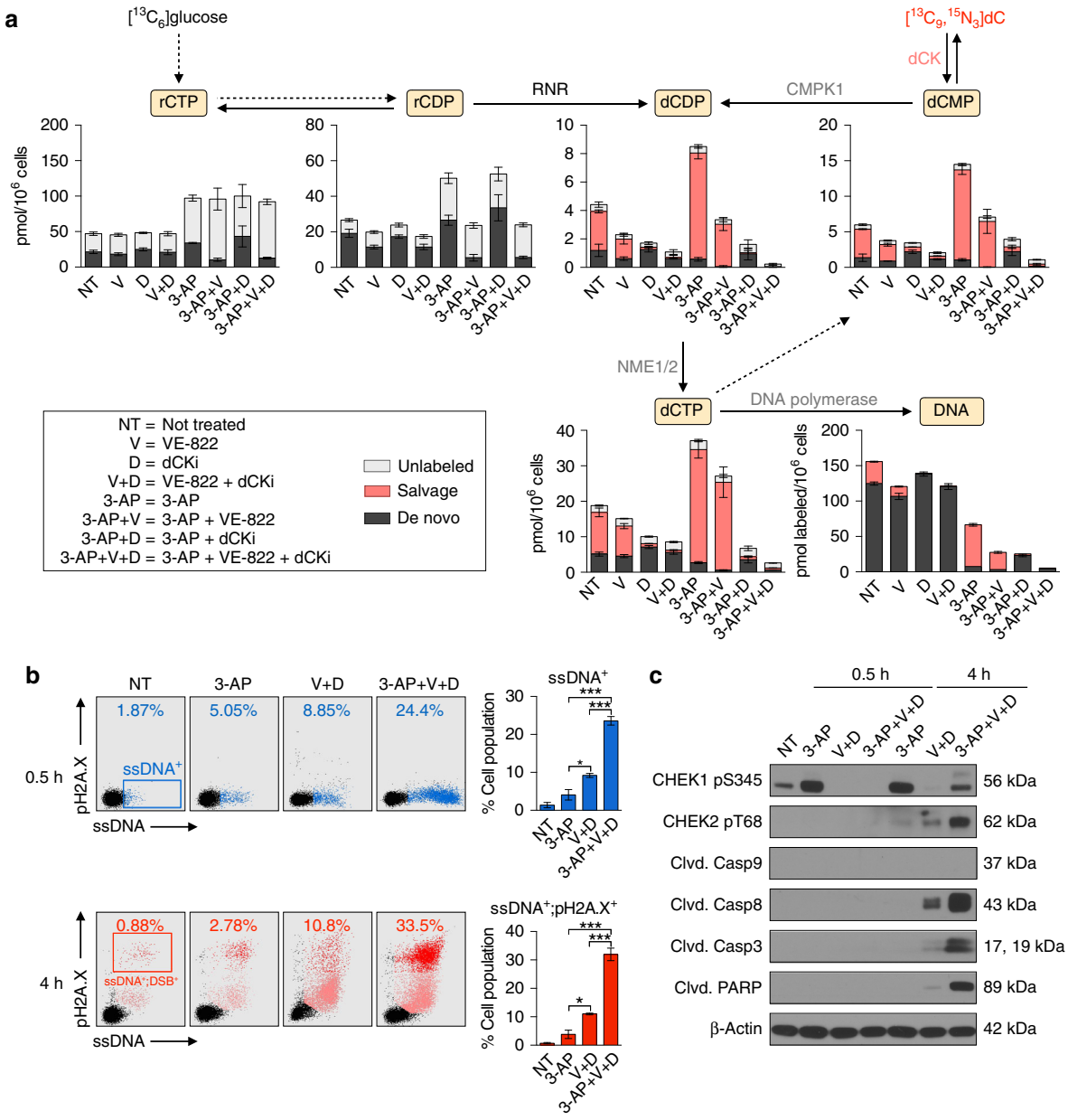

Figure 2.4 | Synthetic lethality induced by combined inhibition of ATR, dCK and RNR. (**A**) LC-MS/MS-MRM analysis of dCTP biosynthesis in CEM cells treated as indicated in the text for 12 h (mean ± s.d., n = 3). Results are representative of two independent experiments. (**B, left panels**) Flow cytometry analyses of ssDNA (F7-26) and pH2A.X levels in CEM cells treated as indicated for 0.5 and 4 h. (**B, right panels**) Bar graphs summarizing the percentage of ssDNA$^+$ and ssDNA$^+$;pH2A.X$^+$ cells at 0.5 and 4 h, respectively (mean ± s.d., n = 2, one-way ANOVA,

Bonferroni corrected). ssDNA-pH2A.X plots are representative two independent experiments. (**C**) Representative immunoblots of CEM cells treated as indicated in the text for 0.5 and 4 h. * $P < 0.05$; ** $P < 0.01$; *** $P < 0.001$; **** $P < 0.0001$.

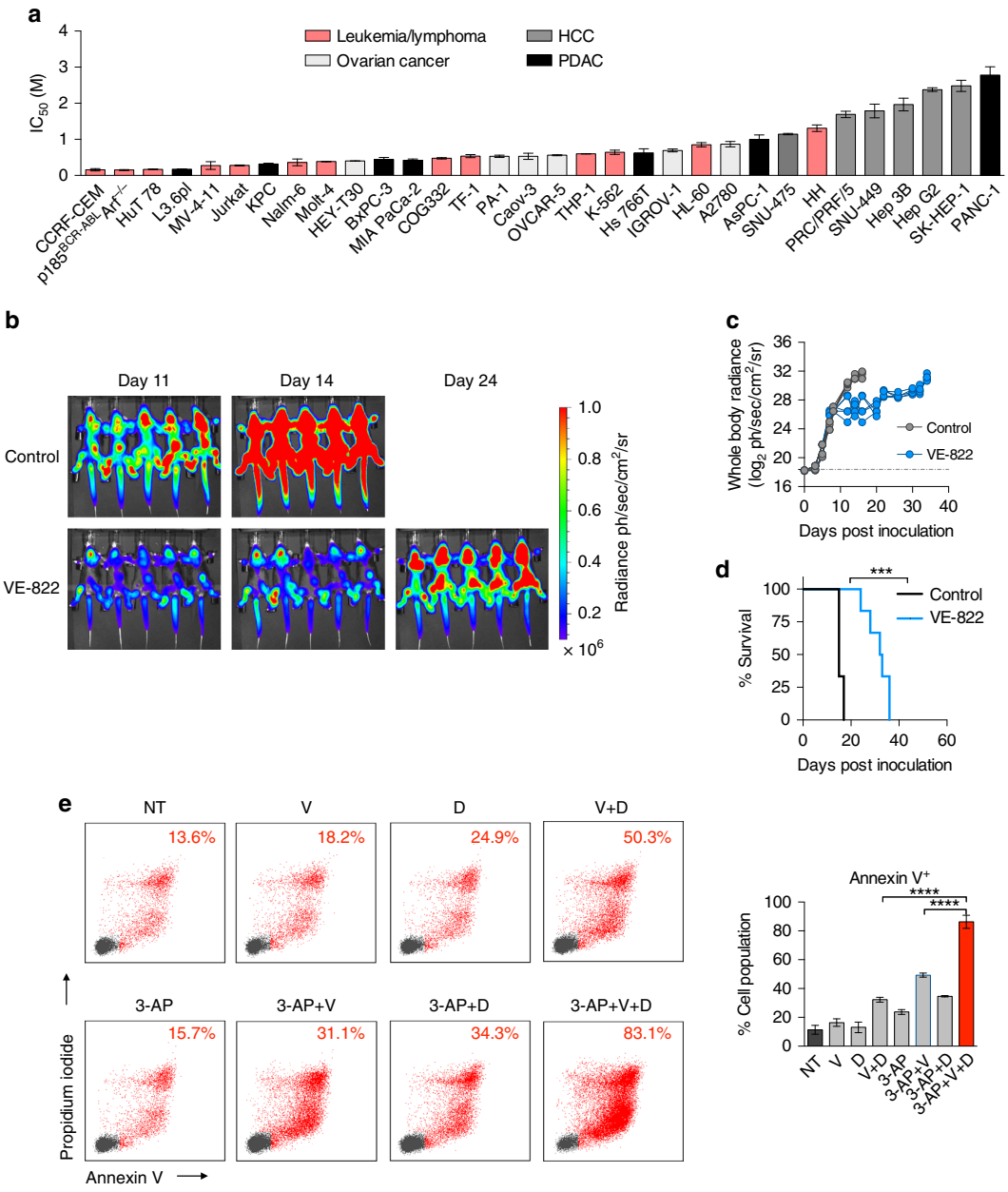

Figure 2.5 | ATR inhibition alone is effective but not sufficient to achieve disease-free survival in a systemic primary B-ALL model. (**A**) IC_{50} values of VE-822 in a panel of cancer cell lines and patient-derived samples (Cell Titer Glo assay at 72 h, mean ± s.d., n = 3). (**B and C**) Bioluminescence images (**B**) and quantification of whole-body radiance (**C**) of leukemia bearing mice treated with 40 mg/kg VE-822 (n = 6) or vehicle (control, n = 6). VE-822 was administered once daily. (**D**) Kaplan-Meier survival analysis of C57BL/6 mice bearing $p185^{BCR\text{-}ABL}Arf^{-/-}$ systemic pre-B-ALL treated with 40 mg/kg/day VE-822 (n = 6) or vehicle (control, n = 6).

Median survival for the control group was 15 days after treatment initiation and 32.5 days for the VE-822 group (Mantel-Cox test). (**E**) Apoptosis induction in p185$^{BCR\text{-}ABL}$*Arf*$^{-/-}$ pre-B-ALL cells treated as indicated (350 nM 3-AP, 100 nM VE-822, and 1 μM dCKi) for 72 h using flow cytometry for Annexin V and PI staining (mean ± s.d., n = 2, one-way ANOVA, Bonferroni corrected).

* $P < 0.05$; ** $P < 0.01$; *** $P < 0.001$; **** $P < 0.0001$.

HCC: hepatocellular carcinoma; PDAC: pancreatic ductal adenocarcinoma.

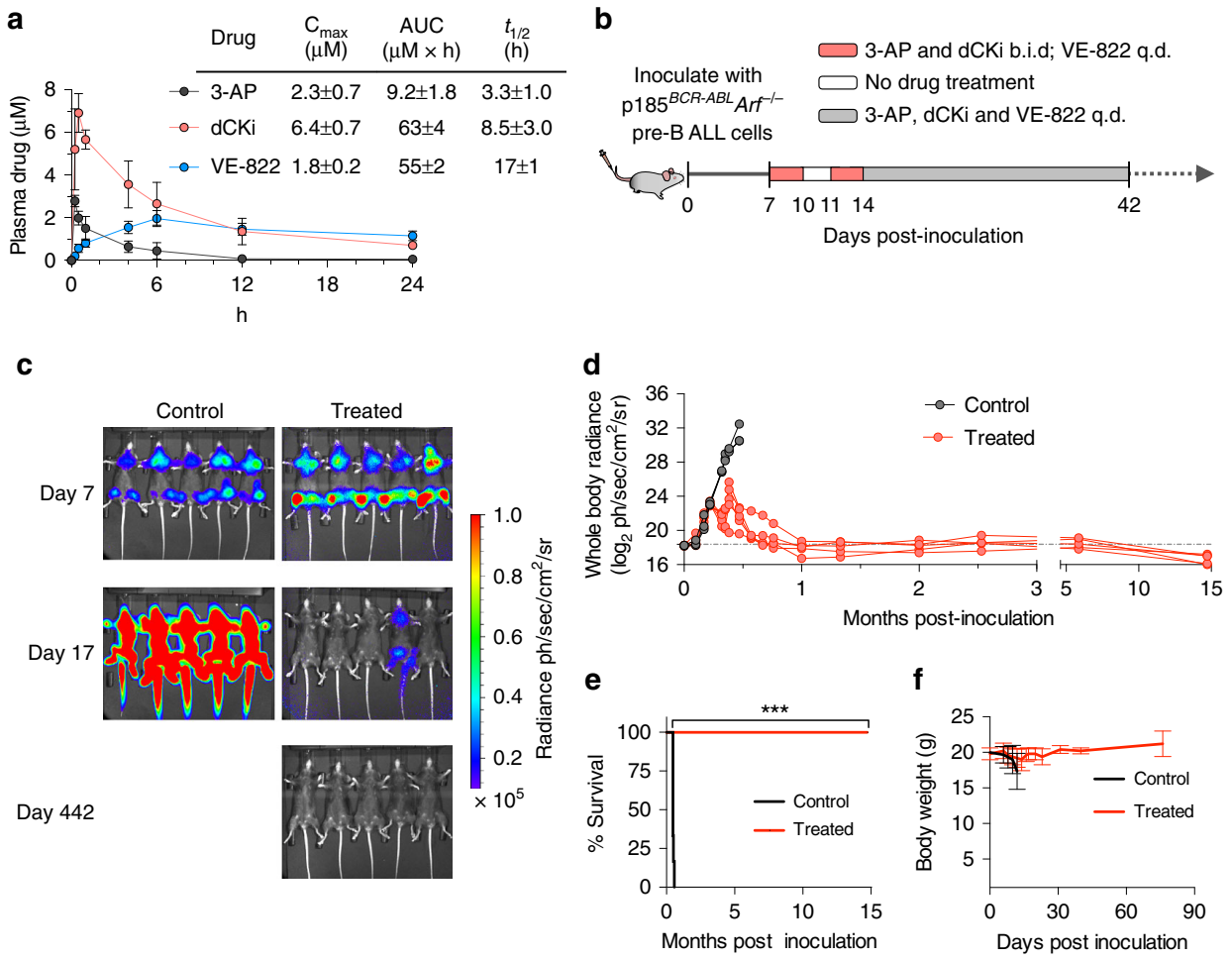

Figure 2.6 | The triple combination therapy is effective and well-tolerated in a systemic primary B-ALL model. (**A**) Plasma pharmacokinetic parameters for 3-AP (15 mg/kg), VE-822 (40 mg/kg) and dCKi (50 mg/kg) in C57BL/6 mice (n ≥ 3) after single dose oral co-administration (mean ± s.d., n ≥ 3). (**B**) Doses and schedules for the triple combination therapy of leukemia bearing mice. (**C and D**) Bioluminescence images (**C**) and quantification of whole body radiance (**D**) of leukemia bearing mice treated with the combination therapy (treated, n = 5) or vehicle (control, n = 5) at indicated days after tumor inoculation. See also Figures S2.11–13. (**E and F**) Kaplan-Meier survival analysis (**E**) and body weight measurements (**f**) of leukemia bearing mice treated with the combination therapy (treated, n = 5) or vehicle (control, n = 5). Median survival for the control group was 14 days after treatment initiation, whereas median survival for the

treated group remains undefined (Mantel-Cox test).* $P < 0.05$; ** $P < 0.01$; *** $P < 0.001$; **** $P < 0.0001$. q.d.: once/day; b.i.d.: twice/day.

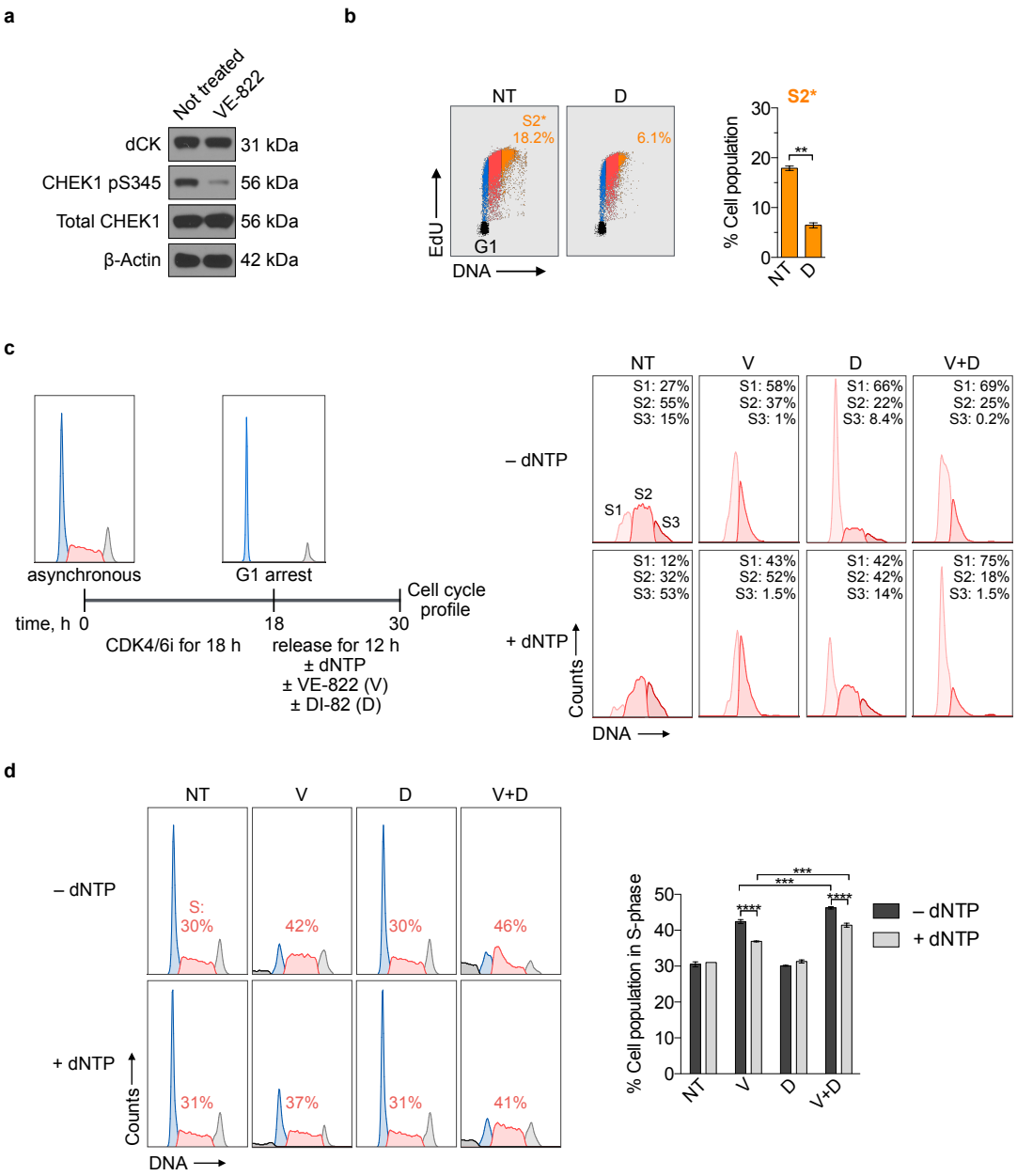

Figure S2.1 | Constitutive ATR activation in CEM T-ALL cells and its role in cell cycle progression. (**A**) Representative pS345 CHEK1 immunoblots of CEM cells ± VE-822 (1 μM) for 24 h. (**B**) Flow cytometry analysis of EdU incorporation in CEM T-ALL cells treated with VE-822 (1 μM) and/or dCKi (DI-82,1 μM) for 12 h following release from G1 arrest. Bar graphs summarize the percentage of cell populations in S3 (late S-phase) 12 h (mean ± s.d., n = 2, one-way ANOVA, Bonferroni corrected). Plots are representative of two independent experiments. (**C**) Cell cycle analyses of synchronous CEM T-ALL cells treated with VE-822

(1 μM) and/or dCKi (DI-82,1 μM) in the presence or absence of 10 μM dNTPs for 12 h following release from G1 arrest. (**D**) Cell cycle analyses of asynchronous CEM T-ALL cells treated with VE-822 (1 μM) and/or dCKi (DI-82,1 μM) in the presence or absence of 10 μM dNTPs for 12 h. Bar graph summarize the percentage of cell populations in S-phase at 12 h (mean ± s.d., n = 2, one-way ANOVA, Bonferroni corrected).

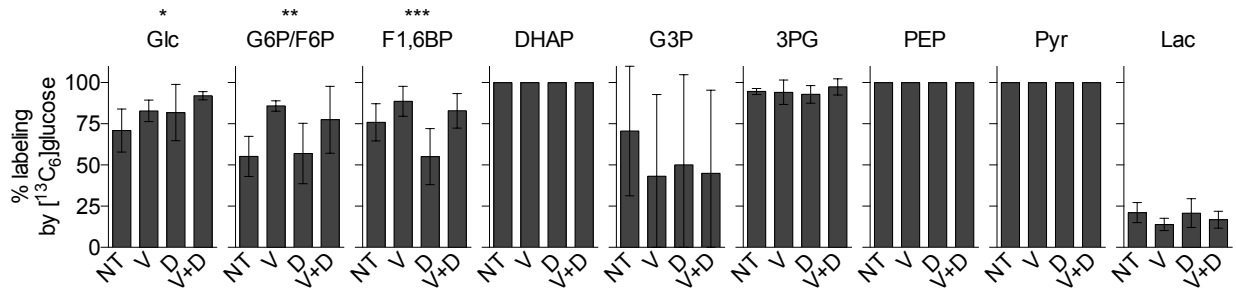

Figure S2.2 | ATR inhibition minimally impacts glucose labeling in the glycolysis of CEM T-ALL cells. Percent glucose labeling of glycolytic metabolites (mean ± s.d., n = 6, one-way ANOVA).

Glc: glucose; G6P/F6P: glucose 6-phosphate/fructose 6-phosphate; F1,6BP: fructose 1,6-bisphosphate; DHAP: dihydroacetone phosphate; G3P: glyceraldehyde 3-phosphate; 3PG: 3-phosphoglycerate; PEP: phosphoenolpyruvate; Pyr: pyruvate; Lac: lactate.

* $P < 0.05$; ** $P < 0.01$; *** $P < 0.001$.

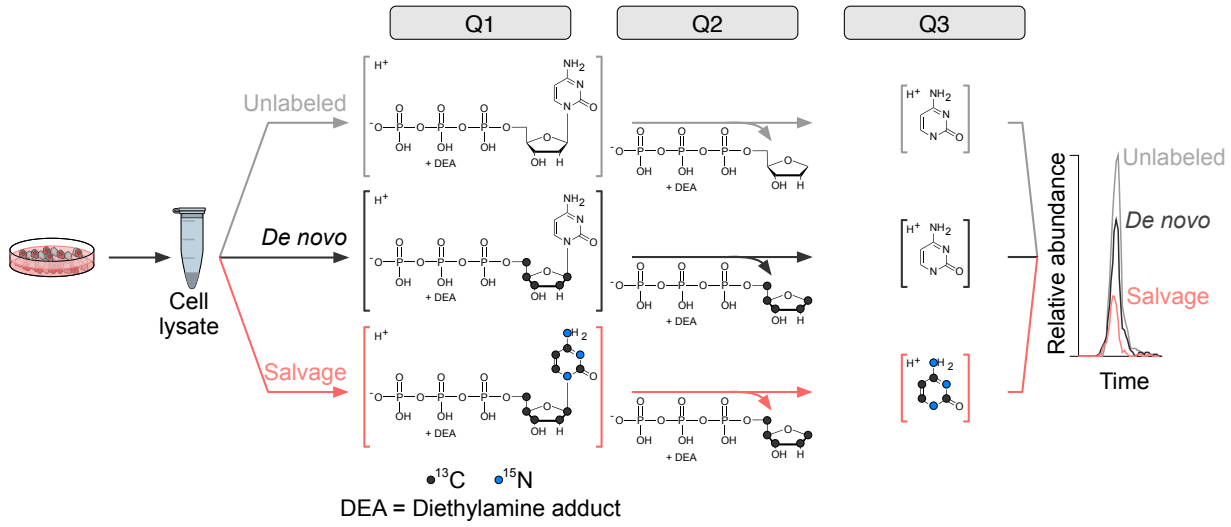

Figure S2.3 | Workflow for the targeted mass spectrometric analysis used to measure dCTP pools. Optimally, nucleotides should be monitored in the positive mode to precisely measure the labeled atoms on the nucleobase and sugar moieties. To enable such measurements, we expanded on the work by Cohen and colleagues[1] who reported the use of ion pairing reagents. With the addition of diethylamine (DEA) in the mobile phase, nucleotides have their negative charge phosphate group masked by DEA and their nucleobase becomes protonated. Under these conditions, nucleotides with the DEA adduct were monitored in the positive mode as $[NTP{-}DEA{-}H]^+$ and the fragmentation of the adduct nucleotide ions resulted in protonated nucleobases.

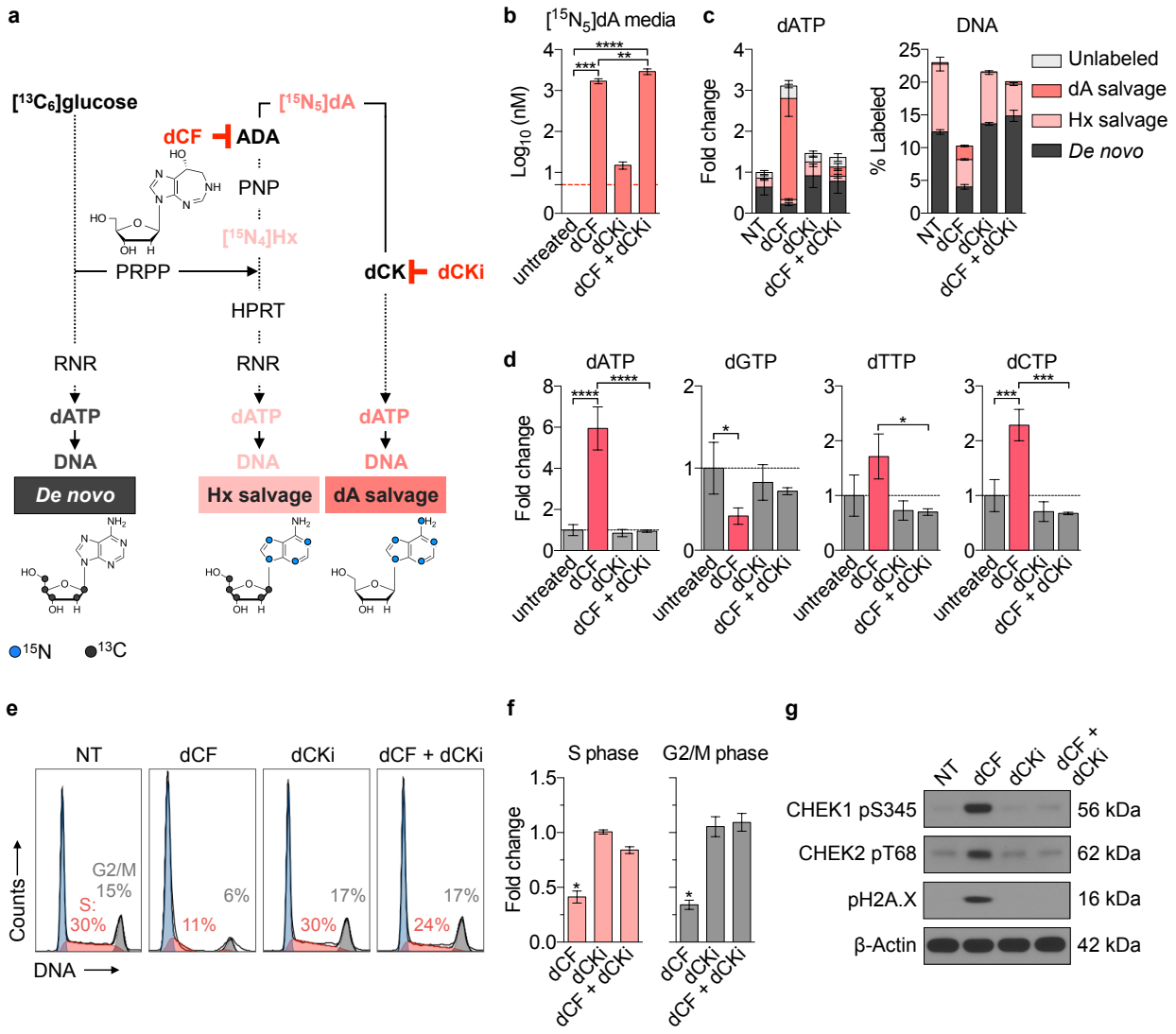

Figure S2.4 | dCK-dependent dATP production from dA requires ADA inhibition. (**A**) Schematic representation and the ^{13}C and ^{15}N labeling pattern of the *de novo* and salvage dATP biosynthetic pathways. dA can be salvaged as a nucleobase through the actions of ADA, PNP, and HPRT or as an intact deoxyribonucleoside via dCK. The former salvage pathway is blocked by Pentostatin (dCF), a specific adenosine deaminase (ADA) inhibitor; the latter salvage pathway is blocked by DI-82, a dCK inhibitor (dCKi). (**B–D**) Jurkat cells were treated with dCF (10 μM) ± dCKi (1 μM) in culture media containing 11 mM [$^{13}C_6$]glucose and 5 μM [$^{15}N_5$]dA for 18 h. (**B**) [$^{15}N_5$]dA levels in the cell culture media 18 h after treatment initiation (mean ± s.d., n = 3, one-way ANOVA, Bonferroni corrected). (**C**) Biosynthetic routes to produce free dATP and

dATP incorporated into newly replicated DNA 18 h after treatment initiation: *de novo* from [$^{13}C_6$]glucose via RNR, [$^{15}N_5$]dA salvage via dCK catalyzed phosphorylation, and HPRT mediated salvage of [$^{15}N_5$]hypoxanthine (Hx) produced from [$^{15}N_5$]dA following deamination, and glycosidic bond cleavage catalyzed by ADA and PNP, respectively (mean ± s.d., n = 3). (**D**) Fold changes in total dNTP levels 18 h after treatment initiation (mean ± s.d., n = 3, one-way ANOVA, Bonferroni corrected). (**E**) Cell cycle analyses of Jurkat cells treated as indicated for 24 h. (**F**) Quantification of cells in S (left panel) and G2/M (right panel) after the indicated treatments for 24 h (mean ± s.d., n = 2). (**G**) Representative immunoblots of CHEK1, CHEK2 and H2A.X phosphorylation; cells were treated as indicated for 24 h.

* $P < 0.05$; ** $P < 0.01$; *** $P < 0.001$; **** $P < 0.0001$.

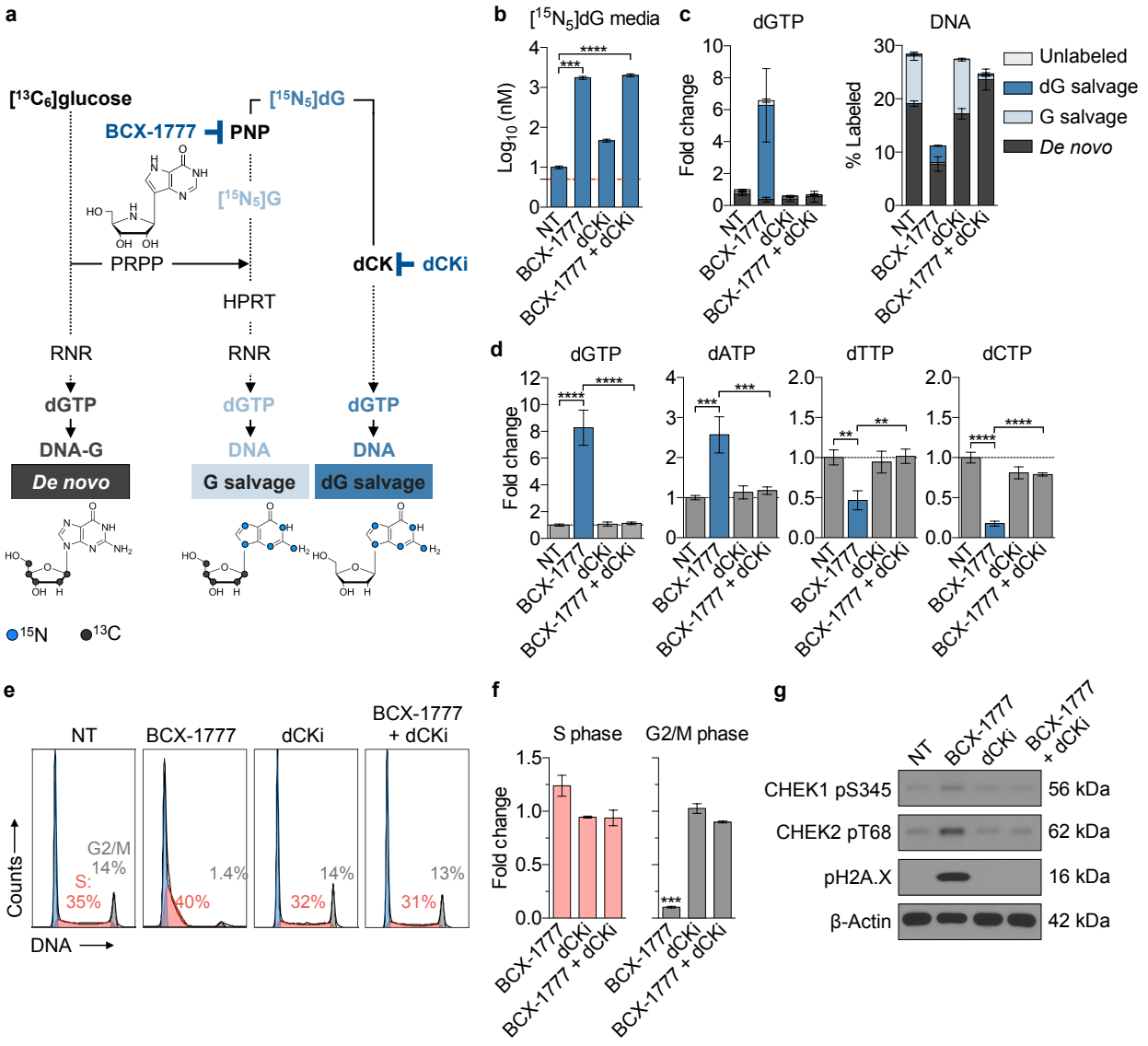

Figure S2.5 | dCK-dependent production from dG requires PNP inhibition. (**A**) Schematic representation and the ^{13}C and ^{15}N labeling pattern of the *de novo* and salvage dGTP biosynthetic pathways. dG can be salvaged as a nucleobase through the actions of PNP and HPRT or as an intact deoxyribonucleoside via dCK. The former salvage pathway is blocked by BCX-1777, a specific inhibitor of PNP; the latter salvage pathway is blocked by DI-82, a dCK inhibitor (dCKi). (**B–D**) Jurkat cells were treated with BCX-1777 (100 nM) ± dCKi (1 μM) in culture media containing 11 mM $[^{13}C_6]$glucose and 5 μM $[^{15}N_5]$dA for 18 h. (**B**) $[^{15}N_5]$dG concentration in the cell culture media 18 h after treatment initiation (mean ± SD, n = 3, one-way ANOVA, Bonferroni corrected). (**C**) Biosynthetic routes to produce free dGTP and dGTP

incorporated into newly replicated DNA 18 h after treatment initiation: *de novo* from [$^{13}C_6$]glucose via RNR, [$^{15}N_5$]dG salvage via dCK catalyzed phosphorylation, and HPRT mediated salvage of [$^{15}N_5$]G produced from [$^{15}N_5$]dG following glycosidic bond cleavage catalyzed by PNP (mean ± SD, n = 3). (**D**) Fold changes in total dNTP levels 18 h after treatment initiation (mean ± SD, n = 3, one-way ANOVA, Bonferroni corrected). (**E**) Cell cycle analyses of Jurkat cells treated as indicated for 24 h. (**F**) Quantification of cells in the S (left panel) and G2/M (right panel) after the indicated treatments for 24 h (mean ± SD, n = 2, one-way ANOVA, Bonferroni corrected). (**G**) Representative immunoblots of CHEK1, CHEK2 and H2A.X phosphorylation; cells were treated as indicated for 24 h

* $P < 0.05$; ** $P < 0.01$; *** $P < 0.001$; **** $P < 0.0001$.

PNP: purine phosphorylase; Hx: hypoxanthine; HPRT: hypoxanthine phosphoribosyltransferase.

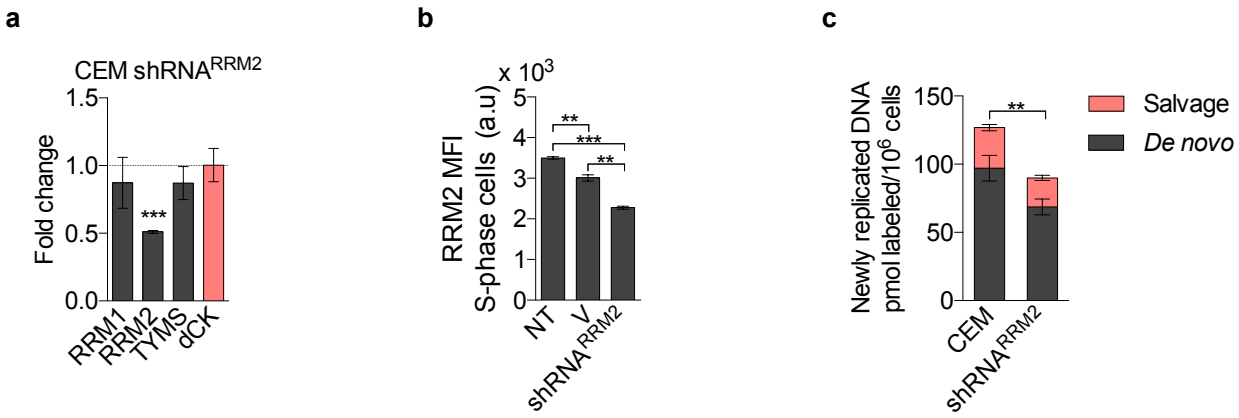

Figure S2.6 | Effects of knocking down RRM2 using shRNA on RRM2 protein levels and RNR-produced dCTP incorporated into newly replicated DNA of CEM T-ALL cells. (**A**) Protein levels in CEM shRNA^{RRM2} cells as determined by nLC-MS/MS (mean ± SD, n = 3, one sample t-test to assess if the mean of the protein level normalized to parental CEM is equal to one). (**B**) Mean fluorescence intensity (MFI) of RRM2 levels in S-phase parental CEM cells treated with 1 μM VE-822 for 12 h (V) and CEM shRNA^{RRM2} cells (mean ± SD, n = 2, one-way ANOVA, Bonferroni corrected). (**C**) Contributions of the *de novo* and salvage pathways to dCTP incorporated into newly replicated DNA in parental CEM and CEM shRNA^{RRM2} cells (mean ± SD, n = 3, two-way ANOVA, Bonferroni corrected, comparing *de novo* contribution between parental CEM and CEM shRNA^{RRM2}).

* $P < 0.05$; ** $P < 0.01$; *** $P < 0.001$; **** $P < 0.0001$.

RRM1: ribonucleotide reductase subunit 1; RRM2: ribonucleotide reductase subunit 2; TYMS: thymidylate synthase; dCK: deoxycytidine kinase.

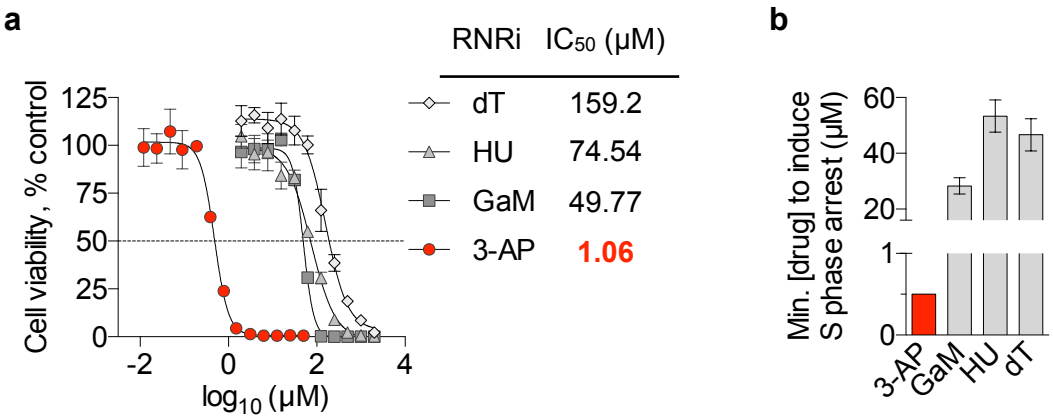

Figure S2.7 | IC_{50} values and minimal concentrations of RNR inhibitors required to cause S-phase arrest. (**A**) IC_{50} values of dT, HU, GaM, and 3-AP in CEM cells (Cell Titer Glo assay at 72 h, mean ± SD, n = 3). (**B**) Minimal concentrations of the four RNR inhibitors required for the induction of S-phase arrest observed in **Figure 2.3B** (see main text for details, mean ± SD, n = 2, one-way ANOVA, $P < 0.0001$).

dT: thymidine; HU: hydroxyurea; GaM: gallium maltolate.

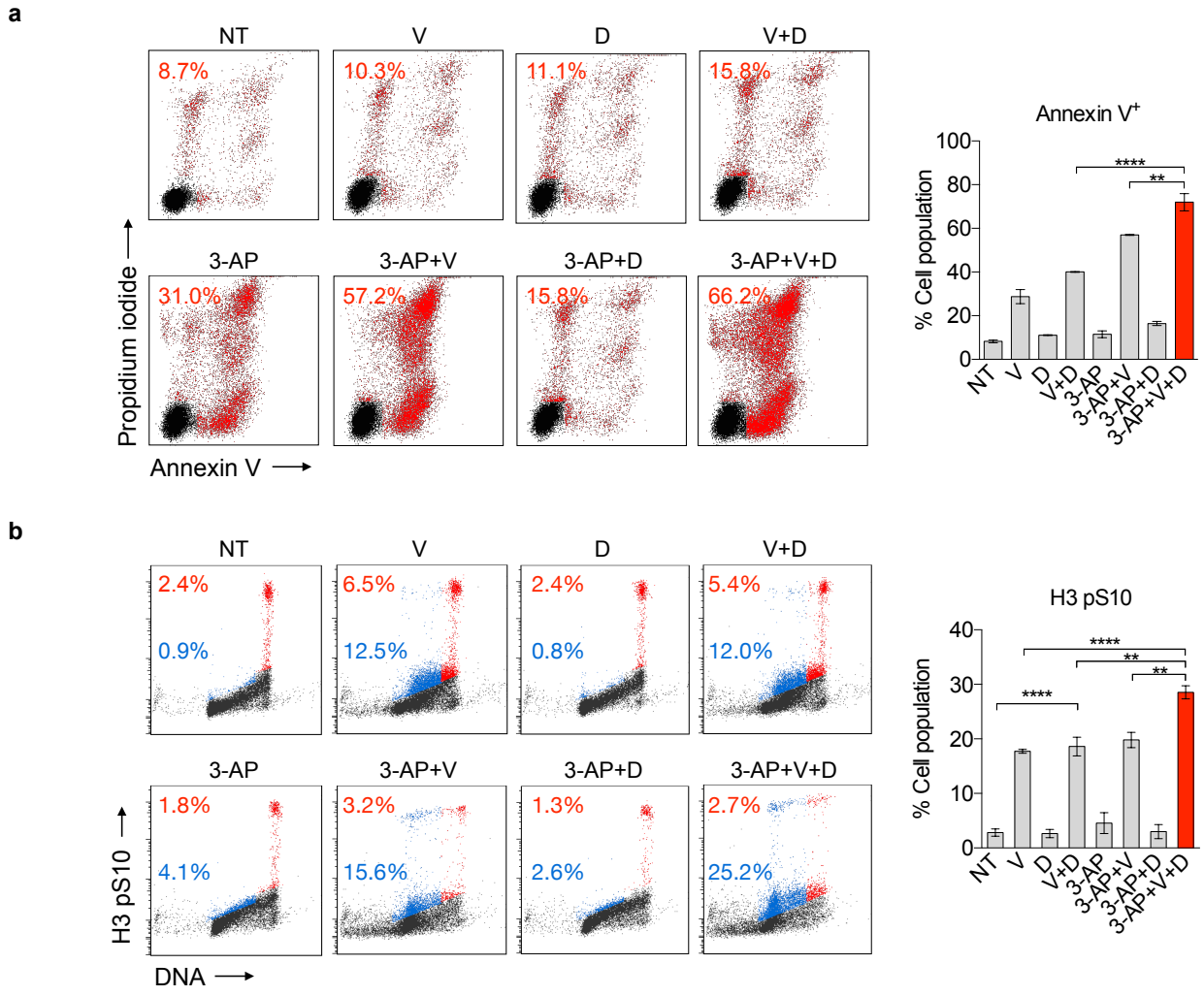

Figure S2.8 | Analyses of apoptosis induction and premature mitotic entry in CEM cells treated with ATR, dCK and RNR inhibitors. (**A**) Apoptosis induction in CEM cells treated as indicated (500 nM 3-AP, 1 μM VE-822, and 1 μM dCKi) for 24 h using flow cytometry for Annexin V and PI staining (mean ± SD, n = 2, one-way ANOVA, Bonferroni corrected). (**B**) Phosphorylated H3 on serine 10 (pS10 H3) levels in CEM cells treated as indicated (500 nM 3-AP, 1 μM VE-822, and 1 μM dCKi) for 24 h using flow cytometry (mean ± SD, n = 2, one-way ANOVA, Bonferroni corrected).

NT: not treated control, V: VE-822, D: dCKi.

* $P < 0.05$; ** $P < 0.01$; *** $P < 0.001$; **** $P < 0.0001$.

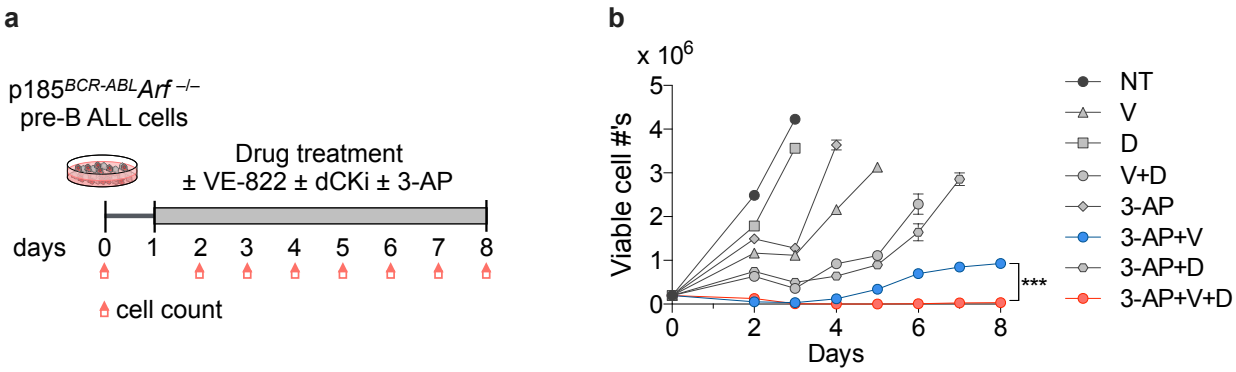

Figure S2.9 | Optimal therapeutic efficacy against p185$^{BCR\text{-}ABL}$*Arf* $^{-/-}$ pre-B-ALL cells in culture requires combined inhibition of ATR, RNR and dCK. (**A and B**) Treatment scheme (**A**) and growth curves (**B**) of p185$^{BCR\text{-}ABL}$*Arf*$^{-/-}$ pre-B-ALL treated as indicated (mean ± SD, n = 2, unpaired two-tailed Student's t-test comparing 3-AP+V and 3-AP+V+D at day 8).

NT: not treated control, V: VE-822, D: dCKi.

*** $P < 0.001$.

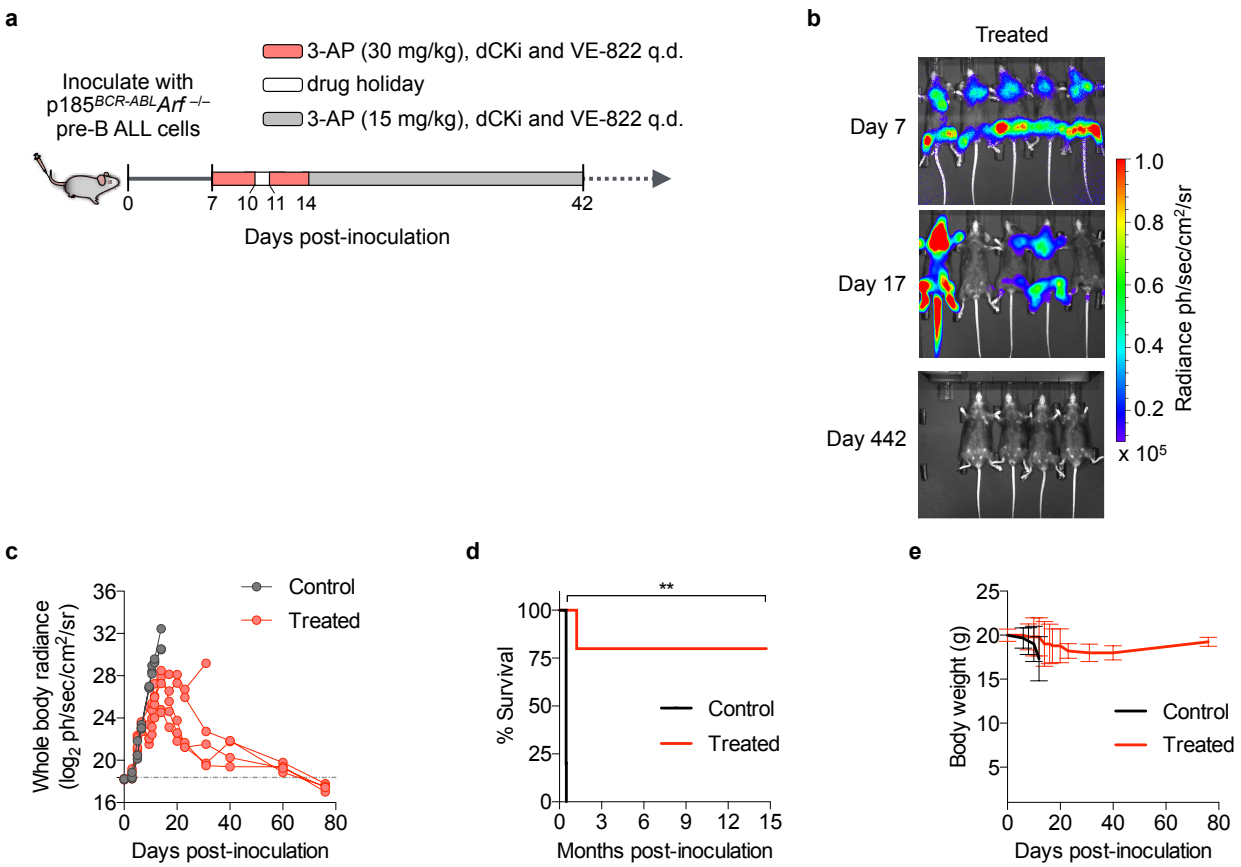

Figure S2.10 | Co-targeting ATR, dCK and RNR is effective and well-tolerated in a systemic primary B-ALL model. (**A, B, C**) Schematic representation of the therapeutic regimen (**A**), bioluminescence images (**B**), and quantification of whole-body radiance (**C**) of leukemia bearing mice treated with a slight modification of the therapeutic regime shown in **Figure 2.6B** (3-AP, 30 mg/kg q.d., treated, n = 5). (**D and E**) Kaplan-Meier survival analysis (**D**) and body weight measurements (**E**) of leukemia bearing mice treated with the combination therapy (treated, n = 5) or vehicle (control from **Figure 2.6C**, n = 5). Median survival for the control group is 14 days after treatment initiation, whereas median survival for the treated group remains undefined (Mantel-Cox test).

** $P < 0.01$.

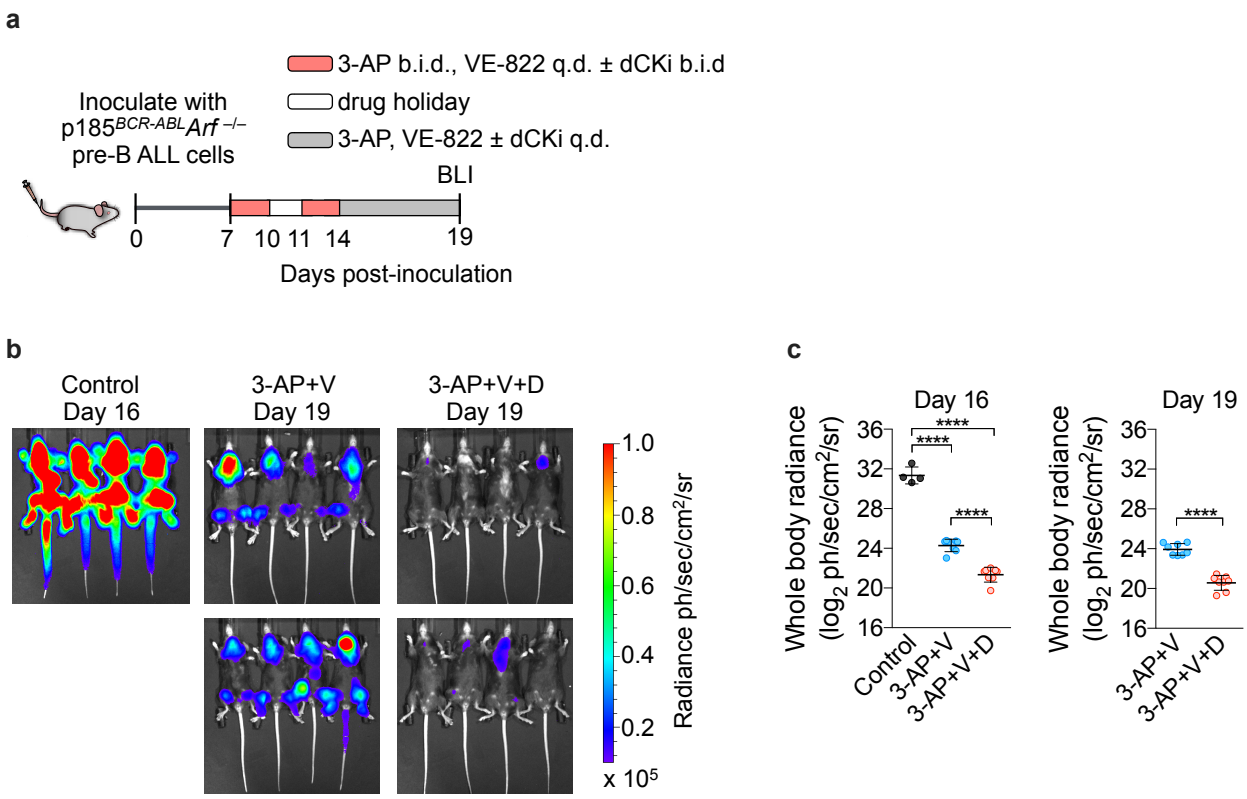

Figure S2.11 | Optimal therapeutic efficacy against p185$^{BCR\text{-}ABL}$*Arf* $^{-/-}$ pre-B-ALL cells *in vivo* requires combined inhibition of ATR, RNR and dCK. (**A**) Schematic representation of the therapeutic regimen; (**B**) bioluminescence images (**C**), and quantification of whole-body radiance of leukemia bearing mice treated with 15 mg/kg 3-AP + 40 mg/kg VE-822 (3-AP+V, n = 8), 15 mg/kg 3-AP + 40 mg/kg VE-822 + 50 mg/kg dCKi (3-AP+V+D, n = 8), and vehicle (control, n = 4). Drugs were formulated in PEG-200, Transcutol, Labrasol, and Tween-80 blended in a ratio of 5:3:1:1 and were administered orally. One-way ANOVA, Bonferroni corrected for the BLI comparisons among three groups at day 16 and unpaired two-tailed Student's t-test for the BLI comparison of 3-AP+V and 3-AP+V+D at day 19. Mice from control group were sacrificed before day 19 due to high leukemic burden.

* $P < 0.05$; ** $P < 0.01$; *** $P < 0.001$; **** $P < 0.0001$.

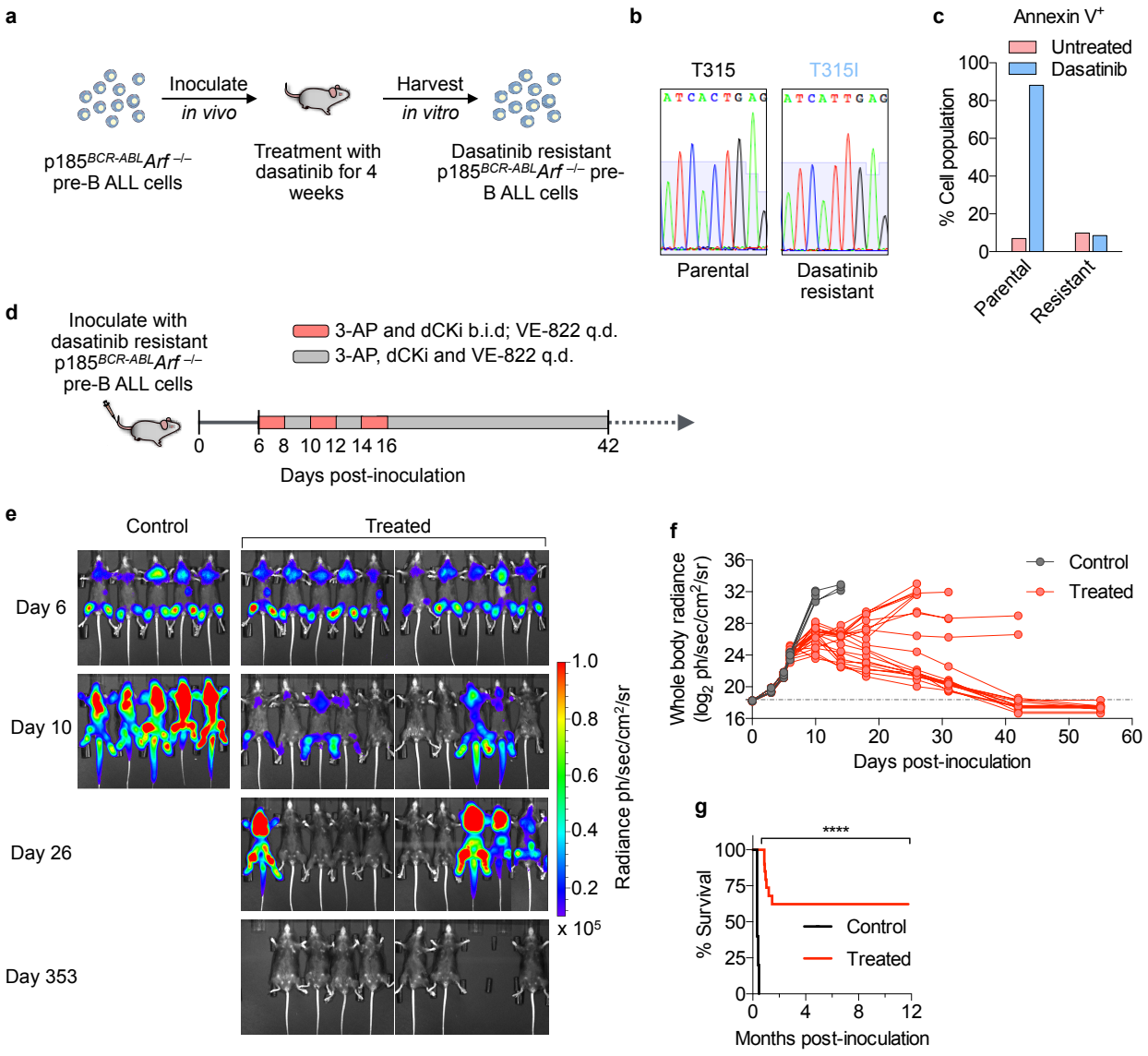

Figure S2.12 | The combination therapy is efficacious against a dasatinib-resistant pre-B-ALL mouse model. (**A**) Generation of dasatinib-resistant p185$^{BCR\text{-}ABL}$*Arf*$^{-/-}$ pre-B-ALL cells. Leukemia bearing C57BL/6 mice, were treated with 10 mg/kg dasatinib q.d. (once/day) for 20 days. Upon presentation of resistance, leukemia cells were harvested from the bone marrow. (**B**) Sequencing of ABL kinase domain of dasatinib-resistant p185$^{BCR\text{-}ABL}$*Arf*$^{-/-}$ pre-B-ALL cells showed the T315I gate-keeper mutation. (**C**) Apoptosis induction in p185$^{BCR\text{-}ABL}$*Arf*$^{-/-}$ pre-B-ALL parental and resistant cells treated as indicated (dasatinib, 1 nM) for 24 h using flow cytometry for Annexin V and PI staining. (**D**) Doses and schedule of the combination treatment (3-AP, dCKi and VE-822) against dasatinib-resistant leukemia bearing mice. (**E and F**) Bioluminescence

images (**E**) and quantification of whole body radiance (**F**) of dasatinib-resistant leukemia bearing mice treated with the combination therapy (treated, n = 20) or vehicle (control, n = 5) at indicated days after tumor inoculation. 10 representative mice are shown for the treated group. (**G**) Kaplan-Meier survival analysis of dasatinib-resistant leukemia bearing mice treated with the combination therapy (treated, n = 20) or vehicle (control, n = 5). Median survival for the control group is 14 days after treatment initiation, whereas median survival for the treated group remains undefined (Mantel-Cox test).

**** $P < 0.0001$.

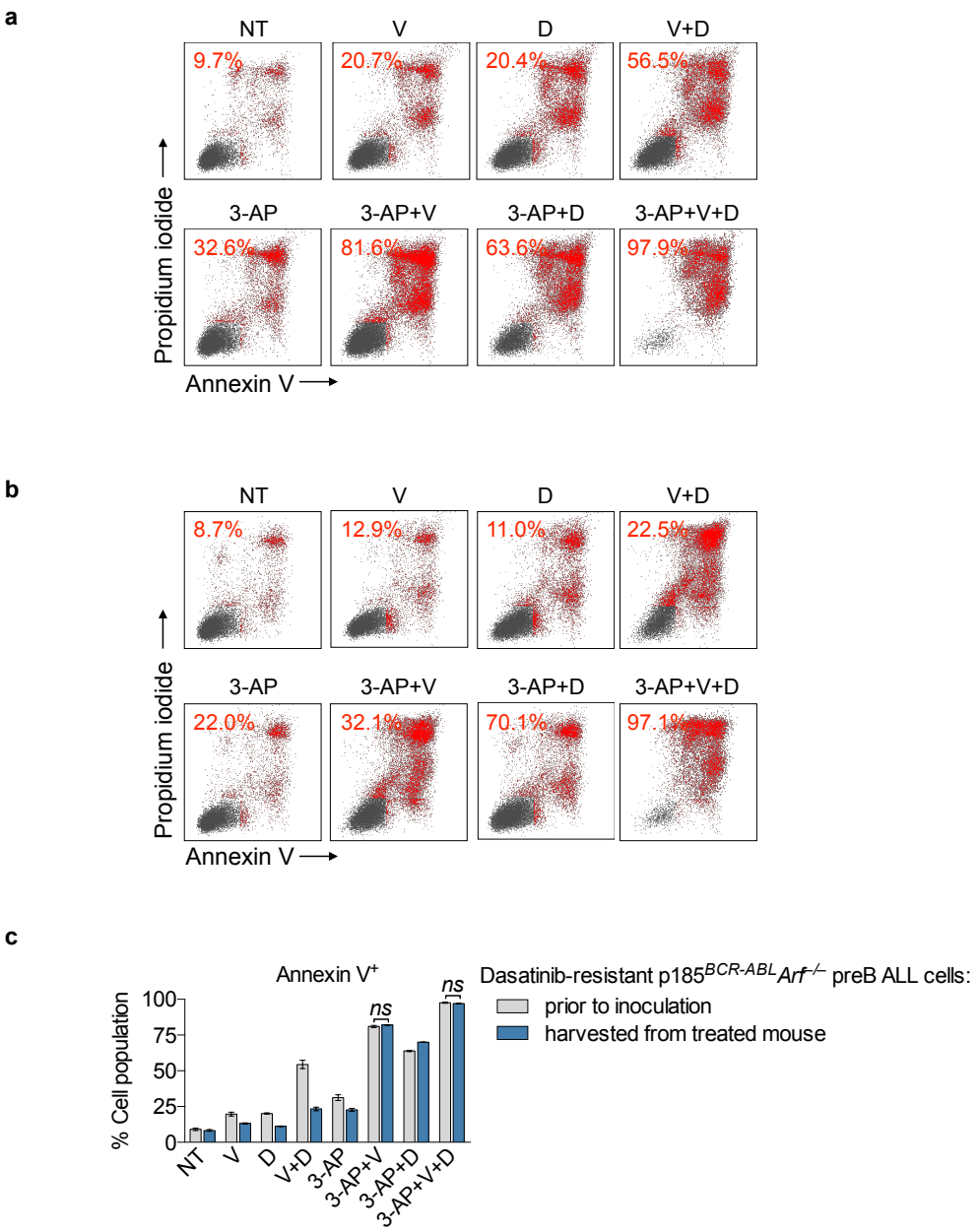

Figure S2.13 | Dasatinib resistant pre-B-ALL cells recovered from a leukemic mouse which was treated with the triple combination therapy and eventually succumbed to disease retain sensitivity to the triple combination therapy. (**A**) Apoptosis induction of dasatinib-resistant p185$^{BCR\text{-}ABL}$*Arf*$^{-/-}$ pre-B-ALL cells, prior to inoculation in mice, treated as indicated (350 nM 3-AP, 100 nM VE-822, and 1 μM dCKi) for 72 h using flow cytometry for Annexin V and PI staining. (**B**) Apoptosis induction of dasatinib-resistant p185$^{BCR\text{-}ABL}$*Arf*$^{-/-}$ pre-B-

ALL cells, harvested from bone marrow of a leukemic mouse treated with the triple combination therapy and eventually succumbed to disease from **Figure 2.13**, treated as indicated (350 nM 3-AP, 100 nM VE-822, and 1 μM dCKi) for 72 h using flow cytometry for Annexin V and PI staining. (**C**) Bar graph summarizes the percentage of Annexin V^+ cell population from (**A**) and (**B**) (mean ± SD, n = 2, one-way ANOVA, Bonferroni corrected).

ns not significant.

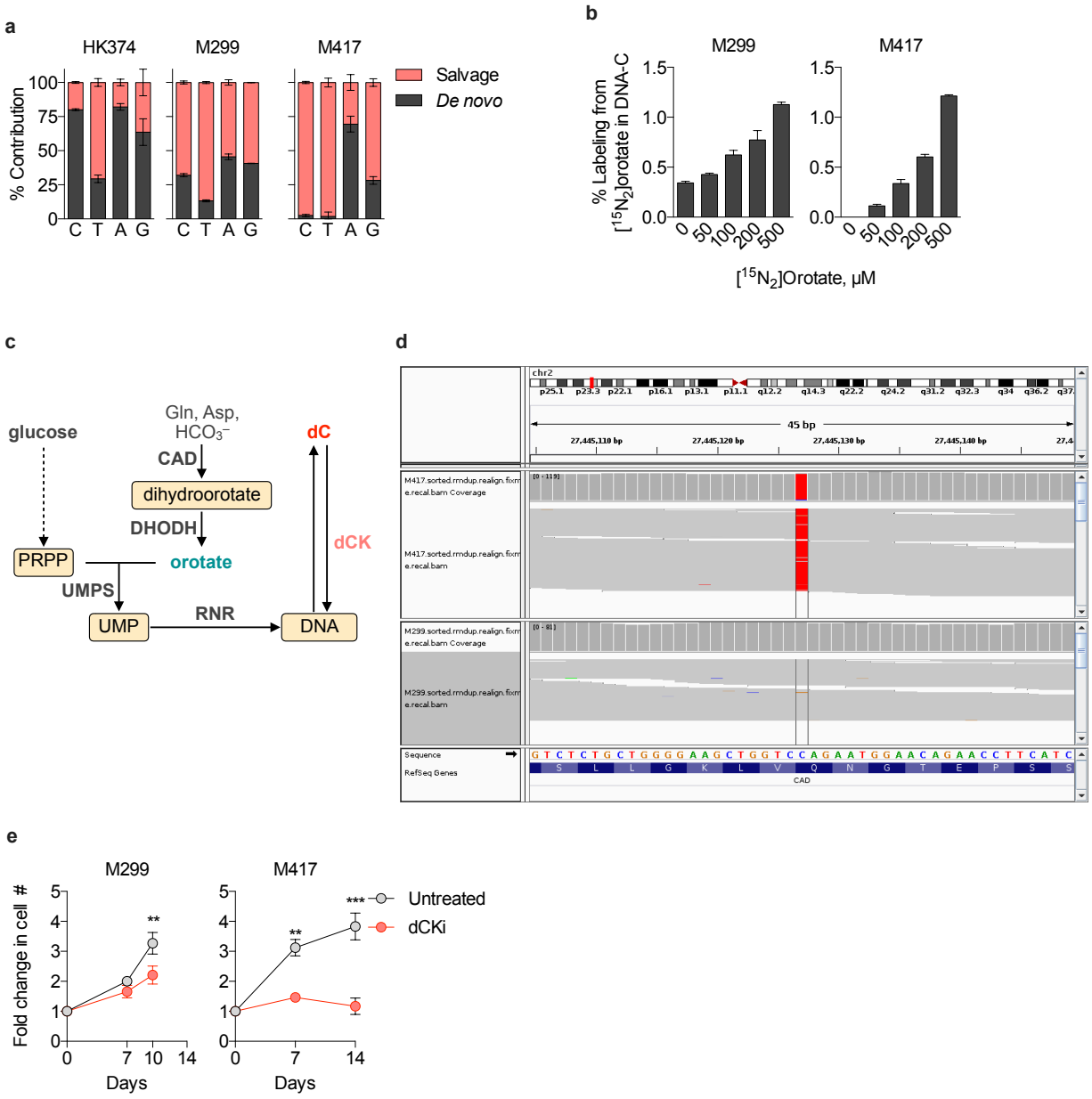

Figure S2.14 | Nucleotide biosynthetic diversity in patient-derived samples. (**A**) Profiling the differential contributions of the *de novo* and salvage pathways to newly replicated DNA in patient-derived primary glioblastoma (HK374) and melanoma (M299 and M417) cells (mean ± SD, n = 3). Cells were incubated in culture media containing 11 mM [$^{13}C_6$]glucose and 5 μM each of the following labeled nucleosides: [$^{13}C_9$,$^{15}N_3$]dC, [$^{13}C_{10}$,$^{15}N_2$]dT, [$^{13}C_{10}$,$^{15}N_5$]dA, [$^{15}N_5$]dG. (**B**) [$^{15}N_2$]orotate enrichment in dCTP incorporated into newly replicated DNA in M299 and M417 cells at 18 h (mean ± SD, n = 3). Cells were incubated in culture media containing 11 mM

[$^{13}C_6$]glucose with indicated varying concentration of [$^{15}N_2$]orotate. (**C**) Schematic representation of the *de novo* and salvage nucleotide pathway involving CAD, DHODH, and UMPS to newly replicated DNA. (**D**) IGV plot from exome sequencing of M417 showing homozygous CAD mutation (Q140*), present in 104 out of 108 reads. Results for M299 shown as negative reference. (**E**) Growth curves for M299 and M417 treated with vehicle or 1 μM dCKi (mean ± SD, n = 2).

* $P < 0.05$; ** $P < 0.01$; *** $P < 0.001$; **** $P < 0.0001$.

CAD: carbamoyl-phosphate synthetase 2, aspartate transcarbamylase, and dihydroorotase; DHODH: dihydroorotate dehydrogenase; UMPS: uridine monophosphate synthase; PRPP: 5'-phosphoribosyl pyrophosphate; UMP: uridine monophosphate.

DISCUSSION

Here we show that ATR inhibition in leukemia cells reduces the output of both *de novo* and salvage pathways. However, significant remaining activities of both pathways were sufficient to prevent ATR inhibition-induced DNA replication shutdown in cell culture, and were sufficient to permit disease-induced lethality in a systemic mouse model of pre-B-ALL. Combining ATR inhibition with specific inhibitors of *de novo* (RNR) and salvage (dCK) rate-limiting enzymes led to rapid accumulation of ssDNA, a hallmark of replication stress[22], followed by extensive DNA damage, caspase-8 and PARP cleavage, and apoptosis. This synthetically lethal combination therapy was well-tolerated *in vivo* and promoted long-term disease free survival in mice with systemic p185$^{BCR\text{-}ABL}$*Arf*$^{-/-}$ pre-B-ALL, as well as in a mouse model of targeted-therapy (dasatinib) pre-B-ALL resistance. Collectively our results quantify the control exerted by ATR on convergent nucleotide biosynthetic routes, and provide the rationale to co-target both signaling (ATR) and metabolic (RNR and dCK) mechanisms in acute leukemia for optimal therapeutic efficacy.

In mammalian cells dCTP and other dNTPs are present in low concentrations (1-50 pmol of dCTP/10^6 cells); amounts far below those required to complete one round of genome duplication (~1089 pmol of dCTP/10^6 cells)[14,57]. This apparent discrepancy between dNTP supply and demand can be explained by a model in which dNTP production is tightly coupled with utilization for DNA synthesis – an “on demand” model. A key prediction of this model is that even small disruptions of dNTP production could significantly impact DNA integrity, unless the demand for dNTPs is reduced by preventing new origin firing, a process regulated by ATR and its effector kinases[43]. This prediction is supported by the synthetic lethality observed with ATR inhibition and pharmacological targeting of the *de novo* and salvage pathways observed in cell culture and *in vivo*. These findings also suggest that more accurate estimates of the nucleotide biosynthetic capacity of cancer cells should account both for alternative free nucleotide pools and for their potential differential accessibility for substrates that are incorporated into replicated DNA.

To what extent are our findings of differential utilization of *de novo* and salvage pathways in leukemia applicable to solid tumors? An examination of three patient-derived primary cells point to significant nucleotide biosynthetic diversity in solid tumors (**Figure S2.15A**). HK-374 glioblastoma multiforme (GBM) cells[58] preferentially use the *de novo* pathways to generate most of their dATP, dGTP, and dCTP pools, with only the dTTP pool displaying a significant salvage component. A distinct nucleotide biosynthetic profile is present in two melanoma patient-derived primary cells, M299 and M417 (**Figure S2.15A**). In M299 cells, the salvage contribution to all four dNTPs exceeds 50%. Except for dATP, a similarly increased reliance on salvage biosynthesis was evident in M417 cells (**Figure S2.15A**). In contrast, *de novo* pyrimidine biosynthesis is almost completely absent in M417 cells, with greater than 98% of the dTTP and dCTP pools originating from salvage pathways. Stable isotope labeling studies using [$^{15}N_2$]orotate show that both M417 and M229 patient-derived primary cells efficiently used this substrate to produce dCTP, thereby suggesting a block in *de novo* pyrimidine biosynthesis in M417 cells either at the level of carbamoylphosphate synthetase II (CAD) or at the level of dihydroorotate dehydrogenase. Indeed, M417 cells were subsequently found to harbor a homozygous nonsense mutation (Q140*) in CAD (**Figure S2.15D**). Predictably, the defect in *de novo* pyrimidine biosynthesis rendered M417 cells hypersensitive to dCK inhibition (**Figure S2.15E**). Confirmation of these findings in larger panels of cell lines and patient derived primary samples would provide the rationale for developing new metabolically targeted therapies and clinically applicable biomarkers to define specific nucleotide biosynthetic subtypes (e.g. predominant *de novo*, predominant salvage, and both *de novo* and salvage) in solid tumors. Such biomarkers could be provided by Positron Emission Tomography (PET) imaging using new probes for nucleotide metabolism developed by us[59,60] as well as by others[61].

Post-translational regulation and modifications (PTMs) can have profound and dynamic effects on the activity of metabolic networks[62]. Both dCK[30] and RRM2[44,63] contain multiple PTMs. Among the four phosphorylation sites reported for dCK[30], phosphorylation on serine 74 (pS74) is an important determinant of dCK substrate specificity and catalytic activity[29]. Both ATR and

ATM have been reported to phosphorylate dCK on S74 in response to replication stress and DNA damage respectively[28,64]. Our data show that the ATR inhibitor VE-822 reduces dCK activity by ~33%, an effect likely attributed to a two-fold decrease in dCK pS74 (**Figure 2.2F**). However, it remains unknown what kinases are responsible for the remaining dCK pS74 present in VE-822 treated leukemia cells. ATM is a potential candidate, given that phosphorylation of CHEK2 on T68 is detected in ATR inhibited cells (**Figure 2.4C**). Further studies are needed to confirm this hypothesis. In this context, it may also be informative to analyze the activity of dCK following ATR inhibition in tumors harboring inactivating mutations in ATM[65–67]. Concerning RNR regulation, the observed consequences of ATR inhibition in T-ALL cells include the following: a decrease in RRM2 protein levels (**Figures 2.2C, 2.2D**), reduced RRM1 protein levels (**Figures 2.2C, 2.2D**), and a significant reduction in RRM2 pT33 (**Figure 2.2E**), a CDK-mediated phosphorylation event which promotes RRM2 proteasomal degradation via interactions with the $SCF^{Cyclin\ F}$ ubiquitin ligase complex[44]. It is currently unknown whether the reduction in RRM2 levels by ATR inhibition in leukemia cells occurs via a post-translational mechanism concerning protein stability and/or by a transcriptional mechanism downstream of E2F family members[68,69]. Moreover, further studies are needed to determine the significance of the observed reductions in RRM1 protein levels following ATR inhibition (**Figures 2.2C, 2.2D**) and to identify the mechanism responsible for this effect.

Our results provide quantitative insights into alterations of nucleotide biosynthetic pathways induced in leukemia cells by inhibiting ATR and rate-limiting *de novo* (RNR) and salvage (dCK) enzymes. These findings support a new therapeutic strategy that uses existing inhibitors to exploit the dependency of leukemia cells on intact *de novo* and salvage biosynthetic pathways and replication stress response mechanisms. This strategy fits within the concept of targeting non-oncogene addiction proposed by Elledge and colleagues[13]. Further refinements in this strategy and expanding its applicability beyond leukemia may come from follow-up studies to define clinically applicable companion biomarkers capable of delineating nucleotide biosynthetic and replication stress subtypes that are predictive of responses in human tumors.

METHODS

Cell culture and culture conditions. Leukemia cell lines: CCRF-CEM, EL4, Jurkat, Molt-4, CEM-R, THP-1, HL-60, TF-1, MV-4-11, HH, HuT 78, K-562; ovarian cancer cell lines: Hey-T30, PA-1, Caov-3, OVCAR-5, IGROV-1, A2780; hepatocellular carcinoma (HCC) cell lines: SNU-475, PRC/PRF/5, SNU-449, Hep 3B, Hep G2, SK-HEP-1; and pancreatic adenocarcinoma (PDAC) cell lines: L3.BP1, KPC, BxPC-3, MIA PaCa-2, Hs 766T, AsPC-1, PANC-1 were obtained from American Type Culture Collection (ATCC). Nalm-6 and p185$^{BCR\text{-}ABL}$Arf$^{-/-}$ pre-B cells were gifts from M. Teitell (UCLA) and N. Boulos (CERN Foundation), respectively. Patient-derived primary cells of leukemia COG332 was gift from Yong-Mi Kim (USC). Patient-derived primary cells of glioblastoma (HK-374) and melanoma (M299 and M417) were derived in the labs of Drs. Kornblum (UCLA) and Ribas, respectively. With a few exceptions, cell lines were cultured in RPMI-1640 (Corning) containing 10% fetal bovine serum (FBS, Omega Scientific) and were grown at 37 ºC, 20% O_2 and 5% CO_2. p185$^{BCR\text{-}ABL}$Arf$^{-/-}$ pre-B cells were cultured in RPMI-1640 containing 10% FBS and 0.1% β-mercaptoethanol. HK374 was cultured in DMEM-F12 (Invitrogen) containing B27 supplement (Life Technologies), 20 ng/mL basic fibroblast growth factor (bFGF; Peprotech), 50 ng/mL epidermal growth factor (EGF; Life Technologies), penicillin/streptomycin (Invitrogen), Glutamax (Invitrogen), and 5 µg/mL heparin (Sigma-Aldrich). All cultured cells, except HK374, were incubated in antibiotic free media and were regularly tested for mycoplasma contamination using MycoAlert kit (Lonza) following the manufacturer's instructions, except that the reagents were diluted 1:4 from their recommended amount.

Cell cycle synchronization. Cells were treated with a CDK4/6 inhibitor, Pablociclib or PD-0332991 (Selleckchem, S1116) for 18 h to synchronize them in the G1 phase. Subsequently, cells were washed twice with PBS containing 2% FBS (Omega Scientific) and released into fresh media.

Proliferation assays. Cells were plated in 384-well plates (1,000 cells/well for suspension cell lines and 500 cells/well for adherent cell lines in 30 µL volume). For suspension cells, the plates were incubated at 37 ºC for 1 h to allow settling. For adherent cell lines, the plates were incubated at 37 ºC overnight to allow the cells to seed. Drugs were serially diluted to the desired concentration and an equivalent amount of DMSO was used in vehicle control. After pre-incubation, 10 µL of the diluted drugs were added to each well. Following a 72 h incubation, Cell Titer Glo reagent was added to each well according to manufacturer's instructions (Promega, Cell Titer Glo Luminescent Cell Viability Assay). The plates were shaken for 2 min, incubated in the dark for 8 min, and then analyzed by SpectraMax luminometer (Molecular Devices).

Isotopic labeling in cell culture. Cells were transferred into RPMI-1640 without glucose and supplemented with 10% dialyzed FBS (Gibco) containing the following labeled substrates: precursors for *de novo* [U-$^{13}C_6$]glucose (Sigma-Aldrich, 389374) at 11 mM; precursors for purine salvage [U-$^{13}C_{10}$,$^{15}N_5$]dA (Cambridge Isotopes, CIL 3896), [$^{15}N_5$]dA (Cambridge Isotopes, NLM-3895), and [$^{15}N_5$]dG (Cambridge Isotopes, NLM-3899) at 5 µM or as indicated; and precursors for pyrimidine salvage: [U-$^{13}C_9$,$^{15}N_3$]dC (Silantes, 124603602) and [U-$^{13}C_{10}$,$^{15}N_2$]dT (Cambridge Isotopes, CNLM-3902) at 5 µM and [$^{15}N_2$]orotate (Cambridge Isotopes, NLM-1048) at indicated concentrations. The cells were incubated for 12 h or as indicated before sample collection and processing.

Western blot. Cells were lysed using RIPA buffer supplemented with protease (ThermoFisher, 78430) and phosphatase (ThermoFisher, 78420) inhibitors, scraped, sonicated, and centrifuged (20,000 x g at 4 ºC). Protein concentrations in the supernatant were determined using the Micro BCA Protein Assay kit (Thermo), and equal amounts of protein were resolved on pre-made Bis-Tris polyacrylamide gels (Life Technologies). Primary antibodies: pS345 CHEK1 (Cell signaling, #2341), pT68 CHEK2 (Cell signaling, #2197), pS139 H2A.X (Millipore, 05-636), clvd. Casp8 (Cell signaling, #8592), clvd. Casp9 (Cell signaling, #9502), clvd. Casp3 (Cell signaling, #9662), clvd. PARP (Cell signaling, #5625), and anti-actin (Cell Signaling Technology, 9470, 1:10,000). Primary antibodies were stored in 5% BSA (Sigma-Aldrich) and 0.1% NaN_3 in TBST solution.

Anti-rabbit IgG HRP-linked (Cell Signaling Technology, 7074) and anti-mouse IgG HRP-linked (Cell Signaling Technology, 7076) were used as secondary antibodies. Chemiluminescent substrates (ThermoFisher Scientific, 34077 and 34095) and autoradiography film (Denville) were used for detection.

Drugs. The following drugs were used: Pablociclib (Selleckchem, S1116, 1 μM), VE-822 (ApeXBio, B1381, 1 μM or as indicated), DI-82 (dCKi[2], 1 μM), thymidine (Sigma-Aldrich, T1895, as indicated), hydroxyurea (Sigma-Aldrich, H8627, as indicated), gallium maltolate (Nanoman Industries, CN-GAM-02-1G00-A00, as indicated), 3-AP (ApeXBio, custom, 500 nM or as indicated), Pentostatin (Santa Cruz Biotechnology, sc-204177, 10 μM), forodesine or BCX-1777 (Chemscene, CS-3781, 100 nM), and dasatinib (LC Laboratories, D-3307, 1 nM).

Sequencing of dasatinib-resistant clones. Bone marrow cells were harvested from dasatinib treated mice with disease relapse during sacrifice and cultured in standard culture conditions. Genomic DNA was collected from resistant cell populations and a 2-step nested PCR strategy was utilized to amplify the human *ABL* kinase domain. PCR products were sequenced and assessed for the presence of T315I mutation.

Melanoma mutation assessment. Exome sequencing for M417 and M299 was performed at the UCLA Clinical Microarray Core on an Illumina HiSeq3000 using the SeqCap EZ Exome Enrichment Kit v3.0 (Roche). Reads were mapped to UCSC hg19 (bwa-mem), deduplicaed (PicardTools), and subjected to base quality score recalibration and realignment around known indels according to the Broad Institute Genome Analysis Toolkit (GATK) Best Practices v3.0. Variants in genes associated with nucleotide biosynthesis were identified using the GATK HaplotypeCaller, and annotated with Oncotator (http://portals.broadinstitute.org/oncotator/).

Mass spectrometry analyses

dNTP sample processing. 0.5 – 1 x 10^6 cells were collected into 1.5 mL microcentrifuge tubes and centrifuged (450 x g, 4 min, 4 ºC). The supernatant was carefully aspirated and the cells were washed twice with 1 mL of cold PBS, followed each time by centrifugation (450 x g, 4 min 4 ºC). The PBS were aspirated. Thereafter, the pellets were treated with 10 µL of 10% trifluoroacetic acid with internal standards (1 µM [$^{15}N_3$]dCMP and [$^{15}N_3$]dCTP, Silantes # 122303802 and # 120303802, respectively) vigorously vortexed for 30 s, and incubated on ice for 10 min. 40 µL of 500 mM ammonium acetate, pH = 9.3, with the same internal standard (1 µM [$^{15}N_3$]dCMP and [$^{15}N_3$]dCTP) was then added and the samples were vigorously vortexed again for 30 s. The samples were centrifuged (14,000 x g, 10 min, 4 ºC) to remove cell debris. The supernatants (~ 40 µL) were transferred into HPLC injector vials. Stock solutions (10 mM) of rCTP, rCDP, dCMP, dCDP, and dCTP (Sigma Aldrich) were prepared individually in water, and stored at –20 ºC before use to generate calibration standards. Calibration standards were prepared and mixed together in water with internal standards (1 µM [$^{15}N_3$]dCMP and [$^{15}N_3$]dCTP) to make working stock concentrations in 100 nM – 100 µM range. Calibration standards were diluted 10-fold into the same nucleotide extraction solution of 10% TFA/500 mM ammonium acetate (1:4, v/v) with internal standards (1 µM [$^{15}N_3$]dCMP and [$^{15}N_3$]dCTP) to give a final concentration in 10 nM – 10 µM. Nucleotide and calibration samples were processed together to minimize variation.

DNA sample processing. Genomic DNA from 0.5 – 1 x 10^4 cells was extracted using the Quick-gDNA MiniPrep kit (Zymo Research, D3021) and hydrolyzed to nucleosides using the DNA Degradase Plus kit (Zymo Research, E2021), following manufacturer-supplied instructions. In the final step of DNA extraction, 50 µL of water was used to elute the DNA into 1.5 mL microcentrifuge tubes. A nuclease solution (5 µL; 10X buffer/DNA Degradase Plus™/water, 2.5/1/1.5, v/v/v) was added to 20 µL of the eluted genomic DNA in an HPLC injector vial. The samples were incubated overnight at 37 ºC.

Media samples processing. Culture media (20 µL) was collected at the indicated time points. Stock solutions (10 mM) of [U-$^{13}C_{10}$,$^{15}N_5$]dA, and [$^{15}N_3$]dC (Cambridge Isotope Laboratories) were prepared individually in dimethyl sulfoxide (DMSO), and stored at – 20 ºC before use as internal standards. The solutions were diluted to 20 nM in methanol to generate working solutions. Calibration standards were prepared by spiking working stock solutions of [U-$^{13}C_{10}$,$^{15}N_5$]dA and [U-$^{13}C_9$,$^{15}N_3$]dC with blank media to give concentrations in the 10 nM - 10 µM range. Each 20 µL calibration standard sample was mixed with 60 µL of internal standard solution, mixed for 30 s and centrifuged (15,000 x g, 10 min, 4ºC). After centrifugation, 60 µL of the supernatant was transferred into an HPLC injector vial for LC-MS/MS-MRM analysis. Media samples were processed similarly and in parallel to the calibration standard samples to minimize the experimental variability.

Targeted LC-MS/MS-MRM assays. For genomic DNA and media analysis, an aliquot of the hydrolyzed DNA or media samples (20 µL) were injected onto a porous graphitic carbon column (Thermo Fisher Scientific Hypercarb, 100 x 2.1 mm, 5 µm particle size) equilibrated in solvent A (water 0.1% formic acid, v/v) and eluted (200 µL/min) with an increasing concentration of solvent B (acetonitrile 0.1% formic acid, v/v) using min/%B/flow rates (µL/min) as follows: 0/0/200, 5/0/200, 10/15/200, 20/15/200, 21/40/200, 25/50/200, 26/100/700, 30/100/700, 31/0/700, 34/0/700, 35/0/200. For free nucleotide analysis, a modified version of the same previously reported method[1] was used in which each dNTP lysate sample (20 µL) was injected directly onto the Hypercarb column equilibrated in solvent C (5 mM hexylamine and 0.5% diethylamine, v/v, pH 10.0) and eluted (200 µL/min) with an increasing concentration of solvent D (acetonitrile/water, 50/50, v/v) at the following min/%D/flow rates (µL/min): 0/0/200, 5/0/200, 10/15/200, 20/15/200, 21/40/200, 25/50/200, 26/100/700, 30/100/700, 31/0/700, 34/0/700, 35/0/200. The effluent from the column was directed to the Agilent Jet Stream ion source connected to the triple quadrupole mass spectrometer (Agilent 6460) operating in the multiple reaction monitoring (MRM) mode using previously optimized settings. The peak areas for each nucleosides and nucleotides (precursor→fragment ion transitions) at predetermined retention

times were recorded using the software supplied by the instrument manufacturer (Agilent MassHunter).

Quantification. The area for nucleotides measurements were obtained from extracted ion chromatograms of MRM ion transitions. These measurements were normalized from the spiked internal standards ([$^{15}N_3$]dCMP and [$^{15}N_3$]dCTP). A calibration curve was prepared to convert the normalized areas of nucleotides to absolute quantitation, pmol/10^6 cells. For DNA, the area for the hydrolyzed labeled nucleosides were obtained from extracted ion chromatograms of MRM ion transitions. These measurements were normalized to the total ion current at that retention time. To calculate the DNA labeled pmol/10^6 cells, the peak area ratio for a given biosynthetic pathway was multiplied by 1089.3, the dCTP pmol amount needed to replicate the entire genomic DNA from 10^6 cells (assuming the size of the genomic DNA per cell to be 3.2 billion base pair with 41% GC content).

Non-targeted LC-MS metabolic assays. 1 x 10^6 cells were washed with ice-cold 150 mM ammonium acetate twice before adding 1 mL of ice-cold 80% methanol with 10 nM norvaline as an internal standard. After vigorous vortexing, samples were centrifuged at maximum speed, the aqueous layer was transferred to a glass vial and the metabolites were dried under vacuum. Metabolites were resuspended in 50 µL 70% acetonitrile (ACN) and 5 µL of this solution used for the mass spectrometer-based analysis. The analysis was performed on a Q Exactive (Thermo Scientific) in polarity-switching mode with positive voltage 4.0 kV and negative voltage 4.0 kV. The mass spectrometer was coupled to an UltiMate 3000RSLC (Thermo Scientific) UHPLC system. Mobile phase A was 5 mM ammonium acetate (NH_4AcO), pH 9.9, B was acetonitrile and the separation achieved on a Luna 3 mm NH2 100 A column (150 × 2.0 mm, Phenomenex). The flow was 200 µL/min, and the gradient ran from 15% A to 95% A in 18 min, followed by an isocratic step for 9 min and re-equilibration for 7 min. Metabolites were detected and quantified as area under the curve based on retention time and accurate mass (≤ 3 p.p.m.) using the TraceFinder 3.1 (Thermo Scientific). Relative amounts of metabolites between various

conditions, as well as percentage of [$^{13}C_6$]glucose labelling, were calculated and corrected for naturally occurring ^{13}C abundance.

Proteomic analyzes. CCRF-CEM cells were treated ± with a CDK4/6 inhibitor, PD-0332991 (Selleckchem) for 18 h to arrest at G1 phase. Cells were then washed twice with PBS and released in fresh media with treatment at a density of 1 x 10^6 cells/mL. Cells were collected at 12 h, washed twice with ice-cold PBS, and lysed by trituration using 1 mL per 5 x 10^7 cells of 0.5% sodium deoxycholate, 12 mM sodium lauryl sarcosine, and 50 mM triethylammonium bicarbonate, pH 8.0. Lysates were heated at 95 ºC for 5 min and water bath sonicated at room temperature (RT) for 5 min. Bicinchoninic acid protein assay (Pierce) was performed to determine protein concentration. Disulfide bridges were reduced with 5 mM tris(2-carboxyethyl)phosphine (final concentration) at RT for 30 min with subsequent treatment with 10 mM iodoacetamide (final concentration) at RT in the dark for 30 min. Solutions were diluted 1:5 (v:v) with 50 mM triethylammonium bicarbonate. Proteins were cleaved with sequencing grade trypsin (Promega) at 1:100 (enzyme:protein) for 4 h at 37 ºC followed by a second aliquot of trypsin 1:100 (enzyme:protein) overnight at 37 ºC. Samples were acidified with 0.5% trifluoroacetic acid (final concentration), vortexed rapidly for 5 min, and centrifuged (16,000 x g for 5 min, RT) to pellet sodium deoxycholate. Supernatants were transferred to new microcentrifuge tubes and 20 µg of total peptide were desalted using C18 StageTips as previously described[3]. On-column dimethyl labeling using C18 StageTips was performed as previously described[4]. Briefly, StageTips were equilibrated with 20 µL of 250 mM 2-(N-morpholino)ethanesulfonic acid (MES) pH 5.5. Tryptic peptides were dimethyl labeled using 60 mM sodium cyanoborohydride, 0.4% formaldehyde, and 250 mM MES pH 5.5 for 10 min. Dimethyl labeled peptides were eluted from StageTips using 20 µL of 80% acetonitrile with 0.1% trifluoroacetic acid and lyophilized to dryness. Labeled peptides were reconstituted with 2% acetonitrile and 0.1% formic acid (loading buffer). The light, medium, and heavy labeled peptides were mixed 1:1:1 (light:medium:heavy), diluted with loading buffer to a final peptide concentration of 0.2 µg/µL and 1 µg total peptide was analyzed using 180 min data-dependent

nLC-MS/MS on Thermo Orbitrap XL as later discussed. Light, medium, and heavy labeled samples were mixed using the protein median ratios as normalization from the “trial” analysis. 48 µg of mixed light, medium, and heavy labeled peptides were sub-fractionated using strong cation exchange (SCX) StageTips as previously described[3]. Briefly, 8 fractions were made using 25, 35, 50, 70, 90, 150, 350, and 750 mM ammonium acetate in 30% acetonitrile and 0.5% acetic acid. Each SCX fraction was desalted using C18 StageTips, vacuum concentrated to 1 µL, and resuspended with 10 µL of loading buffer. 5 µL of each fraction was analyzed using 180 min data-dependent reverse-phase nLC-MS/MS on Thermo Orbitrap XL and Thermo QExactive Plus for synchronous and asynchronous cells, respectively, equipped with Eksigent Spark autosampler, Eksigent 2D nanoLC, and Phoenix ST Nimbus dual column source. Briefly, samples were loaded onto laser-pulled reverse-phase nanocapillary (150 µm I.D., 360 µm O.D. x 25 cm length) with C18 (300 Å, 3 µm particle size) (AcuTech Scientific) for 30 min with mobile phase A (2% acetonitrile and 0.1% formic acid) at 500 nL/min. Peptides were analyzed over 180 min linear gradient of 0-40% mobile phase B (98% acetonitrile and 0.1% formic acid) at 300 nL/min. Electrospray ionization and source parameters for Orbitrap XL were as follows: spray voltage of 2.2 kV, capillary temperature of 200^{o}C, capillary voltage at 35 V, and tube lens at 90 V. Data-dependent MS/MS for Orbitrap XL was operated using the following parameters: full MS from 400-1700 m/z with 60,000 resolution at 400 m/z and target ion count of 3 x 10^5 or fill time of 700 ms, and twelve MS/MS with charge-state screening excluding +1 and unassigned charge states, isolation width of 2.0 m/z, target ion count of 5,000 or fill time of 50 ms, CID collision energy of 35, and dynamic exclusion of 30 sec. For QExactive Plus, the electrospray ionization and source parameters were as follows: spray voltage of 1.6 kV, capillary temperature of 200^{o}C, and S-lens RF level of 50. Data-dependent MS/MS for QExactive Plus was operated using the following parameters: full MS from 400-1700 m/z with 70,000 resolution at 400 m/z and target ion count of 3 x 10^6 or fill time of 100 ms, and twenty MS/MS with charge-state screening excluding +1 and unassigned charge states, 17,500 resolution at 400 m/z, isolation width of 2.0 m/z, target ion count of 50,000 or fill time of 50 ms, HCD collision energy of 27, and dynamic

exclusion of 30 sec. Raw data was searched against Uniprot human database using MaxQuant 1.5.3.30 with standard preset search parameters. Briefly, the search parameters were as follows: 3-plex dimethyl labeling to lysine and peptide N-terminus, trypsin cleavage allowing up to 2 missed cleavages, fixed modification of carbamidomethyl to cysteines, variable modifications of acetylation to protein N-terminus and methionine oxidation, 10 ppm mass error for full MS, 0.5 Da and 20 mmu mass errors for MS/MS for Orbitrap XL and QExactive Plus, respectively, score of 40 or greater for modified peptides, 1% false-discovery rate on peptide and protein identifications, and peptide match between run feature with 1.5 min time window.

Phosphoproteomic analyses. CCRF-CEM cells were prepared same as the asynchronous CEM cells total protein digests above, except that a total of 7.5 mg total protein from 1 x 10^8 cells was collected per treatment condition for phosphoproteomic analysis. tC18 Sep-Pak cartridges (Waters) were used for peptide desalting and Pierce Quantitative Colorimetric Peptide Assay was performed prior to phosphopeptide enrichment. Hydrophilic interaction chromatography (HILIC) and immobilized metal affinity chromatography (IMAC) were performed same as previously described[5]. Data dependent nLC-MS/MS was performed on Thermo QExactive Plus same as above. Raw data was searched against Uniprot human database using MaxQuant 1.5.3.30 with the following search parameters: trypsin cleavage allowing up to 2 missed cleavages, fixed modification of carbamidomethyl to cysteines, variable modifications of acetylation to protein N-terminus, methionine oxidation, and phosphorylation to serine, threonine, and tyrosine, 10 ppm and 20 mmu mass errors for full MS and MS/MS, respectively, score of 40 or greater for modified peptides, and 1% false-discovery rate on peptide and protein identifications. Identified phosphopeptides were manually quantified by area-based extracted ion chromatograms of the monoisotopic peak.

Plasma collection and pharmacokinetic assays. Blood was collected in heparin-EDTA tubes by retro-orbital technique at time points 0.25, 1, 6, and 24 h time points from the first set of mice and 0.5, 4, and 12 h from the second set of mice. Blood samples were spun at 2000 x g for 15 min and the plasma supernatants were collected. All plasma samples were frozen at –20 ºC

before sample processing. The stock solutions of 3-AP, VE-822, DI-82, 3-AP analog (NSC 266749), VE-821 (Selleckchem), DI-39 were prepared individually by dissolving the appropriate amount of each drug in a known volume of dimethyl sulfoxide (DMSO) to a 10 mM concentration and were stored at –20ºC before use. The 3-AP analog, VE-821 and DI-39 (internal standards) were diluted to 200 nM in methanol to make the internal solution. The calibration standards were prepared by spiking working stock solutions of 3-AP, VE-822 and DI-82 in plasma from untreated mice to give 0.01-10 pmol/µL range. Each 20 µL calibration standard sample was mixed with 60 µL of internal solution (methanol with 200 nM internal standards) and vortexed for 30 s. Following centrifugation at 15,000 x g for 10 min, approximately 60 μL of sample was carefully transferred into HPLC injector vials for LC-MS/MS-MRM analysis. Plasma samples were processed the same way as the calibration standard samples. 20 µL samples were injected onto a reverse phase column, (Thermo Scientific Hypersil GOLD column 3.0 μm; 2.1 x 100 mm) equilibrated in water/formic acid, 100/0.1, and eluted (200 µL/min) with an increasing concentration of solvent B (acetonitrile/formic acid, 100/0.1, v/v: min/% acetonitrile; 0/0, 5/0, 15/60, 16/100, 19/100, 20/0, and 25/0). The effluent from the column was directed to the Agilent Jet Stream ion source connected to the triple quadrupole mass spectrometer (Agilent 6460) operating in the multiple reaction monitoring (MRM) mode using previously optimized settings. The following drug precursor→fragment ion transitions were used: 3-AP (196→179), DI-82 (511→369), VE-822 (464→533), VE-821 (369→276), 3AP-analog (199→182), DI-39 (525→383). The peak areas for each drug (precursor→fragment ion transitions) at predetermined retention times were recorded using the software supplied by the instrument manufacturer (Agilent MassHunter).

Flow cytometry analyses

Cell cycle histograms (measurements of DNA content). Cells were plated at a density of 0.5 x 10^6 cells/mL in respective media or drug treated media. Following 24 h incubation, cells were harvested and washed twice with PBS twice before staining with 0.5 ml of propidium iodide

(Calbiochem, #P3566, 1 µg/mL) solution containing Ribonuclease A and 0.3% Triton-X 100. The samples were protected from light before acquisition by flow cytometry.

Cell cycle kinetics (pulse chase analysis) and cell cycle progression (synchronous chase pulse analysis) by intracellular detection of DNA-incorporated 5-ethynyl-2-deoxyuridine (EdU). CEM T-ALL cells were plated at a density of 0.5 x 10^6 cells/mL. Cells were pulsed with 10 µM EdU (Invitrogen) for 1 h, washed twice with PBS, and released in fresh media containing 5 µM deoxyribonucleosides, with and without drugs. Cells were collected at different time points following release in fresh media, and then fixed with 4% paraformaldehyde and permeabilized using saponin perm/wash reagent (Invitrogen). Cells were then stained with azide-Alexa Fluor 647 by Click reaction according to manufacturer's protocol (Invitrogen; Click-iT EdU Flow cytometry kit, #C10634). The total DNA content was assessed by staining the samples with FxCycle-Violet (Invitrogen, #F10347) at 1 µg/mL final concentration in PBS containing 2% FBS. To measure the cell cycle progression of a synchronous population of cells, cells were first arrested in the G1 phase following treatment with 1 µM Palbociclib for 18 h, then washed and released in fresh media supplemented with drugs. Before collecting and fixing the cells at different time points, the cells were pulse-labeled with 10 µM EdU for 1 h, and then labeled with azide-Alexa Fluor 647 (Invitrogen; Click-iT EdU Flow cytometry kit). Total DNA content was assessed by staining with FxCycle-Violet (Invitrogen) at 1 µg/mL final concentration in PBS containing 2% FBS.

pH2A.X staining. Cells were harvested, fixed and permeabilized with cytofix/cytoperm (BD biosciences, #554722) for 15 min on ice protected from light. Cells were washed, then resuspended in 100 µL 1X Perm/wash buffer (BD Sciences) and incubated for 15 min on ice. The cells were washed, then resuspended in 50 µL with phospho-Histone H2A.X (Ser139) antibody conjugated to fluorochrome FITC (EMD Millipore, #05-636, 1:800 dilutions in perm/ wash) for 20 min in the dark at RT. Subsequently, cells were washed and stained with 0.5 mL of DAPI (Invitrogen, #D1306) for DNA content (1 µg/mL in 2% FBS in PBS) before data acquisition.

Measurement of single stranded DNA (ssDNA) levels using the F7-26 monoclonal antibody. Cells were harvested and fixed with ice-cold methanol:PBS (6:1 v/v) for 24h. Staining with F7-26 monoclonal mouse antibody was performed according to manufacturer's instructions (EMD Millipore, #MAB3299). Fixed cells were resuspended in 250 µL of formamide and heated in a water bath at 75 ºC for 10 min. Cells were then allowed to equilibrate to room temperature and then washed with 2 mL of 1% non-fat dry milk in PBS for 15 min. Subsequently, cells were resuspended in 100 µL of anti-ssDNA Mab F7-26 (EMD Millipore, 1:10 in 5% FBS in PBS) and incubated for 45 min at room temperature. Cells were washed with PBS and stained with 100 µL of fluorescence-conjugated goat anti-mouse IgM antibody (Santa Cruz Biotechnology, #sc-3768, 1:50) for 45 min at room temperature. Cells were then washed with PBS, stained with 0.5 mL of DAPI for DNA content (1 µg/mL in 2% FBS in PBS) before data acquisition.

Phospho-histone 3 staining. Cells were treated with drug combinations of three drugs. 24 h following treatment, cells were fixed and permeabilized with 1% PFA and 1X Perm/wash solution respectively. Following fixation and permeabilization, cells were stained intracellularly with pH3 Ser10 antibody conjugated to AF647 (Cell signaling, #12230). Cells were then washed with PBS, stained with 0.5 mL of DAPI for DNA content (1 µg/mL in 2% FBS in PBS) before data acquisition.

Annexin V staining. Cells were treated with the indicated treatments for 24 or 72 h, then collected and washed twice with 1 mL of FACS buffer (2% FBS in PBS). Induction of apoptosis and cell death were assayed by staining the cells with Annexin V-FITC and PI according to manufacturer's instructions (FITC Annexin V Apoptosis Detection Kit, BD Sciences, #556570).

FACS analysis. All flow cytometry data were acquired on five-laser LSRII cytometers (BD) for analysis, and analyzed using FlowJo software (Tree Star). The cell cycle durations were calculated using equations for multiple time-point measurements according to previously published methods (Terry and White, 2006).

Animal studies. Mice were housed under specific pathogen-free conditions and were treated in accordance with UCLA Animal Research protocol guidelines. All C57BL/6 female mice were purchased from the UCLA Radiation Oncology breeding colony. VE-822 (ApeXBio, 40 mg/kg), 3-AP (ApeXBio, dosage as indicated) and DI-82 (dCKi, Sundia Pharmaceuticals, 50 mg/kg) were administered by intraperitoneal (i.p.) injections or oral gavage to recipient animals. For oral administration, single agent or combination of drugs were solubilized in a formulation consisting of the following: PEG-200: Transcutol: Labrasol: Tween-80 mixed in 5:3:1:1 ratio. For i.p. administration, the drugs were solubilized in PEG-400 and 1 mM Tris-HCl in a 1:1 (v:v) ratio. Dasatinib (LC Laboratories) was solubilized in 80 mM citric acid (pH 3.1) and was administered at a dose of 10 mg/kg by oral gavage. 2 x 10^5 luciferase expressing $p185^{BCR\text{-}ABL}Arf^{-/-}$ pre-B-ALL cells were injected intravenously into C57BL/6 female mice for leukemia induction. The treatment was started 6 or 7 days after the intravenous inoculation of leukemia initiating cells, when animals had developed a significant leukemic burden as monitored by bioluminescence imaging (IVIS Bioluminescence Imaging scanner). The dosing schedules are indicated in the text and figure legends. The mice were observed daily and those that became moribund during the trials, (paralysis of hind limbs, significant body weight loss) were sacrificed immediately. Kaplan-Meier curves and bioluminescence quantifications were generated using Prism 6.0h (Graphpad Software).

Bioluminescence imaging (BLI). Mice were anesthetized with 2% isoflurane followed by intraperitoneal injection of 50 µL (50 mg/mL) substrate D-luciferin (Sigma, #L9504). The mice were imaged with the IVIS 100 Bioluminescence Imaging scanner 10 minutes after luciferin administration. All mice were imaged in groups of five with 1-minute exposure time, and the images were acquired at low binning.

Statistical Analyses. Data are presented as means ± SD with indicated biological replicates. Comparisons of two groups were calculated using indicated unpaired or paired two-tailed Student's t-test and *P* values less than 0.05 were considered significant. For some experiments,

generated mean normalized values (ratios from two groups, treated to untreated) were compared to the hypothetical value 1 (indicating equal values between treated and untreated), calculated using one-sample t-test, and P values less than 0.05 were considered significant. Comparisons of more than two groups were calculated using one-way ANOVA followed by Bonferroni's multiple comparison tests, and *P* values less than 0.05/*m*, where *m* is the total number of possible comparisons, were considered significant. The Benjamini–Hochberg false discovery rate (FDR) method was used to adjust the *P* values for multiple testing in metabolomic and proteomic studies. An FDR q value ≤ 0.2 was used as a threshold for significance. All statistical analysis and generated graphs were performed either in R or Graphpad Prism 6.0h.

REFERENCES

1. Kumar, D., Viberg, J., Nilsson, A. K. & Chabes, A. Highly mutagenic and severely imbalanced dNTP pools can escape detection by the S-phase checkpoint. Nucleic Acids Res 38, 3975-3983 (2010).
2. Reichard, P. Interactions between deoxyribonucleotide and DNA synthesis. Annu Rev Biochem 57, 349-374 (1988).
3. Nordlund, P. et al. Ribonucleotide reductases. Annu. Rev. Biochem. 75, 681-706 (2006).
4. Aye, Y., Li, M., Long, M. J. & Weiss, R. S. Ribonucleotide reductase and cancer: biological mechanisms and targeted therapies. Oncogene 34, 2011-2021 (2015).
5. Sabini, E., Hazra, S., Ort, S., Konrad, M. & Lavie, A. Structural basis for substrate promiscuity of dCK. J Mol Biol 378, 607-621 (2008).
6. Tennant, D. A., Durán, R. V. & Gottlieb, E. Targeting metabolic transformation for cancer therapy. Nat Rev Cancer 10, 267-277 (2010).
7. Barretina, J. et al. The Cancer Cell Line Encyclopedia enables predictive modelling of anticancer drug sensitivity. Nature 483, 603-607 (2012).
8. Fernandez-Banet, J. et al. OASIS: web-based platform for exploring cancer multi-omics data. Nat Methods 13, 9-10 (2016).
9. Cerami, E. et al. The cBio cancer genomics portal: an open platform for exploring multidimensional cancer genomics data. Cancer Discov 2, 401-404 (2012).
10. Gao, J. et al. Integrative analysis of complex cancer genomics and clinical profiles using the cBioPortal. Sci Signal 6, pl1 (2013).
11. Boroughs, L. K. & DeBerardinis, R. J. Metabolic pathways promoting cancer cell survival and growth. Nat Cell Biol 17, 351-359 (2015).
12. Nathanson, D. A. et al. Co-targeting of convergent nucleotide biosynthetic pathways for leukemia eradication. J Exp Med 211, 473-486 (2014).
13. Luo, J., Solimini, N. L. & Elledge, S. J. Principles of cancer therapy: oncogene and non-oncogene addiction. Cell 136, 823-837 (2009).

14. Austin, W. R. et al. Nucleoside salvage pathway kinases regulate hematopoiesis by linking nucleotide metabolism with replication stress. J Exp Med 209, 2215-2228 (2012).
15. Toy, G. et al. Requirement for deoxycytidine kinase in T and B lymphocyte development. Proc Natl Acad Sci U S A 107, 5551-5556 (2010).
16. Ben-Sahra, I., Howell, J. J., Asara, J. M. & Manning, B. D. Stimulation of de novo pyrimidine synthesis by growth signaling through mTOR and S6K1. Science 339, 1323-1328 (2013).
17. Robitaille, A. M. et al. Quantitative phosphoproteomics reveal mTORC1 activates de novo pyrimidine synthesis. Science 339, 1320-1323 (2013).
18. Saha, A. et al. Akt phosphorylation and regulation of transketolase is a nodal point for amino acid control of purine synthesis. Mol Cell 55, 264-276 (2014).
19. Cunningham, J. T., Moreno, M. V., Lodi, A., Ronen, S. M. & Ruggero, D. Protein and nucleotide biosynthesis are coupled by a single rate-limiting enzyme, PRPS2, to drive cancer. Cell 157, 1088-1103 (2014).
20. Liu, Y. C. et al. Global regulation of nucleotide biosynthetic genes by c-Myc. PLoS One 3, e2722 (2008).
21. Aird, K. M. et al. Suppression of nucleotide metabolism underlies the establishment and maintenance of oncogene-induced senescence. Cell reports 3, 1252-1265 (2013).
22. Dobbelstein, M. & Sørensen, C. S. Exploiting replicative stress to treat cancer. Nat Rev Drug Discov 14, 405-423 (2015).
23. Weber, A. M. & Ryan, A. J. ATM and ATR as therapeutic targets in cancer. Pharmacol Ther 149, 124-138 (2015).
24. Branzei, D. & Foiani, M. Maintaining genome stability at the replication fork. Nat Rev Mol Cell Biol 11, 208-219 (2010).
25. Pfister, S. X. et al. Inhibiting WEE1 Selectively Kills Histone H3K36me3-Deficient Cancers by dNTP Starvation. Cancer Cell (2015).

26. Buisson, R., Boisvert, J. L., Benes, C. H. & Zou, L. Distinct but Concerted Roles of ATR, DNA-PK, and Chk1 in Countering Replication Stress during S Phase. Mol Cell 59, 1011-1024 (2015).
27. Bester, A. C. et al. Nucleotide deficiency promotes genomic instability in early stages of cancer development. Cell 145, 435-446 (2011).
28. Beyaert, M., Starczewska, E., Van Den Neste, E. & Bontemps, F. A crucial role for ATR in the regulation of deoxycytidine kinase activity. Biochem Pharmacol 100, 40-50 (2016).
29. Hazra, S., Szewczak, A., Ort, S., Konrad, M. & Lavie, A. Post-translational phosphorylation of serine 74 of human deoxycytidine kinase favors the enzyme adopting the open conformation making it competent for nucleoside binding and release. Biochemistry 50, 2870-2880 (2011).
30. Smal, C. et al. Identification of in vivo phosphorylation sites on human deoxycytidine kinase. Role of Ser-74 in the control of enzyme activity. J Biol Chem 281, 4887-4893 (2006).
31. Boulos, N. et al. Chemotherapeutic agents circumvent emergence of dasatinib-resistant BCR-ABL kinase mutations in a precise mouse model of Philadelphia chromosome-positive acute lymphoblastic leukemia. Blood 117, 3585-3595 (2011).
32. Hughes, T. P. et al. BCR-ABL1 mutation development during first-line treatment with dasatinib or imatinib for chronic myeloid leukemia in chronic phase. Leukemia 29, 1832-1838 (2015).
33. Williams, R. T., Roussel, M. F. & Sherr, C. J. Arf gene loss enhances oncogenicity and limits imatinib response in mouse models of Bcr-Abl-induced acute lymphoblastic leukemia. Proc Natl Acad Sci U S A 103, 6688-6693 (2006).
34. Dai, Y. & Grant, S. New insights into checkpoint kinase 1 in the DNA damage response signaling network. Clin Cancer Res 16, 376-383 (2010).
35. Fokas, E. et al. Targeting ATR in vivo using the novel inhibitor VE-822 results in selective sensitization of pancreatic tumors to radiation. Cell Death Dis 3, e441 (2012).

36. Fry, D. W. et al. Specific inhibition of cyclin-dependent kinase 4/6 by PD 0332991 and associated antitumor activity in human tumor xenografts. Mol Cancer Ther 3, 1427-1438 (2004).
37. Toogood, P. L. et al. Discovery of a potent and selective inhibitor of cyclin-dependent kinase 4/6. J Med Chem 48, 2388-2406 (2005).
38. Nomme, J. et al. Structure-guided development of deoxycytidine kinase inhibitors with nanomolar affinity and improved metabolic stability. J Med Chem 57, 9480-9494 (2014).
39. Giblett, E. R. ADA and PNP deficiencies: how it all began. Ann N Y Acad Sci 451, 1-8 (1985).
40. Eykelenboom, J. K. et al. ATR activates the S-M checkpoint during unperturbed growth to ensure sufficient replication prior to mitotic onset. Cell Rep 5, 1095-1107 (2013).
41. Koundrioukoff, S. et al. Stepwise activation of the ATR signaling pathway upon increasing replication stress impacts fragile site integrity. PLoS Genet 9, e1003643 (2013).
42. Marheineke, K. & Hyrien, O. Control of replication origin density and firing time in Xenopus egg extracts: role of a caffeine-sensitive, ATR-dependent checkpoint. J Biol Chem 279, 28071-28081 (2004).
43. Shechter, D., Costanzo, V. & Gautier, J. ATR and ATM regulate the timing of DNA replication origin firing. Nat Cell Biol 6, 648-655 (2004).
44. D'Angiolella, V. et al. Cyclin F-mediated degradation of ribonucleotide reductase M2 controls genome integrity and DNA repair. Cell 149, 1023-1034 (2012).
45. Zhang, Y. W., Jones, T. L., Martin, S. E., Caplen, N. J. & Pommier, Y. Implication of checkpoint kinase-dependent up-regulation of ribonucleotide reductase R2 in DNA damage response. J Biol Chem 284, 18085-18095 (2009).
46. Cory, J. G. et al. Inhibitors of ribonucleotide reductase. Comparative effects of amino- and hydroxy-substituted pyridine-2-carboxaldehyde thiosemicarbazones. Biochem Pharmacol 48, 335-344 (1994).

47. Liu, M. C., Lin, T. S., Cory, J. G., Cory, A. H. & Sartorelli, A. C. Synthesis and biological activity of 3- and 5-amino derivatives of pyridine-2-carboxaldehyde thiosemicarbazone. J Med Chem 39, 2586-2593 (1996).
48. Koc, A., Wheeler, L. J., Mathews, C. K. & Merrill, G. F. Hydroxyurea arrests DNA replication by a mechanism that preserves basal dNTP pools. J Biol Chem 279, 223-230.
49. Chitambar, C. R. Gallium compounds as antineoplastic agents. Curr Opin Oncol 16, 547-552 (2004).
50. Kufe, D. W. et al. High-dose thymidine infusions in patients with leukemia and lymphoma. Blood 55, 580-589 (1980).
51. Toledo, L. I. et al. ATR prohibits replication catastrophe by preventing global exhaustion of RPA. Cell 155, 1088-1103 (2013).
52. Grigoryan, R. S., Yang, B., Keshelava, N., Barnhart, J. R. & Reynolds, C. P. Flow cytometry analysis of single-strand DNA damage in neuroblastoma cell lines using the F7-26 monoclonal antibody. Cytometry A 71, 951-960 (2007).
53. Kulkarni, A. & Das, K. C. Differential roles of ATR and ATM in p53, Chk1, and histone H2AX phosphorylation in response to hyperoxia: ATR-dependent ATM activation. Am J Physiol Lung Cell Mol Physiol 294, L998-L1006 (2008).
54. Mankouri, H. W., Huttner, D. & Hickson, I. D. How unfinished business from S-phase affects mitosis and beyond. EMBO J 32, 2661-2671 (2013).
55. Ruiz, S. et al. A Genome-wide CRISPR Screen Identifies CDC25A as a Determinant of Sensitivity to ATR Inhibitors. Mol Cell 62, 307-313 (2016).
56. Talpaz, M. et al. Dasatinib in imatinib-resistant Philadelphia chromosome-positive leukemias. N Engl J Med 354, 2531-2541 (2006).
57. Cohen, A., Barankiewicz, J., Lederman, H. M. & Gelfand, E. W. Purine metabolism in human T lymphocytes: role of the purine nucleoside cycle. Can J Biochem Cell Biol 62, 577-583 (1984).

58. Laks, D. R. et al. Inhibition of Nucleotide Synthesis Targets Brain Tumor Stem Cells in a Subset of Glioblastoma. Molecular cancer therapeutics 15, 1271-1278 (2016).
59. Kim, W. et al. [18F]CFA as a clinically translatable probe for PET imaging of deoxycytidine kinase activity. Proc Natl Acad Sci U S A 113, 4027-4032 (2016).
60. Radu, C. G. et al. Molecular imaging of lymphoid organs and immune activation by positron emission tomography with a new [18F]-labeled 2'-deoxycytidine analog. Nat Med 14, 783-788 (2008).
61. Shields, A. F. et al. Imaging proliferation in vivo with [F-18]FLT and positron emission tomography. Nat Med 4, 1334-1336 (1998).
62. Humphrey, S. J., James, D. E. & Mann, M. Protein Phosphorylation: A Major Switch Mechanism for Metabolic Regulation. Trends Endocrinol Metab 26, 676-687 (2015).
63. Tang, L.-Y. et al. Quantitative phosphoproteome profiling of Wnt3a-mediated signaling network indicating the involvement of ribonucleoside-diphosphate reductase M2 subunit phosphorylation at residue serine 20 in canonical Wnt signal transduction. Molecular & Cellular Proteomics 6, 1952-1967 (2007).
64. Bunimovich, Y. L. et al. Deoxycytidine kinase augments ATM-Mediated DNA repair and contributes to radiation resistance. PLoS One 9, e104125 (2014).
65. Fokas, E. et al. Targeting ATR in DNA damage response and cancer therapeutics. Cancer Treat Rev 40, 109-117 (2014).
66. Foote, K. M. et al. Discovery of 4-{4-[(3R)-3-Methylmorpholin-4-yl]-6-[1-(methylsulfonyl)cyclopropyl]pyrimidin-2-yl}-1H-indole (AZ20): a potent and selective inhibitor of ATR protein kinase with monotherapy in vivo antitumor activity. J Med Chem 56, 2125-2138 (2013).
67. Reaper, P. M. et al. Selective killing of ATM- or p53-deficient cancer cells through inhibition of ATR. Nat Chem Biol 7, 428-430 (2011).
68. Humbert, P. O. et al. E2f3 is critical for normal cellular proliferation. Genes Dev 14, 690-703 (2000).

CHAPTER 3

Identification of Actionable Vulnerabilities Resulting from Interferon Induced Nucleotide Metabolism Reprogramming in Pancreatic Cancer

ABSTRACT

Pancreatic ductal adenocarcinoma (PDAC) is a devastating disease for which new, rationally designed therapies are urgently needed. In addition to activating KRAS mutations, a dense stromal compartment and an inflammatory, cytokine rich microenvironment are defining characteristics of PDAC tumors. Among cytokines in the PDAC tumor environment, interferons are particularly important as they regulate the expression of hundreds of genes, many of which have established pro- or anti-tumor functions. We determined that a transcriptional type I interferon (IFN) response signature is enriched in TCGA PDAC specimens with a range of expression observed among individual samples. Consistently, we found that IFN signaling is detectable in a subset of PDAC patient-derived and cell line xenografts. In these models, we defined a requirement for PDAC cell cGAS/STING pathway activity for tumor IFN signaling. Despite the marked enrichment of IFN signaling in PDAC tumors its impact on tumor cell signaling, metabolism and response to therapy is poorly defined.

In contrast to our *in vivo* observations, we found that IFN signaling biomarkers are absent in traditional PDAC cell culture models. Using nLC-MS/MS phosphoproteomics we determined that IFN treatment triggers activation of the replication stress response signaling cascade mediated by the kinase ataxia telangiectasia and Rad3-related protein (ATR). This signaling network allows cells to sense and respond to any obstacle to DNA replication in S-phase, one such cause is an insufficient supply of the deoxyribonucleotide triphosphate (dNTP) substrates for DNA replication. Using a targeted LC-MS/MS approach we found that IFN signaling induces a decrease in the abundance of dNTPs in PDAC cells. To systematically investigate the cause of this metabolic reprogramming we evaluated IFN-induced alterations in the expression of nucleotide-metabolism genes using nLC-MS/MS proteomics. We found that IFN signaling induces a subset of metabolic genes which function in nucleotide and nucleoside catabolism, including: sterile alpha-motif and histidine-aspartate domain-containing protein 1 (SAMHD1) and thymidine phosphorylase (TYMP). We confirmed a role for SAMHD1 in IFN-induced dNTP restriction using CRISPR/Cas9 knockout isogenic cells. Furthermore, we found that dNTP

phosphohydrolysis is counteracted by deoxycytidine kinase (dCK) which recycles SAMHD1-produced deoxyribonucleosides. Collectively, these findings suggest that IFN triggers a shift in tumor cell nucleotide metabolism from a biosynthetic to a predominantly catabolic phenotype.

To model IFN-high and -low conditions in PDAC xenograft tumors *in vivo* we engineered a cell line to express a constitutively active mutant STING ($STING^{R248M}$) conditionally in the presence of doxycycline. By performing performing immunoblot and immunohistochemical analysis of tumor explants we confirmed that this model recapitulates our observations of IFN biomarker enrichment in PDAC patient samples. We investigated the impact of IFN signaling on tumor metabolism *in vivo* by evaluating accumulation of [^{18}F]FLT, which is sensitive to TYMP expression, in $STING^{R248M}$ isogenic tumors using position emission tomography (PET). These studies indicated that IFN signaling reprograms nucleotide metabolism both *in vitro* and *in vivo*.

To identify vulnerabilities elicited by IFN signaling we applied a 430 compound *in vitro* chemical genomics high-throughput synthetic lethality screen. We found enrichment of inhibitors of replication stress response kinase, ATR and CHEK1, inhibitors among compounds exhibiting synergy with IFN. Co-treatment of PDAC cells with IFN and an ATR inhibitor triggers S-phase arrest, DNA damage and apoptosis. ATR inhibitors potentiate the IFN-induced dNTP restriction and down-regulate the expression of genes related to dNTP biosynthesis and salvage. We found that the synergy between IFN signaling and ATR inhibitors was restricted to a subset of PDAC cell lines in which IFN induces replication stress.. Collectively, this work furthers our understanding of the crosstalk between cytokine signaling, nucleotide metabolism and DNA replication stress response networks in PDAC and provides the rationale for new therapeutic approaches for the treatment of a precisely defined patient population.

INTRODUCTION

The median overall survival of patients diagnosed with pancreatic ductal adenocarcinoma (PDAC) is less than one year and PDAC is expected to become the second most common cause of cancer related death in the United States by 2020[1,2]. Contributing to this poor prognosis is the near universal resistance of PDAC tumors to current pharmacological and immunotherapy treatment regimens and it is clear that a better understanding of fundamental biology is required for the development of new therapies for this disease[3]. Accordingly, substantial efforts have been dedicated towards defining genomic and transcriptional PDAC subtypes to ultimately guide precision medicine treatment approaches[4,5]. In PDAC, BRCA1/2 mutations are detected in 4-7% of patients and are associated with response to PARP inhibitors[6]. Additionally, two transcriptional subtypes have been recurrently identified in PDAC patient samples and include the basal-like/mesenchymal/squamous and classical/epithelial/progenitor[7]. However, the distinct biological behavior and targetable vulnerabilities of these subtypes are not well defined.

In addition to a near universal penetrance of KRAS mutations and a dense stromal component, PDAC is defined by a pro-inflammatory, cytokine-rich tumor microenvironment. Among cytokines present in PDAC tumors interferons (IFNs), are particularly important and influence cancer development, progression, and response to DNA damaging therapy[8]. Type I IFNs (IFNα, IFNβ and IFNλ) are constitutively produced in the PDAC tumor microenvironment by stromal, immune, and potentially tumor cells (**Figure 3.1**). One signaling network regulating the production of type I IFNs is the cyclic guanosine monophosphate-adenosine monophosphate synthase (cGAS) / stimulator of IFN genes (STING) pathway which is induced by cytoplasmic single-stranded and double-stranded DNA (ssDNA, dsDNA)[9]. Type I IFNs function by binding to specialized receptors, IFNAR1 and IFNAR2, and inducing a JAK1/TYK2-mediated signaling cascade which results in transcriptional activation of hundreds of IFN-stimulated genes including STAT1 and MX1, canonical surrogate markers of type I IFN signaling. Paradoxically, IFNs exert both pro- and anti-tumor effects: IFNs impair cancer cell proliferation *in vitro* but chronic

exposure has been linked with resistance to radiation, chemotherapy and immune checkpoint blockade[10–12]. Additionally, it remains to be determined if IFN signaling in tumors can be leveraged therapeutically.

The roles of type I IFNs in modulating immunity and eliciting anti-pathogen responses are well-characterized, but only recently has emphasis been placed on their metabolic effects. PDAC tumors undergo extensive metabolic reprogramming that enables them to adapt to chronic nutrient deprivation and also functions as a form of immunosuppressive microenvironmental conditioning[13]. Drivers of metabolic reprogramming in PDAC include oncogenes (KRAS)[14], physiologic factors (hypoxia)[15], and heterotypic cellular interactions with stromal cells and immune cells[16,17]. Type I IFNs have been linked to the regulation of lipid and energy metabolism in immune and epithelial cells, however, whether and how type I IFN signaling reprograms PDAC metabolism remains to be determined[18].

Amongst metabolites critical for cancer cell proliferation, nucleotides are particularly important as they are required for a variety of biological processes including nucleic acid (RNA and DNA) biosynthesis. A balanced and sufficient supply of deoxyribonucleotide (dNTP) pools is essential to sustain PDAC cell proliferation and is maintained by the coordinated activity of *de novo* biosynthetic and salvage pathways. The KRAS oncogene is an established positive regulator of *de novo* nucleotide biosynthesis and pharmacological inhibition of pyrimidine biosynthesis using DHODH inhibitors has been proposed as a treatment strategy for PDAC[19]. Additionally, inhibition of lysosome function has been shown to restrict dNTP pools in PDAC cells by limiting aspartate availability, which is critically required for the de novo synthesis of both pyrimidine and purine nucleotides[20]. To resolve the DNA replication stress that results from dNTP insufficiency, cancer cells rely on the replication stress response signaling pathway[21]. The proximal mediator of this response, ataxia telangiectasia and Rad3-related protein (ATR) initiates a signaling cascade which slows DNA replication by suppressing origin firing, promotes replication fork stabilization and activates the G2/M checkpoint[22]. Importantly, ATR has been shown to promote

nucleotide biosynthesis and salvage via activation of rate-limiting enzymes in these pathways: ribonucleotide reductase (RNR) and deoxycytidine kinase (dCK)[23]. ATR is recruited and activated by replication protein A (RPA)-bound single stranded DNA, which can arise at stalled replication forks and also occurs following DNA end resection during the early stages of homologous recombination for DNA double strand break repair. CHEK1, an established substrate of ATR, serves to inhibit cyclin-dependent kinase (CDK) activity through the inhibition of the phosphatase CDC25A. ATR inhibitors M6620 (EMD Serano; also known as VE-822) and AZD6738 (AstraZeneca) are currently being evaluated in clinical trials in combination with chemotherapy, DNA damaging therapy (PARP inhibitors) or immunotherapy (immune checkpoint blockade) for multiple cancer types including PDAC[22]. Additionally, ATR inhibitors may be particularly effective for the treatment of tumor cells with oncogenic signaling driven by activation KRAS mutations and mutant TP53. ATR has been shown to mitigate DNA damage triggered by mutant RAS activation in tumor cells[24,25]. Mutant TP53 has been implicated in similar phenotypes[26]. The links between other hallmarks of PDAC, including cytokine signaling, and the replication stress response pathway remain unexplored.

In this study, we determined that PDAC primary patient-, patient-derived xenograft- and cell line xenograft- tumors exhibit a type I IFN response signature (**Figure 3.2**). We found that constitutive type I IFN signaling in xenograft tumors was dependent on PDAC cell cGAS/STING pathway functionality. *In vitro*, IFN signaling triggers replication stress and alters nucleotide metabolism in PDAC cells. Using a chemical genomics high-throughput screening approach we determined that type I IFN signaling renders PDAC cells addicted to replication stress response signaling. We found that inhibiting this pathway at the level of ATR induces catastrophic DNA damage and cell death in cells exposed to IFN. PARP inhibitors further sensitize PDAC cells to ATR inhibition together with type I IFN signaling. Collectively, this work begins to define the crosstalk between cytokine signaling, stress response networks and metabolism in PDAC and identifies a targetable, tumor cell collateral dependency resulting from STING-driven IFN signaling.

RESULTS

IFN signaling is constitutive in a subset of PDAC tumors

Type I IFNs are produced by epithelial and immune cells and have been linked to the regulation of cancer cell proliferation, apoptosis and immune-recognition via the transcriptional regulation of effector IFN-stimulated genes[8]. According to the TCGA dataset, pancreatic adenocarcinoma ranks among cancers exhibiting the greatest increase in transcript enrichment of a previously defined IFN response signature relative to organ specific normal tissue controls (normalized for CD4-positive cell infiltration as previously described; **Figures S3.1A, S3.1B**)[27,28]. Furthermore, a subset of PDAC tumors in the TCGA collection exhibit a particularly high enrichment of genes contained within this signature with a correlation observed amongst these genes (**Figure 3.3A**). In contrast, no such correlation was observed in the PDAC CCLE cell line RNAseq dataset derived from *in vitro* samples (**Figure S3.1C**). Consistent with TCGA mRNA expression data, a subset of surgical PDAC specimens exhibit high levels of STAT1 protein notably localized to the tumor cell compartment (**Figure 3.3B**). To model these findings, we established subcutaneous xenografts of 33 primary patient-derived PDAC samples and 17 established PDAC cell lines in NSG mice. A subset of primary patient-derived and cell line-derived PDAC xenograft tumors were found to express high levels of IFN-stimulated genes STAT1 and MX1 while a minority scored as negative (**Figures S3.2A, S3.2B, S3.2C**). Because of the lack of IFN species cross reactivity these data suggest that IFN-stimulated gene expression in xenograft tumors is driven by a tumor cell autonomous mechanism. One explanation for the lack of IFN-stimulated gene expression in a subset of xenograft tumors is low expression or impaired activity of IFN receptors or downstream kinases, a characteristic of some tumor cells and an established mechanism of acquired resistance to immune checkpoint blockade[29,30]. To investigate this possibility this we treated a panel of PDAC cell lines with type I IFN (IFNβ) *in vitro* and all models responded to IFNβ by upregulating STAT1 expression, including those scoring as STAT/MX1 low when grown as xenograft tumors (**Figure S3.3A**). Using immunoblot analysis we found that MX1, and STAT1 were expressed at high levels in lysates prepared from DANG xenograft

tumors compared to cell culture samples and supplementing these cultures with recombinant IFNβ restored STAT1 and MX1 to levels observed in tumor samples (**Figure 3.3C**). Collectively, these results indicate that IFN signaling is constitutive in PDAC tumors and is driven by a tumor cell-autonomous mechanism.

Type I IFN signaling activates the replication stress response pathway in PDAC cells

Because IFNs impair cancer cell proliferation *in vitro*, we hypothesized that IFN exposure triggers adaptive signaling alterations in PDAC cells that can be exploited for the treatment of IFN-signaling high tumors[8]. To systematically profile such mechanisms we applied an nLC-MS/MS phospho-proteomics analysis of SUIT2 PDAC cells 24 h following IFNβ treatment (**Figure 3.3D**). We identified 1,077 significantly altered proteins (among 9,350 detected, 1% FDR), many if which were enriched in pathways related to established IFN functions which validated our approach (**Figure S3.3B**), and 911 significantly altered phosphopeptides (among 17,368 detected, 0.1% FDR). Kinase substrate enrichment analysis (KSEA) of the significantly altered phosphopeptides identified enriched phosphorylation of ATM/ATR, HIPK2, and MAPK1/3 (ERK1/2) substrates following treatment (**Figure 3.3D**)[31]. While activation of the MAPK pathway by type I IFN has been reported, little is known about the connection between IFN signaling and the replication stress response pathway mediated by ATR[32,33]. We detected increased phosphorylation of $CHEK1_{S317}$, an established substrate of ATR, in our phospho-proteomics dataset and we confirmed this finding using immunoblot analysis in which $pCHEK1_{S345}$ was observed 12 h after the addition of IFNβ to PDAC cell culture (**Figures 3.3E**, **3.3F**).

ATR activation is a compensatory response to replication stress, caused by any obstacle to DNA replication, and results in decreased proliferation and cell cycle arrest in S-phase[21]. Consistently, we found that IFN treatment resulted in both impaired proliferation (**Figure 3.3F**) and induced S-phase arrest in SUIT2 cells (**Figure 3.3G**). We expanded this analysis to a panel of PDAC cell lines and observed varying degrees of IFN-induced $pCHEK1_{S345}$ (**Figure 3.3I**). A

similar pattern of heterogeneity was observed in the induction of S-phase accumulation (**Figure 3.3J**). pCHEK1 induction appears to predict IFN-induced S-phase arrest in this panel. The co-existence of pCHEK1$_{S345}$ and IFN markers was validated in subsets of surgical PDAC specimens and we observed several cases in which high levels of both markers were apparent in serial sections of a single specimen (**Figures 3.3K, S3.3C, S3.3D**). Taken together, our results indicate that type I IFN signaling induces replication stress in PDAC cells, suggesting a potential vulnerability of PDAC tumor exhibiting constitutive type I IFN signaling.

IFN signaling restricts nucleotide pools

An established cause of replication stress an insufficient or imbalanced supply of the substrates for DNA replication (dNTPs)[21]. We applied a targeted LC-MS/MS approach to: (*i*) evaluate IFNβ-induced alterations in total dNTP abundance and (*ii*) evaluate the contribution of stable isotope [$^{13}C_6$]glucose to dNTP pools, an indicator of *de novo* synthesis (**Figure 3.4A**). We found that IFN treatment triggers in a decrease in dCTP, dTTP, dATP and dTTP pools in both SUIT2 and YAPC cells (**Figures 3.4B, 3.4C**). To systematically investigate the cause of this metabolic reprogramming we evaluated IFN-induced alterations in the expression of nucleotide-metabolism genes in the nLC-MS/MS proteomics dataset obtained for **Figure 3.3D**. Notably, the expression of proteins that catabolize nucleotides and nucleosides, including sterile alpha-motif and histidine-aspartate domain-containing protein 1 (SAMHD1), thymidine phosphorylase (TYMP), and cytosolic 5'-nucleotidase 3A (NT5C3A), exhibited significant upregulation in IFNβ-treated cells (**Figures 3.4E, S3.5A**). Additionally, we observed a signification down-regulation of dihydrofolate reductase (DHFR) and thymidylate synthase (TYMS) which are required for *de novo* dNTP biosynthesis. Taken together, these observations suggest a model in which type I IFNs restrict dNTP pools via the combination of impaired biosynthesis and enhanced catabolism (**Figure 3.4F**).

SAMHD1 emerged as a potential mediator of IFN-induced replication stress as it has been previous linked to the regulation of cell cycle progression and functions as a central mediator of dNTP homeostasis by catalyzing the phosphohydrolysis of dNTP to deoxyribonucleosides (dN) which are effluxed into the environment[34,35]. Recently, SAMHD1 has been shown to possess a novel moonlighting function which is to promote DNA repair by acting as a molecular scaffold for CtIP at replication forks[35]. Interestingly, this secondary function of SAMHD1 negatively regulates cytosolic DNA sensing pathways and autocrine IFN signaling explaining the observation that mutational inactivation of SAMHD1 is associated with development of the autoimmune interferonopathy Aicardi-Goutieres Syndrome[36].

To investigate the role of SAMHD1 in IFN-induced nucleotide pool restriction, we generated SUIT2 SAMHD1 knockout cells using CRISPR/Cas9 (**Figure S3.4B**). dNs produced by phosphohydrolysis are either effluxed from cells, re-enter metabolism via the actions of nucleoside kinases dCK and TK1 or catabolized via deaminases (CDA and ADA) or phosphorylases (PNP and TYMP). We reasoned that upregulation of SAMHD1 expression would result in increased dNTP phosphohydrolysis and nucleoside efflux in PDAC cells. To test this we utilized a previously described LC-MS/MS assay to evaluate the contribution of [$^{13}C_6$]glucose to dNTP pools, extracellular dNs and newly replicated DNA in SUIT2 parental and SAMHD1 knockout cells (**Figure S3.5C**)[23]. In parental cells IFN treatment resulted in a 2-fold decrease in dCTP pools and a 3-fold increase in dC efflux (**Figure S3.5D**). At baseline, SAMHD1 knockout cells had a nearly 3-fold greater labeled dCTP pool than parental cells and in this model IFN failed to induce dCTP pool decreases or enhance dC efflux. We found a similar pattern in our evaluation of the dATP pool but determined that IFN was still capable of decreasing this pool in SAMHD1 knockout cells, albeit by a small degree. Interestingly, we did not detect efflux of the purine nucleoside deoxyadenosine (dA) in this model. We then hypothesized that the nucleoside kinase dCK could maintain dCTP pools in the presence of IFN by recycling SAMHD1-produced nucleosides thereby preventing dC efflux. To test this hypothesis we expanded our analysis to include an evaluation of SUIT2 dCK knockout cells

alongside parental and SAMHD1 knockout cells (**Figure S3.5C**). We found that dCK knockout decreased dCTP pools and increased dC efflux at baseline and amplified IFN-induced dCTP pool depletion and dC efflux. Expectedly, dCK knockout did not influence dATP pool alterations induced by IFN.

We found that IFN impaired the contribution of [$^{13}C_6$]glucose to the dC and dA compartment of DNA in each of the isogenic lines indicating that while SAMHD1 is a critical mediator of IFN-induced intracellular dNTP pool alterations and dN efflux it is not solely responsible for impaired DNA replication in this model (**Figure S3.5E**). SAMHD1 induction and dNTP pool reduction were not a transient response to acute IFN exposure and were sustained and detectable following 21 days of chronic exposure (**Figures S3.5F, S3.5G**). Collectively these results demonstrate that SAMHD1 is a critical mediator of IFN-induced alterations in dNTP abundance and dN efflux but that is not solely responsible for IFN-induced replication defects.

The purine nucleosides dA and dG produced by SAMHD1-mediated dNTP phosphohydrolysis can either be recycled by dCK or catabolized by the combined actions of ADA and PNP. We reasoned that our inability to detect dA nucleoside efflux in SUIT2 cells is because of its rapid catabolism by these enzymes (**Figure S3.4A**). We found that [$^{13}C_6$]glucose-derived dG was only detectable in cells co-treated with the PNP inhibitor BCX-1777 and was enhanced by IFNβ (**Figure S3.4B**). Additionally ,we determined that SAMHD1 expression was required for dG efflux in SUIT2 cells (**Figure S3.4B**).

While dCK can accept dC, dA and dG, salvage of thymidine (dT) requires the nucleoside kinase thymidine kinase 1 (TK1). dCK and TK1 are well studied for their role in nucleoside salvage (i.e. the scavenging and trapping of environmental nucleosides) but their cell autonomous role in preventing efflux is unexplored[37]. Utilizing a combination of a small molecule dCK inhibitor developed by our group (DI-82) and CRISPR/Cas9 knockout of TK1 we found that both pyrimidine deoxyribonucleoside kinases prevent efflux of [$^{13}C_6$]glucose labeled pyrimidine nucleosides at baseline as efflux was elevated in knockout cells (**Figures S3.4D, S3.4E, S3.4F,**

S3.4G)[23]. Interestingly, we found that while IFN triggered an increase in dC efflux, dT efflux was decreased. We hypothesize that this decrease reflects enhanced dT catabolism by TYMP which is induced by IFN. These results indicate that IFN triggers a metabolic shift in PDAC cells from an anabolic to a catabolic phenotype mediated by SAMHD1 and that nucleoside kinases counteract SAMHD1, and potentially TYMP activities. Interestingly, these findings suggest that a substrate cycle exists between SAMHD1 and dCK/TK1 which could serve to fine-tune dNTP pool sizes or to promote a futile cycle of ATP consumption.

The cGAS/STING pathway drives autocrine type I IFN signaling in PDAC tumors

Our observation that patient-derived and cell xenograft PDAC tumors exhibit IFN signaling biomarker enrichment suggested that tumor cells produce IFN as IFN is species-restricted. In epithelial cells, type I IFN production can be initiated downstream of cytosolic nucleic acid sensor activation triggered by pathogen or mis-localized self DNA (Figure 3.1). One such sensor is cyclic GMP-AMP synthase (cGAS) which binds ssDNA and dsDNA and in turn activates stimulator of interferon genes (STING) via production of the cyclic dinucleotide 2'-3'-cGAMP. In contrast to other cancers in which cGAS and STING are suppressed by mutational inactivation or epigenetic silencing, cGAS and STING promoters are generally hypo-methylated in PDAC and STING is transcriptionally up-regulated in PDAC tumors compared to normal pancreas(**Figure S3.6A**)[38]. Moreover, IHC staining of our PDAC tissue microarray revealed detectable STING expression in tumor cells at varying levels in >90% of samples, a finding consistent with a previous report (**Figure S3.6B**)[39]. To evaluate the functionality of the cGAS/STING pathway in tumor cells we transfected a panel of PDAC cell lines with IFN stimulatory DNA (ISD, a cGAS ligand) and measured induction of the IFNβ transcript using RT-PCR. We determined that ISD triggered an increase in the IFNβ transcript only in a subset of lines (**Figure S3.6C**). We reasoned that cell lines not responsive to ISD are defective in either cGAS or STING expression. However, we determined that there is no correlation between cGAS or

STING protein levels and ISD response in this panel and identified several cell lines, including SUIT2, which are ISD non-responders but express both cGAS and STING at levels comparable to ISD-responsive cells (**Figure S3.6D**). In SUIT2 cells, we found that despite their lack of response to ISD, direct activation of STING via transfection with a bisphosphorothioate 2'-3'-cGAMP analog (cGAMP) trigged an increase in IFNβ transcript levels (**Figure S3.6E**). This finding suggests that in SUIT2 cells cGAS is mis-localized or inhibited by a post-translational mechanism of which several have been described[40]. Expectedly, cGAMP transfection triggered rapid phosphorylation of $IRF3_{S139}$, which is mediated by TBK1 downstream of STING-dependent cGAMP sensing, and phosphorylation of STAT1 which was temporally followed by induction of STAT1 and MX1 protein expression (**Figures S3.6F, S3.6G**). Additionally, cGAMP transfection triggered secretion of IFNβ protein into culture supernatants in STING-proficient DANG cells (**S3.6H**). Inhibition of JAK1 using ruxolitinib (RUX) abrogated cGAMP induced STAT1 phosphorylation and interferon stimulated gene induction further indicating that interferon stimulated gene expression initiated by STING functions via an autocrine/paracrine mechanism (**Figures S3.6F, S3.6G**). Consistent with our *in vitro* observation, STAT1 and MX1 proteins were highly expressed in untreated xenograft tumors derived from the STING pathway-active DANG cells. STAT1 and MX1 protein levels in DANG tumors were comparable to their levels observed in cell culture following 24 h treatment with IFN, a finding which indicates that cell culture can mask a constitutive endogenous IFN response (**Figure 3.1C**). Furthermore, MX1 and STAT1 were expressed at low levels in xenograft tumors derived from STING pathway-inactive SUIT2 cells (**Figure S3.7A**). Collectively, these results indicated that the cGAS/STING pathway drives constitutive IFN signaling in xenograft tumors and that profiling of cGAS and STING expression is not sufficient to predict pathway functionality in PDAC cells.

IFN signaling modulates PDAC cell proliferation and nucleotide metabolism *in vivo*

To model the IFN-high and -low conditions observed in PDAC patient specimens in an isogenic system we engineered SUIT2 cells to express a previously described constitutively active STING mutant ($STING^{R248M}$) or a GFP control conditionally in the presence of doxycycline

(**Figures 3.5A, S3.7B**)[41]. Activation of STING^{R248M} resulted in impaired cell proliferation in 3D cultures, similar to our findings with recombinant IFN (**Figure 3.5B**). We confirmed that this model recapitulates IFN exposure by performing immunoblot analysis of IFN stimulated in gene expression following doxycycline treatment which was comparable to treatment with recombinant IFN (**Figure 3.5C**). Pharmacological inhibition of JAK abrogated IFN stimulated gene induction mediated by the STING^{R248M} transgene.

To determine if these phenotypes occur *in vivo* we implanted SUIT2-STING^{R248M} cells subcutaneously in NCG mice and provided doxycycline-supplemented diet. We found that STING^{R248M} induction significantly impaired xenograft tumor growth. We performed immunoblot analysis of explanted tumors and determined that doxycycline treatment induced STING, IFN stimulated gene expression and phosphorylation of CHEK1.

To compliment these findings and to determine if endogenously produced IFN, mediated by STING, impairs tumor growth *in vivo* we knocked out STING using CRISPR/Cas9 in DANG cells which exhibit constitutive IFN signaling when grown as xenograft tumors (**Figures 3.3C; S3.7C**). In this loss-of-function model, STING knockout abrogated xenograft tumor expression of MX1 and STAT1 as determined by IHC staining (**Figure S3.7D**). We found that STING knockout promoted DANG tumor growth, completely blocked expression of MX1 and resulted in decreased CHEK1 phosphorylation in tumors (**Figures 3.5F, 3.5G**). Collectively, these findings provide a link between STING activity, PDAC cell IFN signaling, tumor growth and replication stress *in vitro* and *in vivo.*

To validate this findings we generated a second STING knockout isogenic cell line system in HS766T which stably express a firefly luciferase (fLUC)-linked IFN stimulated response element (ISRE) reporter to non-invasively track type I IFN signaling activity in xenograft PDAC tumors. Under cell culture conditions only STING-proficient HS766T cells exhibit reporter ISRE promoter activation following 2'-3'-cGAMP transfection while both isogenic lines were responsive to IFNβ (**Figure S3.7E**). Consistently, STING proficient HS766T ISRE-fLUC tumors exhibited a higher

luminescence intensity when compared to STING knockout isogenic tumors (**Figure S3.7F**) and substantially decreased levels of pSTAT1$_{Y701}$, STAT1, and MX1 (**Figure S3.7G**).

We further investigated the proliferation of STING isogenic models using an orthotopic system in which PDAC cells are injected into the pancreata of immunodeficient mice. For this model we engineered our SUIT2-STING^{R248M} cells to constitutively express a fLUC reporter that allows for non-invasive monitoring of tumor burden using bioluminescence imaging. We found that activation of STING using doxycycline results in impaired growth of orthotopic PDAC tumors (**Figure 3.5H**). We performed immunoblot analysis of orthotopic tumor explants and found enrichment of IFN stimulated gene expression in STING^{R248M} active tumors (**Figure 3.5I**). We also observed down-regulation of the nucleotide biosynthetic genes DHFR and TYMS in STING^{R248M} tumors, consistent with our *in vitro* observations (**Figure 3.4D**). Collectively, these results demonstrate that the cGAS/STING signaling pathway is intact in a subset of PDAC models and that its activity in tumor cells is a non-redundant contributor to cell type I IFN signaling in PDAC xenograft tumors.

We next asked if IFN signaling mediated by STING triggers metabolic alterations *in vivo*. We hypothesized that we could leverage the induction of TYMP by IFN for the detection of STING-active tumors using positron emission tomography (PET) as environmental thymidine levels have been shown to influence [^{18}F]fluorothymidine ([^{18}F]FLT) PET probe accumulation in tumors[42,43]. TYMP is a key metabolic enzyme which degrades dT into thymine and 2-deoxy-alpha-D-ribose 1-phosphate and depletes free dT pools (**Figure S3.8A**). Additionally, TYMP has also been identified as a positive regulator of angiogenesis by promoting the growth and proliferation of endothelial cells[44]. Both thymidine and [^{18}F]FLT require phosphorylation by thymidine kinase 1 (TK1) for their intracellular accumulation, however, the affinity of dT for TK1 greatly exceeds that of [^{18}F]FLT[43]. [^{18}F]FLT is not a substrate for TYMP but its accumulation is surrogate marker of its activity: [^{18}F]FLT accumulation is a function of both TK1 expression and dT levels (which are mediated by TYMP). In this model, IFN-dependent depletion of dT will result in increased accumulation of the [^{18}F]FLT PET probe in tumors. To test this hypothesis we

evaluated the impact of IFN treatment on [^{18}F]FLT uptake under varying dT concentrations (**Figure S3.8B**). We found that dT competitively inhibited [^{18}F]FLT uptake but treatment with IFN prevented this effect. To confirm a role for TYMP in this phenotype we generated TYMP knockdown cells using shRNA in SUIT2 cells (**Figure S3.8C**). We found that both knockdown of TYMP and treatment with a JAK inhibitor impaired IFN-induced [^{18}F]FLT uptake in SUIT2 cells in the presence of dT (**Figure S3.8D**). We determined that type II IFN (IFNγ) elicited similar induction of TYMP in SUIT2 cells and that YAPC cells are deficient for TYMP at baseline and in the presence of either IFNβ or IFNγ (**Figure S3.8E**). We found that IFNs induced [^{18}F]FLT uptake in a TYMP-dependent manner (**Figure S3.8F**) and that IFN did not enhance [^{18}F]FLT uptake in TYMP-deficient YAPC cells (**Figure S3.8G**).

Using PET imaging of tumor bearing mice we determined that [^{18}F]FLT accumulation is significantly increased after doxycycline treatment in STING^{R248M} tumors compared to GFP expressing isogenic controls (**Figure 3.5J**). We confirmed that this alteration was specific to [^{18}F]FLT and not the consequence of global metabolic reprogramming as [^{18}F]FDG uptake in the same animal model was unaffected by IFN signaling (**Figure 3.5K**). Additionally, we performed [^{18}F]FLT and [^{18}F]FDG imaging of NCG mice bearing bilateral SUIT2-GFP and -STING^{R248M} tumors and found that [^{18}F]FLT accumulation was significantly enriched in STING tumors whereas no impact on [^{18}F]FDG accumulation was observed, indicating that STING induced metabolic reprogramming is locally confined (**Figure S3.8H**). Consistently, we found that STING^{R248M} induction does not alter nucleotide metabolism systemically as we did not observe significant differences in plasma dT levels in mice bearing either SUIT2-GFP or -STING^{R248M} tumors treated with doxycycline (**Figure S3.8I**). In summary, we confirmed that IFN signaling driven by STING reprograms tumor cell metabolism both *in vitro* and *in vivo*.

The replication stress response pathway is a collateral dependency triggered by IFN signaling in a subset of PDAC cells

To compliment our phosphoproteomic profiling and with the goal of systematically identifying signaling pathway co-dependencies triggered by IFN in tumor cells we applied a high-throughput 430 compound chemical genomics screen using SUIT2 cells treated ± IFN (**Figure 3.6A**). Inhibitors of key replication stress response effectors, including ATR (AZD6738) and CHEK1 (LY2603618, PF-477736 and AZD-7762), scored among top hits and exhibited significantly increased activity in SUIT2 cells treated with IFNβ. Expectedly, JAK kinase inhibitors (LY278544, tofacitinib and ruxolitinib) which block type I IFN signaling abrogated the anti-proliferative effects of IFNβ in our screen. These hits are are consistent with our phosphoproteomics results and identified the replication stress response pathway as an IFNβ-induced co-dependency in PDAC cells.

The replication stress response pathway is initiated by ATR which phosphorylates and activates downstream effectors CHEK1 and WEE1 in response to any obstacle to DNA replication. Small molecule inhibitors of these kinases have entered clinical trials in various cancers combined with genotoxic chemotherapy, PARP inhibitors or immunotherapy (**Figure S3.9A**)[22]. To validate our screen we evaluated the interaction between IFNβ and VE-822 (also known as M6620, currently being evaluated in clinical trials) in an anchorage independent growth assay and found that while single agents had a cytostatic effect only the combination completely prevented PDAC cell proliferation (**Figure 3.6B**). Using Cell Titer Glo we found synergy between IFNβ and inhibitors of each of the replication stress response pathway kinases ATR, CHEK1 and WEE1 (**Figure S3.9B**). We found a synergistic increase in cleaved PARP and cleaved caspase 3 in cells co-treated with IFN and either of two ATR inhibitors VE-822 or AZD6738 (**Figure S3.9C**). Collectively, these results confirm that the replication stress response pathway, and not ATR or CHEK1 alone, is an IFN-induced co-dependency in PDAC cells

We next directly measured ssDNA abundance an established consequence of replication fork stalling and replication stress, by evaluating F7.26 ssDNA-specific antibody cross-reactivity[23]. Both IFN and ATRi triggered ssDNA accumulation alone and combination treatment resulted in the greatest degree of induction (**Figures 3.6C, S3.10A**). We performed flow cytometry analysis of pH2A.X_{S139} to determine if combination treatment induces DNA damage (**Figure 3.6D**). While only inducing a 3% increase alone, IFNβ increased the percentage of pH2A.X_{S139} positive cells from 33% to 72% when VE-822 was present. Interestingly, we found that while the percentage of pH2A.X_{S139} positive cells was synergistically increased in the combination group the overall pH2A.X_{S139} intensity decreased compared to VE-822 treatment alone. This observation is reminiscent of previous findings that pan-nuclear pH2AX, as opposed to foci accumulation, is a marker for replication catastrophe (**Figure S3.10B**)[45]. In addition, apoptosis was synergistically induced by IFNβ and VE-822 as determined by AnnexinV/PI flow cytometry (**Figures 3.6E, S3.10C**). To determine if mitotic entry is required for the lethal effects of IFNβ+VE-822 we simultaneously treated cells with a CDK4/6 inhibitor (CDK4/6i) which expectedly arrested SUIT2 cells in G1 (**Figure S3.10D**). We found that CDK4/6i treatment did not alter IFN stimulated gene expression but completely prevented IFNβ+VE822-induced H2AX_{S139} phosphorylation and cleaved PARP accumulation (**Figure S3.10D**). Taken together, these data indicate that mitotic entry is required for synergy between IFNβ and ATRi.

We expanded our findings to a panel of PDAC cell lines and found a heterogenous degree of sensitivity to IFN, VE-822 and the combination using live-cell imaging (**Figure 3.6F**). Models with the highest degree of synergy exhibited highest pCHEK1$_{S345}$ induction by IFNβ (**Figure 3.3J**). Furthermore, IFN and VE-822 synergistically induced S-phase accumulation selectively in lines in which an anti-proliferative synergy was observed (**Figure 3.6G**). We identified a synergistic interaction between IFNβ and VE-822 on proliferation inhibition and S-phase accumulation in A13A primary PDAC cultures (**Figures S3.10E, S3.10F**) whereas no significant anti-proliferative effect nor S-phase arrest was observed in the non-transformed human pancreatic ductal epithelial cells (HPDE; **Figures S3.10G, S3.10H**).

Type I IFN and ATR signaling collaboratively control PDAC cell nucleotide metabolism.

As ATR has been shown to regulate both *de novo* and scavenging nucleotide biosynthesis by transcriptional and post-translational mechanisms we reasoned that VE-822 could enhance dNTP restriction triggered by IFN[23]. Consistent with our previous work in leukemia we found that VE-822 treatment down-regulated the expression of nucleotide biosynthetic genes, TYMS, RRM1 and RRM2, and the nucleoside kinase TK1 in a dose dependent manner in the presence of IFN (**Figure S3.11C**)[23]. We expanded this analysis to a panel of PDAC cell lines representative of the heterogeneity in synergy between IFN and VE-822. We determined the VE-822 alone only triggered down-regulation of RRM1, RRM2, TK1 and TYMS in cell lines in which synergy between IFN and VE-822 was observed (**Figure 3.7A**). Furthermore, we found that IFN potentiated the down-regulation of these genes selectively in “sensitive” models. To investigate the mechanism of down-regulation we performed RT-PCR analysis of nucleotide metabolism gene expression following treatment with IFN ± VE-822 (**Figure S3.11B**). We determined that IFN alone decreased the levels of TYMS transcript, consistent with our findings in **Figure 3.4**, and induced upregulation of RRM2 and TK1 transcripts which is likely the consequence of S-phase arrest as the expression of these genes is restricted to S-phase. VE-822 treatment resulted in decreased levels of TYMS, TK1, RRM1 and RRM2 transcripts. This down-regulation is likely not an artifact of cell cycle alterations as treated cells significantly accumulated in S-phase (**Figure S3.6G**). ATR has been previously associated with the transcriptional control of these genes via stabilization of their transcription factor, E2F1[46]. Intriguingly, the anti-proliferative effects of IFN have also been linked to their ability to down-regulate E2F activity[47]. In addition to regulating transcription, ATR has been demonstrated to promote RRM2 protein stability by preventing its phosphorylation on T33 by CDK1 which positively regulates its degradation mediated by the $SCF^{Cyclin\ F}$ ubiquitin ligase complex[48]. We found that supplementation with aproteasome inhibitor partially rescued ATRi-mediated down regulation of TYMS, TK1, RRM1 and RRM2 both alone and in the presence of IFN (**Figure**

S3.11C). These results indicate that ATR coordinates nucleotide metabolism by both promoting of gene transcription and preventing protein degradation.

Using LC-MS/MS analysis we found that both IFN and VE-822 decreased dCTP pool abundance with the lowest levels observed in the combination treatment group (**Figure 3.7B**). To evaluate the impact of IFN and VE-822 on replication dynamics we adapted an LC-MS/MS assay previously used by our group to track the incorporation of glucose-derived or nucleoside-derived nucleotides using stable isotope tracers[23]. We found that both IFN and VE-822 decreased the total degree of deoxycytidine labeling in DNA (DNA-C) mediated by the *de novo* pathway ([$^{13}C_6$]glucose-derived nucleosides; **Figure 3.7C**). Furthermore, the greatest degree of inhibition was observed in cells treated with both IFN and VE-822. Collectively, these results indicate that IFNβ primarily restricts dNTP abundance by initiating nucleotide and nucleoside catabolism whereas ATR inhibition limits dNTP biosynthesis via down-regulation of the expression of anabolic genes, including both *de novo* pathway genes and nucleoside salvage kinases. This down-regulation is likely mediated by ATRi-mediated impairment of E2F1 transcription factor activity.

STING activation triggers a collateral dependency on ATR

To determine if tumor cell-autonomous IFN signaling drives a collateral dependency on ATR we evaluated the sensitivity of our SUIT2-STING^{R248M} cells to VE-822 using live cell imaging of 3D cultures. We found that both DOX treatment (STING activation) and VE-822 impaired sphere growth the combination completely prevented proliferation (**Figures 3.8A, 3.8B**). We generated a second conditional STING^{R248M} model using YAPC cells to expand these findings and confirmed doxycycline treatment induces STING and interferon stimulated gene expression that is dependent on JAK activity (**Figure S3.12A**). We observed similar synergy between STING activation and VE-822 in this model using 2D cultures (**Figure S3.12B**). Signaling through JAK is essential for this synergy as supplementation with ruxolitinib restored the proliferation of

combination treated cells (**Figure S3.12C**). To test this model in vivo we engineered SUIT2 TetR fLuc cells with either the STINGR248M transgene an ATR targeting shRNA or the combination. These cells were injected into the pancreas of NCG mice and tumor burden was monitored using bioluminescence imaging following doxycycline treatment. Knockdown of ATR using shRNA impaired the proliferation of SUIT2-STING^{R248M} cells *in vivo* while ATR knockdown had no effect on tumor growth alone (**Figures 3.8C, 3.8D, 3.8E**). Collectively, these results indicate that STING-driven IFN signaling triggers a collateral dependency on ATR *in vitro* and *in vivo* and suggest that ATR inhibitors may exhibit increased activity against tumors exhibiting constitutive IFN signaling.

PARP inhibitors synergize with IFN and ATRi

ATR inhibitors have progressed into phase I and phase II clinical trials in combination with chemotherapy, radiation or PARP inhibitors. DNA repair by homologous recombination (HR) is required for resolution of PARP inhibitor-induced DNA damage and thus PARP inhibitors have been shown to be particularly effective against HR-deficient tumors such as BRCA1/2-deficient breast and pancreatic cancer[6]. Additionally, mediators of HR, including BRCA1 and CtIP are known targets of E2F1 and down-regulated by ATRi in PDAC cells (**Figure S3.13A**). We reasoned that IFN/ATRi treatment would induce a HR-deficient like cellular state and serve as an effective approach to sensitive PDAC cells to PARP inhibitors. We found that ATR inhibition sensitizes PDAC cells to olaparib, a response which is amplified by IFN supplementation (**Figure S3.13B**). We used pH2AX$_{S139}$ flow cytometry to evaluate the extent of DNA damage in treated cells and we observed the highest levels in SUIT2 cells treated with VE-822 and olaparib in the presence of IFNβ (**Figure S3.13C**). Annexin V/PI analysis revealed that type I IFN signaling increases apoptosis-induction by the VE-822/olaparib combination in SUIT2 cells (**Figure S3.13D**). To expand these findings we evaluated the effects of the VE-822/olaparib combination SUIT2, DANG, and in the primary PDAC culture model A13A and we found that

VE-822 and olaparib synergize to impair proliferation in the presence of IFNβ across all models tested (**S3.13C**). Using Annexin V/PI flow cytometry we observed a synergistic induction of apoptosis by the combination of IFN, VE-822 and olaparib in the primary A13A model. Collectively, these results suggest that constitutive IFN signaling driven by STING in combination with a ATR inhibitor may trigger an HR deficiency-like phenotype that may render tumor cells particularly vulnerable to PARP inhibitor combinations.

IFNs reprogram nucleotide metabolism in PDAC cancer-associated fibroblasts

In addition to constitutive inflammatory cytokine signaling, a heterotypic cellular microenvironment is a hallmark of PDAC. Among the cell types present in the PDAC microenvironment cancer associated fibroblasts (CAFs) are particularly important and as they constitute the bulk of the majority of tumors and influence response to therapy[49]. Recently, CAF and macrophage-derived nucleosides have been shown to influence the activity of anti-metabolite chemotherapy gemcitabine by competing with dCK for phosphorylation[50].

Having observed that IFNs promote dC efflux in tumor cells we asked whether a similar phenotype can be observed in CAF cultures (**Figure S3.14A**). We treated an immortalized human PDAC CAF culture with IFNβ and observed robust up-regulation of $pSTAT1_{Y701}$ and SAMHD1 (**Figure S3.14B**). We found that CAF cells overproduce dC and efflux *de novo* produced dC into the media. [$^{13}C_6$]glucose labeled-derived dC levels were nearly 3-fold higher when CAFs were exposed to IFNβ (**Figure S3.14C**). These results indicate that PDAC CAFs, like tumor cells, phosphohydrolyze dNTPs via a mechanism presumably mediated by SAMHD1. While some nucleoside-analog chemotherapies, including cytarabine, have been shown to be inactivated by SAMHD1 directly by phosphohydrolysis of their triphosphate forms, gemcitabine-triphosphate (dFdCTP) is resistant to this mechanism[51]. We propose that SAMHD1 can promote gemcitabine resistance indirectly by increasing dC levels in the microenvironment thereby increasing competition for phosphorylation by dCK. Thus, we hypothesize that PDAC tumors

exhibiting high IFN signaling are poorly responsive to gemcitabine because of increased levels of microenvironmental SAMHD1-derived nucleosides. In addition to preventing antimetabolite activity CAF-derived nucleosides can be potentially utilized as a nutrient source in PDAC cells. The metabolic significance of CAF-derived nucleosides in tumors remains to be determined.

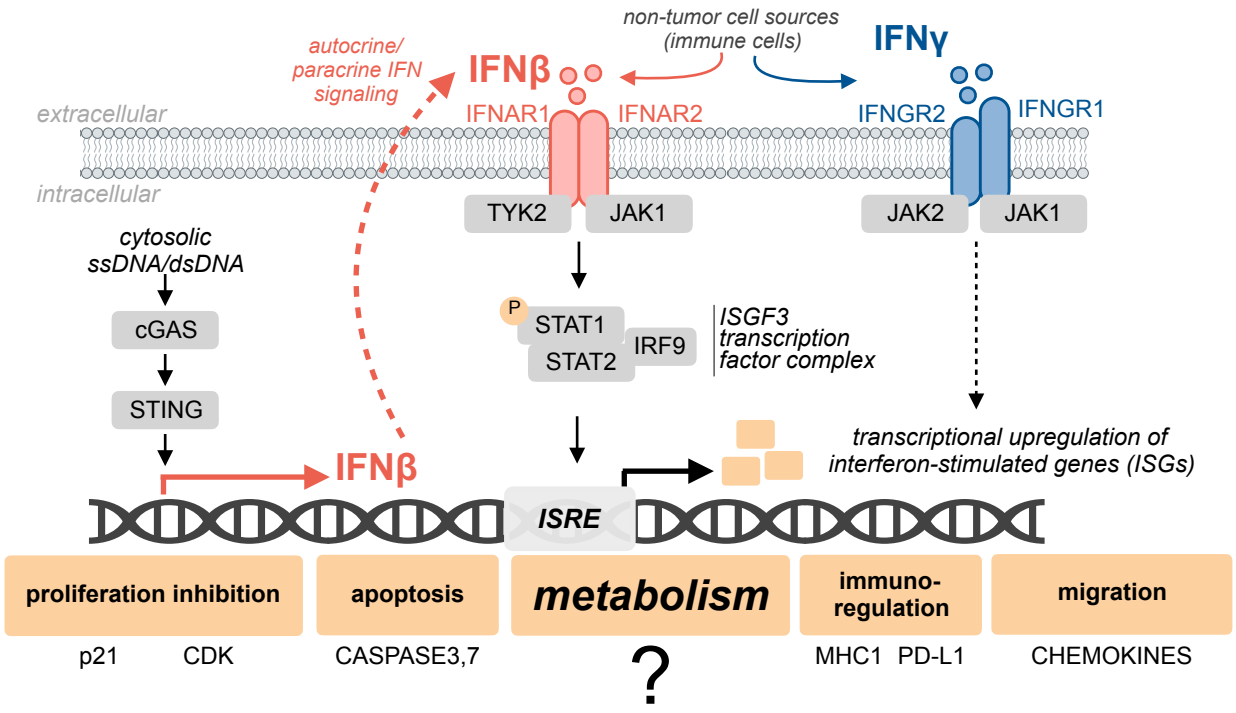

Figure 3.1 | Interferons (IFNs) are pleiotropic cytokines that modulate multiple aspects of cancer cell biology. Summary of causes and consequences of IFN signaling. cGAS: cyclic GMP-AMP synthase; STING: stimulator of interferon genes; ISRE: interferon-sensitive response element; IFNAR: interferon-alpha/beta receptor; IFNGR: interferon-gamma receptor; STAT1: signal transducer and activator of transcription 1.

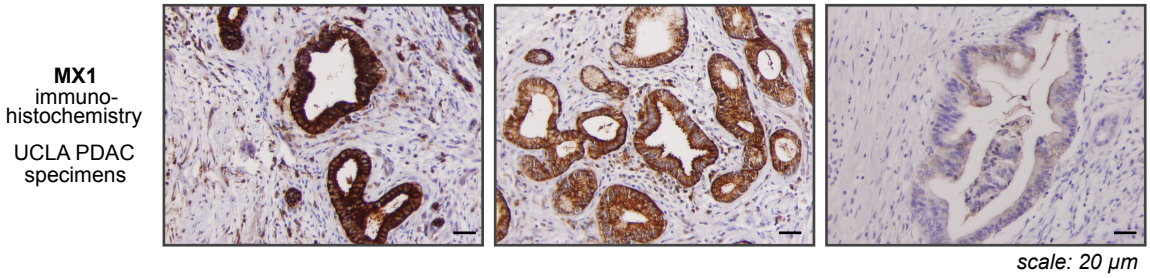

Figure 3.2 | IFN signaling biomarkers are enriched in PDAC tumors. Representative immunohistochemistry (IHC) images of primary PDAC samples probed for the interferon regulated gene MX1 obtained at 20x magnification.

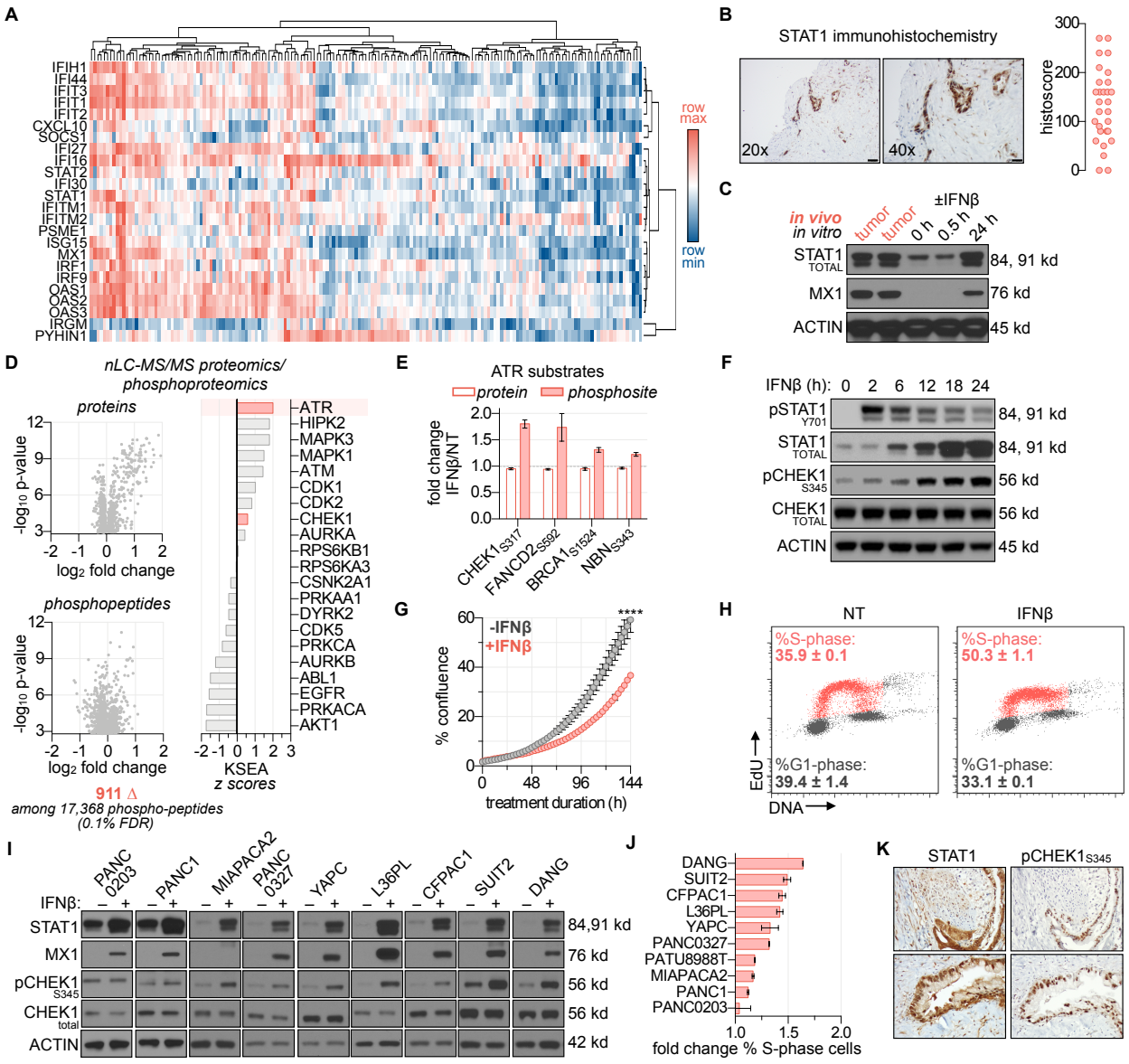

Figure 3.3 | IFN signaling biomarkers are enriched in PDAC and IFN activates the replication stress response pathway. (**A**) Analysis of IFN response metagene signature in the TCGA PDAC dataset. (**B**) Representative immunohistochemistry (IHC) images of primary PDAC samples probed for total STAT1 and plot histoscores from 26 PDAC tumors. Histoscores were calculated as a sum of the intensity of staining (0, negative; 1, weak; 2, median; or 3, strong) multiplied by the percentage of tumor cells at that intensity (0-300 range). (**C**) Immunoblot analysis of DANG cells treated ± 100 U/mL IFNβ for the indicated timepoints *in vitro* and lysates prepared from SUIT2 cells grown as subcutaneous tumors in NSG mice. Immunoblot analysis of

DANG PDAC cells. (**D**) nLC-MS/MS proteomics/phosphoproteomics analysis of SUIT2 cels treated ± 100 U/mL IFNβ for 24 h. An FDR of 1% was used to identify significantly altered proteins. n FDR of 0.1% was used to identify significantly altered proteins. KSEA analysis was used to identify significantly-altered phosphoproteins. (**E**) ATR substrates identified by KSEA as being significantly altered by IFNβ from experiment in panel **D**. (**F**) Immunoblot analysis of SUIT2 cells treated with 100 U/mL IFNβ for indicated time-points. (**G**) IncuCyte live-cell imaging analysis of SUIT2 cells treated 100 U/mL IFNβ (mean±SD, n=6, student's t-test, **** P<0.0001). (**H**) EdU-pulse flow cytometry analysis of SUIT2 cells. Cells were treated for 24 h ± 100 U/mL IFNβ and subsequently pulsed with 10 μM EdU for 2 h (mean±SD; n=2). (**I**) Immunoblot analysis of a panel of PDAC cell lines treated ± 100 U/mL IFNβ for 24 h. (**J**) Fold change in the percentages of S-phase cells following treatment ± 100 U/mL IFNβ for 24 h in a panel of 13 PDAC cell lines (mean±SD, n=2, one-way ANOVA: P< 0.0001). (**K**) Representative STAT1 and phospho-CHEK1$_{S345}$ IHC analysis of serial sections of PDAC patient tumor samples.

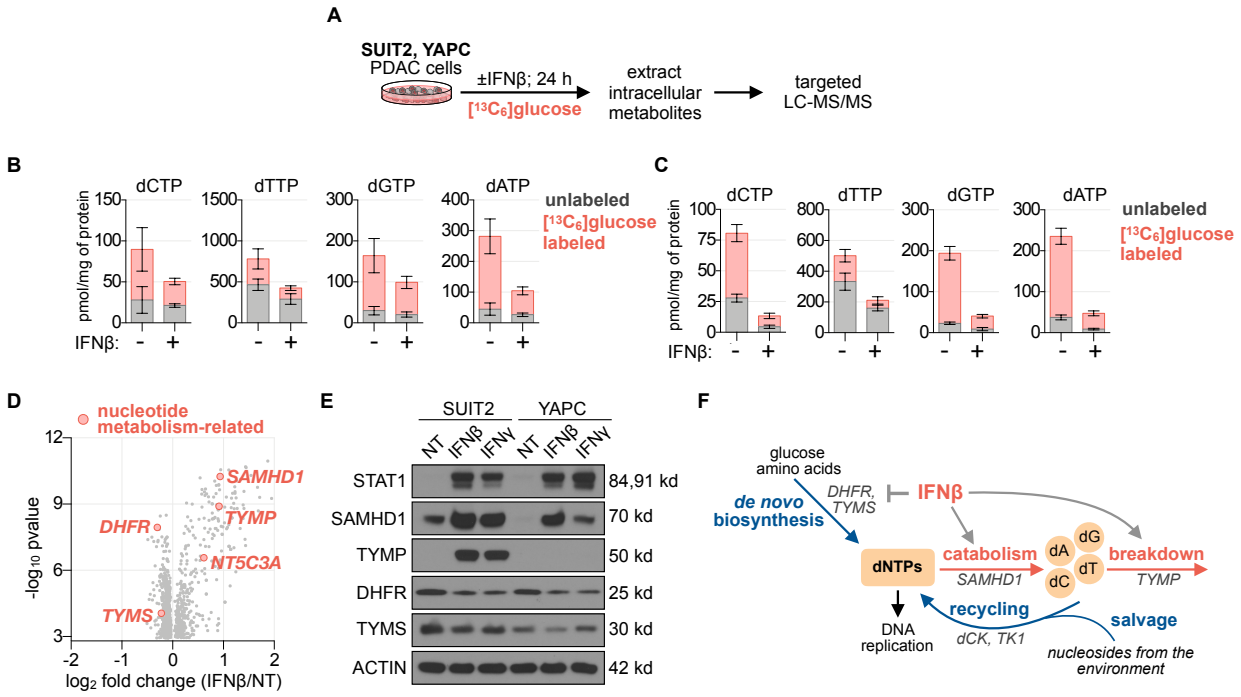

Figure 3.4 | Type I IFN signaling restricts dNTP pools. (**A**) Experimental approach to investigate the effects of IFN signaling on nucleotide metabolism in PDAC cells. (**B,C**) LC-MS/MS analysis of dNTP pools in SUIT2 (**B**) and YAPC (**C**) cells treated for 24 h ± 100 U/mL IFNβ in media containing 1 g/L [$^{13}C_6$]glucose (mean±SD; n=3). (**D**) Summary of nucleotide metabolism genes significantly altered by IFNβ treatment as determined by nLC-MS/MS in **Figure 1D**. (**E**) Immunoblot analysis of SUIT2 and YAPC cells treated ± 100 U/mL IFNβ or ± 10 ng/mL IFNγ for 24 h. (**F**) Working model summarizing the interactions between IFN and nucleotide metabolism.

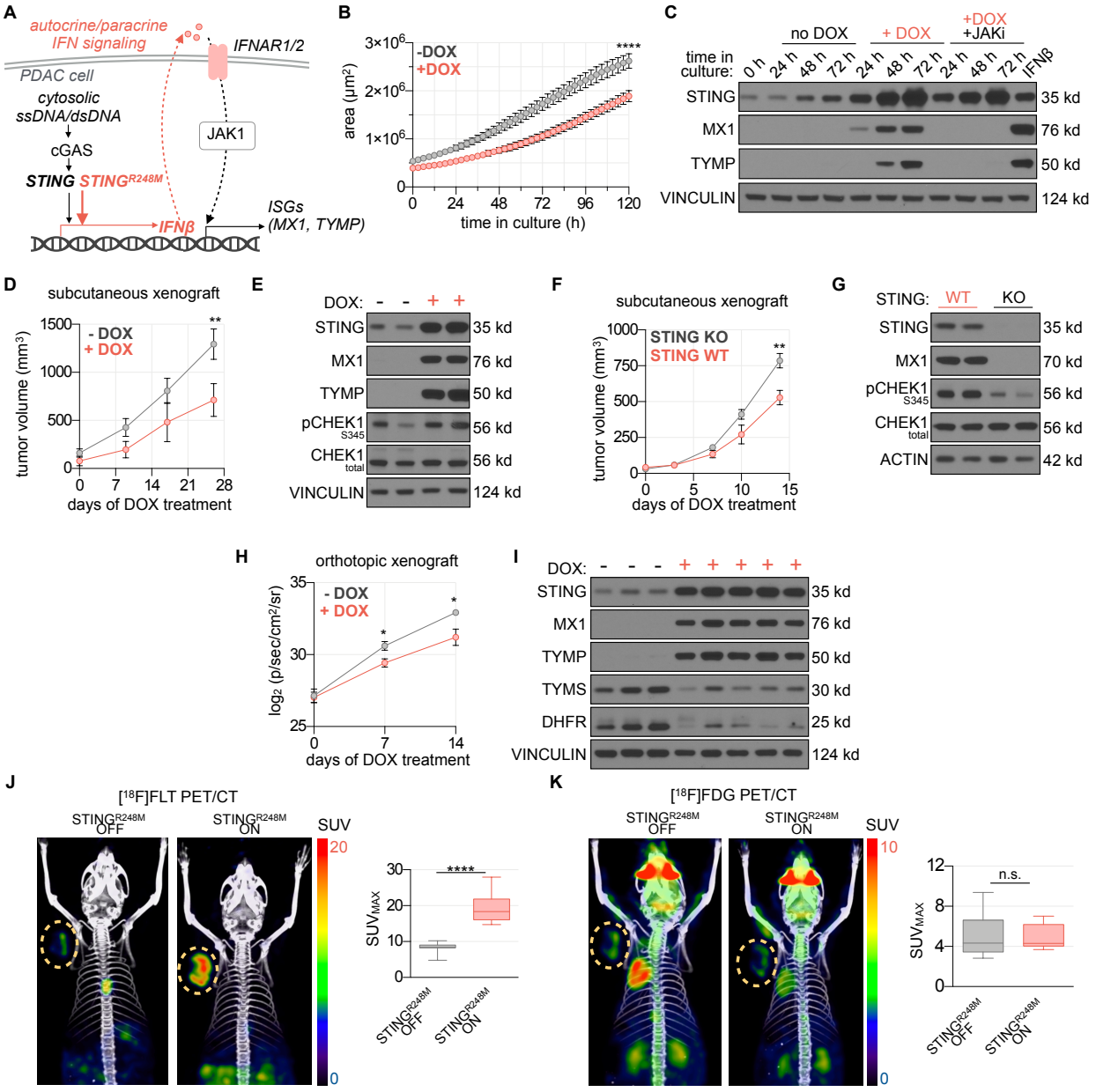

Figure 3.5 | STING controls IFN signaling and nucleotide metabolism in xenograft tumors. (**A**) Schematic of the regulation of autocrine/paracrine IFNβ production by the cGAS/STING signaling pathway. (**B**) IncuCyte live-cell imaging analysis of SUIT2 TetR; STING^{R248M} cells treated + 50 ng/mL DOX in anchorage-independent culture (mean±SD; n=6; student's t-test, **** P<0.0001). (**C**) Immunoblot analysis of SUIT2 TetR; STING^{R248M} cells treated ± 50 ng/mL doxycycline (DOX) ± 1 µM ruxolintinib (JAKi) ± 100 U/mL IFNβ for the indicated timepoints (mean±SD, n=6, student's t-test, **** P<0.0001). (**D**) Growth curves of SUIT2 TetR; STING^{R248M}

subcutaneous tumors in NSG mice treated ± DOX measured using CT imaging (mean±SEM, n=6, student's t-test, *** P<0.001). (**E**) Immunoblot analysis of STING^{R248M} subcutaneous tumors at the endpoint of experiment in **D**. (**F**) Growth curves of DANG STING WT and STING KO subcutaneous tumors in NCG mice measured using caliper measurements (mean±SEM, n=6, student's t-test, *** P<0.001). (**G**) Immunoblot analysis of DANG STING WT and STING KO tumors at the endpoint of experiment in **F**. (**H**) Growth curves of SUIT2 TetR; STING^{R248M}; LUC orthotopic tumors in NCG mice treated ± DOX measured using bioluminescence (BLI) imaging (mean±SD, n=6, student's t-test, * P<0.05). (**I**) Immunoblot analysis of SUIT2 TetR; STING^{R248M}; LUC orthotopic tumors at the endpoint of experiment in **H**. (**J**) [^{18}F]FLT PET analysis of SUIT2 TetR; STING^{R248M} subcutaneous tumors. (**K**) [^{18}F]FDG PET analysis of SUIT2 TetR; STING^{R248M} subcutaneous tumors.

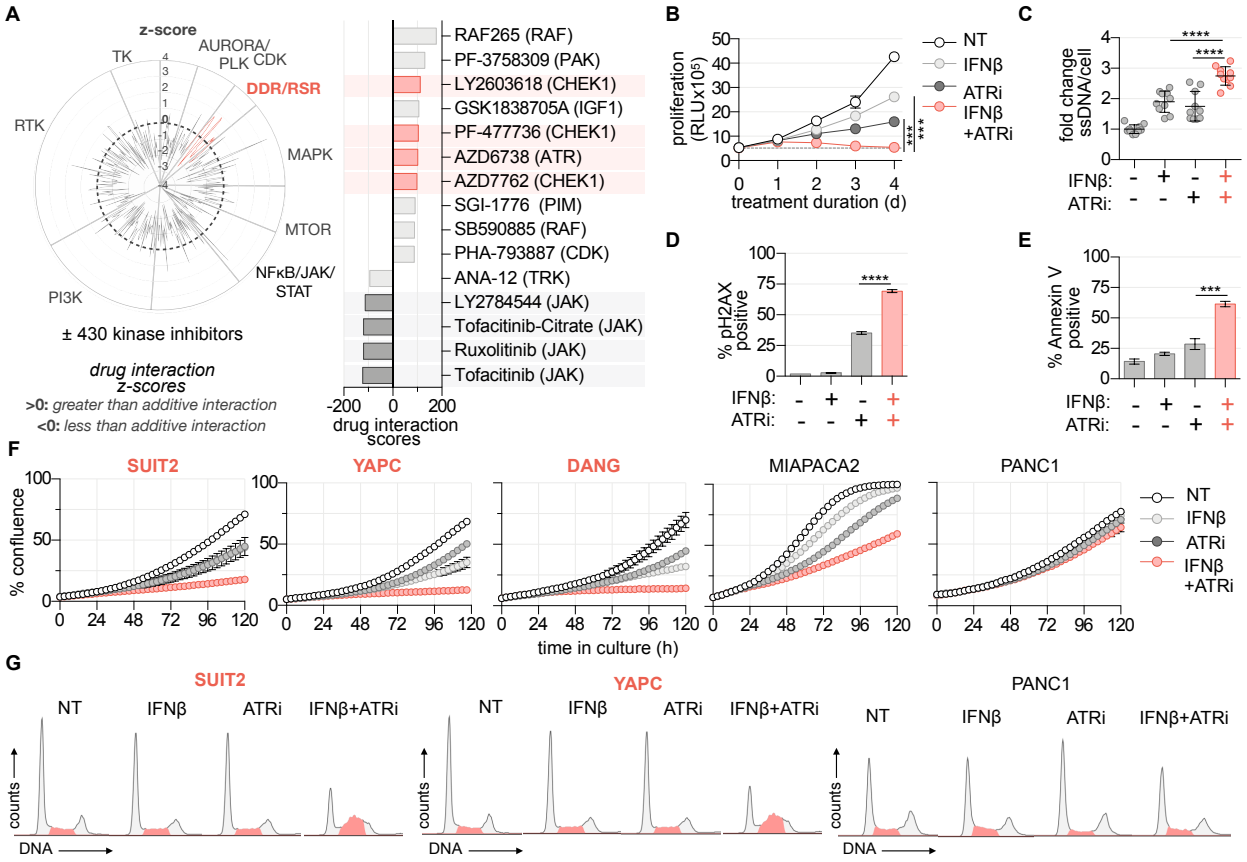

Figure 3.6 | ATR inhibitors synergize with IFN. (**A**) High-throughput phenotypic screen evaluating the anti-proliferative effects of 430 protein kinase inhibitors, tested at 7-point dose response, against SUIT2 cells treated ± 100 U/mL IFNβ for 72 h (DDR: DNA damage response; RSR: replication stress response). (**B**) Cell Titer Glo analysis of SUIT2 cells treated ±100 U/mL IFNβ ± 500 nM ATRi in anchorage-independent culture conditions (mean±SD; n=4; one-way ANOVA corrected for multiple comparisons by Bonferroni adjustment, **** P<0.0001). (**C**) Immunofluorescence microscopy analysis of ssDNA in SUIT2 cells treated ± 100 U/mL IFNβ ± 500 nM ATRi for 24 h (mean±SD; n=10; one-way ANOVA corrected for multiple comparisons by Bonferroni adjustment, **** P<0.0001). (**D**) Flow cytometry analysis of pH2A.X$_{S139}$ levels in SUIT2 cells treated ± 100 U/mL ± 500 nM ATRi for 48 h (mean±SD; n=2; one-way ANOVA corrected for multiple comparisons by Bonferroni adjustment, **** P<0.0001). (**E**) AnnexinV/PI flow cytometry analysis of SUIT2 cells treated for 72 h ± 100 U/mL IFNβ ± 500 nM ATRi (mean±SD; n=2; one-way ANOVA corrected for multiple comparisons by Bonferroni adjustment,

**** P<0.0001). (**F**) Incucyte live cell imaging analysis of a panel of PDAC cell lines in 2D culture treated ± 100 U/mL ± 250 nM ATRi (mean±SD, n=6). (**G**) Propidium iodide (PI) cell cycle analysis of a panel of PDAC cell lines treated ± 100 U/mL ± 250 nM ATRi for 48 h.

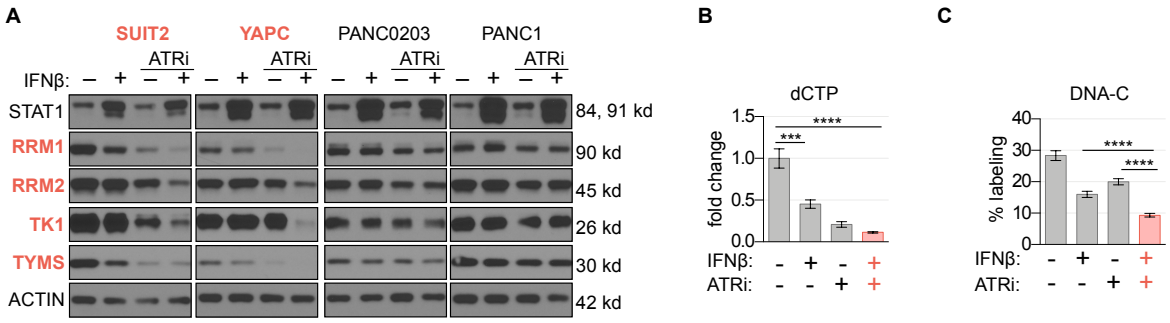

Figure 3.7 | ATR inhibitors and IFN synergistically impair *de novo* nucleotide biosynthesis by down-regulating E2F target genes. (**A**) Immunoblot analysis of PDAC cell lines characterized as sensitive (red) or insensitive (black) to the combination of IFNβ and VE-822 (ATRi). Cells were treated for 48 h ± 100 U/mL IFNβ ± 250 nM ATRi. (**B**) LC-MS/MS analysis of dCTP pools in SUIT2 cells treated for 24 h ± 100 U/mL IFNβ ± 500 nM ATRi (mean±SD; n=3; one-way ANOVA corrected for multiple comparisons by Bonferroni adjustment, *** P<0.001; **** P<0.0001). (**C**) LC-MS/MS analysis of the contribution of [$^{13}C_6$]glucose to newly replicated DNA in SUIT2 cells treated for 24 h ± 100 U/mL IFNβ ± 500 nM ATRi (mean±SD; n=3; one-way ANOVA corrected for multiple comparisons by Bonferroni adjustment, **** P<0.0001).

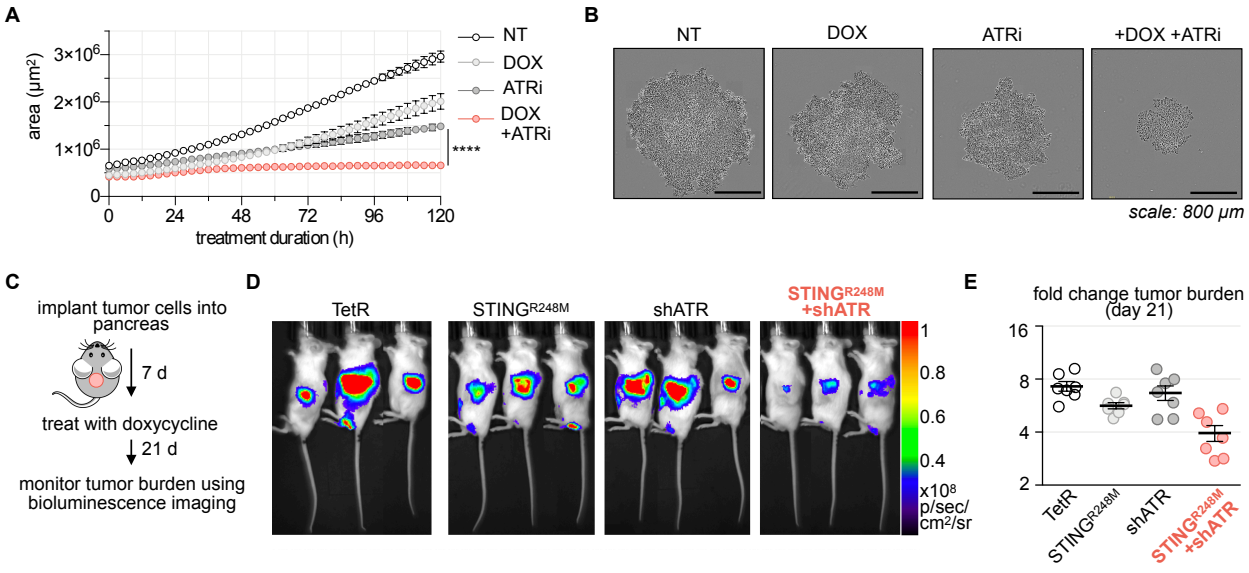

Figure 3.8 | ATR inhibition impairs the growth of PDAC cells with high interferon signaling. (**A**) IncuCyte live-cell imaging analysis of SUIT2 TetR STING^{R248M} cells treated + 50 ng/mL DOX ± 500 nM ATRi in anchorage-independent culture (mean±SD; n=6; one-way ANOVA corrected for multiple comparisons by Bonferroni adjustment, **** P<0.0001). (**B**) Representative images from the endpoint of experiment in **A**. (**C**) Approach to test the interaction between STING activation and ATR inhibition in vivo. SUIT2 TetR fLuc cells were engineered with a STING^{R248M} or shATR transgene and implanted into the pancreas of NCG mice. (**D**) Representative BLI images of tumor bearing mice 21 days following initiation of doxycycline treatment. (**E**) Fold change in BLI signal on day 21 compared to baseline signal.

A

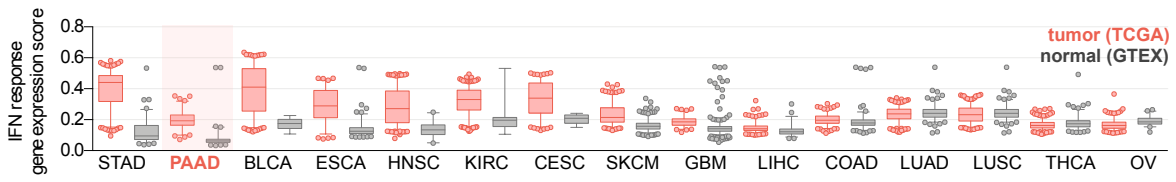

B

dataset	ID	*n*	median
BLCA	Bladder urothelial carcinoma	426	0.41
GTEX-bladder		9	0.18
CESC	Cervical squamous cell carcinoma	309	0.34
GTEX-cervix		10	0.21
COAD	Colon adenocarcinoma	331	0.20
GTEX-colon		308	0.18
ESCA	Esophageal carcinoma	195	0.29
GTEX-esophagus		273	0.13
GBM	Glioblastoma multiforme	171	0.19
GTEX-brain		850	0.14
HNSC	Head and Neck squamous cell carcinoma	564	0.27
GTEX-salivary		55	0.13
KIRC	Kidney renal clear cell carcinoma	603	0.33
GTEX-kidney		28	0.20
LIHC	Liver hepatocellular carcinoma	421	0.14
GTEX-liver		110	0.12
LUAD	Lung adenocarcinoma	574	0.24
GTEX-lung		288	0.24
LUSC	Lung squamous cell carcinoma	548	0.23
GTEX-lung		288	0.24
OV	Ovarian serous cystadenocarcinoma	427	0.16
GTEX-ovary		88	0.19
PAAD	Pancreatic adenocarcinoma	183	0.19
GTEX-pancreas		167	0.06
SKCM	Skin cutaneous melanoma	470	0.22
GTEX-skin		557	0.16
STAD	Stomach adenocarcinoma	450	0.44
STEC-stomach		175	0.09
THCA	Thyroid carcinoma	571	0.16
GTEX-thyroid		279	0.17

C

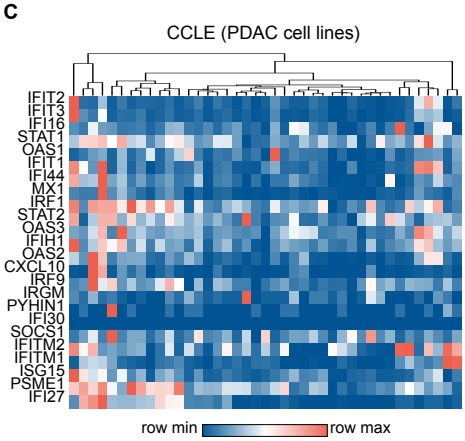

Figure S3.1 | Analysis of IFN signature enrichment in TCGA, GTEX and CCLE datasets.

(**A**) Analysis of the IFN response metagene signature across TCGA and GTEX datasets ordered by fold change in median tissue-matched TCGA/GTEX values (PAAD: pancreatic adenocarcinoma). (**B**) Extended analysis of data in panel **A**. (**C**) Analysis of the IFN response metagene signature in the CCLE pancreatic cancer cell line dataset. Columns represent individual pancreas cancer cell lines.

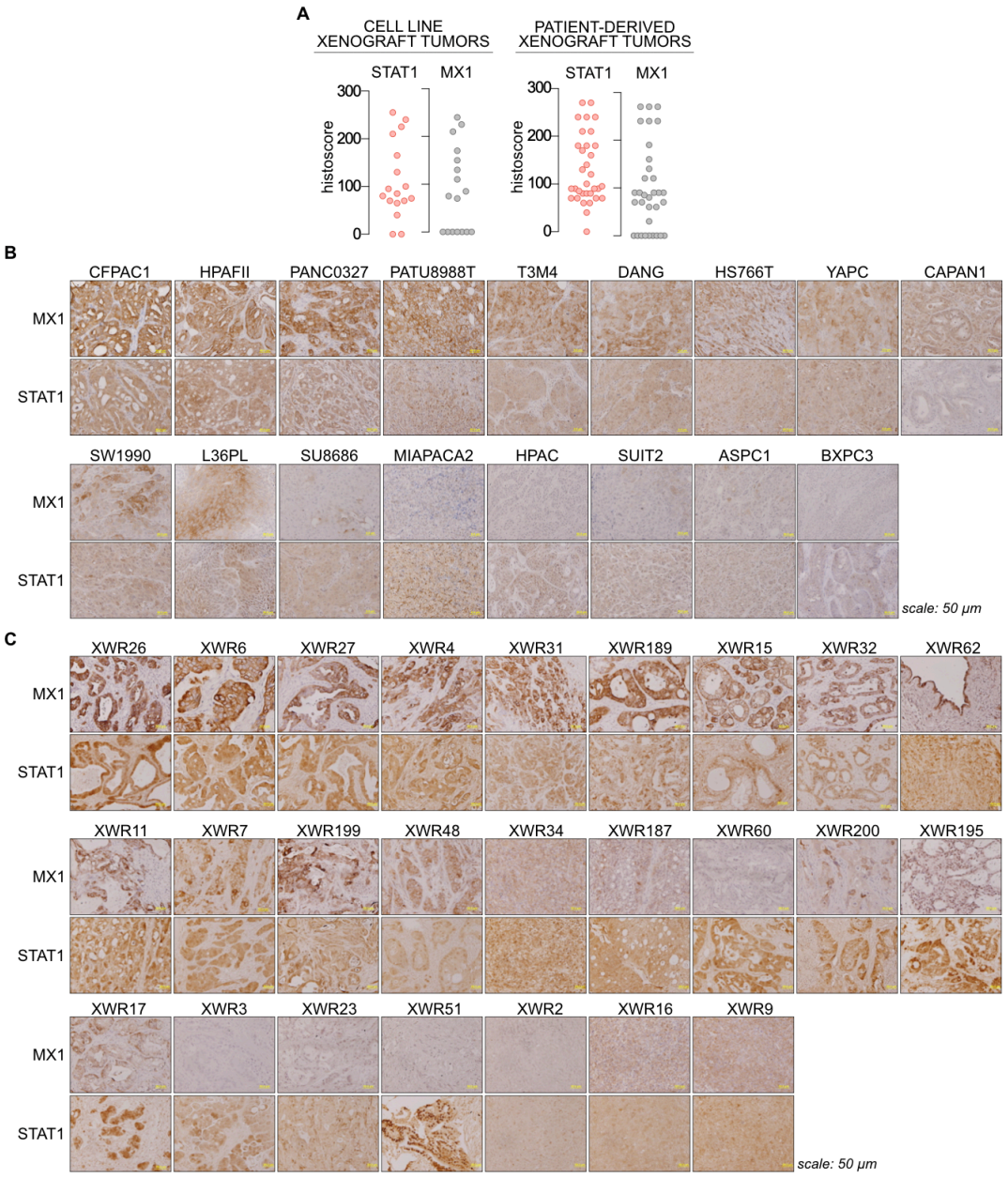

Figure S3.2 | Immunohistochemistry analysis of IFN signaling biomarkers in primary patients specimens. (**A**) Summary of STAT1 and MX1 immunohistochemistry (IHC) analysis of PDAC patient derived (n=33) and cell line (n=17) xenograft tumors. Histoscores were calculated as a sum of the intensity of staining (0, negative; 1, weak; 2, median; or 3, strong) multiplied by the percentage of tumor cells at that intensity (0-300 range). (**B**) Representative STAT1 and MX1 IHC analysis of PDAC cell line xenograft tumors. (**C**) Representative STAT1 and MX1 IHC analysis of PDAC patient derived xenograft tumors.

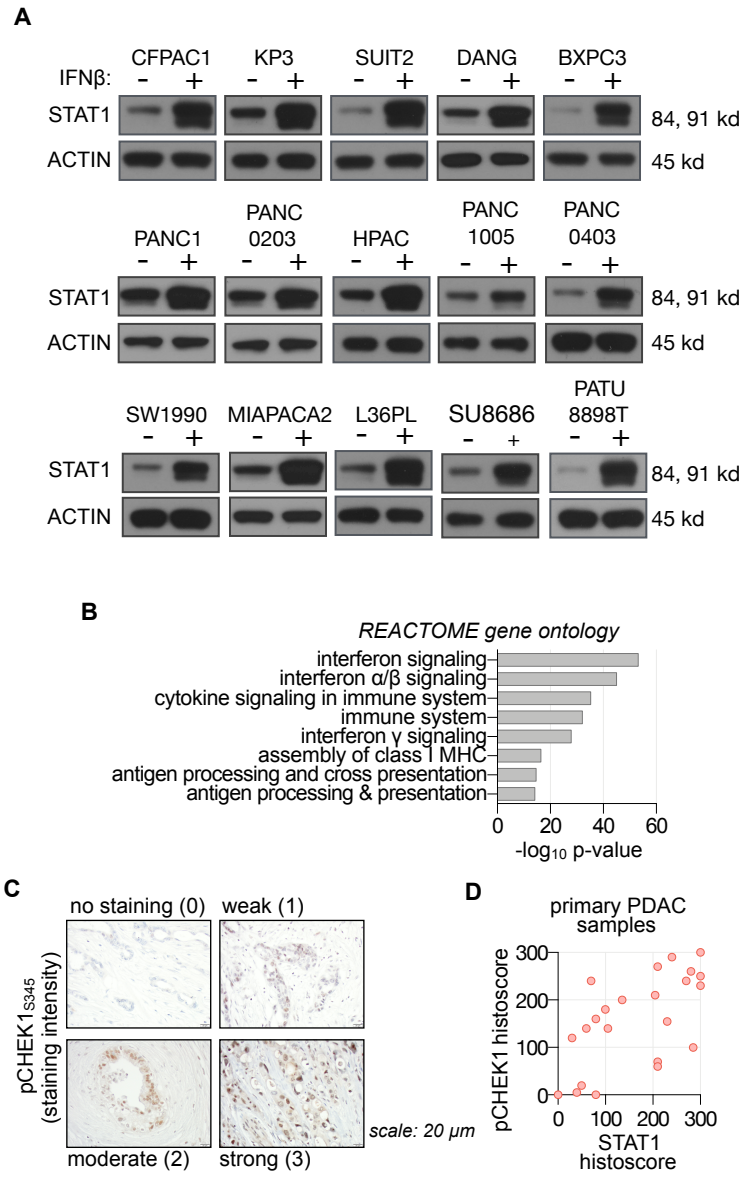

Figure S3.3 | Extended analysis of IFN signaling in PDAC cells and patient samples. (**A**) Immunoblot analysis of a panel of PDAC cell lines treated ± 100 U/mL IFNβ for 24 h. (**B**) Reactome gene ontology analysis significantly altered proteins following treatment with IFN for 24 h from **Figure 3.3D**. (**C**) Representative pCHEK1$_{S345}$ IHC analysis of primary PDAC samples. Histoscores are indicated. (**D**) Correlation between STAT1 and pCHEK1$_{S345}$ IHC histoscores across panel of PDAC patient samples (n=23).

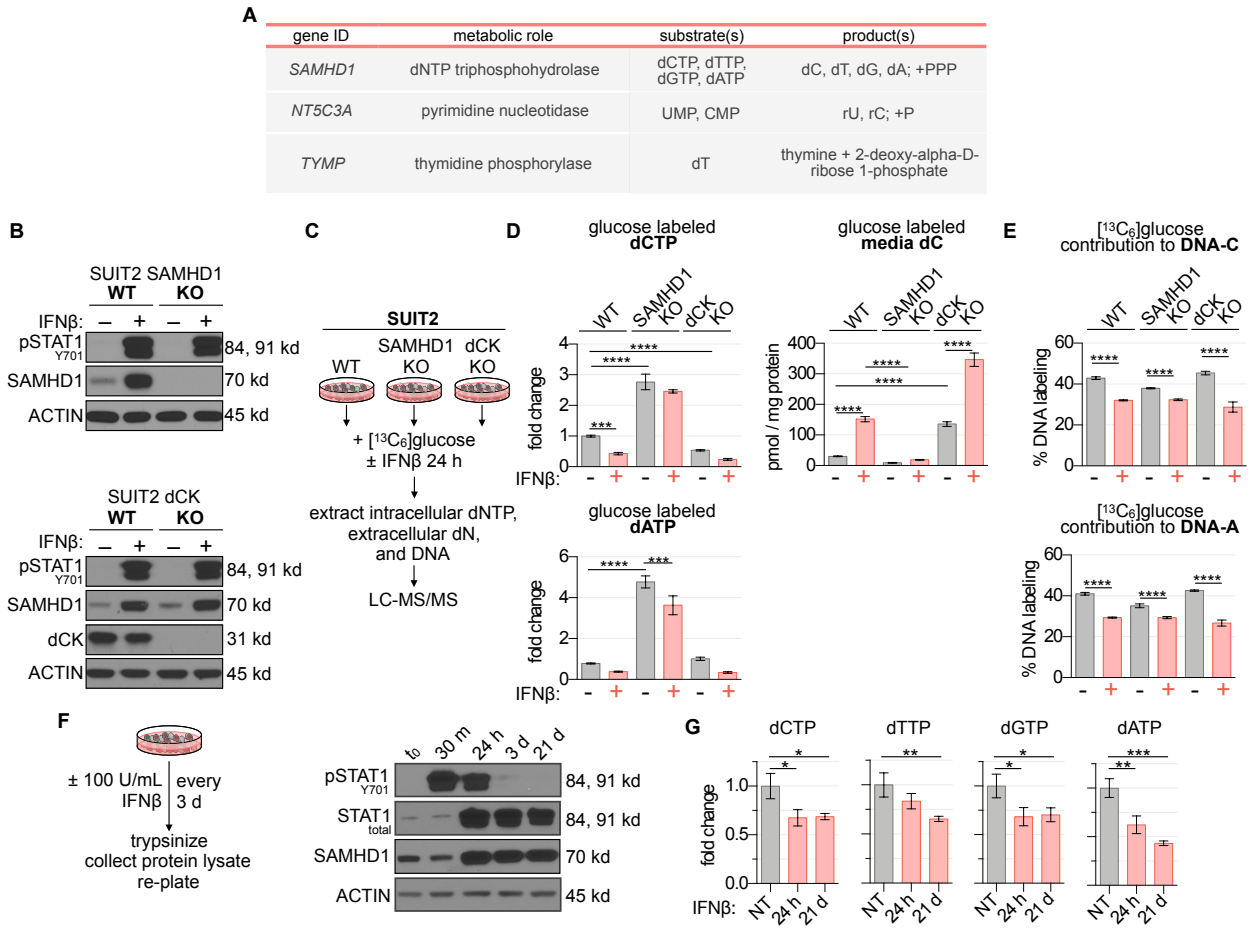

Figure S3.4 | Type I IFN signaling up-regulates SAMHD1 mediated nucleotide pool phosphohydrolysis and restricts DNA synthesis. (**A**) Summary of genes related to nucleotide catabolism significantly altered by IFNβ in SUIT2 cells. (**B**) Immunoblot validation of SUIT2 SAMHD1 CRISPR/Cas9 knockout (KO) and dCK KO isogenic cells. (**C**) Experimental design. (**D**) Total [$^{13}C_6$]glucose labeled intracellular metabolite and extracellular media metabolite levels of SUIT2 WT, SAMHD1 KO and dCK KO cells using LC-MS/MS (mean±SD; n=3; one-way ANOVA corrected for multiple comparisons by Bonferroni adjustment, ** P<0.01; **** P<0.0001). (**E**) Contribution of [$^{13}C_6$]glucose to newly replicated DNA in SUIT2 WT, SAMHD1 KO and dCK KO cells treated for 24 h ± 100 U/mL IFNβ for 24 h using LC-MS/MS (mean±SD; n=3; one-way ANOVA corrected for multiple comparisons by Bonferroni adjustment, **** P<0.0001). (**F**) Time-course immunoblot analysis of IFNβ treated SUIT2 cells. For extended treatment studies cells were passaged and media was refreshed every 72 h. (**G**) LC-MS/MS

analysis of dNTP pools in SUIT2 cells treated for 24 h or 21 d (mean±SD; n=3; one-way ANOVA corrected for multiple comparisons by Bonferroni adjustment, * P<0.05; ** P<0.01; *** P<0.001).

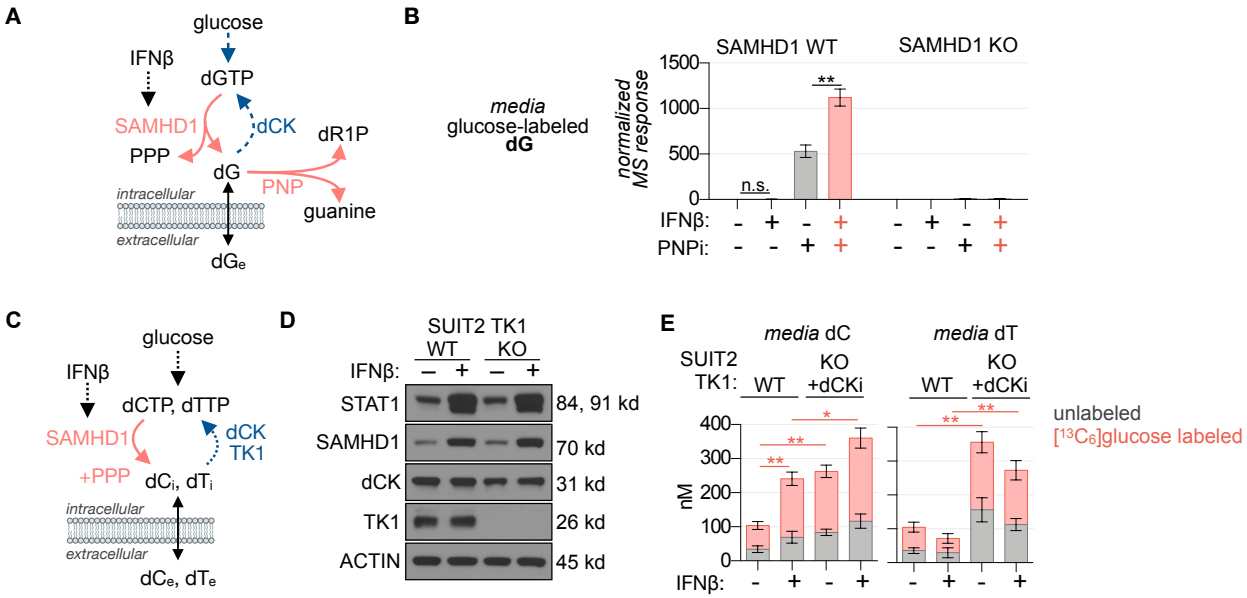

F

Efflux (fmol/h/cell) x10^{-3}	WT		pyrimidine salvage deficient	
	- IFNβ	+ IFNβ	- IFNβ	+ IFNβ
dC	10.1 ± 0.80	28.9 ± 4.15	21.3 ± 2.22	36.1 ± 4.95
dT	10.2 ± 0.68	8.52 ± 0.28	30.5 ± 5.16	27.4 ± 4.05

Figure S3.5 | Nucleoside phosphorylases and kinases mediate nucleoside efflux. (**A**) Schematic overview of dGTP biosynthesis, catabolism and recycling. (**B**) LC-MS/MS analysis of glucose labeled media dG and dC in SUIT2 cells treated for 24 h ± 100 U/mL IFNβ ± 1 μM BCX-1777 (PNPi) in media containing 1 g/L [$^{13}C_6$]glucose (mean±SD; n=3). For calculation of normalized MS response glucose labeled (n+5) dG or dC counts were normalized to internal standard counts. (**C**) Schematic representation of the roles of SAMHD1 and nucleoside kinases deoxycytidine kinase (dCK) and thymidine kinase 1 (TK1) in regulating dN efflux in IFN-treated cells. (**D**) Immunoblot validation of TK1 KO SUIT2 cells treated with 100 U/mL IFNβ for 24 h. (**E**) LC-MS/MS analysis of dT and dC efflux following 24 h treatment of SUIT2 parental and TK1 KO cells with 100 U/mL IFNβ in media containing 1 g/L [$^{13}C_6$]glucose. TK1 cells were maintained in the presence of 1 μM DI-82 (dCKi) (mean±SD; n=3; one-way ANOVA corrected for multiple comparisons by Bonferroni adjustment, * P<0.05; ** P<0.01). (**F**) Calculation of normalized dC and dT efflux rates from experiment in **E** (mean±SD; n=3). dR1P: deoxyribose-1-phosphate; PNP: purine nucleoside phosphorylase.

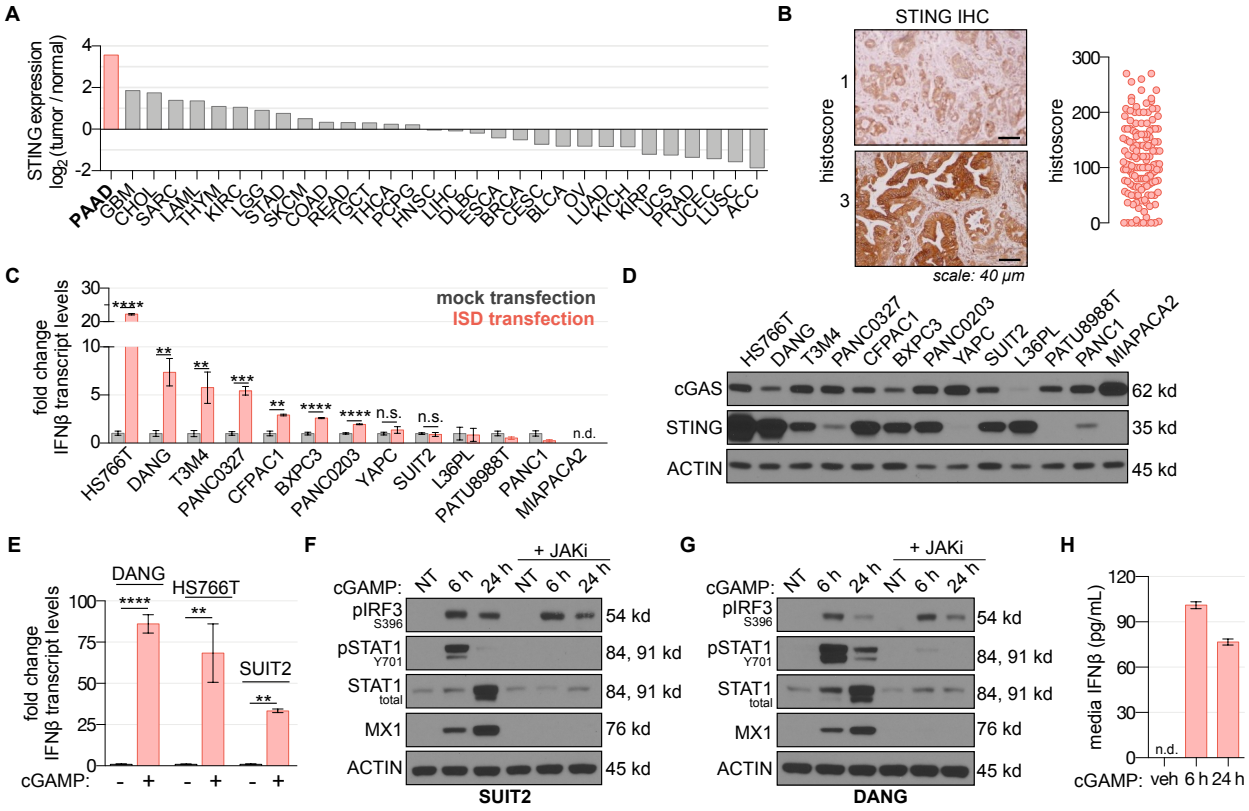

Figure S3.6 | The cGAS/STING pathway is active in a subset of PDAC cell lines. (**A**) Analysis of STING (TMEM173) transcript levels across TCGA tumor datasets relative to normal tissue (PAAD: pancreatic adenocarcinoma). (**B**) IHC analysis of STING expression in PDAC tumors (n=145). (**C**) RT-PCR analysis of IFNβ transcript levels in a panel of PDAC cell lines 6 h subsequent to transfection with 25 µg/mL interferon stimulatory DNA (ISD; n.d.: not detected, mean±SD, n=2, student's t-test, n.s.: not significant; ** P<0.01; ** P<0.001; **** P<0.0001). (**E**) RT-PCR analysis of IFNβ transcript levels in a panel of PDAC cell lines 6 h subsequent to transfection with 10 µg/ml of a non-hydrolyzable bisphosphorothioate 2'-3'-cGAMP analog (cGAMP; mean±SD, n=2, student's t-test, ** P<0.01; **** P<0.0001). (**F**) Immunoblot analysis of DANG cells following transfection with 10 µg/mL 2'-3'-cGAMP ± 1 µM ruxolitinib (JAKi). (**G**) Immunoblot analysis of DANG cells following transfection with 10 µg/mL cGAMP ± 1 µM JAKi. (**H**) ELISA analysis of IFNβ levels in DANG cell supernatant 6 or 24 following transfection with 10 µg/ml cGAMP for (veh: vehicle, 24 h lipofectamine alone, mean±SD, n=3).

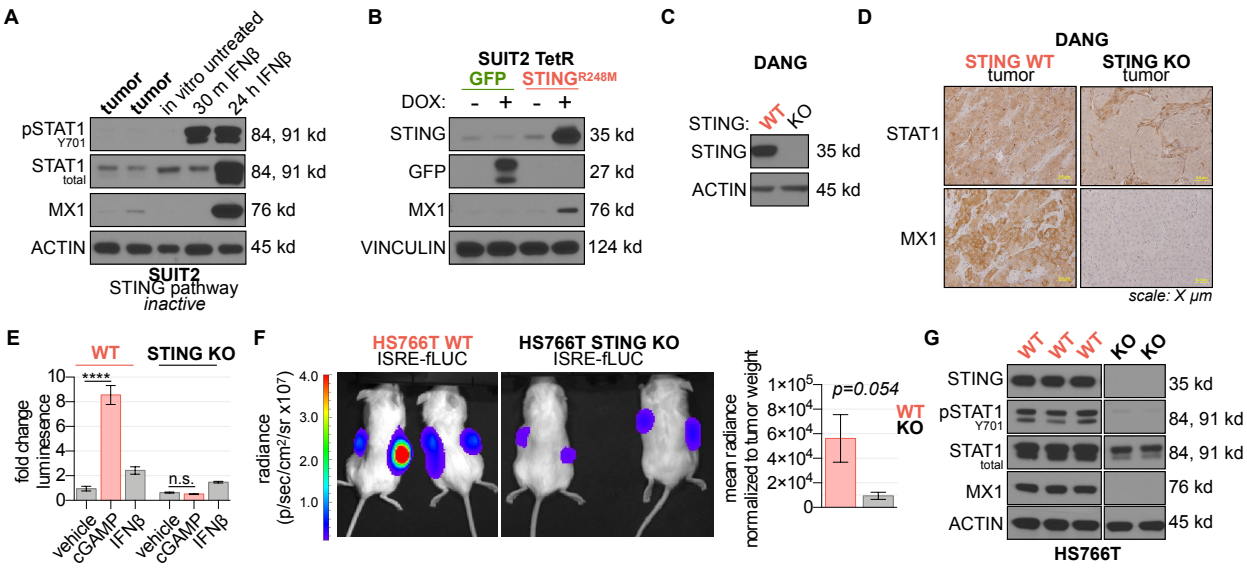

Figure S3.7 | Tumor cell STING mediates constitutive IFN signaling in PDAC tumors. (**A**) Immunoblot analysis of SUIT2 cells treated ± 100 U/mL IFNβ for the indicated timepoints *in vitro* and lysates prepared from SUIT2 cells grown as subcutaneous tumors in NSG mice. (**B**) Immunoblot analysis of SUIT2 TetR-GFP or TetR-STING^{R248M} cells treated ± 50 ng/mL DOX for 72 h. (**C**) Immunoblot validation of DANG parental and STING CRISPR/Cas9 knockout (KO) cells. (**D**) IHC analysis of subcutaneous DANG WT and STING KO xenograft tumors from **Figure 3.3l**. (**E**) Analysis of ISRE-luciferase reporter activity in HS766T WT ISRE-fLUC and STING KO ISRE-fLUC cells *in vitro* following 6 h transfection with cGAMP or treatment with 100 U/mL IFNβ (mean±SD; n=3; one-way ANOVA corrected for multiple comparisons by Bonferroni adjustment, **** P<0.0001). (**F**) Analysis of ISRE-fLUC reporter activity in HS766T WT and STING KO ISRE-fLUC subcutaneous xenograft tumors *in vivo* using bioluminescence imaging (mean±SEM, n=4, student's t-test). (**G**) Immunoblot analysis of protein lysates prepared from HS766T WT and STING KO subcutaneous xenograft tumors.

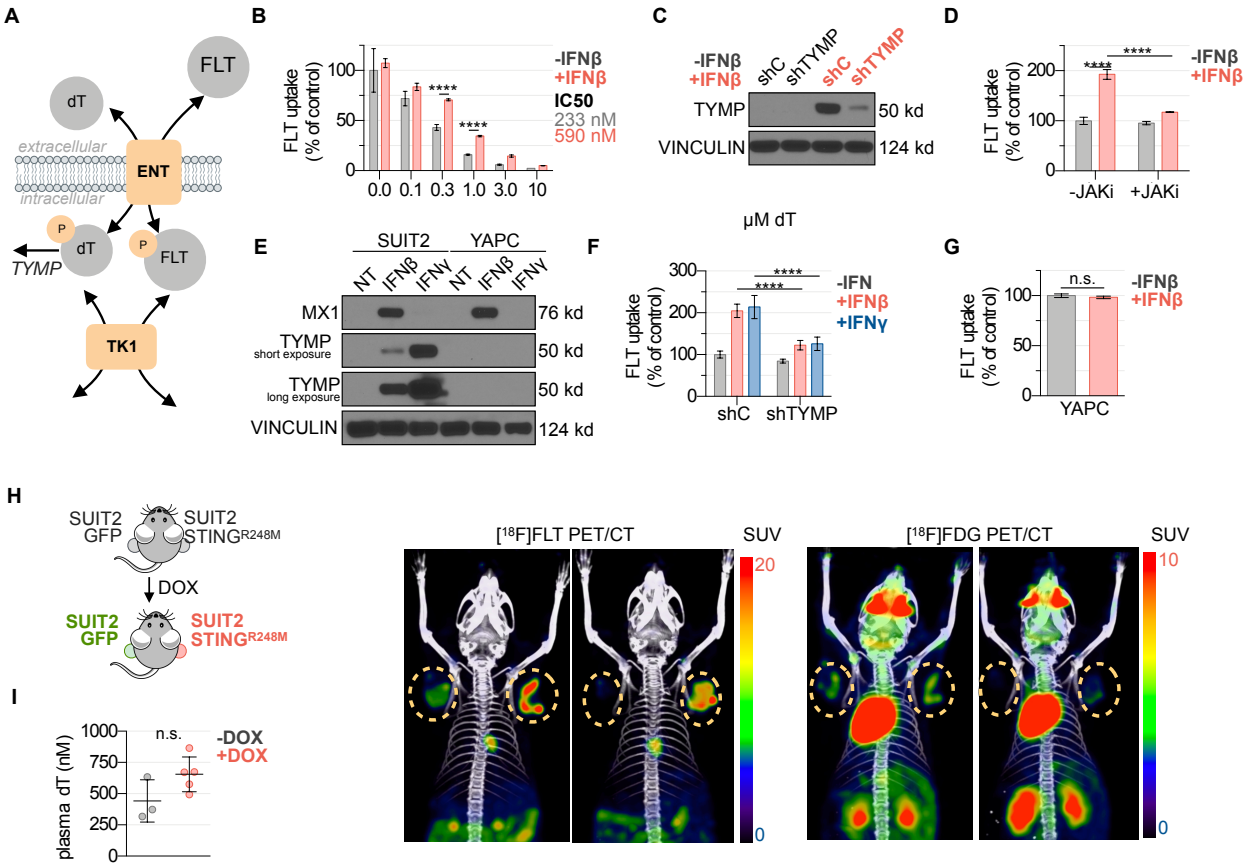

Figure S3.8 | IFN signaling increases tumor cell [^{18}F]FLT accumulation *in vitro* and *in vivo*. (**A**) Schematic of the regulation of FLT accumulation by competition with the endogenous substrate for TK1, thymidine (dT). (**B**) [^{18}F]FLT uptake assay in SUIT2 cells treated ± 100 U/mL IFNβ for 24 h and subsequently pulsed with 18.5 kBq [^{18}F]FLT ± indicated amount of dT for 2 h (mean±SD; n=3; one-way ANOVA corrected for multiple comparisons by Bonferroni adjustment, **** P<0.0001). Insert indicated dT concentration required to inhibit [^{18}F]FLT accumulation by 50% (IC-50). (**C**) Immunoblot analysis of SUIT2 shC and shTYMP cells treated ± 100 U/mL IFNβ for 24 h. (**D**) [^{18}F]FLT uptake assay in SUIT2 cells treated with 100 U/mL IFNβ ± 1 μM ruxolitinib (JAKi) for 24 h and subsequently pulsed with 18.5 μCi [^{18}F]FLT + 1 μM dT for 2 h (mean±SD; n=3; one-way ANOVA corrected for multiple comparisons by Bonferroni adjustment, **** P<0.0001). (**E**) Immunoblot analysis of SUIT2 and YAPC cells treated with either 100 U/mL IFNβ or 10 ng/mL IFNγ for 24 h. (**F**) [^{18}F]FLT uptake assay in SUIT2 shC and shTYMP cells treated ± 100 U/mL IFNβ or ± 10 ng/mL IFNγ for 24 h and subsequently pulsed with 18.5 μCi

[^{18}F]FLT ± 1 μM dT for 2 h (mean±SD; n=3; one-way ANOVA corrected for multiple comparisons by Bonferroni adjustment, **** P<0.0001). (**G**) [^{18}F]FLT uptake assay in YAPC cells treated with 100 U/mL IFNβ for 24 h and subsequently pulsed with 18.5 mBq [^{18}F]FLT + 1 μM dT for 2 h (mean±SD, n=3, student's t-test, n.s.: non significant). (**H**) [^{18}F]FLT and [^{18}F]FDG analysis bilateral SUIT2 TetR; STING^{R248M} and SUIT2 TetR; STING^{R248M} tumor-bearing mice treated with DOX. (**I**) LC-MS/MS analysis of plasma dT levels in SUIT2 TetR-STING^{R248M} tumor bearing mice treated ± DOX from **Figures 3.5E and 3.5F** (mean±SD, n=3, student's t-test, n.s.: not significant).

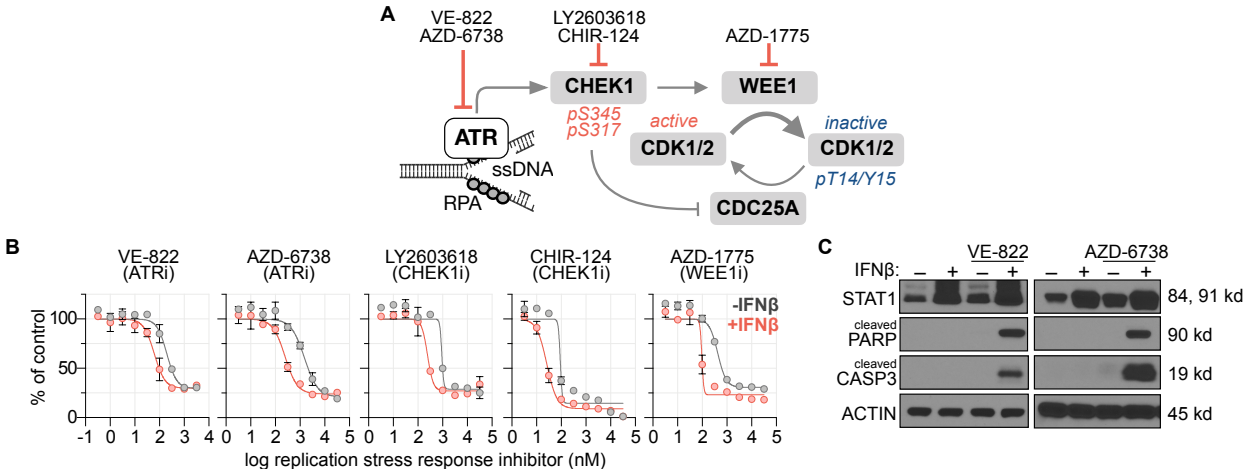

Figure S3.9 | Replication stress response inhibitors and IFNβ exhibit synergy in PDAC cells. (**A**) Schematic of the replication stress response pathway pathway and related small molecule inhibitors. (**B**) Cell Titer Glo analysis of replication stress response inhibitor IC-50 in SUIT2 cells treated ± 100 U/mL IFNβ for 72 h (mean±SD, n=4). (**C**) Immunoblot analysis of SUIT2 cells treated with 100 U/mL IFN ± 500 nM VE-822 or 1 μM AZD-6738.

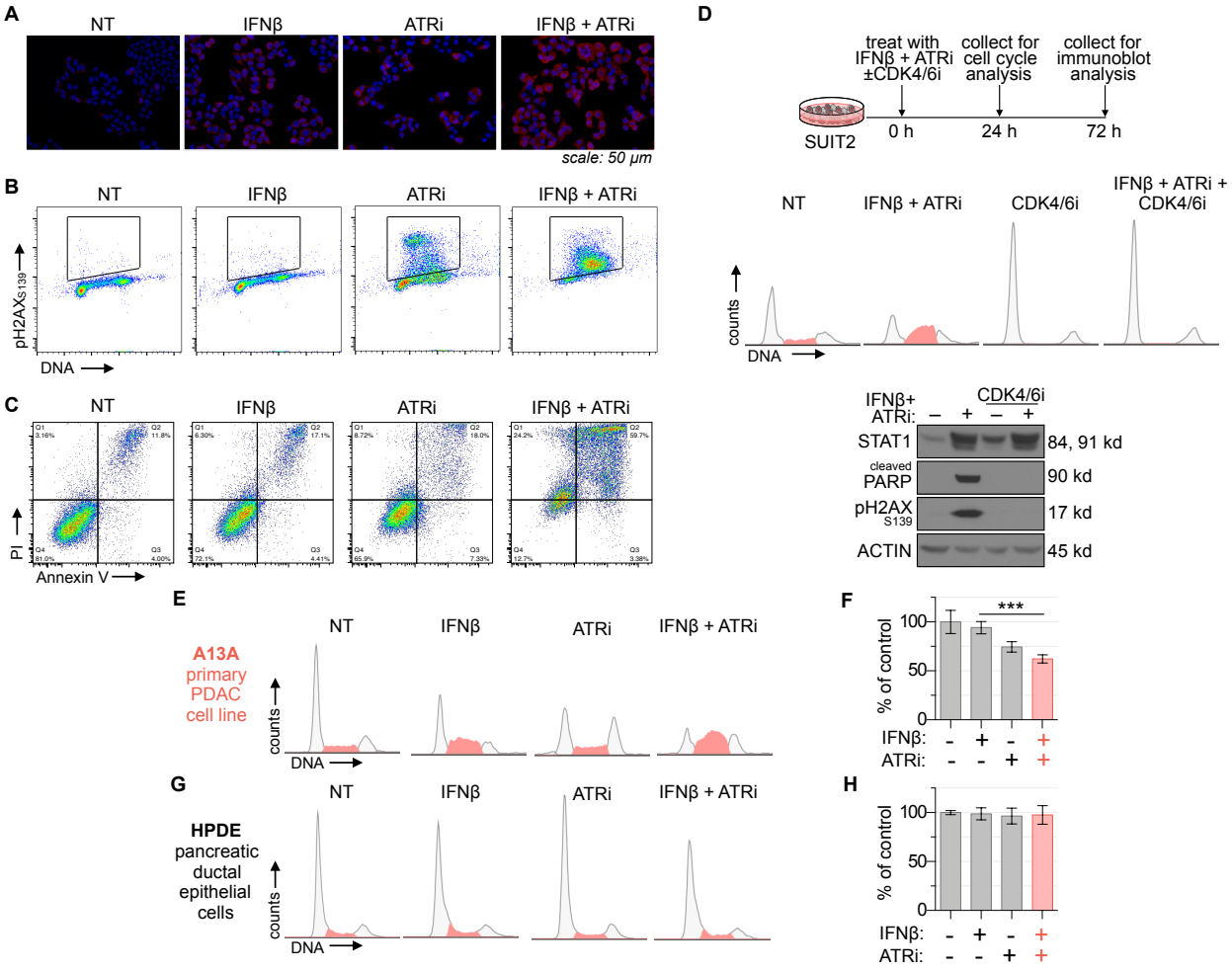

Figure S3.10 | IFN and ATR inhibitors synergistically induce DNA damage and apoptosis.

(**A**) Representative ssDNA immuno-fluorescence microscopy images from experiment in **Figure 3.4C**. (**B**) Representative inflow cytometry plots from experiment in **Figure 3.4D**. (**C**) Representative inflow cytometry plots from experiment in **Figure 3.4E**. (**D**) Cell cycle and immunoblot analysis analysis of SUIT2 cells treated with 100 U/mL IFNβ + 500 nM VE-822 (ATRi) ± 5 μM palbociclib (CDK4/6i) as indicated. (**E**) Cell cycle analysis of A13A primary PDAC cells treated ± 100 U/mL IFNβ + 500 nM ATRi for 24 h. (**F**) Cell Titer Glo analysis of A13A cells treated ± 100 U/mL IFNβ + 500 nM ATRi for 72 h (mean±SD; n=4; one-way ANOVA, * P<0.05; ** P<0.01; **** P<0.0001). (**G**) Flow cytometry cell cycle analysis of human pancreatic ductal epithelial (HPDE) cell treated ± 100 U/mL IFNβ + 500 nM ATRi for 24 h. (**H**) Cell Titer Glo analysis of HPDE cells treated ± 100 U/mL IFNβ + 500 nM ATRi for 72 h (mean±SD; n=4).

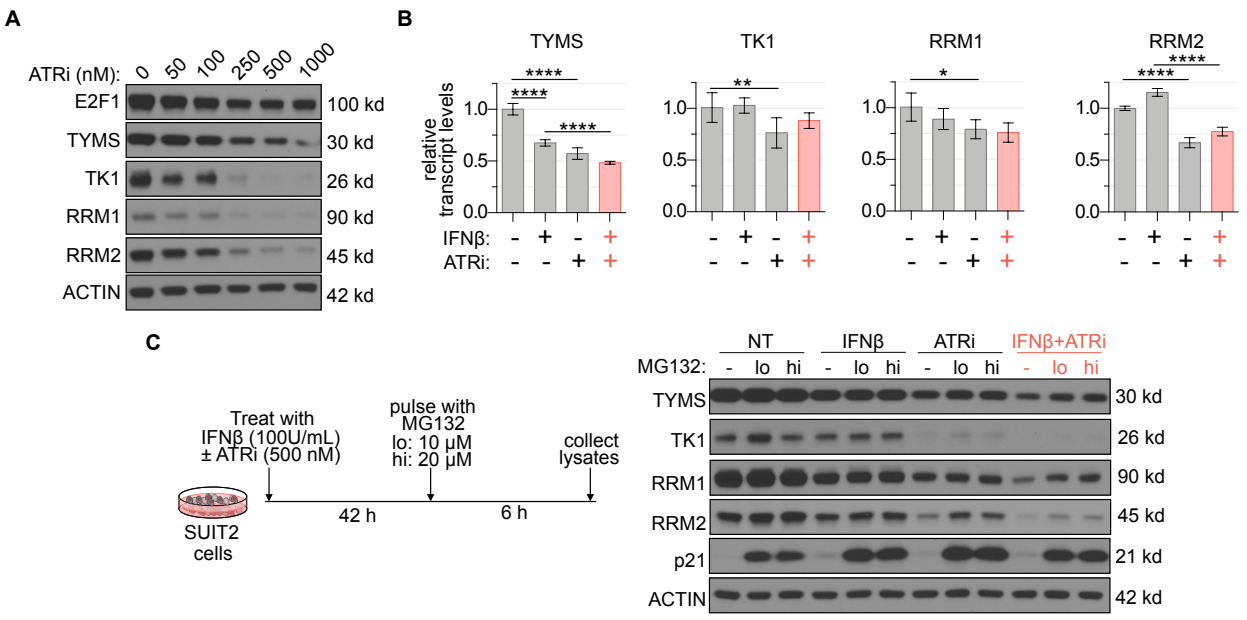

Figure S3.11 | ATR inhibition down-regulates nucleotide metabolism related protein expression in IFN-exposed PDAC cells. (**A**) Immunoblot analysis of SUIT2 cells treated for 48 h with a titration of VE-822 (ATRi) in the presence of 100 U/mL IFNβ. (**B**) RT-PCR analysis of SUIT2 cells treated for 24 h with 100 U/mL IFNβ ± 250 nM ATRi (mean±SD; n=6; one-way ANOVA corrected for multiple comparisons by Bonferroni adjustment, * P<0.05; ** P<0.01; **** P<0.0001). (**C**) Immunoblot analysis of SUIT2 cells treated as indicated in the presence of the proteasome inhibitor MG132.

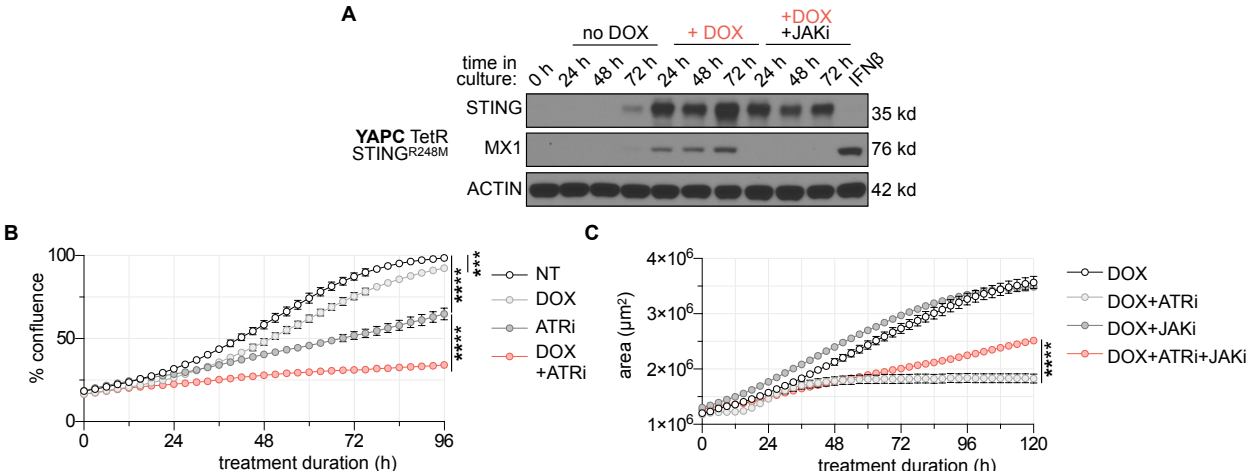

Figure S3.12 | STING activation sensitizes PDAC cells to ATR inhibition. (**A**) Immunoblot analysis of YAPC STING^{R248M} cells treated ± 50 ng/mL doxycycline (DOX) ± 1 μM ruxolintinib (JAKi) ± 100 U/mL IFNβ for the indicated timepoints. (**B**) IncuCyte live-cell imaging analysis of YAPC TetR STING^{R248M} cells treated ± 50 ng/mL DOX ± 500 nM ATRi in anchorage-dependent culture (mean±SD; n=6; one-way ANOVA corrected for multiple comparisons by Bonferroni adjustment, *** P<0.001; **** P<0.0001). (**C**) IncuCyte live-cell imaging analysis of SUIT2 TetR STING^{R248M} cells treated + 50 ng/mL DOX ± 500 nM ATRi ± 1 μM JAKi in anchorage-independent culture (mean±SD; n=6; one-way ANOVA corrected for multiple comparisons by Bonferroni adjustment, **** P<0.0001).

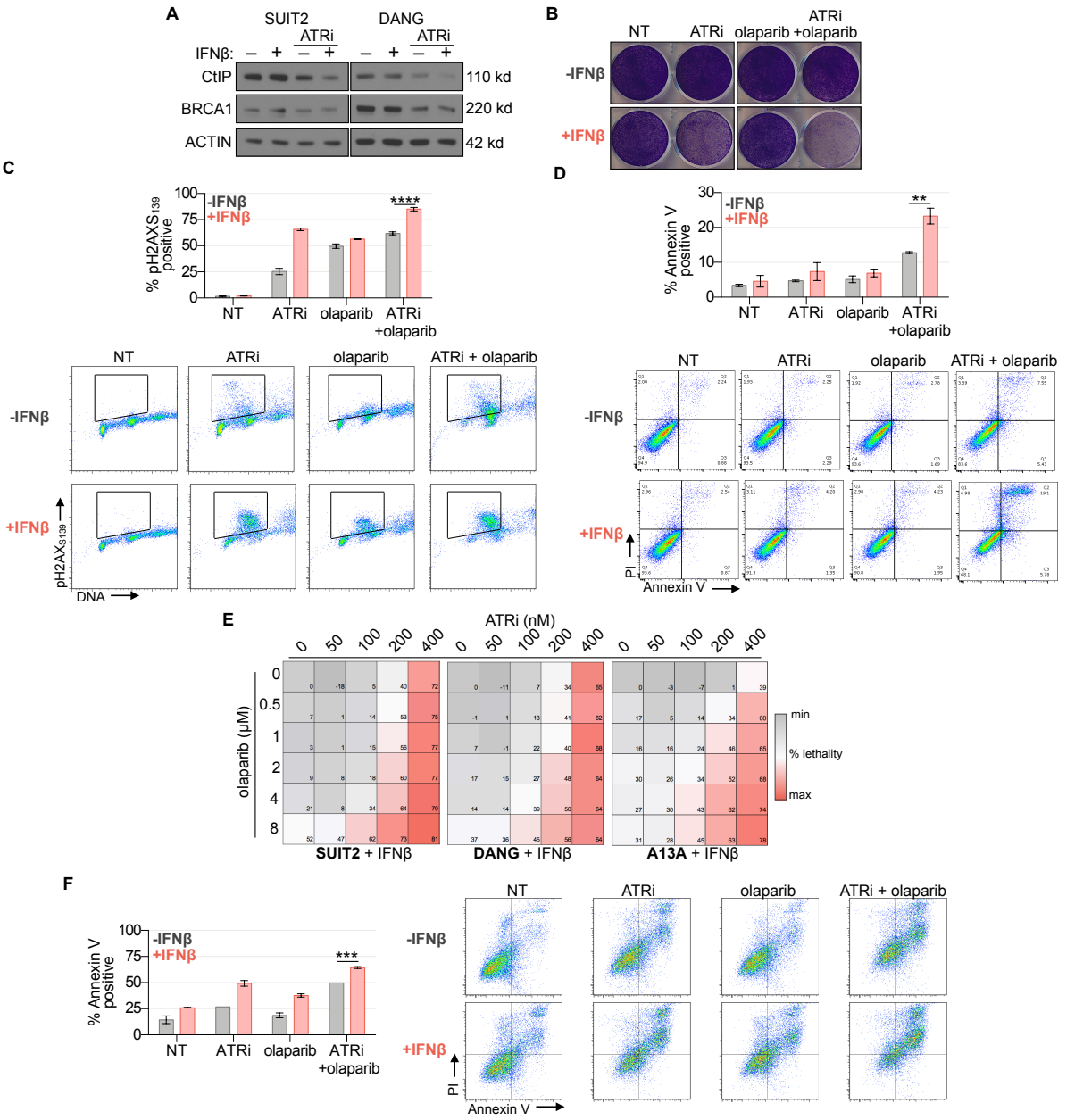

Figure S3.13 | IFNβ and ATR inhibitors synergistically enhance sensitivity to olaparib in PDAC cells. (**A**) Immunoblot analysis of SUIT2 and DANG PDAC cell lines treated for 24 h ± 100 U/mL IFNβ ± 250 nM ATRi. (**B**) Crystal violet proliferation analysis of SUIT2 cells treated with 100 U/mL IFNβ ± 100 nM ATRi ± 4 μM olaparib for 7 d. (**C**) Flow cytometry analysis of pH2A.X_{S139} levels in SUIT2 cells treated with 100 U/mL ± 200 nM ATRi ± 4 μM olaparib for 48 h (mean±SD; n=2; one-way ANOVA corrected for multiple comparisons by Bonferroni adjustment, **** P<0.0001). (**D**) Annexin V/PI flow cytometry analysis of SUIT2 cells treated for 72 h with

100 U/mL IFNβ ± 200 nM ATRi ± 4 μM olaparib (mean±SD; n=2; one-way ANOVA corrected for multiple comparisons by Bonferroni adjustment, ** P<0.01). (**E**) Cell Titer Glo analysis of SUIT2, DANG and A13A cells treated for 72 h with olaparib ± ATRi in the presence of 100 U/mL IFNβ (mean, n=4). (**F**) AnnexinV/PI flow cytometry analysis of A13A primary culture treated for 72 h with 100 U/mL IFNβ ± 200 nM ATRi ± 4 μM olaparib (mean±SD; n=2; one-way ANOVA corrected for multiple comparisons by Bonferroni adjustment, *** P<0.001).

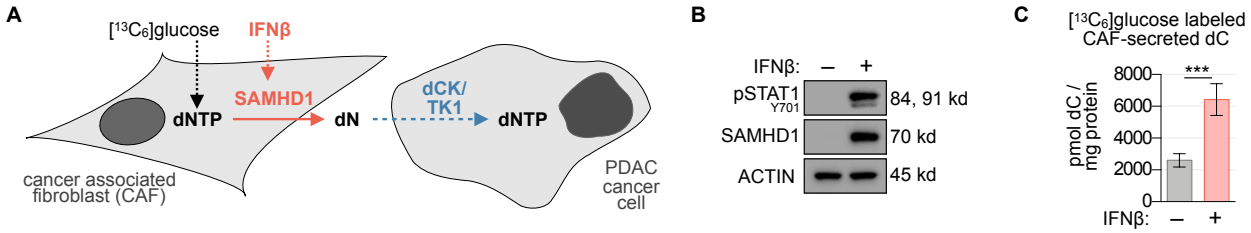

Figure S3.14 | SAMHD1 is induced by IFNβ in cancer-associated fibroblasts. (**A**) Schematic representation of potential metabolic crosstalk between PDAC cancer cells and PDAC cancer associated fibroblasts (CAFs). (**B**) Immunoblot of human pancreatic CAFs treated with 100 U/mL IFNβ for 24 h. (**C**) [$^{13}C_6$]glucose-labeled deoxycytidine efflux measured in the culture media levels of CAFs cultured in [$^{13}C_6$]glucose and treated ± 100 U/mL IFNβ for 24h measured using LC-MS/MS. MS counts were normalized to extracted protein (mean±SD, n=3, student's t-test, *** P<0.001).

DISCUSSION

This work begins to define the causes and consequences of IFN signaling in PDAC tumors. We found that the cGAS/STING pathway is active in a subset of PDAC cells and is required for constitutive type I IFN signaling in PDAC tumors. Using orthogonal phospho-proteomics and chemical genomics approaches we implicated the replication stress response pathway as a IFN-induced collateral dependency in PDAC cells. Pharmacological inhibition of replication stress response kinases ATR, CHEK1 or WEE1 induce replication catastrophe in IFNβ-treated PDAC cell lines and primary cells but not in non-transformed cells. ATR inhibition impairs nucleotide metabolism by restricting the expression of rate limiting nucleotide biosynthetic enzymes. Finally, we determined that IFNβ signaling sensitizes PDAC cells to the clinically viable combination of small molecule ATR and PARP inhibitors.

In addition to mutations in KRAS and TP53, chronic inflammation is a hallmark feature of PDAC tumors. This low grade inflammatory response observed has been termed “para-inflammation” and is a defined transcriptional signature resembling a type I IFN response[28]. Intriguingly, among TCGA datasets PDAC ranks highest in terms of para-inflammation signature enrichment which is a negative prognostic factor in this disease [28]. Type I IFN production is induced by the activation of cytosolic or endosomal pathogen sensing pathways including the cGAS-STING pathway which initiates type I IFN production in epithelial, stromal, endothelial and immune cells in response to accumulation of cytosolic ssDNA and dsDNA. The cGAS-STING pathway is tightly regulated by transcriptional and post-translational mechanisms and indirectly by proteins which control the levels of cytosolic ssDNA and dsDNA, including SAMHD1, TREX1, and RPA/RAD51[52]. Importantly, mutational inactivation of several of these proteins results in Aicardi-Goutieres Syndrome (AGS), an early onset inflammatory disorder characterized and aberrantly high systemic levels of type I IFNs. Additionally, germ-line STING gain of function mutations have been associated with a lupus-like autoimmune disease in humans[53].

STING agonists are currently being evaluated as immune stimulating anti-cancer vaccines and analogs of the endogenous STING ligand 2'-3'-cGAMP which overcome its susceptibility to hydrolysis by ENPP1 are in development[54,55]. Interestingly, covalent STING inhibitors have also been recently described and may be useful tools to reprogram cytokine signaling in inflamed PDAC tumors[56].

cGAS and/or STING are down-regulated in various cancers, including colorectal cancer and melanoma, and thus this pathway has been classified as tumor suppressive[57,58]. cGAS and STING down-regulation appears to be primarily mediated by epigenetic mechanisms and treatment with DNA de-methylating agents can restore pathway functionality in some cases. PDAC is an exception as cGAS and STING exhibit decreased promoter methylation in patient samples[38]. Consistently, STING expression in PDAC appears to be elevated compared to normal pancreas and STING has previously been shown to be expressed extensively in both the cancer cell and stromal compartments of tumors, a finding we confirmed in this study[39]. It has been proposed that tumors exhibiting low cGAS-STING expression may be especially vulnerable to oncolytic virus therapy. Consistently, we observe a high degree of concordance between the PDAC cell lines we identified as ISD responders/non-responders and those previously reported to be resistant/sensitive to oncolytic virus therapy[59]. Regarding the discrepancy between basal interferon-stimulated gene expression in cGAS/STING proficient cells *in vitro* and *in vivo* it is possible that these lines constitutively secrete minimal amounts of IFN that is diluted in culture media and removed with passaging. A second explanation is that the cGAS ligand responsible for constructive activation is absent *in vitro* and only produced when PDAC cells are grown *in vivo*. In addition to the cGAS/STING pathway, other stimuli and pathways, such as TLR agonists and the NF-kB pathway, also activate type I IFN production and their contributions to type I IFN production in PDAC remains unclear[60]. Further, more detailed studies are required to interrogate these possibilities. As STING activation has been

shown mediate to inflammation-induced carcinogenesis it is intriguing to speculate that STING activation may play a role in the development or progression of a subset of PDAC tumors.

Paradoxically, IFNs have been shown to exert both pro- and anti-tumor functions. *in vitro*, IFNs are well studied for their ability to restrict cancer cell proliferation, however, IFN regulated genes also have been investigated in the context of a DNA damage resistance gene expression signature (IRDS) which is associated with resistance to chemotherapy and radiation[10]. Additionally, chronic IFN pathway agonism has been associated with resistance to immune checkpoint blockade[61]. It is intriguing to speculate that constitutive STING-driven IFN signaling is a mechanism by which PDAC cells condition a immunosuppressive microenvironment. In this model, tumor cells in the PDAC microenvironment may hijack the pro-tumor functions of IFNs and mitigate their anti-tumor effects by activating compensatory signaling and metabolic pathways (*i.e.* ATR and dCK).

Tumor cell vulnerabilities elicited by IFN signaling have not been systematically evaluated. However, IFN treatment has been shown to amplify the cytotoxic effects of MEK inhibitors in a subset of melanoma cell lines exhibiting low basal IFN signaling pathway activity[62]. In addition, multiple groups have independently demonstrated that IFN signaling induces a collateral dependency on ADAR to prevent dsRNA-mediated proliferation inhibition driven by PKR activity, a finding that is limited by the current lack of clinically viable ADAR inhibitors[63,64]. Here we identify an additional dependency driven by IFN signaling that is immediately actionable.

We have observed three major consequences of type I IFN signaling in PDAC cells: induction of nucleotide catabolism, cell cycle delay in S-phase and activation of the replication stress response. Multiple IFN-stimulated genes have been annotated in each are of these processes, rendering the identification of a single mediator of these phenotypes a significant challenge. Moreover, several of IFN-relegated metabolic genes have moonlighting functions; SAMHD1

possesses both metabolic (dNTP hydrolase) and DNA repair (CtIP scaffold) functions[35,65]. SAMHD1 induction by type I IFN signaling could reduce dNTP abundance and simultaneously facilitate DNA repair. The K312 residue in SAMHD1 is essential for its dNTPase function, whereas T592, which is phosphorylated by cyclin-dependent kinases (CDKs), is critical for its role in end resection[35]. Future studies incorporating the investigation of SAMHD1 mutants (K312A or T592A) will further define the specific function of SAMHD1 in the IFN signaling impact on PDAC cells.

IFN signaling has been reported to regulate metabolism in macrophages and dendritic cells however, the impact of IFNs on tumor cell metabolism has not yet been systematically evaluated[18,66,67]. Early work on IFNs demonstrated that they influence nucleotide metabolism nucleic acid biosynthesis in tumor cells and here we build on this foundation and characterize molecular mediators of this phenotype[68]. Our findings demonstrate that IFN signaling in cell culture and in vivo PDAC models triggers a shift in nucleotide metabolism toward a predominately catabolic phenotype. Interestingly, dT catabolism has been identified as a stress response to starvation in cancer cells which provides carbon for glycolysis via the actions of TYMP and DR5P aldolase (DERA)[69]. IFN may promote this process and catabolized nucleotides and nucleosides serve as a carbon source for other biochemical processes to fuel PDAC cell progression. Additionally, the restriction of thymidine pools resulting from IFN-induced up-regulation of TYMP can be leveraged using [^{18}F]FLT PET/CT. We anticipate that [^{18}F]FLT PET will have utility as a pharmacodynamic biomarker for STING agonists as well as other IFN-stimulating immunotherapies such as immune checkpoint blockade.

In addition to the cell autonomous effects, IFNs may also play an important role in regulating the landscape and composition of the metabolic synapse between tumor cells and immune cells[16]. Evidence for the competition between cancer cells and immune cells for nucleosides in tumor microenvironment is provided by the observation that nucleoside kinases and transporters, such

as dCK, uridine-cytidine kinase 2 (UCK2) and SLC29A1are up-regulated in T-cells following activation[70–72]. Additionally, purine efflux triggered by IFN signaling may have local immunosuppressive effects[73]. These observations justify the investigation of nucleotide metabolism-related IFN regulated genes in the context of immunotherapy in PDAC as well as other cancers with constitutive type I IFN signaling.

In our study, a range of response to the IFNβ/ATRi combination was observed in our human PDAC models. This variation may be reflective of the well-documented genomic, transcriptional and metabolic heterogeneity of PDAC cells[4,7,74]. Genomic alterations previously linked to ATR inhibitor sensitivity in PDAC, such as mutations of KRAS, TP53, ATM or ARID1A, may also influence response to endogenous IFNβ and ATRi therapy[75]. Similar heterogeneity has been documented in melanoma cell lines where type I IFN treatment enhanced the cytotoxic response of MEK inhibition only in a subset of cell lines[62]. Potentially related is the observation that hyper-activating JAK2V617F mutations have been linked to replication stress in myeloproliferative neoplasms[76].

Our findings are have high translational significance as ATR inhibitors and IFN-inducing therapies (such as immune checkpoint blockade and TLR agonists) are currently being evaluated in the clinic. Interestingly, ATR inhibition has been shown to enhance the efficacy of immune checkpoint blockade in pre-clinical models[77]. Collectively, our work begins to define the intersection between cytokine signaling, nucleotide metabolism and replication stress in PDAC and rationalizes the use of an IFN-related transcriptional signature to stratify patients for the ATR inhibitor / PARP inhibitor combinations currently being evaluated for the treatment of solid tumors.

METHODS

Experimental Model and Subject Details

Cell culture

All cell cultures were maintained in antibiotic free DMEM +10% FBS at 37ºC in 5% CO_2. Mycoplasma contamination was monitored using the PCR-based Venor Mycoplasma kit. PDAC cell lines were acquired either from commercial vendors or from collaborators. Cell line identity was independently authenticated by PCR. For anchorage-independent culture PDAC cells were grown on tissue-culture plates treated with poly(2-hydroxyethyl methacrylate (poly-HEMA)[78]. Briefly, Poly-HEMA was dissolved at 20 mg/mL concentration in 95% Ethanol and then added to the plate to fully cover growth area and dried overnight. Plates were sterilized by UV irradiation.

Drugs

Stocks were prepared in DMSO or H_2O and diluted fresh in cell culture media for treatments. The nonhydrolyzable bisphosphorothioate 2'-3'-cGAMP analog (2'-3'-cGAMP) and ISD were complexed with Lipofectamine 3000 before treatment.

In vivo mouse studies

All animal studies were approved by the UCLA Animal Research Committee (ARC). 4-6 week-old female NCG (CRL572; Charles River Laboratories) mice were injected subcutaneously on the flanks with $0.5x10^6$ cells resuspended 1:1 in PBS:matrigel. For orthotopic studies $3x10^4$ cells were resuspended 1:1 in PBS:matrigel and injected into the pancreata of NCG mice.

Patient samples

PDAC samples were collected during surgical tumor resection at UCLA.

Method Details

Live cell imaging

For live cell imaging cells were plated at $2x10^3$ cells / well in either ultra-low attachment or treated flat-bottom clear 96-well plates. After 24-72 h treatments were added and cell proliferation was tracked using the IncuCyte Zoom live-cell imaging system. Images were acquired at 3 h intervals over the indicated time periods.

LC-MS/MS DNA measurements

Cells were transferred into DMEM without glucose and supplemented with 10% dialyzed FBS containing the following labeled substrates: precursors for de novo [$^{13}C_6$]glucose at 11 mM and [$^{13}C_{10}$,$^{15}N_2$]dT at 5 μM. Genomic DNA was extracted using the Quick-gDNA MiniPrep kit and hydrolyzed to nucleosides using the DNA Degradase Plus kit following manufacturer-supplied instructions. In the final step of DNA extraction, 50 μL of water was used to elute the DNA into 1.5 mL microcentrifuge tubes. A nuclease solution (5 μL; 10X buffer/DNA Degradase PlusTM/ water, 2.5/1/1.5, v/v/v) was added to 20 μL of the eluted genomic DNA in an HPLC injector vial. The samples were incubated overnight at 37 oC. For genomic DNA and media analysis, an aliquot of the hydrolyzed DNA or media samples (20 μL) were injected onto a porous graphitic carbon column (Thermo Fisher Scientific Hypercarb, 100 x 2.1 mm, 5 μm particle size) equilibrated in solvent A (water 0.1% formic acid, v/v) and eluted (200 μL/min) with an increasing concentration of solvent B (acetonitrile 0.1% formic acid, v/v) using min/%B/flow rates (μL/min) as follows: 0/0/200, 5/0/200, 10/15/200, 20/15/200, 21/40/200, 25/50/200, 26/100/700, 30/100/700, 31/0/700, 34/0/700, 35/0/200. The effluent from the column was directed to the Agilent Jet Stream ion source connected to the triple quadrupole mass spectrometer (Agilent 6460) operating in the multiple reaction monitoring (MRM) mode using previously optimized settings. The peak areas for each nucleosides and nucleotides

(precursor→fragment ion transitions) at predetermined retention times were recorded using the software supplied by the instrument manufacturer (Agilent MassHunter).

RT-PCR

Total RNA was isolated from cells using the Zymo Quick-RNA MiniPrep kit. Reverse transcription was performed using the High Capacity cDNA Reverse Transcription kit. Quantitative PCR was performed using EvaGreen qPCR Master Mix. RNA expression values were normalized and calculated relative to control.

Immunohistochemistry (IHC)

Formalin-fixed, paraffin-embedded tumor samples were incubated at 60°C for 1h, deparaffinized in xylene, and rehydrated with graded alcohol washes. Slides were then boiled in 0.01 M sodium citrate buffer for 15 m followed by quenching of endogenous peroxidase with 3% hydrogen peroxide for antigen retrieval. After 1 h of blocking with 5% donkey serum at room temperature, primary antibodies were added and incubated overnight at 4°C. Biotin-conjugated anti-rabbit secondary antibody (1:500 Jackson Labs) was added and developed using Elite Vectastain ABC kit.

Immunoblot analysis

PBS-washed cell pellets were resuspended in cold RIPA buffer supplemented with protease and phosphatase inhibitors. Protein lysates were normalized using BCA assay, diluted using RIPA and 4x laemmli loading dye, resolved on 4-12% Bis-Tris gels and electro-transferred to nitrocellulose membranes. After blocking with 5% nonfat milk in TBS + 0.1% Tween-20 (TBS-T), membranes were incubated overnight in primary antibodies diluted (per manufactures instructions) in 5% BSA in TBS-T. Membranes were washed with TBST-T and incubated with HRP-linked secondary antibodies prepared at a 1:2500 dilution in 5% nonfat dry milk in TBS-T. HRP was activated by incubating membranes by incubating membranes with mixture of

SuperSignal Pico and SuperSignal Femto ECL reagents (100:1 ratio). Exposure of autoradiography film was used for detection.

Tumor tissue homogenization

Snap-frozen tumor tissue was transferred to Omni Hard Tissue homogenization vials. 750 µl of tissue Lysis buffer spiked with 1x protease and phosphatase inhibitor cocktails were added to each vial. Vials were homogenized using an Omni Bead Ruptor Elite (8 cycles of 15 s on, 30 s off, speed 8) chilled to 4C. Tissue homogenates were cleared by centrifugation at 12,000xg for 10 m at 4C. Cleared lysates were normalized using the BCA method and prepared for immunoblot analysis as described for cell culture samples.

Immuno-fluorescence microscopy

Cells cultured on coverslips were fixed with 4% (w/v) paraformaldehyde in PBS for 15 min, permeabilized with 0.2% (v/v) Triton X-100, blocked with 3% (w/v) BSA in PBS for 30 min, and then incubated with primary antibodies containing 1% (w/v) BSA and 0.1% (w/v) saponin in PBS for overnight, washed with PBS then incubated with fluorescence secondary antibodies for 1 hr. Following washing, cells were stained with DAPI, washed with PBS, and mounted onto microscope slides and imaged using a NIKON fluorescence microscope.

Clonogenic survival and viability analysis

For crystal violet staining, PDAC cells were plated in 6-well plates at $1x10^4$ cells/well and treated as described. Following treatment cells were fixed by incubating in 4% PFA in PBS for 15 m at room temperature. Plates were subsequently washed with PBS and stained with 0.1% crystal violet in H_2O for 15 m at room temperature.

For anchorage-dependent Cell Titer Glo analysis cells were plated at $1x10^3$ cells / well in at 50 µl / well in white opaque 384-well plates and treated as described. Following incubation 50 µl of Cell Titer Glo reagent (Diluted 1:5 in dH2O) was added to each well, plates incubated at room

temperature for 5 m and luminescence was measured using a BioTek microplate luminescence reader.

For anchorage-independent culture Cell Titer Glo analysis cells were plated at $5x10^3$ cells / well in at 100 µl /well poly-HEMA treated 96-well plates and treated as described. Following incubation 100 µl of 3D Cell Titer Glo reagent (Diluted 1:5 in dH_2O) was added to each well, plates incubated at room temperature for 5 m and luminescence was measured.

Flow cytometry

All flow cytometry data were acquired on five-laser BD LSRII, and analyzed using FlowJo software.

AnnexinV/PI: Treated PDAC cells were washed with PBS and incubated with AnnexinV and propidium iodide diluted in 1x Annexin binding buffer.

Propidium iodide cell cycle analysis: Treated PDAC cells were washed with PBS and suspended in cell cycle staining solution (100 µg/ml propidium iodide; 20 µg/ml Ribonuclease A; 1 mg/ml sodium citrate; 0.3% Triton-X 100 prepared in dH_2O).

EdU: PDAC cells were pulsed with 10 µM EdU for 2 h, washed twice with PBS, and released in fresh media containing 5 µM deoxyribonucleosides. Cells were collected 4 h following release in fresh media, fixed with 4% paraformaldehyde and permeabilized using saponin perm/wash reagent (Invitrogen), and then stained with azide-AlexaFluor 647 by Click reaction. The total DNA content was assessed by staining with FxCycle-Violet at 1 µg/mL final concentration. The cell cycle durations were calculated using equations for multiple time-point measurements according to previously published methods (CITE).

pH2A.X_{S139}: Cells were harvested, fixed, permeabilized with cytofix/cytoperm for 15 m on ice, prior to staining with a phospho-Histone H2A.X_{S139} antibody conjugated to FITC (1:800 dilutions

in perm/wash) for 20 m at room temperature shielded from light. Subsequently, cells were washed and stained with 0.5 mL of DAPI for DNA content before analysis.

Protein kinase inhibitor phenotypic screen

A library of 430 protein kinase inhibitors (SelleckChem Cat. L1200) was arrayed in polypropylene 384-well plates at 200x concentrations covering a 7-point concentration range (corresponding to 1x concentrations: 5μM, 1.65μM, 550nM, 185nM, 61.5nM, 20.6nM, 6.85nM). 25μl per well of growth media with or without 200 U/mL IFNβ supplementation (for a final concentration of 100 U/mL) was plated in opaque-white 384-well plates using a BioTek multidrop liquid handler. Protein kinase inhibitors were added by 250 nL pin-tool transfer (BioMek FX, Beckman-Coulter) and inhibitor/media mixtures were incubated at room temperature for 30 m. 25 μL of a 40,000 cells/mL SUIT2 suspension (for 1000 cells / well) was subsequently added to each well. After 72 h, 50 μL of Cell Titer Glo reagent diluted 1:4 in dH_2O was added to each well and luminescence was measured using a Wallac plate reader (Perkin Elmer). Each condition was assayed in duplicate (n=2) and % proliferation values were calculated by normalizing experimental wells to plate negative controls and averaging replicate values. Composite IFNβ synergy scores for each test compound were defined as the sum of the Synergy Score (% proliferation inhibition observed - % proliferation inhibition expected) between IFNβ and individual protein kinase inhibitor concentrations across the 7-point concentration range. Z factor scores for individual assay plates were calculated using eight positive and eight negative control wells on each plate. All plates gave a Z factor > 0.5.

CRISPR/Cas9 knockout cell line generation

All gRNA sequences were cloned into LentiCrisprV2. Lipofectamine 3000 was used to transfect PDAC cells with 1 μg/ml gRNA-specific LentiCrisprV2 vectors. Following puromycin selection cells were singly cloned.

shRNA knockdown cell line generation

For generation of stable knockdown cell lines PDAC cells were transduced with lentivirus harvested from HEK293FT cells in the presence of polybrene. Following transduction cells underwent antibiotic selection and knockdown efficiency was confirmed using immunoblot analysis. For virus production lentivirval vectors and packaging plasmids (psPAX2, pMD2G) at a 2:1:1 ratio were transfected into FT293 cells using polyethylenimine. Lentivirus-containing supernatants were filtered using a 0.45 μm filter prior to use.

Bioluminescence imaging

Mice were anesthetized with 2% isoflurane prior to intraperitoneal injection of 100 μl (50 mg/mL) D-luciferin. Images were acquired on an IVIS 100 Bioluminescence Imaging scanner 10 m after D-luciferin administration.

IFNβ ELISA

Cells were plated at 250k cells/well in treated 24-well tissue culture plates and allowed to seed overnight. 2'-3'-cGAMP was completed with Lipofectamine 3000 in OptiMEM at a 1:1:2 cGAMP:lipofectamine 3000:OptiMEM ratio. Before transfection cells were washed with PBS, 400 μL of culture media was added to each well and 100 μL of complexed 2'-3'cGAMP was added drop-wise for a final concentration of 25 μg/mL. Media was collected, centrifuged for 4 m at 450x*g* at 4C at indicated timepoints. ELISA analysis was performed per manufacturers instructions.

Statistical analyses

Data are presented as mean ± SD with number of biological replicates indicated. Comparisons of two groups were calculated using indicated unpaired or paired two-tailed Student's t-test and P values less than 0.05 were considered significant. For some experiments, generated mean normalized values (ratios from two groups, treated to untreated) were compared to the

hypothetical value 1 (indicating equal values between treated and untreated), calculated using one-sample t-test, and P values less than 0.05 were considered significant. Comparisons of more than two groups were calculated using one-way ANOVA followed by Bonferroni's multiple comparison tests, and P values less than 0.05/m, where m is the total number of possible comparisons, were considered significant.

CHAPTER 3 Key Resource Table

Reagents	Source	Identifier
DMEM	Corning	10-107-CV
Fetal Bovine Serum	Omega Scientific	FB-11
Lipofectamine 3000	ThermoFisher Scientific	L3000001
polyethyleneimine	Polysciences	23966-1
poly-HEMA	Sigma-Aldrich	P3932
VitaminE-TPGS	Sigma-Aldrich	57668
Matrigel	ThermoFisher Scientific	CB-40234
D-Luciferin	Sigma-Aldrich	L9504
Human IFNβ	PBL Assay Science	11415-1
Tetrahydrouridine (CDAi)	Cayman Chemicals	16402
Pemetrexed	SelleckChem	S1135
Olaparib	SelleckChem	S1060
M6620	Cayman Chemicals	24198
AZD6738	Cayman Chemicals	21035
LY2603618	Cayman Chemicals	20351
AZD1775	Cayman Chemicals	21266
ISD	Invivogen	tlrl-isdn
2'3'-cGAM(PS)$_2$ (Rp/Sp)	Invivogen	tlrl-nacga2srs
Ruxolintinib	Cayman Chemicals	11609
BCA Assay	ThermoFisher Scientific	23225
RIPA protein lysis buffer	Boston BioProducts	BP-115
Laemmli Loading Dye	Boston BioProducts	BP-110R
4-12% Bis-Tris Gels	ThermoFisher Scientific	NP0336
Nitrocellulose Membrane	ThermoFisher Scientific	88018
Nonfat Dry Milk	ThermoFisher Scientific	M-0841
Tris-Buffered Saline	ThermoFisher Scientific	50-751-7046
Tween-20	Sigma-Aldrich	P9416
SuperSignal West Pico	ThermoFisher Scientific	34580
SuperSignal West Femto	ThermoFisher Scientific	34095
Autoradiography Film	Denville	E3012
Crystal violet	Sigma-Aldrich	C0775
FX Cycle Violet	Invitrogen	F10347
DAPI	Invitrogen	D1306
CytoFIX/CytoPERM	BD Biosciences	554722
[$^{13}C_6$]glucose	Sigma-Aldrich	389374
DNA degrease PLUS	Zymo	E2021
Hard Tissue Homogenizing Mix	Omni International	19-628
Halt Protease Inhibitor Cocktail	ThermoFisher Scientific	PI78430
Halt Phosphatase Inhibitor	ThermoFisher Scientific	PI78428

Critical Commercial Assays	Source	Identifier
AnnexinV-FITC Apoptosis Detection Kit	BD Biosciences	556547
Click-iT Plus EdU Alexa Fluor 647 Flow Cytometry Assay Kit	ThermoFisher Scientific	C10634
CellTiter-Glo	Promega	G7572
3D CellTiter-Glo	Promega	G9683
MycoPlasma Detection Kit	Sigma-Aldrich	MP0025
Quick gDNA Miniprep Kit	Zymo	D3021

Antibodies	Source	Identifier
TOTAL STAT1	Cell Signaling Technology	14994
PHOSPHO STAT1 Y701	Cell Signaling Technology	9167
MX1	Cell Signaling Technology	37849
ACTIN	Cell Signaling Technology	3700
SAMHD1	Cell Signaling Technology	12361
TOTAL CHEK1	Cell Signaling Technology	2360
PHOSPHO CHEK1 S345	Cell Signaling Technology	2348
PHOSPHO H2AX S139	Cell Signaling Technology	9718
dCK	Owen Witte Lab (UCLA)	Clone #9D4
TK1	Cell Signaling Technology	8960
TYMS	Cell Signaling Technology	9045
CLEAVED PARP	Cell Signaling Technology	5625
CLEAVED CASPASE 3	Cell Signaling Technology	9662
RRM1	Cell Signaling Technology	8637
RRM2	Santa Cruz Biotechnology	SC-10846
STING (TMEM173)	Cell Signaling Technology	13647
PHOSPHO IRF3 S396	Cell Signaling Technology	37829
ANTI-RABBIT IgG, HRP-LINKED	Cell Signaling Technology	7074
ANTI-MOUSE IgG, HRP-LINKED	Cell Signaling Technology	7076
pH2AX S139 - FITC	Millipore	05-636
F7.26 ssDNA	Millipore	MAB3299

Vector	Source	Identifier
pMD2G	Addgene	12259
psPAX2	Addgene	12260
Lenticrispr V2	Addgene	52961

Oligonucleotides	Sequence	Vector
SAMHD1 gRNA	GTCATCGCAACGGGGACGCT	LENTICRISPR V2 (addgene #52961)
TK1 gRNA	GCTGCTGTAGCGAGTGTCTT	LENTICRISPR V2 (addgene #52961)
dCK gRNA	AAGGTAAAAGACCATCGTTC	LENTICRISPR V2 (addgene #52961)
STING (TMEM173) gRNA	AGAGCACACTCTCCGGTACC	LENTICRISPR V2 (addgene #52961)
TYMP shRNA	GCCTCCATTCTCAGTAAGAAA	pLKO.1 (addgene #10878)

Software	Source	Identifier
Prism 6	GraphPad Software	N/A
Flowjo 7.6	TreeStar	N/A

Instrument	Manufacturer	Assay
LSRII	BD	Flow Cytometry
Q-Exactive Mass Spectrometer	Thermo	Proteomics/Phosphoproteomics
LTQ OrbitrapXL Mass Spectrometer	Thermo	Non-targeted metabolomics
QQQ Mass Specgtrometer	Agilent	Targeted DNA/dNTP metabolites
Microplate reader	BioTek	Luminesence Cell Viabilioty Assays
BeadRuptor Elite	OMNI International	Tissue Homogenization
ECLIPSE Ci-S	Nikon	Fluorescence Microscopy

REFERENCES

1. Siegel, R. L., Miller, K. D. & Jemal, A. Cancer statistics, 2018. CA Cancer J Clin 68, 7-30 (2018).
2. Rahib, L. et al. Projecting cancer incidence and deaths to 2030: the unexpected burden of thyroid, liver, and pancreas cancers in the United States. Cancer Res 74, 2913-2921 (2014).
3. Kamisawa, T., Wood, L. D., Itoi, T. & Takaori, K. Pancreatic cancer. Lancet 388, 73-85 (2016).
4. Collisson, E. A. et al. Subtypes of pancreatic ductal adenocarcinoma and their differing responses to therapy. Nat Med 17, 500-503 (2011).
5. Bailey, P. et al. Genomic analyses identify molecular subtypes of pancreatic cancer. Nature 531, 47-52 (2016).
6. Golan, T. et al. Maintenance Olaparib for Germline. N Engl J Med 381, 317-327 (2019).
7. Cancer, G. A. R. N. E. A. A. & Cancer, G. A. R. N. Integrated Genomic Characterization of Pancreatic Ductal Adenocarcinoma. Cancer Cell 32, 185-203.e13 (2017).
8. Parker, B. S., Rautela, J. & Hertzog, P. J. Antitumour actions of interferons: implications for cancer therapy. Nat Rev Cancer 16, 131-144 (2016).
9. Motwani, M., Pesiridis, S. & Fitzgerald, K. A. DNA sensing by the cGAS-STING pathway in health and disease. Nat Rev Genet (2019).
10. Weichselbaum, R. R. et al. An interferon-related gene signature for DNA damage resistance is a predictive marker for chemotherapy and radiation for breast cancer. Proc Natl Acad Sci U S A 105, 18490-18495 (2008).
11. Benci, J. L. et al. Tumor Interferon Signaling Regulates a Multigenic Resistance Program to Immune Checkpoint Blockade. Cell 167, 1540-1554.e12 (2016).
12. Katlinskaya, Y. V. et al. Suppression of Type I Interferon Signaling Overcomes Oncogene-Induced Senescence and Mediates Melanoma Development and Progression. Cell Rep 15, 171-180 (2016).

13. Halbrook, C. J. & Lyssiotis, C. A. Employing Metabolism to Improve the Diagnosis and Treatment of Pancreatic Cancer. Cancer Cell 31, 5-19 (2017).
14. Ying, H. et al. Oncogenic Kras maintains pancreatic tumors through regulation of anabolic glucose metabolism. Cell 149, 656-670 (2012).
15. Vasseur, S., Tomasini, R., Tournaire, R. & Iovanna, J. L. Hypoxia induced tumor metabolic switch contributes to pancreatic cancer aggressiveness. Cancers (Basel) 2, 2138-2152 (2010).
16. Lyssiotis, C. A. & Kimmelman, A. C. Metabolic Interactions in the Tumor Microenvironment. Trends Cell Biol 27, 863-875 (2017).
17. Binnewies, M. et al. Understanding the tumor immune microenvironment (TIME) for effective therapy. Nat Med 24, 541-550 (2018).
18. Wu, D. et al. Type 1 Interferons Induce Changes in Core Metabolism that Are Critical for Immune Function. Immunity 44, 1325-1336 (2016).
19. Santana-Codina, N. et al. Oncogenic KRAS supports pancreatic cancer through regulation of nucleotide synthesis. Nat Commun 9, 4945 (2018).
20. Elliott, I. A. et al. Lysosome inhibition sensitizes pancreatic cancer to replication stress by aspartate depletion. Proc Natl Acad Sci U S A 116, 6842-6847 (2019).
21. Zeman, M. K. & Cimprich, K. A. Causes and consequences of replication stress. Nat Cell Biol 16, 2-9 (2014).
22. Brown, J. S., O'Carrigan, B., Jackson, S. P. & Yap, T. A. Targeting DNA Repair in Cancer: Beyond PARP Inhibitors. Cancer Discov 7, 20-37 (2017).
23. Le, T. M. et al. ATR inhibition facilitates targeting of leukemia dependence on convergent nucleotide biosynthetic pathways. Nat Commun 8, 241 (2017).
24. Schoppy, D. W. et al. Oncogenic stress sensitizes murine cancers to hypomorphic suppression of ATR. J Clin Invest 122, 241-252 (2012).

25. Gilad, O. et al. Combining ATR suppression with oncogenic Ras synergistically increases genomic instability, causing synthetic lethality or tumorigenesis in a dosage-dependent manner. Cancer Res 70, 9693-9702 (2010).
26. Nghiem, P., Park, P. K., Kim Ys, Y. S., Desai, B. N. & Schreiber, S. L. ATR is not required for p53 activation but synergizes with p53 in the replication checkpoint. J Biol Chem 277, 4428-4434 (2002).
27. Doherty, M. R. et al. Interferon-beta represses cancer stem cell properties in triple-negative breast cancer. Proc Natl Acad Sci U S A 114, 13792-13797 (2017).
28. Aran, D. et al. Widespread parainflammation in human cancer. Genome Biol 17, 145 (2016).
29. Alavi, S. et al. Interferon Signaling Is Frequently Downregulated in Melanoma. Front Immunol 9, 1414 (2018).
30. Zaretsky, J. M. et al. Mutations Associated with Acquired Resistance to PD-1 Blockade in Melanoma. N Engl J Med 375, 819-829 (2016).
31. Wiredja, D. D., Koyutürk, M. & Chance, M. R. The KSEA App: a web-based tool for kinase activity inference from quantitative phosphoproteomics. Bioinformatics (2017).
32. Noser, J. A. et al. The RAS/Raf1/MEK/ERK signaling pathway facilitates VSV-mediated oncolysis: implication for the defective interferon response in cancer cells. Mol Ther 15, 1531-1536 (2007).
33. David, M. et al. Requirement for MAP kinase (ERK2) activity in interferon alpha- and interferon beta-stimulated gene expression through STAT proteins. Science 269, 1721-1723 (1995).
34. Antonucci, J. M., St Gelais, C. & Wu, L. The Dynamic Interplay between HIV-1, SAMHD1, and the Innate Antiviral Response. Front Immunol 8, 1541 (2017).
35. Coquel, F. et al. SAMHD1 acts at stalled replication forks to prevent interferon induction. Nature 557, 57-61 (2018).

36. Rice, G. I. et al. Mutations involved in Aicardi-Goutières syndrome implicate SAMHD1 as regulator of the innate immune response. Nat Genet 41, 829-832 (2009).
37. Austin, W. R. et al. Nucleoside salvage pathway kinases regulate hematopoiesis by linking nucleotide metabolism with replication stress. J Exp Med 209, 2215-2228 (2012).
38. Konno, H. et al. Suppression of STING signaling through epigenetic silencing and missense mutation impedes DNA damage mediated cytokine production. Oncogene 37, 2037-2051 (2018).
39. Baird, J. R. et al. Radiotherapy Combined with Novel STING-Targeting Oligonucleotides Results in Regression of Established Tumors. Cancer Res 76, 50-61 (2016).
40. Seo, G. J. et al. TRIM56-mediated monoubiquitination of cGAS for cytosolic DNA sensing. Nat Commun 9, 613 (2018).
41. Tang, E. D. & Wang, C. Y. Single amino acid change in STING leads to constitutive active signaling. PLoS One 10, e0120090 (2015).
42. Shields, A. F. et al. Imaging proliferation in vivo with [F-18]FLT and positron emission tomography. Nat Med 4, 1334-1336 (1998).
43. Zhang, C. C. et al. [(18)F]FLT-PET imaging does not always “light up” proliferating tumor cells. Clin Cancer Res 18, 1303-1312 (2012).
44. Moghaddam, A. et al. Thymidine phosphorylase is angiogenic and promotes tumor growth. Proc Natl Acad Sci U S A 92, 998-1002 (1995).
45. Turinetto, V. & Giachino, C. Multiple facets of histone variant H2AX: a DNA double-strand-break marker with several biological functions. Nucleic Acids Res 43, 2489-2498 (2015).
46. Carcagno, A. L. et al. E2F1 transcription is induced by genotoxic stress through ATM/ATR activation. IUBMB Life 61, 537-543 (2009).
47. Iwase, S. et al. Modulation of E2F activity is linked to interferon-induced growth suppression of hematopoietic cells. J Biol Chem 272, 12406-12414 (1997).
48. D’Angiolella, V. et al. Cyclin F-mediated degradation of ribonucleotide reductase M2 controls genome integrity and DNA repair. Cell 149, 1023-1034 (2012).

49. Dauer, P. et al. Inactivation of Cancer-Associated-Fibroblasts Disrupts Oncogenic Signaling in Pancreatic Cancer Cells and Promotes Its Regression. Cancer Res 78, 1321-1333 (2018).
50. Halbrook, C. J. et al. Macrophage-Released Pyrimidines Inhibit Gemcitabine Therapy in Pancreatic Cancer. Cell Metab 29, 1390-1399.e6 (2019).
51. Herold, N. et al. With me or against me: Tumor suppressor and drug resistance activities of SAMHD1. Exp Hematol 52, 32-39 (2017).
52. Li, T. & Chen, Z. J. The cGAS-cGAMP-STING pathway connects DNA damage to inflammation, senescence, and cancer. J Exp Med 215, 1287-1299 (2018).
53. König, N. et al. Familial chilblain lupus due to a gain-of-function mutation in STING. Ann Rheum Dis 76, 468-472 (2017).
54. Li, L. et al. Hydrolysis of 2'3'-cGAMP by ENPP1 and design of nonhydrolyzable analogs. Nat Chem Biol 10, 1043-1048 (2014).
55. Ramanjulu, J. M. et al. Design of amidobenzimidazole STING receptor agonists with systemic activity. Nature 564, 439-443 (2018).
56. Haag, S. M. et al. Targeting STING with covalent small-molecule inhibitors. Nature 559, 269-273 (2018).
57. Sokolowska, O. & Nowis, D. STING Signaling in Cancer Cells: Important or Not. Arch Immunol Ther Exp (Warsz) 66, 125-132 (2018).
58. Bakhoum, S. F. & Cantley, L. C. The Multifaceted Role of Chromosomal Instability in Cancer and Its Microenvironment. Cell 174, 1347-1360 (2018).
59. Moerdyk-Schauwecker, M. et al. Resistance of pancreatic cancer cells to oncolytic vesicular stomatitis virus: role of type I interferon signaling. Virology 436, 221-234 (2013).
60. Di Franco, S., Turdo, A., Todaro, M. & Stassi, G. Role of Type I and II Interferons in Colorectal Cancer and Melanoma. Front Immunol 8, 878 (2017).

61. Benci, J. L. et al. Opposing Functions of Interferon Coordinate Adaptive and Innate Immune Responses to Cancer Immune Checkpoint Blockade. Cell 178, 933-948.e14 (2019).
62. Litvin, O. et al. Interferon α/β Enhances the Cytotoxic Response of MEK Inhibition in Melanoma. Mol Cell 57, 784-796 (2015).
63. Liu, H. et al. Tumor-derived IFN triggers chronic pathway agonism and sensitivity to ADAR loss. Nat Med 25, 95-102 (2019).
64. Gannon, H. S. et al. Identification of ADAR1 adenosine deaminase dependency in a subset of cancer cells. Nat Commun 9, 5450 (2018).
65. Ballana, E. & Esté, J. A. SAMHD1: at the crossroads of cell proliferation, immune responses, and virus restriction. Trends Microbiol 23, 680-692 (2015).
66. Blanc, M. et al. Host defense against viral infection involves interferon mediated down-regulation of sterol biosynthesis. PLoS Biol 9, e1000598 (2011).
67. York, A. G. et al. Limiting Cholesterol Biosynthetic Flux Spontaneously Engages Type I IFN Signaling. Cell 163, 1716-1729 (2015).
68. Barankiewicz, J., Kaplinsky, C. & Cohen, A. Modification of ribonucleotide and deoxyribonucleotide metabolism in interferon-treated human B-lymphoblastoid cells. J Interferon Res 6, 717-727 (1986).
69. Tabata, S. et al. Thymidine Catabolism as a Metabolic Strategy for Cancer Survival. Cell Rep 19, 1313-1321 (2017).
70. Radu, C. G. et al. Molecular imaging of lymphoid organs and immune activation by positron emission tomography with a new [18F]-labeled 2'-deoxycytidine analog. Nat Med 14, 783-788 (2008).
71. Tan, H. et al. Integrative Proteomics and Phosphoproteomics Profiling Reveals Dynamic Signaling Networks and Bioenergetics Pathways Underlying T Cell Activation. Immunity 46, 488-503 (2017).

72. Kim, W. et al. [18F]CFA as a clinically translatable probe for PET imaging of deoxycytidine kinase activity. Proc Natl Acad Sci U S A 113, 4027-4032 (2016).
73. Yin, J. et al. Potential Mechanisms Connecting Purine Metabolism and Cancer Therapy. Front Immunol 9, 1697 (2018).
74. Daemen, A. et al. Metabolite profiling stratifies pancreatic ductal adenocarcinomas into subtypes with distinct sensitivities to metabolic inhibitors. Proc Natl Acad Sci U S A 112, E4410-7 (2015).
75. Williamson, C. T. et al. ATR inhibitors as a synthetic lethal therapy for tumours deficient in ARID1A. Nat Commun 7, 13837 (2016).
76. Chen, E. et al. JAK2V617F promotes replication fork stalling with disease-restricted impairment of the intra-S checkpoint response. Proc Natl Acad Sci U S A 111, 15190-15195 (2014).
77. Vendetti, F. P. et al. ATR kinase inhibitor AZD6738 potentiates CD8+ T cell-dependent antitumor activity following radiation. J Clin Invest 128, 3926-3940 (2018).
78. Yu, M. et al. RNA sequencing of pancreatic circulating tumour cells implicates WNT signalling in metastasis. Nature 487, 510-513 (2012).

CHAPTER 4

Defective Nucleotide Catabolism Defines a Subset of Cancers Sensitive to Purine Nucleoside Phosphorylase Inhibition

ABSTRACT

Small molecule inhibitors of purine nucleoside phosphorylase (PNP) have been developed and applied as a treatment for leukemia and lymphoma, however, the determinants of response to this class of drugs are incompletely understood. PNP inhibitors impair cell proliferation by preventing catabolism of the nucleoside deoxyguanosine (dG) which induces toxic imbalances in intracellular deoxyribonucleotide triphosphate (dNTP) pools following its phosphorylation and trapping by nucleoside kinases. We hypothesized that differential nucleoside uptake or catabolism defines cancer cell lines as either sensitive or resistant to PNP inhibition. Among cancer cell lines we found that T-cell acute lymphoblastic leukemia (T-ALL) cells are uniquely and acutely sensitive to PNP inhibition whereas the B-cell leukemia and solid tumor models are completely resistant. We determined that although the nucleoside scavenging kinase deoxycytidine kinase (dCK) was active in all cells tested, PNP inhibitors only induced dGTP pool increases in sensitive models. By evaluating the expression of key genes involved in nucleotide scavenging, biosynthesis, and phosphohydrolysis in a panel of sensitive and resistant cell lines we found that the dNTP phosphohydrolase sterile alpha-motif and histidine-aspartate domain-containing protein 1 (SAMHD1) was exclusively expressed in resistant cells.

Using CRISPR/Cas9 SAMHD1 knockout cell lines, we verified that PNP inhibitor sensitivity is a function of SAMHD1 expression and determined that the pharmacological inhibition of dCK or genetic restoration of SAMHD1 conferred resistance to PNP inhibition. Importantly, we determined that low expression of SAMHD1 is not limited to T-ALL as subset of established and primary solid tumors models are SAMHD1-deficient. These solid tumor models were consistently acutely sensitive to PNP inhibitors which indicates that the utility of PNP inhibitors extends beyond hematological malignancies. Additionally, we found that deoxycytidine (dC) can limit the anti-proliferative effects of PNP inhibitors by competing with dG for phosphorylation by dCK but this effect can be overcome by expression of dC-catabolizing gene cytidine deaminase (CDA). Collectively, these results indicate that SAMHD1, dCK and CDA are critical biomarkers that must be used to stratify patients in clinical trials evaluating pharmacological PNP inhibition.

INTRODUCTION

A sufficient supply of deoxyribonucleotide triphosphates (dNTPs) is essential for cell growth, survival and proliferation[1,2]. Thus, the metabolic network that is responsible for the synthesis of dNTPs is tightly regulated by transcriptional, post-translational and allosteric control mechanisms[3,4]. Actively proliferating cancer cells are particularly reliant on dNTP biosynthesis and this non-oncogene addiction has been leveraged clinically by the use of small molecule inhibitors of rate-limiting metabolic enzymes including dihydroorotate dehydrogenase (DHODH), ribonucleotide reductase (RNR), dihydrofolate reductase (DHFR) and thymidylate synthase (TYMS)[5]. These drugs restrict the ability of cancer cells to synthesize dNTPs and trigger cell cycle arrest: effectively preventing cell proliferation.

Beyond insufficiency, imbalance among dNTP pools results in mutagenesis, altered cell cycle progression or death in specific cell types and has been linked to defects in development. Examples include development of mitochondrial neurogastrointestinal encephalopathy syndrome (MNGIE) as a consequence of down-regulation of the thymidine catabolizing gene thymidine phosphorylase (TYMP) and impaired T-cell development in deoxycytidine kinase (dCK) knockout mice resulting from unchecked expansion of dTTP pools in developing hematopoietic cells[6,7]. Intriguingly, the cell type specific lethality resulting from dNTP imbalance has also been linked to the pathology of severe-combined immuno-deficiency (SCID) a hereditary genetic disorder in humans that is characterized by compromised immune function and premature death. Giblett and colleagues were among the first to identify that inherited inactivating mutations in the nucleotide catabolic enzymes adenosine deaminase (ADA) and purine nucleoside phosphorylase (PNP) drive the development of SCID[8,9]. ADA and PNP function sequentially in the catabolism of purine deoxyribonucleosides dA and dG and counter their intracellular accumulation mediated by deoxycytidine kinase dCK[4]. For reasons not well understood defective dG catabolism results in remarkably selective T-cell defects, and otherwise normal cellular development, in individuals with PNP-linked SCID (**Figure 4.1**)[10].

The T-cell specific phenotype associated with PNP-SCID is thought to be related to the expression pattern of the nucleoside kinases dCK and preferential dG uptake in these tissues[11].

Decades later, the observations made by Giblett and colleagues were leveraged for the treatment of cancer with the rationale that pharmacological inhibition of ADA or PNP could be an effective strategy for patients affected by T- and B- cell leukemias and lymphomas[12]. In the 1990s, Schramm and colleagues spearheaded the effort to develop small molecule PNP inhibitors using their knowledge of the transition state substrate-enzyme structure to rationally design drugs with exceptionally high potency and selectivity (**Figure 4.2**)[13,14]. PNP inhibitors prevent the catabolism of deoxyguanosine (dG) to guanine and deoxyribose-1-phosphate thereby allowing the intracellular conversion of dG to dGTP which can prevent *de novo* biosynthesis of pyrimidine dNTPs via allosteric inhibition of RNR[15,16]. Pharmacological PNP inhibition was found to selectively eradicate T-cell leukemias *in vitro* thus mimicking the phenotype of SCID[14]. With these encouraging results, the PNP inhibitor Forodesine (also known as BCX-1777 or Immucillin H) progressed to clinical trials for the treatment of relapsed/refectory T- and B-cell leukemias and lymphomas and received approval for the treatment of peripheral T-cell lymphoma in Japan in 2017[17,18]. Despite excellent tolerability and pharmacodynamic properties in humans (evidenced by plasma accumulation of the PNP substrate dG and depletion in the product of dG catabolism, uric acid) efficacy was observed only in a small subset of patients.

It remains an open challenge to identify biomarkers predictive of PNP inhibitor response in cancer. Multiple markers such as ATM, p53, ZAP-70, HGPRT and various nucleoside transporters have been studied in this context but alone do not predict sensitivity[19,20]. With the goal of identifying metabolic determinants of PNP inhibitor response, we focused our investigation on heterogeneity in nucleoside uptake, accumulation and catabolism across panels of cancer cell lines (**Figure 4.3A**). We found that the dNTP phosphohydrolase sterile alpha-motif and histidine-aspartate domain-containing protein 1 (SAMHD1), which catabolizes dGTP into dG and triphosphate, is exclusively expressed in resistant cell lines (**Figure 4.3B**).

We confirmed a role for SAMHD1 in the activity of PNP inhibitors using both loss-of-function and gain-of-function genetic models. Additionally, we identified several solid tumor cell lines, including lung cancer and melanoma, which are SAMHD1-deficient and confirmed that these models were sensitive to PNP inhibition. Collectively these results demonstrate that SAMHD1 activity and not disease type *per se* defines PNP inhibitor sensitivity.

RESULTS

SAMHD1 mediates response to PNP inhibition in leukemia cell lines

To identify cell line models sensitive and resistant to PNP inhibition, we evaluated the anti-proliferative effects of dG, Forodesine (PNPi), and the combination across a panel of T- and B-acute lymphoblastic leukemia (ALL) cell lines using Cell Titer Glo. Importantly, PNP deficiency alone does not impair cell proliferation or survival *in vitro* and endogenously generated concentrations of its substrate dG must be supplemented to recapitulate the PNP-loss of function phenotype observed *in vivo*. We found that the T-ALL cell lines CCRF-CEM, JURKAT and MOLT4 were eradicated by the combination whereas the B-ALL models NALM6 and RS411 were unaffected (**Figure 4.4A**). We confirmed these findings using flow cytometry cell cycle analysis in which we observed an increase in the percentage of sub-G1 cells, a maker for cell death, following PNP inhibition only in T-ALL models (**Figure 4.4B**). Using immunoblot analysis, we found that PNP inhibitor treatment only induced DNA damage (evidenced by $H2AX_{S139}$ phosphorylation) and apoptosis (evidenced by cleaved caspase 3 accumulation) in CCRF-CEM and not in NALM6 cells (**Figure 4.4C**).

We reasoned that heterogeneity in the sensitivity to PNP inhibition could arise from the differential expression of key metabolic genes essential for the synthesis and accumulation of dGTP. These genes include PNP itself, dCK, essential and non-redundant for its ability to phosphorylate dG to dGMP, and SAMHD1, a dNTP phosphohydrolase that catabolizes dGTP to dG (**Figure 4.4D**). By probing the Cancer Cell Line Encyclopedia (CCLE) gene expression database, we found that dCK and PNP were expressed at similar levels across T- and B-ALL cell line models[21]. In contrast, SAMHD1 was found to be expressed at high levels exclusively in B-ALL cell lines and undetectable in a subset of T-ALL cell lines (**Figure 4.4E**). Using immunoblot analysis, we confirmed at the protein level that dCK is expressed at similar levels across T- and B-ALL models but SAMHD1 is only detected in B-ALL cell lines (**Figure 4.4F**). To functionally validate the role of SAMHD1 in the response to PNP inhibition we engineered a

CCRF-CEM genetic variant that constitutively expresses human SAMHD1 (**Figure 4.4G**). We found that expression of SAMHD1 rendered CCRF-CEM cells completely resistant to the anti-proliferative (**Figure 4.4H**) and cytotoxic effects of PNP (**Figure 4.4I**).

SAMHD1-deficient solid tumor models are sensitive to PNP inhibitors.

To evaluate the spectrum of SAMHD1 expression across cancers and to determine if low SAMHD1 expression was unique to T-ALL, we extended our analysis to the complete CCLE gene expression dataset (**Figure 4.5A**). We identified several additional cell lines exhibiting low expression of SAMHD1, including melanoma, lung adenocarcinoma and acute myeloid leukemia cell lines. We hypothesized that low SAMHD1 expression, and not disease type *per se*, predicts response to PNP inhibitors across cancer cell line models. To test this we evaluated the activity of PNPi in the EGFR-mutant, SAMHD1-deficient lung adenocarcinoma cell line HCC827 and found that the combination of dG and PNPi induced cell cycle arrest in this model (**Figure 4.5B**). We determined that this associated with proliferation inhibition by performing crystal violet analysis of HCC827 cell cultured treated for 7 days (**Figure 4.5C**).

To functionally validate the role of SAMHD1 in the response of solid tumor cell line models to PNP inhibition, knocked out SAMHD1 in the pancreatic cancer cell line SUIT2 using CRISPR/Cas9. We found that while parental cells were completely resistant to PNPi, SAMHD1 knockout cells exhibited DNA damage in response to PNPi. While dCK is the only cytosolic nucleoside kinase capable of phosphorylating dG, dG is also a substrate for the mitochondria-localized deoxyguanosine kinase (dGK) and SAMHD1 has been shown to generate substrates for dGK in the mitochondria[22]. Furthermore, dCK inactivation has also been associated with resistance to dG-mediated toxicity in PNP-deficient T-lymphoma cells[15]. We found that the lethality of PNP inhibitors be completely prevented by supplementing with a small molecule dCK inhibitor indicating that phosphorylation of dG by dGK does not contribute to the observed lethality at these timepoints (**Figure 4.5D**)[4]. Additionally, using crystal violet analysis we found that the

proliferation of only SAMHD1 knockout cells could be prevented by PNP inhibitors and that this anti-proliferative effect could be completely blocked by a dCK inhibitor (**Figure 4.5E**). Collectively, these results demonstrate that SAMHD1 expression predicts sensitivity to PNP inhibitors across leukemia and solid tumor cell line models.

A subset of primary melanoma cell line models are deficient in SAMHD1 expression and are sensitive to PNP inhibitors

To investigate the extent of SAMHD1-deficiency across solid tumor models we profiled the expression of SAMHD1 in a panel of 51 primary melanoma cell lines derived at UCLA (**Figure 4.6A**). We found that among these models, 2 exhibited undetectable levels of the SAMHD1 transcript (M230, M418) and we confirmed these findings using immunoblot analysis (**Figure 4.6B**). SAMHD1 function is tightly regulated by transcriptional, post-transcriptional and allosteric control mechanisms and SAMHD1 has been identified as an interferon (IFN)-stimulated gene [23,24]. To determine if SAMHD1 expression can be induced in M230 and M418 cells by IFN, we exposed a panel of melanoma cell lines to either type I (IFNβ) or type II (IFNγ) IFN for 24 h and measured SAMHD1 expression using immunoblot analysis (**Figure 4.6B**). We found that all models tested responded to both type I and type II interferon by increasing the expression of a canonical interferon stimulated gene STAT1, however, SAMHD1 expression was only induced by IFN in cell line models in which SAMHD1 is detectable at baseline. Impaired SAMHD1 expression in M418 and M230 cells could result from mutational inactivation, which has been described in the contested of chronic lymphocytic leukemia, or aberrant promoter methylation which as been described in the context of lung cancer[25,26].

We confirmed that PNP inhibition selectively inhibited proliferation in SAMHD1-deficient primary melanoma models using crystal violet analysis (**Figure 4.6C**). Similarly, we observed that PNPi only induced cell cycle arrest in SAMHD1-deficient models (**Figure 4.6D**).

dC mitigates the anti-proliferative effects of PNP inhibitors

An additional factor influencing the cytotoxicity of PNP inhibitors is the competition between dG and other deoxyribonucleosides, for dCK (**Figure 4.7B**). dCK can accept dC, dG and dA as substrates but exhibits an 15-fold higher affinity for dC over the other purine deoxyribonucleosides (BRENDA:EC2.7.1.74). Furthermore, phosphorylation of dCK by ATR further increases its ability to phosphorylate dC while not impacting dA, or dG phosphorylation[27,28]. In this model, the dC catabolizing enzyme cytidine deaminase (CDA) can promote the activity of PNP inhibitors by eliminating dC and decreasing competition with dG for dCK. To test this model, we evaluated the ability of dC to prevent the anti-proliferative effect of PNP Inhibition in CCEF-CEM YFP control cells and CDA over-expressing cells (**Figure 4.7B**). In CCRF-CEM YFP cells, PNP inhibition decreased proliferation to 1% of control and supplementation 1 μM dC was sufficient to counteract the effects of PNPi and restored proliferation to 60% of control. Overexpression of CDA prevented this rescue. We have previously reported that plasma dC various greatly across species with levels ranging from 10 nM in human plasma and non-human primates to > 1 μM in rodents (**Figure 4.7C**; figure adapted from Kim et al. PNAS. 2016). It is conceivable that plasma deoxycytidine can prevent the activity of PNPi and can confound the study of PNP inhibitors in mice. Thus, high-CDA expression should be considered a requisite biomarker for PNP inhibitor sensitivity alongside low-SAMHD1 expression.

SAMHD1 prevents the anti proliferative effects of thymidine

Having observed that SAMHD1 can protect cancer cells from dGTP pool imbalance resulting from PNP inhibition we investigated whether SAMHD1 can prevent the anti-proliferative effects of imbalances in other dNTP pools. Elevations in dTTP, dATP or dGTP, but not dCTP, have been linked to impaired cell proliferation which results from allosteric inhibition of RNR[4]. Supplementation of cell cultures with high levels of the pyrimidine nucleoside thymidine is a well

established approach to inhibit cell proliferation and synchronize cells in S-phase[29]. Thymidine induced cell cycle arrest is the result of unchecked dTTP pool expansion and allosteric inhibition of CDP reduction by RNR. This “thymidine block” can be completely reversed by supplementation with dC in a dCK-dependent manner. This phenotype extends *in vivo* and is the cause of impaired T-cell development observed in dCK knockout mice[30]. We found that SAMHD1 KO cells exhibited a 200-fold lower thymidine IC_{50} than SAMHD1 WT controls (**Figure 4.8A**). This selectivity was unique to thymidine and did not extend to other RNR inhibitors, including 3-AP, which function by preventing RNR tyrosyl radical regeneration[4]. Similar selectivity was observed using crystal violet proliferation analysis (**Figure 4.8B**). Additionally, we found that the induction of $pCHEK1_{S345}$ and $pH2A.X_{S139}$ by dT treatment was enhanced in the SAMHD1 KO cells. Collectively these results indicate that SAMHD1 protects cancer cells from toxic imbalances in both purine and pyrimidine dNTP pools.

Ulodesine and forodesine exhibit comparable potency and selectivity

In addition to forodesine an additional small molecule inhibitor of PNP, Ulodesine (also known as BCX-4208) has been developed and evaluated in humans for the treatment of gout[31]. To determine if ulodesine exhibits similar potency and selectivity towards SAMHD1-deficient cancer cells we evaluated inhibition of cell proliferation using Cell Titer Glo (**Figure 4.9**). We found that both forodesine and ulodesine impaired HCC827 proliferation selectively in the presence of dG with IC50 values of 71 and 21 nM respectively. We expanded this analysis to a panel of cancer cells and found that ulodesine selectively impaired the proliferation of SAMHD1 deficient cancer cell lines JURKAT, CCRF-CEM, and HCC827 while exhibiting negligible activity against SAMHD1-proficient SUIT2 and NALM6 cells (**Figure 4.10A**). We confirmed a role for SAMHD1 by demonstrating that overexpression of SAMHD1 in CCRF-CEM resulted in resistance and CRISPR/Cas9 knockout of SAMHD1 in SUIT2 cells rendered them sensitive to ulodesine (**Figure 4.10B**).

CDA overexpression mitigates competition between dC and dG in HCC827 cells

To determine if CDA can prevent the competition between dC and dG in HCC827 cells we generated CDA over-expressing HCC827 cells using retroviral transduction. We found that HCC827 cells express CDA endogenously which was enhanced with overexpression (**Figure 4.11A**). We found that dC could prevent the lethality of the dG/ulodesine combination with an EC_{50} of 1.9 μM in control cells. The dC EC_{50} was increased over 11-fold to 21 μM in the CDA over-expressing isogenic cells (**Figures 4.11B, 4.11C**).

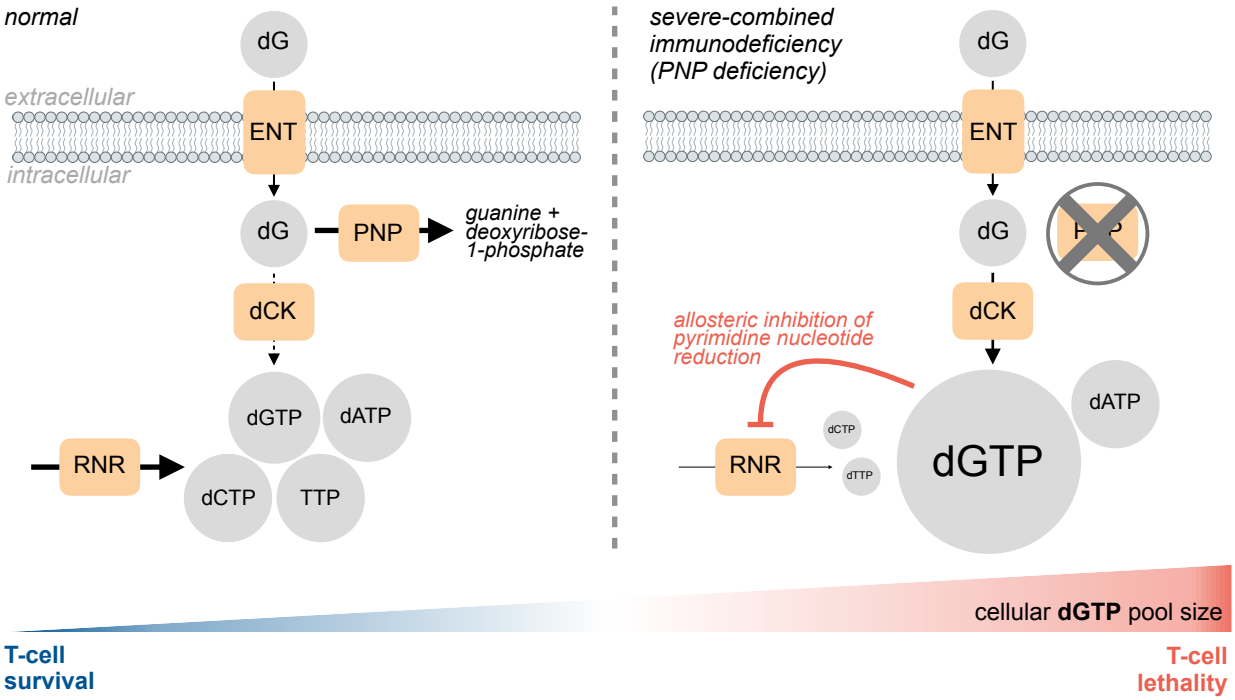

Figure 4.1 | Impaired purine nucleoside phosphorylase activity results in toxic dGTP accumulation in T-cells. RNR: ribonucleotide reductase; dCK: deoxycytidine kinase; PNP: purine nucleoside phosphorylase; ENT: equilibrative nucleoside transporter.

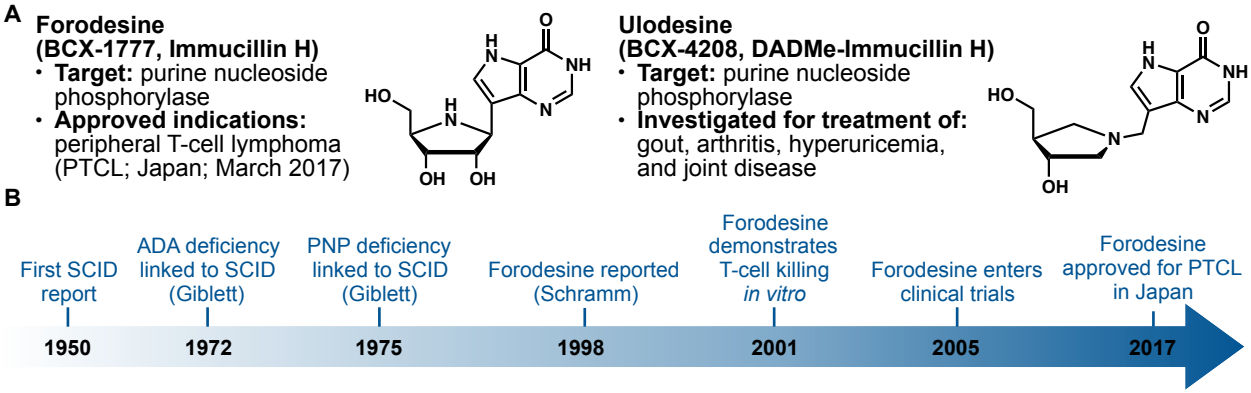

4.2 | Potent, selective inhibitors of PNP have been developed and applied in the treatment of cancer. (**A**) Summary of small molecule PNP inhibitors. (**B**) Timeline of the development and translation of PNP inhibitors for the treatment of cancer.

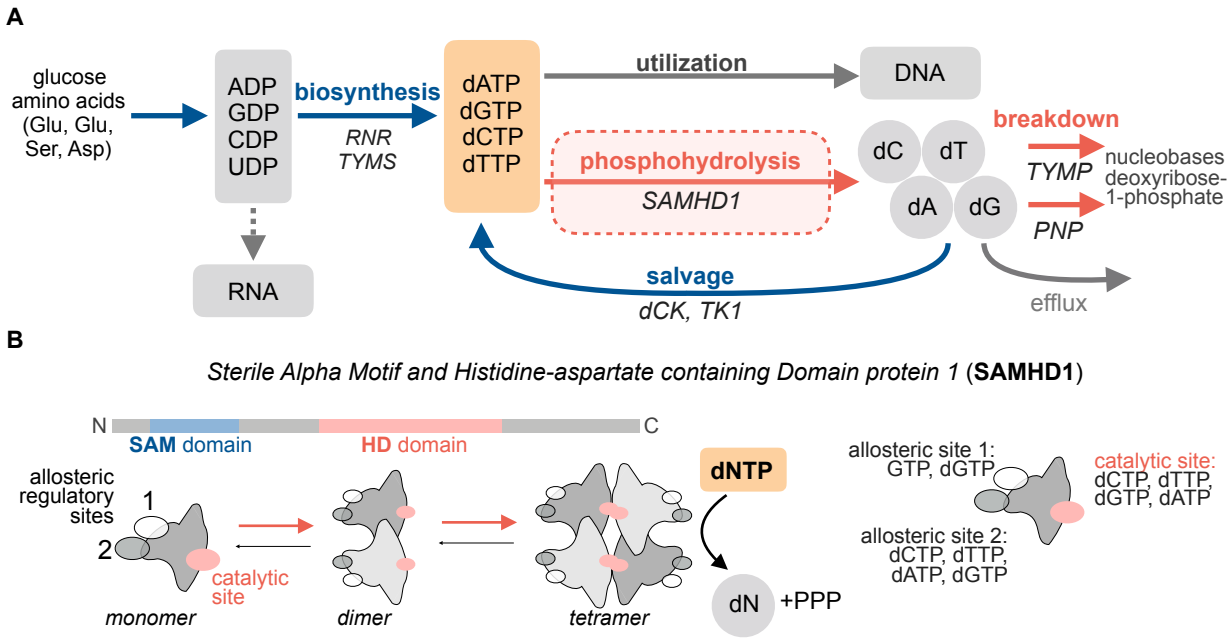

Figure 4.3 | Metabolic determinants of PNP inhibitor sensitivity. (**A**) Lack of response to PNP inhibition can be explained by insufficient dG phosphorylation (dCK activity) or enhanced catabolism. (**B**) SAMHD1 is a dNTP triphosphohydrolase. Summary of nucleotide binding to allosteric regulation sites.

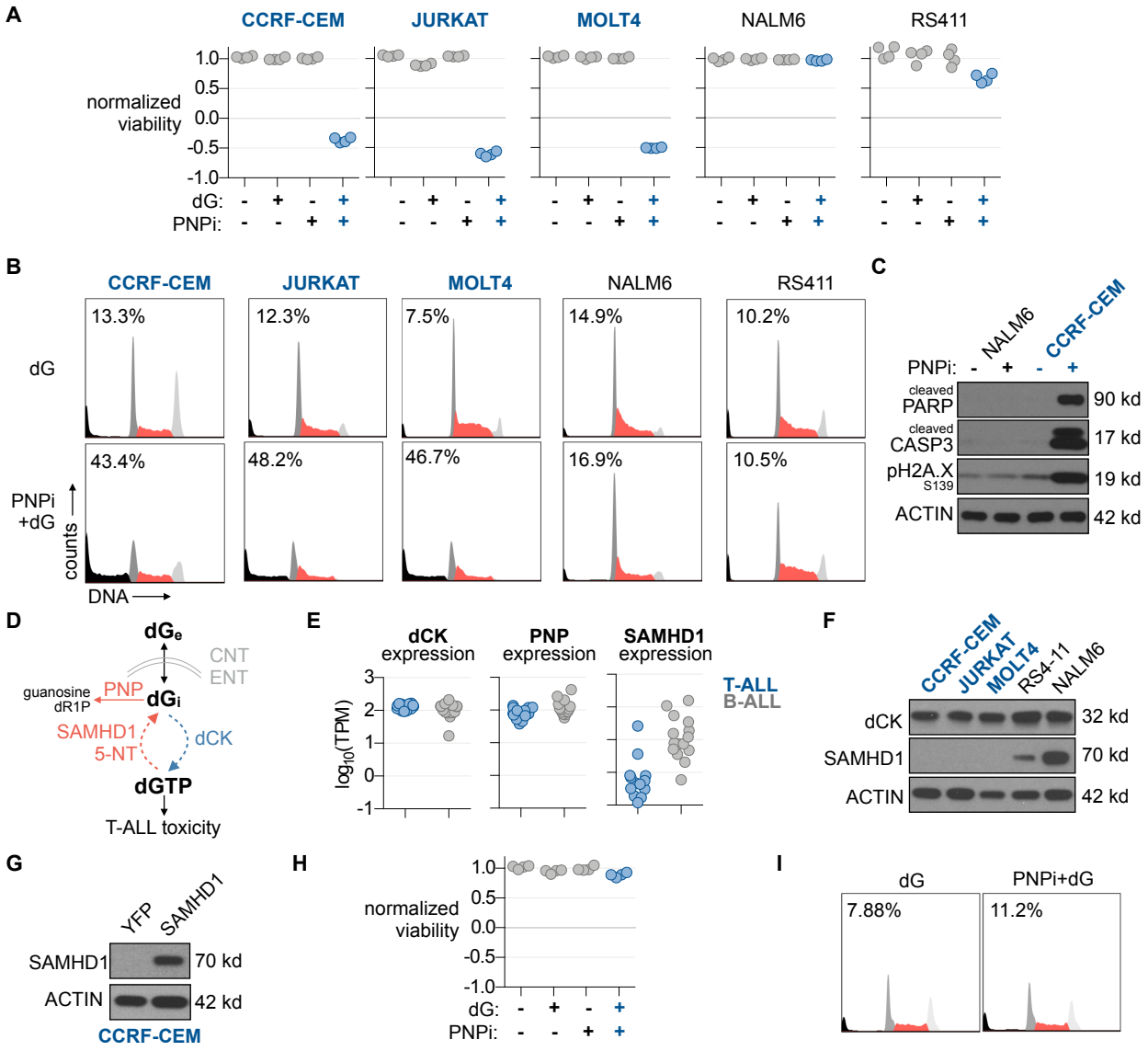

Figure 4.4 | Purine nucleoside phosphorylase (PNP) inhibition is selectively lethal in a subset of acute lymphoblastic leukemia cell lines. (**A**) Cell Titer Glo analysis of acute lymphoblastic leukemia cell line panel treated with 5 μM dG ±1 μM BCX-1777 for 72 h (PNPi, n=4). (**B**) Propidium iodide (PI) cell cycle analysis of acute lymphoblastic leukemia cell lines treated with 5 μM dG ± 1 μM BCX-1777 for 24 h. Insert indicate percentage of Sub-G1 population. (**C**) Immunoblot analysis of NALM6 or CCRF-CEM cells treated with 5 μM dG ± 1 μM BCX-1777 for 24 h. (**D**) Model summarizing metabolic defects potentially explaining sensitivity to PNP inhibitors. (**E**) Expression of dCK, PNP and SAMHD1 across T-ALL cell lines in the Cancer Cell Line Encyclopedia (CCLE) RNAseq dataset. (**F**) Immunoblot analysis of dCK

and SAMHD1 expression in T- and B- ALL cell lines. (**G**) Immunoblot validation of SAMHD1 overexpression in CCRF-CEM T-ALL cells. (**H**) Cell Titer Glo analysis of CCRF-CEM YFP control and SAMHD1-over-expressing isogenic cells treated with 5 μM dG ± 1 μM BCX-1777 for 72 h (PNPi, n=4). (**I**) PI cell cycle analysis of CCRF-CEM YFP control and SAMHD1-over-expressing isogenic cells treated with 5 μM dG ± 1 μM BCX-1777 for 24 h. Insert indicates percentage of sub-G1 population.

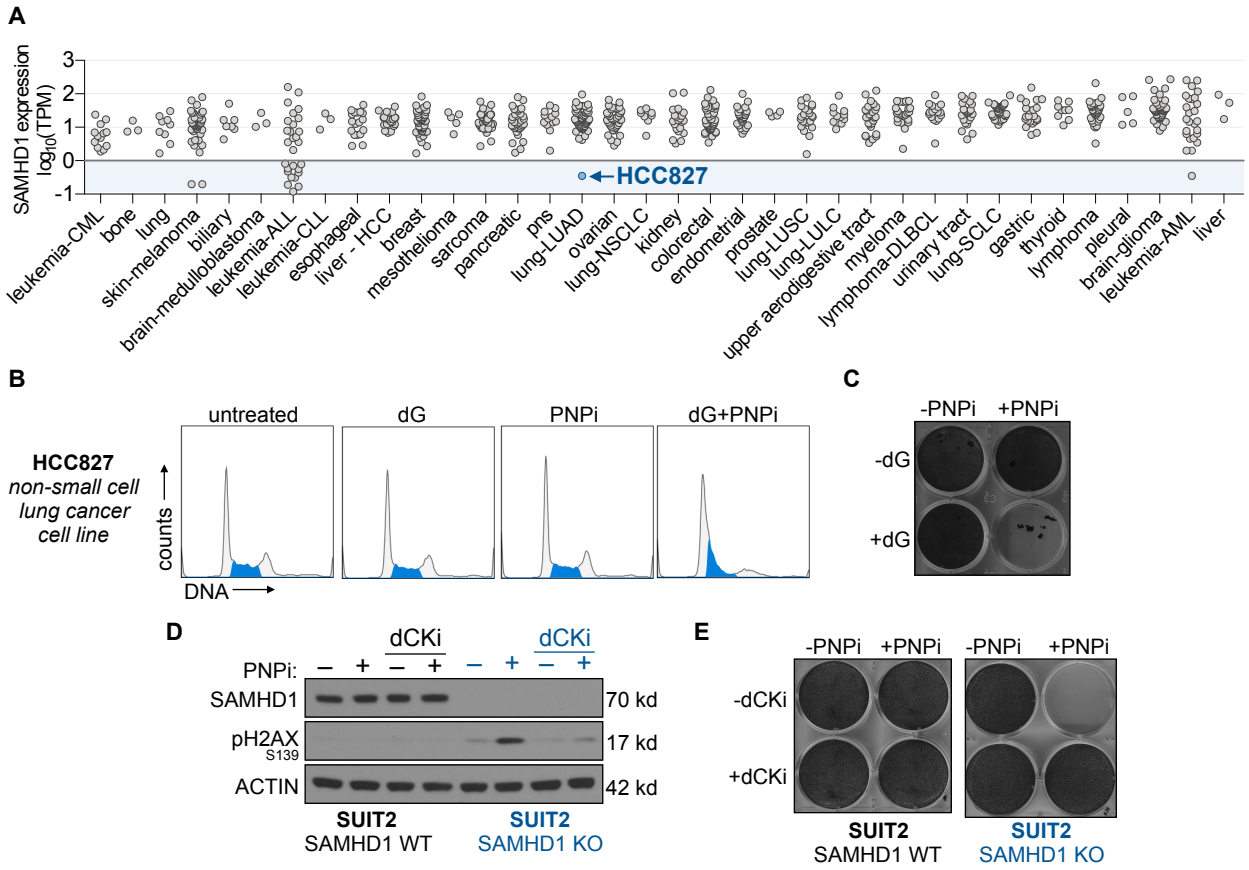

Figure 4.5 | SAMHD1 protects solid tumor-derived cell lines from PNP inhibition. (**A**) SAMHD1 expression in the cancer cell line encyclopedia (CCLE) RNAseq dataset. (**B**) PI cell cycle analysis of the HCC827 non-small cell lung cancer cell line treated with 5 μM dG ± 1 μM BCX-1777 (PNPi) for 24 h. (**C**) Crystal violet analysis of HCC827 cells treated for 7 d with 5 μM dG ± 1 μM PNPi for 7 d. Media was refreshed every 72 h. (**D**) Immunoblot analysis of SUIT2 wild-type (WT) and SAMHD1 knockout (KO) cells treated for 24 h + 5 μM dG ± 1 μM forodesine ± 1 μM (R)-DI-82 (dCKi). (**E**) Crystal violet analysis of SUIT2 WT and SAMHD1 KO cells treated for 7 d with 5 μM dG ± 1 μM PNPi ± 1 μM dCKi for 7 d. Media was refreshed every 72 h.

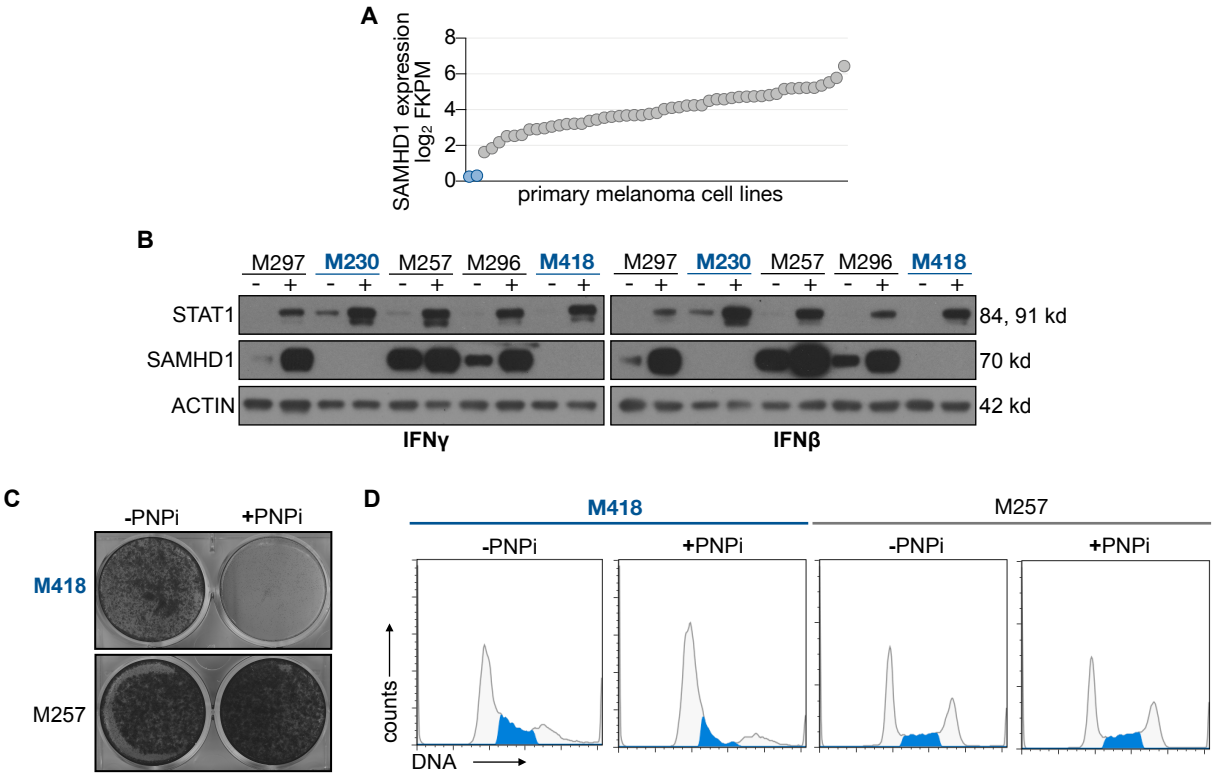

Figure 4.6 | SAMHD1 expression is heterogeneous in primary melanoma cell lines and SAMHD1 deficient cells are sensitive to PNP inhibition. (A) RNAseq analysis of SAMHD1 transcript levels in a panel of 51 primary melanoma cell lines. (**B**) Immunoblot analysis of representative melanoma cell lines following 24 h treatment with 100 U/mL IFNβ or 1 ng/mL IFNγ. (**C**) Crystal violet staining following 7 d treatment with 1 μM PNPi (BCX-1777) in the presence of 10 μM dG. (**D**) PI cell cycle analysis following 24 h treatment with 1 μM PNPi in the presence of 10 μM dG.

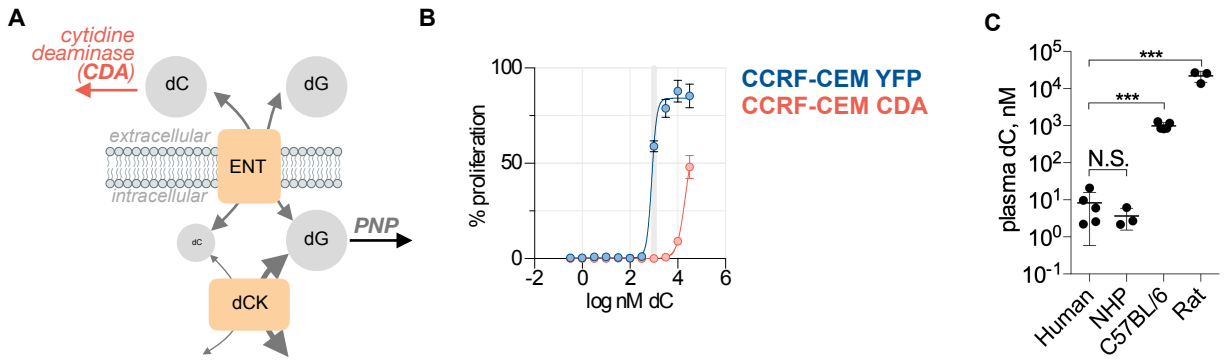

Figure 4.7 | Deoxycytidine (dC) competes with dG for phosphorylation by dCK. (**A**) Schematic overview of the competition between dC and dG for dCK. Cytidine deaminase (CDA) breaks down dC and prevents competition with dG. ENT: equilibrate nucleoside transporter. (**B**) Cell Titer Glo analysis of CCRF-CEM YFP and CCRF-CEM CDA over expressing cell lines treated +10 μM dG +1 μM BCX-1777 ± a titration of dC for 72 h.(**C**) Plasma dC in human, non-human primate (NHP), C57BL/6 and rats (figure adapted from Kim et al. PNAS. 2016).

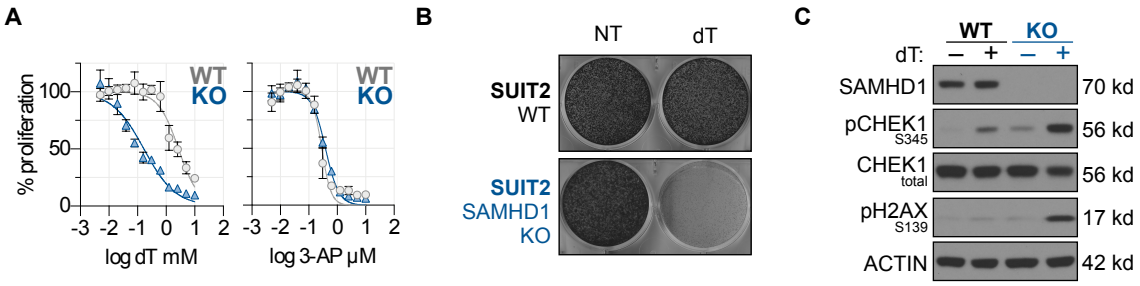

Figure 4.8 | SAMHD1 prevents the toxicity of thymidine. (**A**) Cell Titer Glo analysis of SUIT2 WT and SAMHD1 KO cells treated with a titration of dT or 3-AP for 72 h (mean±SD; n=4). (**B**) Crystal violet analysis of SUIT2 WT and SAMHD1 KO cells treated for 7 d ±100 µM dT. Media was refreshed every 72 h. (**C**) Immunoblot analysis of SUIT2 WT and SAMHD1 KO cells treated for 24 h ±100 µM dT.

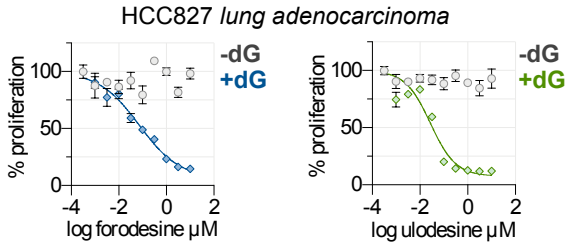

Figure 4.9 | Ulodesine exhibits potency and selectivity similar to forodesine. Cell Titer Glo analysis of HCC827 cells treated with a titration of forodesine (BCX-1777) or ulodesine for 72 h ±10 µM dG (mean±SD; n=4).

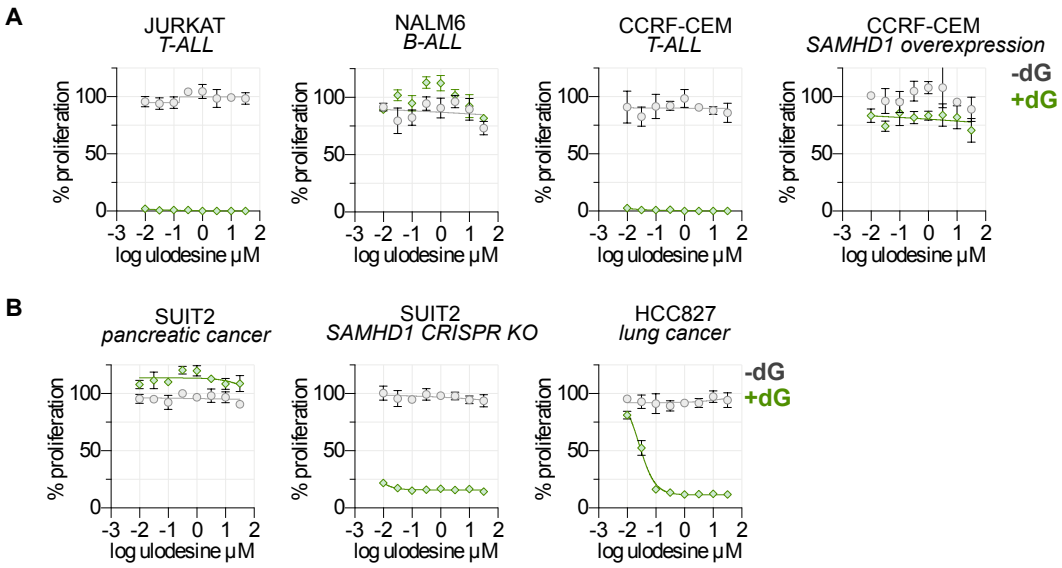

Figure 4.10 | Ulodesine exhibits selective activity in SAMHD1-deficient cancer cell lines.

(**A**) Cell Titer Glo analysis of hematopoietic cancer cell lines JURKAT, NALM6, CCRF-CEM and CCRF-CEM SAMHD1 over-expressing cells treated with a titration of ulodesine for 72 h ±1 µM dG (mean±SD; n=4). (**B**) Cell Titer Glo analysis of solid cancer cell lines SUIT2, HCC827 and SUIT2 SAMHD1 CRISPR/Cas9 KO cells treated with a titration of ulodesine for 72 h ±5 µM dG (mean±SD; n=4).

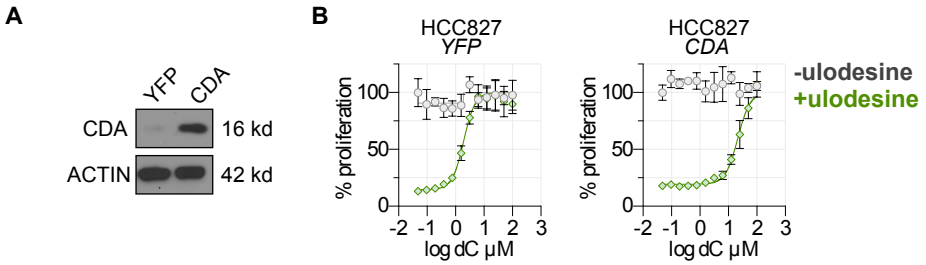

Figure 4.11 | CDA overexpression mitigates competition between dC and dG, enhancing ulodesine activity. (**A**) Immunoblot analysis of HCC827-YFP and -CDA over-expressing isogenic cells. (**B**) Cell Titer Glo analysis of solid cancer cell lines HCC827 isogenic cells treated with 5 µM dG ±1 µM ulodesine ±dC for 72 h (mean±SD; n=4). (**C**) EC_{50} values for dC from experiment in **C**.

DISCUSSION

Synthetic lethality refers to the scenario where impaired function of either of two genes alone is tolerated where simultaneous loss results in cell death[32]. This concept has been explored extensively in the context of anti-cancer therapy with the goal of identifying synthetic lethal partners with cancer-associated genomic alterations. Perhaps the most well-studied example is the acute sensitivity of BRCA1/2-deficient cancer cells to PARP inhibitors[33]. Here we add to the library of synthetic lethal interactions in cancer and identify PNP activity as a targetable co-dependency of cells for deficient for SAMHD1.

Mutational inactivation of PNP has been linked linked to a remarkably selective T-cell deficiency phenotype in humans. We propose that the lack of SAMHD1 expression in developing thymocytes, and not dCK expression alone, underlies this selectivity. Interestingly, similar tissue selective-developmental defects were observed in dCK knockout mice and has been linked to an imbalanced dTTP pool, and observation which suggests that SAMHD1 may play a role in this phenotype[30]. SAMHD1 has been shown to be expressed in mature T-cells but the reasons for its inactivation in developing hematopoietic tissues are unclear[34]. This altered expression may be linked to the high-rate of proliferation, and high dNTP demand, of these developing cells and is likely that ALL cells are progeny of this SAMHD1-deficient immature T-cell population. An important corollary of our work is the finding that pharmacological dCK inhibition mitigates the phenotypes associated with PNP inactivation which suggests that dCK inhibitors could have utility in the treatment of PNP or ADA-linked SCID.

Interestingly, dGTP functions not only as a substrate by also as an allosteric activator of SAMHD1 which possesses two nucleotide-binding allosteric regulatory sites that effectively tune its function. Allosteric site 1 binds either GTP or dGTP and allosteric site 2 binds either dGTP, dATP, dCTP or dTTP. While the species of allosteric site-bound nucleotides influences the K_m of SAMHD1 for its substrate, the K_m for dGTP is lowest regardless of the combination of bound

regulatory nucleotides[24]. Taken together, these findings suggest that a primary function of SAMHD1 is to sense and restrict any increases in dGTP pool size.

We found that PNP inhibition triggers replication stress, DNA damage and apoptosis in SAMHD1-deficient cells. However, the mechanistic link between dGTP pool expansion and induction of these phenotypes remains incompletely defined. The lethal effects of dGTP pool imbalance could reflect dNTP insufficiency resulting from allosteric inhibition of pyrimidine nucleotide reduction by RNR[15]. Small molecule inhibitors of ATR, including VE-822 and AZD6738, are currently being investigated in phase I/II trials against solid tumors and may represent rational companions for PNP inhibitors[35]. Furthermore, as SAMHD1-deficiency is a requirement for PNP activity in cancer cells the development of SAMHD1 inhibitors would broaden the patient population that could be treated with forodesine or ulodesine. However, systemic non-specific toxicity is a potential limitation of this approach and it remains to be determined whether a sufficient therapeutic window exists for combinations of PNP and SAMHD1 inhibitors.

Several nucleoside analog PET probes have been developed and are routinely used in the clinic in the oncology setting. The purine nucleoside analog [^{18}F]CFA may be particularly useful in identifying tumors most likely to accumulate dGTP following PNP Inhibition as it is sensitive to alterations in the expression of both CDA and dCK[36].

SAMHD1 has been implicated as a regulator of multiple biological processes, including: retrovirus (HIV) restriction, cGAS/STING activation and therapeutic efficacy of nucleoside-analog chemotherapies in acute myeloid leukemia[37–39]. Here, we expand the understanding of SAMHD1 function by demonstrating that it also prevents lethal imbalances among natural dNTP pools and we identify SAMHD1 expression as a biomarker for PNP inhibitor activity.

As PNP inhibitors have demonstrated excellent bioavailability in humans our work strongly strongly supports reigniting their evaluation in biomarker driven clinical trials for the treatment of cancer. Collectively, our results indicate that SAMHD1, CDA and dCK expression are requisite

biomarkers that must be taken into consideration in any future clinical trials evaluating PNP inhibitors. Additionally, our findings challenge the dogma that disease type (i.e. T-cell leukemia/ lymphoma) predicts PNP inhibitor activity and provides evidence that PNP inhibitors may have utility in the treatment of a precisely defined subset of both hematological cancers and solid tumors.

METHODS

Experimental Model and Subject Details

Cell culture

All cell cultures were between passages 3 and 20 and maintained in antibiotic free DMEM or RPMI +10% dialyzed FBS, at 37ºC in 5% CO_2. We routinely monitored for mycoplasma contamination using the PCR-based Venor Mycoplasma kit. PDAC cell lines were acquired either from a commercial vendor (ATCC, DSMZ) or from collaborators. Cell line identity was independently authenticated by PCR.

Drugs

Drug stocks were prepared in DMSO or H_2O and diluted fresh in cell culture media prior to treatment.

Method Details

Propidium iodide cell cycle analysis

Treated cells were washed with PBS and suspended in propidium iodide cell cycle staining solution (100 µg/ml propidium iodide; 20 µg/ml Ribonuclease A). 10,000 events were collected per sample. All flow cytometry data were acquired on five-laser BD LSRII, and analyzed using FlowJo software (Tree Star).

Viability analysis

For Cell Titer Glo analysis cells were plated at $1x10^3$ cells / well in 50 µl / well in white opaque 384-well plates and treated as described. Following incubation 50 µl of Cell Titer Glo reagent (Diluted 1:5 in dH_2O) was added to each well, plates incubated at room temperature for 5 m and luminescence was measured using a BioTek microplate luminescence reader. Proliferation rate normalized growth inhibition was calculated using the previously described GR metric.

For crystal violet staining, cells were plated in 6-well cell culture plates at $1x10^4$ cells/well and treated as described. Following treatment cells were fixed by incubating in 4% PFA in PBS for 15 m at room temperature. Plates were subsequently washed with PBS and stained with 0.1% crystal violet in H_2O for 15 m at room temperature.

Immunoblot analysis

PBS-washed cell pellets were resuspended in cold RIPA buffer supplemented with protease and phosphatase inhibitors. Protein lysates were normalized using BCA assay, diluted using RIPA and 4x laemmli loading dye, resolved on 4-12% Bis-Tris gels and electro-transferred to nitrocellulose membranes. After blocking with 5% nonfat milk in TBS + 0.1% Tween-20 (TBS-T), membranes were incubated overnight in primary antibodies diluted (per manufacturers instructions) in 5% BSA in TBS-T. Membranes were washed with TBST-T and incubated with HRP-linked secondary antibodies prepared at a 1:2500 dilution in 5% nonfat dry milk in TBS-T. HRP was activated by incubating membranes with a mixture of SuperSignal Pico and SuperSignal Femto ECL reagents (100:1 ratio). Exposure of autoradiography film was used for detection.

Retroviral transduction and stable cell line generation

The pMSCV-hCDA-IRES-EYFP plasmid was described previously[40]. Amphotropic retroviruses were generated by transient co-transfection of the MSCV retroviral plasmid and pCL-10A1 packaging plasmid into Phoenix-Ampho packaging cells.

Generation of SAMHD1 knockout cells using CRISPR/Cas9

A SAMHD1-targeting gRNA was cloned into the lentiCRISPRv2 backbone and used for transfection of SUIT2 cells using Lipofectamine3000. Following transfection, SUIT2 cells were selected with 5 µg/mL puromycin for 72 h and singly cloned in 96-well plates. Knockout clones were validated using immunoblot analysis.

CHAPTER 4 Key Resource Table

Reagents	Source	Identifier
DMEM	Corning	10-107-CV
Fetal Bovine Serum	Omega Scientific	FB-11
Forodesine	MedChem Express	HY-16209
BCA Assay	ThermoFisher Scientific	23225
RIPA protein lysis buffer	Boston BioProducts	BP-115
Laemmli Loading Dye	Boston BioProducts	BP-110R
4-12% Bis-Tris Gels	ThermoFisher Scientific	NP0336
Nitrocellulose Membrane	ThermoFisher Scientific	88018
Nonfat Dry Milk	ThermoFisher Scientific	M-0841
Tris-Buffered Saline	ThermoFisher Scientific	50-751-7046
Tween-20	Sigma-Aldrich	P9416
SuperSignal West Pico	ThermoFisher Scientific	34580
SuperSignal West Femto	ThermoFisher Scientific	34095
Autoradiography Film	Denville	E3012
Crystal Violet	Sigma-Aldrich	C0775

Critical Commercial Assays	Source	Identifier
CellTiter-Glo	Promega	G7572
MycoPlasma Detection Kit	Sigma-Aldrich	MP0025

Antibodies	Source	Identifier
TOTAL STAT1	Cell Signaling Technology	14994
ACTIN	Cell Signaling Technology	3700
SAMHD1	Cell Signaling Technology	12361
TOTAL CHEK1	Cell Signaling Technology	2360
PHOSPHO CHEK1 S345	Cell Signaling Technology	2348
PHOSPHO H2AX S139	Cell Signaling Technology	9718
dCK	Owen Witte Lab (UCLA)	Clone #9D4
ANTI-RABBIT IgG, HRP-LINKED	Cell Signaling Technology	7074
ANTI-MOUSE IgG, HRP-LINKED	Cell Signaling Technology	7076

Vector	Source	Identifier
Lenticrispr V2	Addgene	52961

Oligonucleotides	Sequence	Vector
SAMHD1 gRNA	GTCATCGCAACGGGGACGCT	LENTICRISPR V2 (addgene #52961)

Software	Source	Identifier
Prism 6	GraphPad Software	N/A
Flowjo 7.6	TreeStar	N/A

REFERENCES

1. Kumar, D., Viberg, J., Nilsson, A. K. & Chabes, A. Highly mutagenic and severely imbalanced dNTP pools can escape detection by the S-phase checkpoint. Nucleic Acids Res 38, 3975-3983 (2010).
2. Pai, C. C. & Kearsey, S. E. A Critical Balance: dNTPs and the Maintenance of Genome Stability. Genes (Basel) 8, (2017).
3. Evans, D. R. & Guy, H. I. Mammalian pyrimidine biosynthesis: fresh insights into an ancient pathway. J Biol Chem 279, 33035-33038 (2004).
4. Le, T. M. et al. ATR inhibition facilitates targeting of leukemia dependence on convergent nucleotide biosynthetic pathways. Nat Commun 8, 241 (2017).
5. Mathews, C. K. DNA synthesis as a therapeutic target: the first 65 years. FASEB J 26, 2231-2237 (2012).
6. Nishino, I., Spinazzola, A. & Hirano, M. Thymidine phosphorylase gene mutations in MNGIE, a human mitochondrial disorder. Science 283, 689-692 (1999).
7. Toy, G. et al. Requirement for deoxycytidine kinase in T and B lymphocyte development. Proc Natl Acad Sci U S A 107, 5551-5556 (2010).
8. Giblett, E. R., Anderson, J. E., Cohen, F., Pollara, B. & Meuwissen, H. J. Adenosine-deaminase deficiency in two patients with severely impaired cellular immunity. Lancet 2, 1067-1069 (1972).
9. Giblett, E. R., Ammann, A. J., Wara, D. W., Sandman, R. & Diamond, L. K. Nucleoside-phosphorylase deficiency in a child with severely defective T-cell immunity and normal B-cell immunity. Lancet 1, 1010-1013 (1975).
10. Giblett, E. R. ADA and PNP deficiencies: how it all began. Ann N Y Acad Sci 451, 1-8 (1985).
11. Carson, D. A., Kaye, J. & Seegmiller, J. E. Lymphospecific toxicity in adenosine deaminase deficiency and purine nucleoside phosphorylase deficiency: possible role of nucleoside kinase(s). Proc Natl Acad Sci U S A 74, 5677-5681 (1977).

12. Kazmers, I. S. et al. Inhibition of purine nucleoside phosphorylase by 8-aminoguanosine: selective toxicity for T lymphoblasts. Science 214, 1137-1139 (1981).
13. Miles, R. W., Tyler, P. C., Furneaux, R. H., Bagdassarian, C. K. & Schramm, V. L. One-third-the-sites transition-state inhibitors for purine nucleoside phosphorylase. Biochemistry 37, 8615-8621 (1998).
14. Kicska, G. A. et al. Immucillin H, a powerful transition-state analog inhibitor of purine nucleoside phosphorylase, selectively inhibits human T lymphocytes. Proc Natl Acad Sci U S A 98, 4593-4598 (2001).
15. Ullman, B., Gudas, L. J., Clift, S. M. & Martin, D. W. Isolation and characterization of purine-nucleoside phosphorylase-deficient T-lymphoma cells and secondary mutants with altered ribonucleotide reductase: genetic model for immunodeficiency disease. Proc Natl Acad Sci U S A 76, 1074-1078 (1979).
16. Jordan, A. & Reichard, P. Ribonucleotide reductases. Annu Rev Biochem 67, 71-98 (1998).
17. Makita, S., Maeshima, A. M., Maruyama, D., Izutsu, K. & Tobinai, K. Forodesine in the treatment of relapsed/refractory peripheral T-cell lymphoma: an evidence-based review. Onco Targets Ther 11, 2287-2293 (2018).
18. Maruyama, D. et al. Multicenter phase 1/2 study of forodesine in patients with relapsed peripheral T cell lymphoma. Ann Hematol 98, 131-142 (2019).
19. Alonso, R. et al. Forodesine has high antitumor activity in chronic lymphocytic leukemia and activates p53-independent mitochondrial apoptosis by induction of p73 and BIM. Blood 114, 1563-1575 (2009).
20. Huang, M. et al. Determinants of sensitivity of human T-cell leukemia CCRF-CEM cells to immucillin-H. Leuk Res 32, 1268-1278 (2008).
21. Fernandez-Banet, J. et al. OASIS: web-based platform for exploring cancer multi-omics data. Nat Methods 13, 9-10 (2016).

22. Franzolin, E., Salata, C., Bianchi, V. & Rampazzo, C. The Deoxynucleoside Triphosphate Triphosphohydrolase Activity of SAMHD1 Protein Contributes to the Mitochondrial DNA Depletion Associated with Genetic Deficiency of Deoxyguanosine Kinase. J Biol Chem 290, 25986-25996 (2015).
23. Riess, M. et al. Interferons Induce Expression of SAMHD1 in Monocytes through Down-regulation of miR-181a and miR-30a. J Biol Chem 292, 264-277 (2017).
24. Jang, S., Zhou, X. & Ahn, J. Substrate Specificity of SAMHD1 Triphosphohydrolase Activity Is Controlled by Deoxyribonucleoside Triphosphates and Phosphorylation at Thr592. Biochemistry 55, 5635-5646 (2016).
25. Clifford, R. et al. SAMHD1 is mutated recurrently in chronic lymphocytic leukemia and is involved in response to DNA damage. Blood 123, 1021-1031 (2014).
26. Wang, J. L., Lu, F. Z., Shen, X. Y., Wu, Y. & Zhao, L. T. SAMHD1 is down regulated in lung cancer by methylation and inhibits tumor cell proliferation. Biochem Biophys Res Commun 455, 229-233 (2014).
27. Hazra, S., Szewczak, A., Ort, S., Konrad, M. & Lavie, A. Post-translational phosphorylation of serine 74 of human deoxycytidine kinase favors the enzyme adopting the open conformation making it competent for nucleoside binding and release. Biochemistry 50, 2870-2880 (2011).
28. Beyaert, M., Starczewska, E., Van Den Neste, E. & Bontemps, F. A crucial role for ATR in the regulation of deoxycytidine kinase activity. Biochem Pharmacol 100, 40-50 (2016).
29. Nathanson, D. A. et al. Co-targeting of convergent nucleotide biosynthetic pathways for leukemia eradication. J Exp Med 211, 473-486 (2014).
30. Austin, W. R. et al. Nucleoside salvage pathway kinases regulate hematopoiesis by linking nucleotide metabolism with replication stress. J Exp Med 209, 2215-2228 (2012).
31. Diaz-Torné, C., Perez-Herrero, N. & Perez-Ruiz, F. New medications in development for the treatment of hyperuricemia of gout. Curr Opin Rheumatol 27, 164-169 (2015).

32. O'Neil, N. J., Bailey, M. L. & Hieter, P. Synthetic lethality and cancer. Nat Rev Genet 18, 613-623 (2017).
33. Helleday, T. The underlying mechanism for the PARP and BRCA synthetic lethality: clearing up the misunderstandings. Mol Oncol 5, 387-393 (2011).
34. Baldauf, H. M. et al. SAMHD1 restricts HIV-1 infection in resting CD4(+) T cells. Nat Med 18, 1682-1687 (2012).
35. Mei, L., Zhang, J., He, K. & Zhang, J. Ataxia telangiectasia and Rad3-related inhibitors and cancer therapy: where we stand. J Hematol Oncol 12, 43 (2019).
36. Kim, W. et al. [18F]CFA as a clinically translatable probe for PET imaging of deoxycytidine kinase activity. Proc Natl Acad Sci U S A 113, 4027-4032 (2016).
37. Goldstone, D. C. et al. HIV-1 restriction factor SAMHD1 is a deoxynucleoside triphosphate triphosphohydrolase. Nature 480, 379-382 (2011).
38. Coquel, F. et al. SAMHD1 acts at stalled replication forks to prevent interferon induction. Nature 557, 57-61 (2018).
39. Schneider, C. et al. SAMHD1 is a biomarker for cytarabine response and a therapeutic target in acute myeloid leukemia. Nat Med 23, 250-255 (2017).
40. Lee, J. T., Campbell, D. O., Satyamurthy, N., Czernin, J. & Radu, C. G. Stratification of nucleoside analog chemotherapy using 1-(2'-deoxy-2'-18F-fluoro-β-D-arabinofuranosyl)cytosine and 1-(2'-deoxy-2'-18F-fluoro-β-L-arabinofuranosyl)-5-methylcytosine PET. J Nucl Med 53, 275-280 (2012).

CHAPTER 5

A Metabolic Modifier Screen Reveals Secondary Targets of Protein Kinase Inhibitors Within Nucleotide Metabolism

ABSTRACT

Biosynthesis of the pyrimidine nucleotide uridine monophosphate (UMP) is essential for cell proliferation and is achieved by the activity of convergent *de novo* and salvage metabolic pathways. Here, we report the development and application of a cell-based metabolic modifier screening platform that leverages the redundancy in pyrimidine metabolism for the discovery of selective UMP biosynthesis modulators. In evaluating a library of protein kinase inhibitors we identified multiple compounds with previously uncharacterized nucleotide metabolism-modifying activity. The JNK inhibitor JNK-IN-8 was found to potently inhibit nucleoside transport,. The PDK1 inhibitor OSU-03012 (also known as AR-12) and the RAF inhibitor TAK-632 were shown to inhibit the therapeutically-relevant enzyme dihydroorotate dehydrogenase (DHODH) and their affinities were unambiguously confirmed through *in vitro* assays and co-crystallization with human DHODH.

INTRODUCTION

The redundant and plastic nature of metabolic networks represents a significant obstacle in the targeting of cancer metabolism. This redundancy manifests in two ways; the first is the expression of multiple enzymes that perform identical biochemical reactions, such as the hexokinase isozymes which each phosphorylate glucose[1]; the second is the existence of convergent metabolic pathways that produce a common metabolite from unique precursors. Such convergent metabolic nodes have been noted in nucleotide[2], lipid (cholesterol)[3] and amino acid (aspartate) metabolism[4].

Despite these difficulties, the development of metabolism modifiers remains a robust area of research. One such therapeutically relevant target is pyrimidine nucleotide biosynthesis which consists of nucleoside salvage (NSP) and *de novo* (DNP) pathways which converge to generate uridine monophosphate (UMP), the common precursor for all pyrimidine nucleotides[5]. The NSP salvages uridine from the extracellular environment, shuttling it into the cell via nucleoside transporters where they are phosphorylated by uridine-cytidine kinases (UCKs) to produce UMP. UCK2 is thought to be the primary NSP kinase, given its 20-fold higher catalytic efficiency compared to UCK1[6]. The DNP is a six-step process that utilizes glutamine, aspartate, bicarbonate and glucose to produce UMP through the action of 3 enzymes: trifunctional CAD, electron transport chain-linked dihydroorotate dehydrogenase (DHODH), and bifunctional UMP synthase (UMPS). Among DNP enzymes, DHODH in particular has emerged as a therapeutic target in multiple cancers including pancreatic ductal adenocarcinoma (PDAC)[7–9]. Additionally, over 90 patent applications involving DHODH inhibition have been filed in the last decade[10].

In this study, we show that the pyrimidine NSP and DNP are interchangeable in their ability to sustain cancer cell proliferation and that a synthetic lethal phenotype can be achieved through their simultaneous inhibition. We leverage this observation to construct a metabolic modifier screen that allows for the identification of selective modulators of NSP and DNP pathways. In screening a library of protein kinase inhibitors, we found that the c-Jun N-terminal kinase (JNK)

inhibitor JNK-IN-8 is a potent inhibitor of uridine transport which is vital for NSP function, and that the 3-phosphoinositide-dependent protein kinase 1 (PDK1) inhibitor OSU-03012 (also known as AR-12) and the pan-RAF inhibitor TAK-632 both bind and inhibit the pyrimidine DNP enzyme DHODH.

RESULTS

Design of a differential metabolic modifier screen for identification of novel modulators of pyrimidine nucleotide metabolism

While the UMP-DNP and -NSP are interchangeable in their ability to sustain cell proliferation, their relative activity at baseline (when both pathways are functional) is poorly defined. *De novo* pyrimidine biosynthesis is allosterically inactivated by its end product, UTP, which is also produced by the uridine (rU) NSP. This allosteric control functions at the level of the CPSase activity of the tri-functional metabolic enzyme CAD, which performs the first committed step in *de novo* pyrimidine biosynthesis (**Figure S5.1A**)[12]. To quantitatively evaluate the discrete activities of the pyrimidine *de novo* and salvage pathways, we modified and applied a LC-MS/MS assay previously used by our group to track the contribution of stable isotope-labeled glucose and deoxycytidine to newly replicated DNA[2]. In this assay, cells are cultured in the presence of [$^{13}C_6$]glucose (to track DNP activity) and 10 μM [$^{13}C_9$; $^{15}N_2$]rU (to track NSP activity). Their DNA is then extracted and hydrolyzed and the abundance of stable isotope-labeled nucleosides is evaluated using LC-MS/MS in the multiple reaction monitoring (MRM) mode (**Figure S5.1B**). We applied this assay to a panel of cancer cell lines and observed a heterogenous degree of total labeling ([$^{13}C_6$]glucose + [$^{13}C_9$; $^{15}N_2$]rU) in the deoxycytidine compartment of DNA (DNA-C) after 24 h (**Figure S5.1C**). Consistent with the aforementioned model in which UTP produced by uridine savage allosterically impairs *de novo* biosynthesis, we found that the fractional contribution of [$^{13}C_9$; $^{15}N_2$]rU exceeded that of [$^{13}C_6$]glucose in all models tested (**Figure S5.1D**). Interestingly, we found heterogeneity in the relative contribution of [$^{13}C_6$]glucose and [$^{13}C_9$; $^{15}N_2$]rU to DNA-C across the cell line panel, which likely reflects differential expression or regulation of the various transporters, kinases, nucleotidases, and phosphorylases involved in rU salvage. Importantly, we confirmed that the contribution of [$^{13}C_6$]glucose to DNA-C could be blocked by NITD-982, an established DHODH inhibitor, and likewise the contribution of [$^{13}C_9$; $^{15}N_2$]rU could be prevented by the FDA-approved nucleoside transport inhibitor dipyridamole (DPA; **Figure S5.1E**)[35]. Collectively, these results indicate that,

under the conditions tested, both the UMP-DNP and -NSP pathways are simultaneously, but not equally, active.

While redundant routes for UMP biosynthesis can complicate targeting, impaired proliferation resulting from simultaneous restriction of both *de novo* (DNP) and salvage (NSP) pathways can be used to identify selective modifiers of either NSP or DNP pathway activity (**Figure S5.1F**). A metabolic modifier screen was developed for the discovery of small molecule modulators of UMP production by leveraging this biosynthetic redundancy. This cell-based screening platform concurrently tests the effects of small molecule compounds on the proliferation of cells in baseline (both NSP and DNP active), NSP-only, and DNP-only conditions (**Figure 5.1A**). Molecules which inhibit proliferation in baseline conditions are classified as non-specific inhibitors. Those which inhibit proliferation in NSP-only conditions are NSP inhibitors, while those that inhibit growth in DNP-only conditions are DNP inhibitors. The screen design was validated using the known DHODH inhibitor NITD-982 and the FDA-approved nucleoside transport inhibitor dipyridamole (DPA), using Cell Titer Glo (CTG) to evaluate proliferation impairment (**Figure S5.1G**)[11].

Cancer cell lines exhibited varying degrees of sensitivity to DHODH inhibition (as determined by doubling-time-normalized proliferation inhibition) and were all rescued by rU supplementation (**Figure S5.2**)[13]. MIAPACA2 PDAC cells were utilized in the screen due to their ability to maintain baseline proliferation levels in NSP-only or DNP-only conditions, while also exhibiting a significant decrease in proliferation upon simultaneous NSP and DNP inhibition (**Figure S5.3A**). A library of 430 protein kinase inhibitors was chosen for evaluation, the rationale being twofold. First, we hypothesized that our synthetic lethality screen may identify compounds that indirectly target pyrimidine metabolism through regulatory signal transduction pathway inhibition. Second, because a substantial fraction of kinase inhibitors are ATP-mimetics, thus resembling nucleotides, we predicted that protein kinase inhibitors may posses secondary, non-canonical targets within nucleotide metabolism. Consistently, several protein kinase inhibitors, specifically

those exhibiting similarities with the phenylamino pyrimidine (PAP) imatinib scaffold, and a subset of p38 MAPK inhibitors, exhibit activity against nucleoside transporters[14,15]. This kinase inhibitor library was screened at 7-point dose response in duplicate. Composite NSP and DNP pathway selectivity scores were calculated for each compound as the sum of condition-specific anti-proliferative effects across the dose range (**Figure S5.3B**). Phenotypic screen quality was monitored using the Z-factor metric (**Figure S5.3C**)[16].

The JNK inhibitor JNK-IN-8, the BTK inhibitor CNX-774, and the VEGFR inhibitor AMG-706 were active in the NSP-only condition, exhibiting positive NSP-selectivity scores (**Figure 5.1B**). The selectivity of these hits for the NSP was unique among inhibitors of JNK (**Figure 5.1C**), BTK, and VEGFR (**Figures S5.3D, S5.3F**), indicating this phenotype likely did not result from on-target effects. The PDK1 inhibitor OSU-03012 (also known as AR-12) and the pan-RAF inhibitor TAK-632 elicited potent and selective inhibition of proliferation in the DNP-only condition (**Figure 5.1D**)[17,18]. Among the four PDK1 inhibitors and 14 RAF inhibitors tested, OSU-03012 and TAK-632 were unique in their ability to selectively inhibit the DNP, suggesting that their ability to inhibit the pyrimidine DNP was not the consequence of on-target effects (**Figures 5.1E, 5.1F**).

Microplate immunofluorescence microscopy nuclei scoring analysis of MIAPACA2 cells stained with Hoechst 33342 was performed as an orthogonal approach to validate the screen hits. These studies confirmed the culture-condition selectivity of our hits and validated the results of the CTG-based screen (**Figures S5.3G, 5.H**). Additionally, we performed trypan-blue exclusion cell scoring in a second cancer cell line, JURKAT, to confirm hit selectivity (**Figure 5.3J**).

In addition to its non-redundant role in *de novo* pyrimidine nucleotide biosynthesis, DHODH functions as an electron donor in the mitochondrial electron transport chain[19]. To exclude the possibility that the selective activity of JNK-IN-8 reflects an interaction with NITD-982 at the level of electron transport chain modulation, we synthesized and evaluated N-phosphonacetyl-L-aspartate (PALA), an inhibitor of CAD which functions upstream of DHODH[20,21]. We determined

that JNK-IN-8 inhibits JURKAT cell proliferation when both PALA and rU are present in the culture media, supporting that its selective activity results from the inhibition of uridine salvage (**Figure S5.4A**).

We next applied our LC-MS/MS stable isotope tracking approach to evaluate the impact of JNK-IN-8, OSU-03012, and TAK-632 on the incorporation of [$^{13}C_6$]glucose and [$^{13}C_9$; $^{15}N_2$]rU into newly replicated DNA (**Figure 5.1I**). In MIAPACA2 cells, we found that JNK-IN-8 blocked the NSP contribution while triggering a compensatory upregulation of the DNP. Conversely, OSU-03012 and TAK-632 selectively impaired DNP contribution(**Figure 5.1J**). Similar selectivity was observed in JURKAT cells, where both OSU-03012 and TAK-632 blocked the DNP while inducing compensatory up-regulation of NSP activity (**Figure 5.1K**).

JNK-IN-8 inhibits nucleoside uptake

While three protein kinase inhibitors were identified as selective inhibitors of the pyrimidine NSP, JNK-IN-8 was exceptionally potent with IC_{50} values in the low nanomolar range. We reasoned that the activity of JNK-IN-8 could arise from the inhibition of nucleoside shuttling across the plasma membrane, which is achieved by concentrative (CNT) or equilibrative (ENT) nucleoside transporters, or the inhibition of pyrimidine nucleoside phosphorylation by UCKs. To determine the level at which JNK-IN-8 is active, we determined the effects of JNK-IN-8 on the uptake of a panel of ^{3}H-labeled purine (dA, dG) and pyrimidine nucleosides (rU, dC) in MIAPACA2 cells. These nucleosides rely upon the same equilibrative transporters (ENT1/2) to enter the cell but require different kinases (UCKs in the case of rU and deoxycytidine kinase in the case of dC, dA and dG) for conversion into their respective monophosphate forms and resultant intracellular accumulation (**Figure 5.2A**)[2]. We found that JNK-IN-8 prevented the uptake of all nucleosides tested, but exhibited greater potency toward rU and dC. Importantly, JNK-IN-8 exhibits a selectivity pattern similar to the established ENT1 inhibitor DPA (**Figures 5.2B, S5.4B**). We confirmed JNK-IN-8 inhibited the uptake of both rU and dC with similar potency (33 nM and 31

nM, respectively), further suggesting that the compound inhibits nucleoside transport (**Figure S5.4C**). Additionally, JNK-IN-8 treatment prevented the anti-proliferative effects of gemcitabine, a dCK-dependent nucleoside analog prodrug which relies upon transporters to enter the cell, with an EC_{50} of 15.2 nM (**Figure S5.4D**). A similar pattern of dA, dG, rU and dC uptake inhibition was observed in a second cell line the murine pancreatic cancer model KP4662(**Figures S5.4E, S5.4F**)[22].

7 nucleoside transporters have been described and categorized into 2 families. Concentrative nucleoside transporters (CNT1-3; SLC28A1-3) are unidirectional inward transporters which co-transport Na^+. Equilibrative nucleoside transporters (ENT1-4; SLC29A1-4) are bidirectional, energy-independent, and accept a broad range of purine and pyrimidine nucleosides. We evaluated the expression of these transporters in MIAPACA2 and JURKAT cells and found that ENT1 (SLC29A1) is the predominantly expressed transporter in both models (**Figure S5.4G**)[23]. ENT1 is an established transporter of a variety of nucleosides including natural purine and pyrimidine nucleosides as well as therapeutic analogs such as gemcitabine. We next utilized the cellular thermal shift assay (CETSA), an approach that leverages the altered thermostability of proteins following ligand binding, to confirm ENT1 engagement by JNK-IN-8 (**Figure S5.4H**)[24]. Collectively, these results indicate the JNK-IN-8 inhibits UMP-NSP activity by interfering with the transport of rU.

OSU-03012 and TAK-632 target *de novo* UMP biosynthesis and activate the DNA replication stress response pathway

Two kinase inhibitors, TAK-632 and OSU-03012, were identified as potent and selective inhibitors of MIAPACA2 proliferation cultured in the DNP-only condition (**Figure S5.4J**). We reasoned that these compounds could inhibit *de novo* pyrimidine biosynthesis by targeting either CAD, DHODH, or UMPS (**Figure 5.3A**). Both OSU-03012 and TAK-632 induced S-phase arrest in MIAPACA2 cells, a phenotype associated with insufficient dNTP biosynthesis to sustain

DNA replication and activation of intra-S phase signaling checkpoints. This effect was rescued by orotate (the product of DHODH) supplementation and could be completely reversed by rU supplementation (**Figures 5.3B, 5.3C**). DHODH inhibition emerged as a likely mechanism, as it catalyzes one of three committed steps within the DNP and is a druggable protein[7]. Additionally, both OSU-03012 and TAK-632 posses fluorine substituents which have been shown to stabilize bioactive conformations of DHODH inhibitors [26]. In an *in vitro* colorimetric recombinant human DHODH activity assay, TAK-632 and OSU-03012 both inhibited DHODH activity in a dose-dependent manner (**Figure 5.3D**). Importantly, the response to TAK-632 or OSU-03012 correlated with the response to a known DHODH inhibitor in this cell line panel (**Figure 5.3E**).

OSU-03012 was recently reported to synergize with replication stress response kinase inhibitors in RSK-subtype mutant KRAS cancer models[27]. However, after confirming that OSU-03012 binds DHODH, we hypothesized that the observed synergy resulted from DHODH inhibition rather than PDK1 inhibition. Immunoblot analysis of S6K and S6 phosphorylation, PDK1 downstream targets, confirmed that GSK-2334470, a known PDK1 inhibitor, potently blocked PDK1 while OSU-03012 triggered S345 CHEK1 phosphorylation, a replication stress biomarker, only in the absence of rU (**Figure 5.3F**). Similarly, TAK-632 only triggered CHEK1 phosphorylation in the absence of rU whereas an established pan-RAF inhibitor, LY3009120 which does not exhibit paradoxical activation, down-regulated ERK1/2 phosphorylation but had no impact on CHEK1 phosphorylation (**Figure 5.3G**)[28]. Consistently, we found that neither GSK-2334470 or LY3009120 induced S-phase arrest at doses where we observed down-regulation of their target substrates whereas a known DHODH inhibitor induced potent S-phase accumulation that was completely reversed by rU (**Figures 5.S4J, 5.S4K**). To compliment our evaluation of replication stress response biomarker induction we performed an assessment DNA damage induced by OSU-03012, TAK-632 and the ATR inhibitor VE-822 as a positive control using γ-H2A.X flow cytometry. We found that while OSU-03012 and TAK-632 trigger activation of the replication stress response they do not significantly induce γ-H2A.X. We hypothesize that activation of the replication stress response pathway by OSU-03012 or

TAK-632 limits DNA double-strand breaks by preventing the collapse of stalled replication forks (**Figure. S5.4L**)[29].

To investigate the interaction between OSU-03012 and replication stress response inhibitors we treated MIAPACA2 cells VE-822, an inhibitor of the proximal replication stress response kinase ATR, and either OSU-03012 or GSK-2334470 for 72 h. A synergistic increase in cell death was observed when OSU-03012 and an ATR inhibitor were combined, whereas the combination of GSK-2334470 and VE-822 demonstrated only a nominal increase in cell death as determined by AnnexinV/PI flow cytometry (**Figure 5.3H**). Taken together, these data indicate that replication stress triggered by OSU-03012 is the consequence of DHODH inhibition rather than inhibition of its canonical target.

Co-crystal structures of OSU-03012 and TAK-632 in complex with human DHODH

To determine the molecular interactions between the protein and its putative inhibitors, complete DHODH co-crystallization data sets were obtained and processed to 1.4 Å and 2.7 Å for OSU-03012 and TAK-632, respectively (**Figure 5.6**). Both compounds bind in a hydrophobic channel composed by two N-domain α-helices through which ubiquinone travels, a mechanism consistent with previously identified DHODH inhibitors[30]. A long-range hydrogen bond between Arg 69 and OSU-03012 helps orient the molecule to the hydrophobic pocket where the phenanthrene moiety inserts, while the remainder of the molecule lies on the outer surface of DHODH, blocking the hydrophobic channel (**Figures 5.4A, 5.S4A**). Three hydrogen bonds stabilize TAK-632 in the same hydrophobic pocket: two with Tyr 37 and Leu 66 help stabilize the inhibitor at the opening of the channel, while a third with Gln 46 helps pull the inhibitor deep into the pocket (**Figures 5.4B, 5.S4B**).

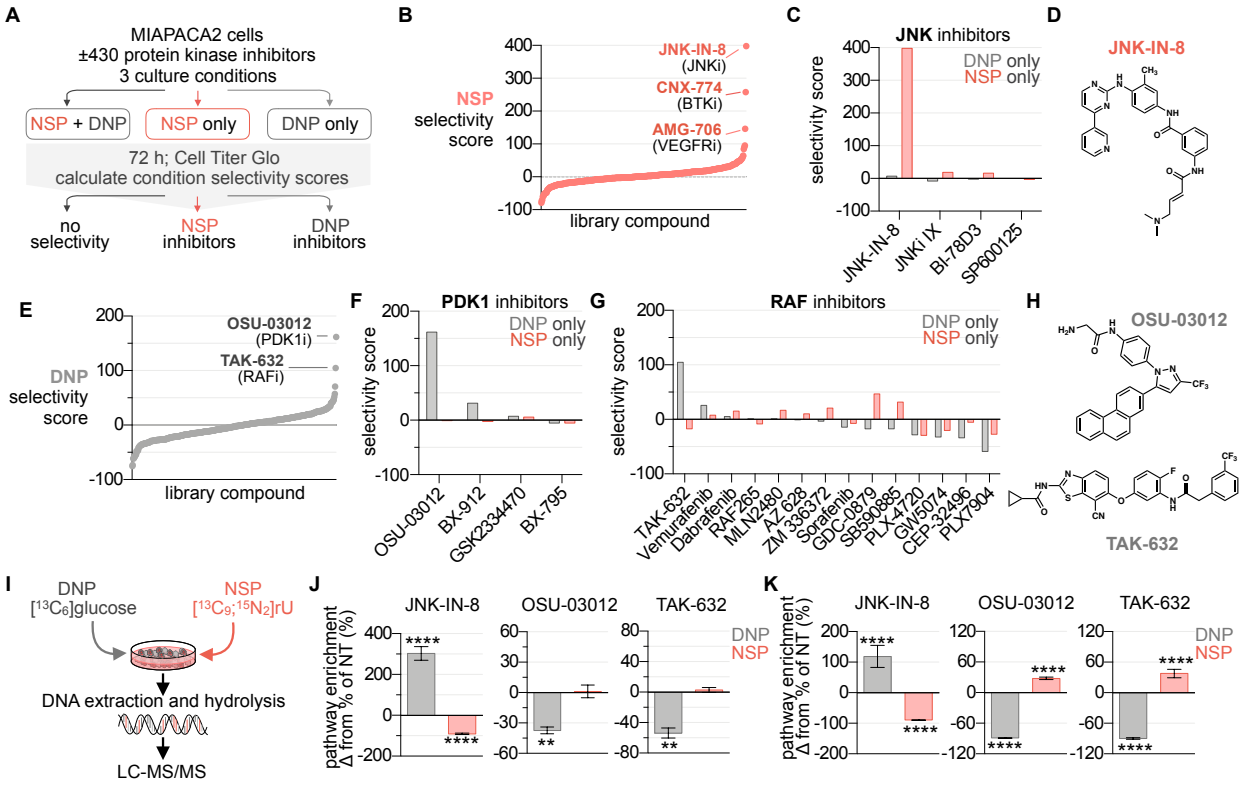

Figure 5.1 | Identification of UMP-NSP and -DNP modulators in a small molecule protein kinase inhibitor library. (**A**) Phenotypic screening strategy. The impact of 430 protein kinase inhibitors on cell proliferation was evaluated in MIAPACA2 cells plated in 3 distinct growth conditions; 1) NSP+DNP (media +10 μM uridine (rU)); 2) NSP only (media +10 μM rU +1 μM NITD-982); or 3) DNP only (media alone). % proliferation values were calculated using Cell Titer Glo (CTG) following 72 h treatment (7-point dose response; n=2). (**B**) Waterfall plot ranking library compounds based on NSP pathway selectivity score. (**C**) Summary of NSP and DNP selectivity scores across library compounds annotated as JNK inhibitors. (**D**) Structure of JNK-IN-8. (**E**) Waterfall plot ranking library compounds based on DNP pathway selectivity score. (**F,G**) Summary of NSP and DNP selectivity scores across library compounds annotated as PDK1 (**F**) or RAF inhibitors (**G**). (**H**) Structures OSU-03012 and TAK-632. (**I**) Experimental design to track contribution of UMP-DNP and -NSP using newly replicated DNA using stable isotope labeled metabolite tracers. (**J,K**) LC-MS/MS analysis of [$^{13}C_6$]glucose (5.5 mM) and

[$^{13}C_9$; $^{15}N_2$] rU (10 μM) utilization for DNA-C replication in MIAPACA2 (**J**) or JURKAT (**K**) cells treated +1 μM JNK-IN-8 +5 μM OSU-03012 or +5 μM TAK-632 for 24 h (mean±SD; n=3; unpaired T-test; ** P < 0.01, **** P < 0.0001).

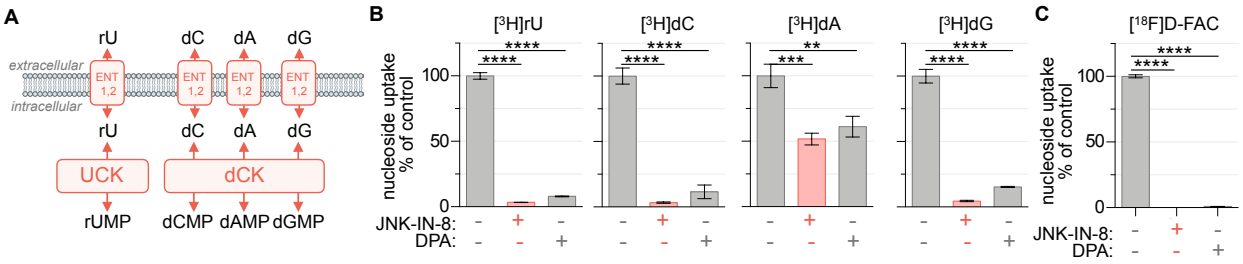

Figure 5.2 | JNK-IN-8 inhibits nucleoside transport *in vitro*. (**A**) Nucleoside uptake can be prevented by inhibition of either nucleoside transporters or kinases. (**B**) Uptake of [3H]rU, [3H]dC, [3H]dA (+ 10 μM dCF), [3H]dG (+1 μM BCX-1777) in MIAPACA2 cells following 2 h incubation ± 1 μM JNK-IN-8 or 1 μM dipyridamole (DPA; 18.5 kBq; mean±SD; n=3; one-way ANOVA corrected for multiple comparisons by Bonferroni adjustment; ** P<0.01; *** P<0.001; **** P<0.0001). (**C**) Uptake of [18F]D-FAC, in CCRF-CEM cells following 2 h incubation ± 1 μM JNK-IN-8 or 1 μM DPA (18.5 kBq; mean±SD; n=3; one-way ANOVA corrected for multiple comparisons by Bonferroni adjustment; **** P<0.0001).

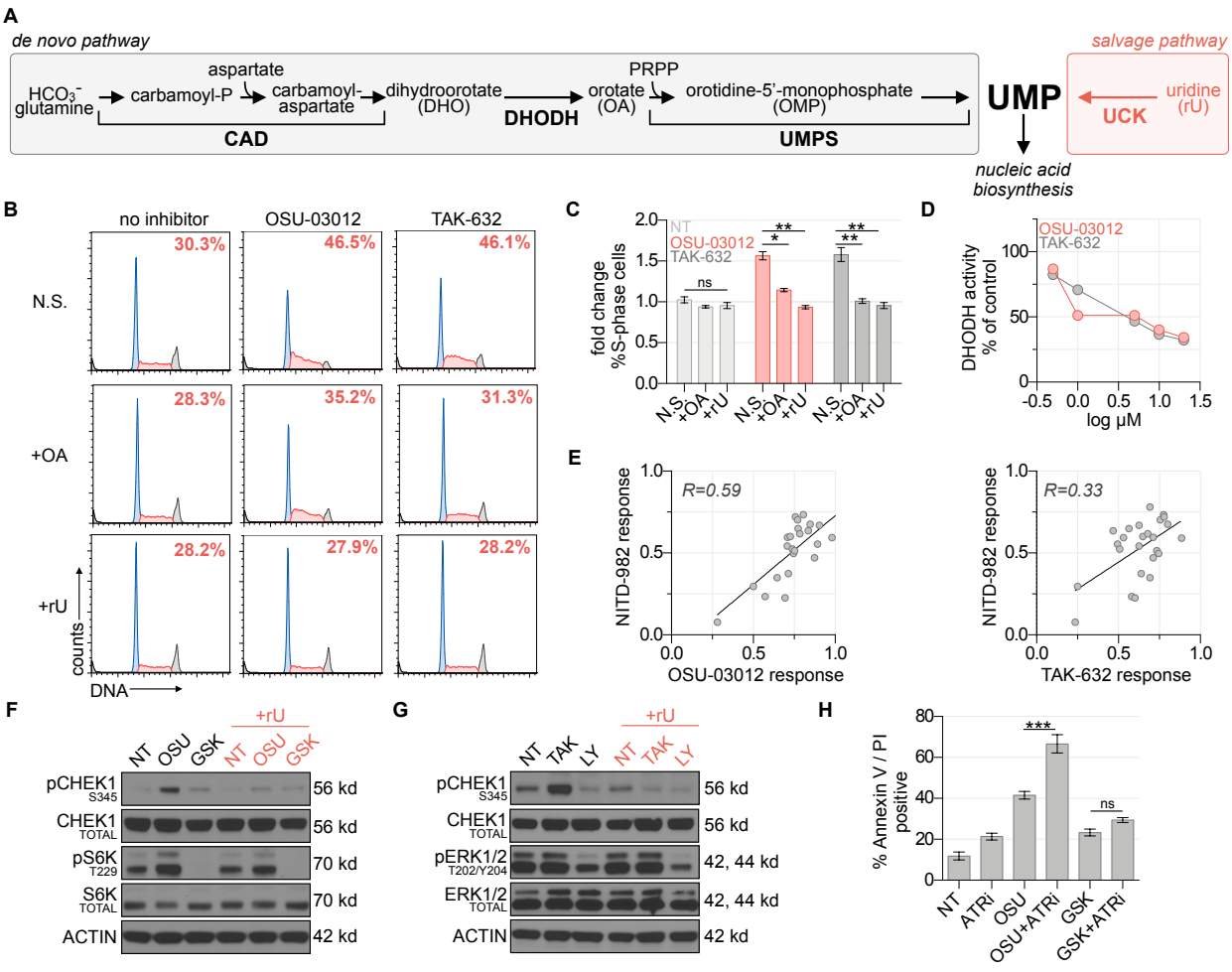

Figure 5.3 | OSU-03012 and TAK-632 inhibit DHODH and activate the DNA replication stress response pathway. (**A**) UMP biosynthesis via the *de novo* and salvage pathways. (**B**) Propidium iodide cell cycle analysis of MIAPACA2 PDAC cells treated ±5 µM TAK-632 or ±5 µM OSU-03012 and supplemented with 50 µM orotate (OA) or 10 µM rU (N.S.: no supplement). Insert indicates % S-phase cells. (**C**) Summary of fold changes in S-phase cells from **B** (mean±SD; n=2; one-way ANOVA corrected for multiple comparisons by Bonferroni adjustment, ns: not significant; * P<0.05; ** P<0.01). (**D**) *in vitro* DHODH enzyme assay performed in the presence of OSU-03012 or TAK-632. (**E**) Correlation between DHODH inhibitor (1 µM NITD-982) and OSU-03012 (3.17 µM) or TAK-632 (3.17 µM) response across a panel of 25 PDAC cell lines determined using CTG following 72 h treatment. Response calculated as doubling time normalized proliferation inhibition. Pearson correlation coefficient is indicated. (**F**) Immunoblot analysis of MIAPACA2 cells treated ±1 µM PDK1 inhibitor GSK-2334470 (GSK) ±1

μM OSU-03012 (OSU) ±10 μM rU for 24 h. (**G**) Immunoblot analysis of MIAPACA2 cells treated ±10 μM RAF inhibitor LY3009120 (LY) ±10 μM TAK-632 (TAK) ±10 μM rU for 24 h. (**H**) Annexin V/PI flow cytometry analysis of MIAPACA2 PDAC cells treated ±1 μM OSU-03012 or 1 μM GSK-2334470 (GSK) ±500 nM VE-822 (ATRi) ±25 μM rU for 72 h (mean±SD; n=2; one-way ANOVA corrected for multiple comparisons by Bonferroni adjustment; ns: not significant; ** P<0.01; *** P<0.001).

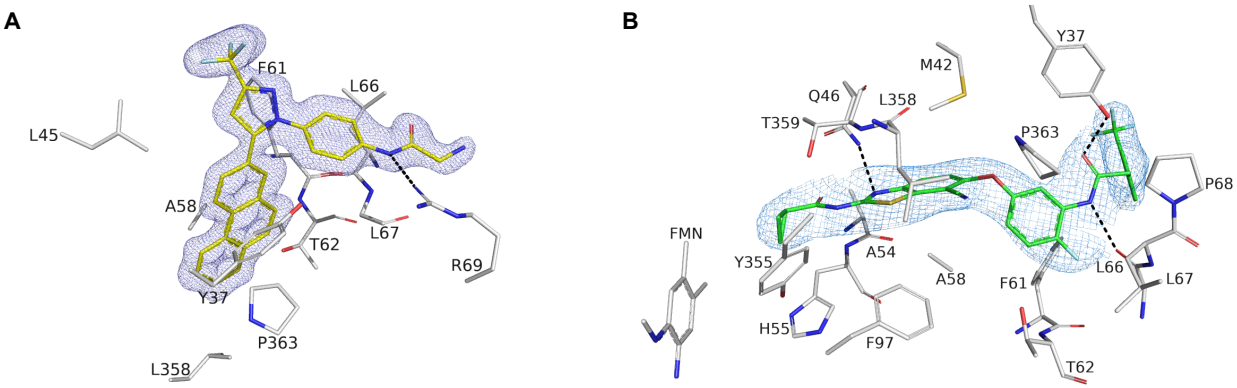

Figure 5.4 | OSU-03012 and TAK-632 bind DHODH. (**A,B**) Crystal Structure of DHODH with compounds OSU-03012 (**A**) or TAK-632 (**B**). 2mFo-DFc electron density for OSU-03012 (carbons in yellow) or TAK-632 (carbons in green) contoured at 1 σ. Dashed black lines represent hydrogen bonds between the ligands and DHODH. Interacting residues as predicted by LigPlot+ are shown and labeled.

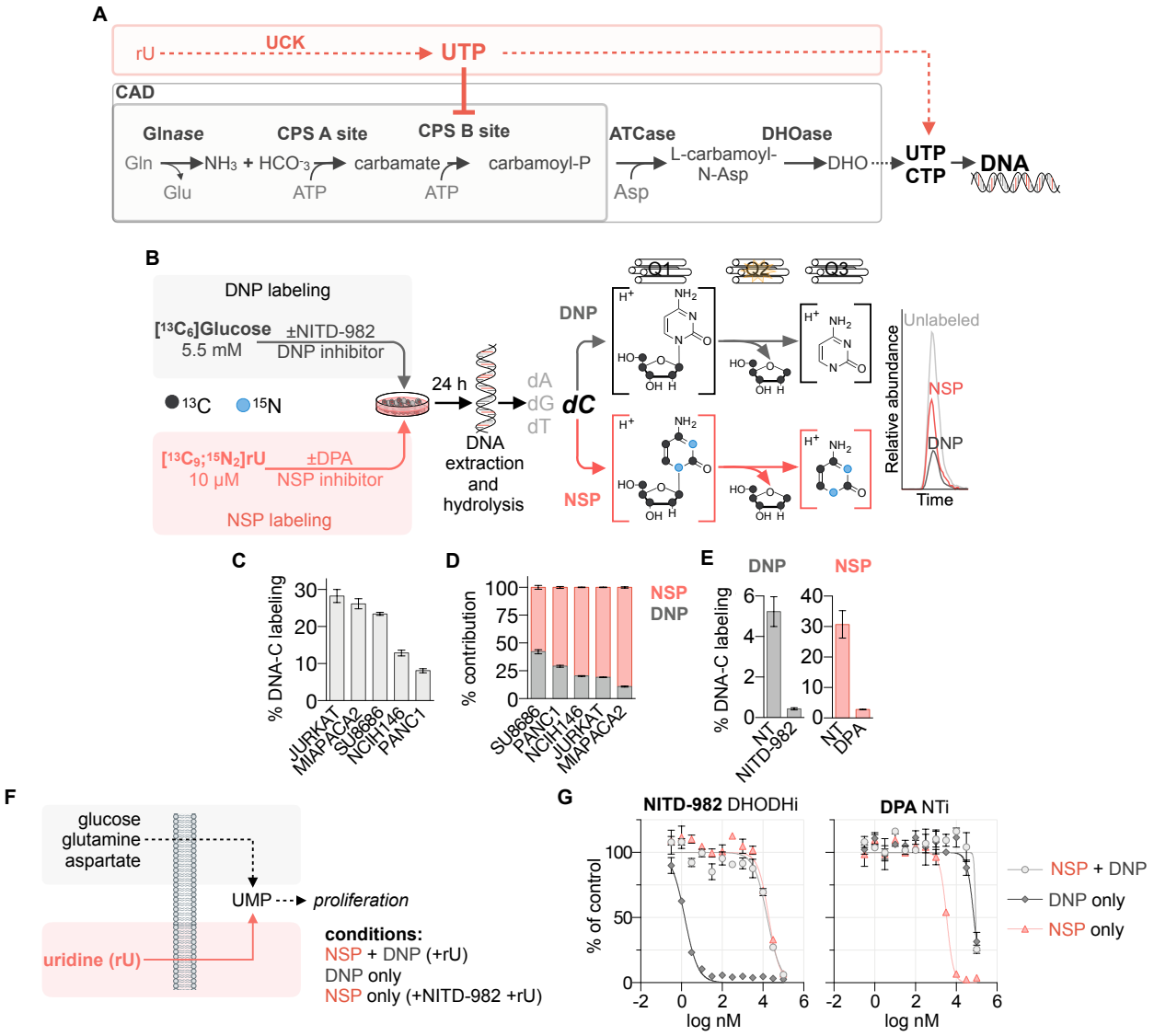

Figure S5.1 | Validation of UMP as a critical, convergent metabolic node in cancer cells.

(**A**) Schematic of CAD regulation by NSP produced UTP. (**B**) Schematic of the LC-MS/MS methodology used to determine the fractional contribution of UMP-DNP or -NSP specific stable isotope-labeled metabolite tracers to deoxycytidine (dC) in DNA (DNA-C). (**C**) Total % DNA-C labeling ([$^{13}C_6$]glucose + [$^{13}C_9$; $^{15}N_2$]uridine (rU) contribution) across a panel of cancer cell lines cultured for 24 h determined by LC-MS/MS. (**D**) Relative contribution of DNP and NSP pathways to DNA biosynthesis as determined by LC-MS/MS following 24 h treatment (n=3). % contribution values are normalized to total % labeling in **E**. (**E**) LC-MS/MS analysis DNP([$^{13}C_6$]glucose) and NSP([$^{13}C_9$; $^{15}N_2$]rU) contribution to DNA-C in JURKAT cells cultured for 24 h in media containing

5.5 mM [$^{13}C_6$]glucose and 10 μM [$^{13}C_9$; $^{15}N_2$]rU treated ±1 μM NITD-982 or ±1 μM dipyridamole (DPA; mean±SD; n=3). (**F**) UMP can be produced by a *de novo* pathway (DNP) from glucose, glutamine, bicarbonate and aspartate or from extracellular rU by a nucleoside transporter and kinase-dependent salvage pathway (NSP). (**G**) Dose response curves of DHODH inhibitor NITD-982 and nucleoside transport inhibitor (NTi) dipyridamole (DPA) in JURKAT cells cultured in NSP+DNP (media +10 μM rU), NSP only (media +10 μM rU +1 μM NITD-982), or DNP only (media alone) for 72 h as determined by Cell Titer Glo (mean±SD; n=4).

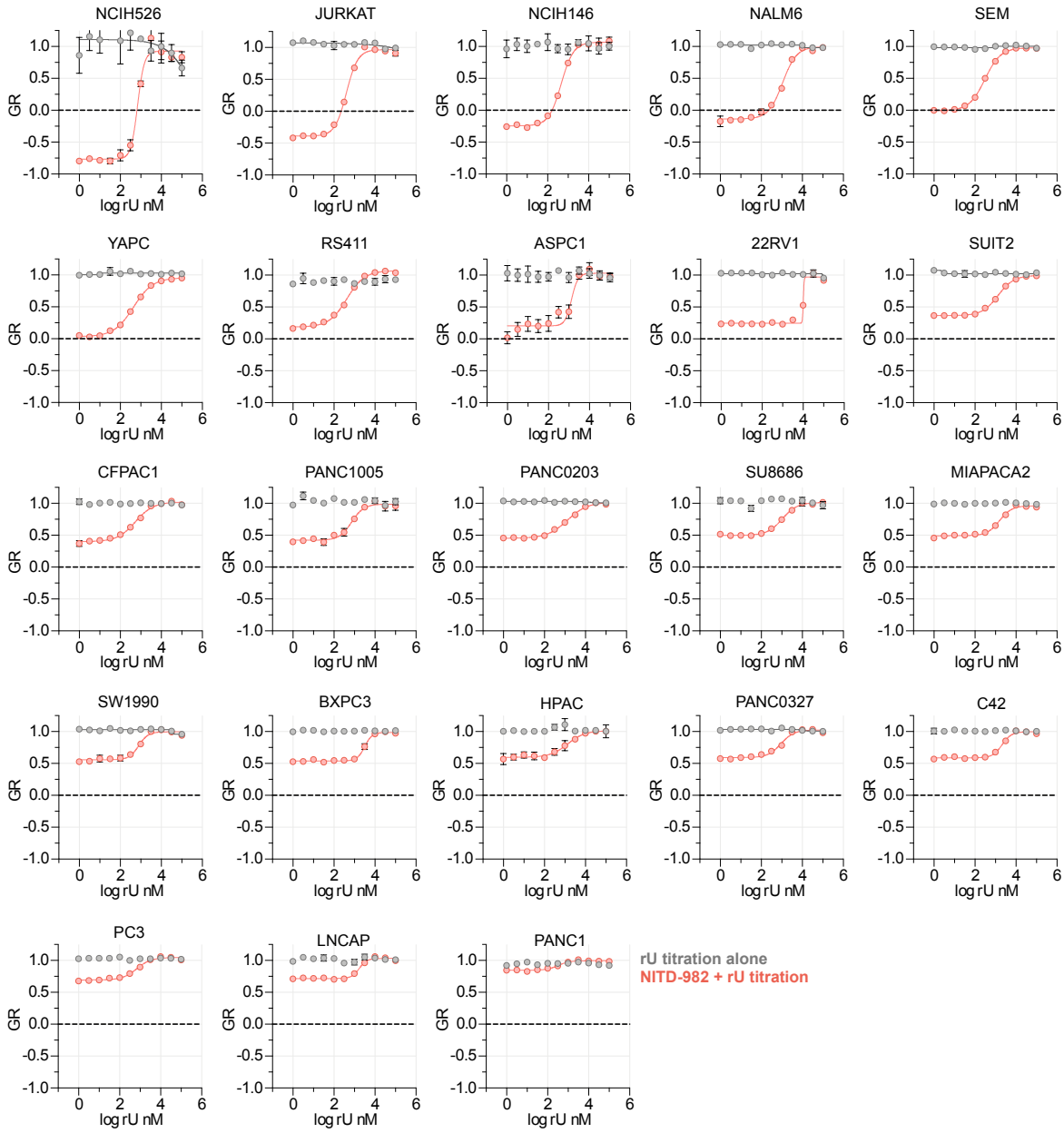

Figure S5.2 | UMP-DNP and NSP are interchangeable in sustaining proliferation across a panel of cancer cell lines. Uridine titration in cancer cell lines cultured in media + 10% dFBS ±1 μM NITD-982 (mean±SD; n=4). Relative proliferation rate (GR) was calculated by normalizing % proliferation values at 72 h to cell line proliferation rate. Proliferation rates were calculated utilizing CTG measurements at the time of treatment and vehicle-treated controls at 72 h.

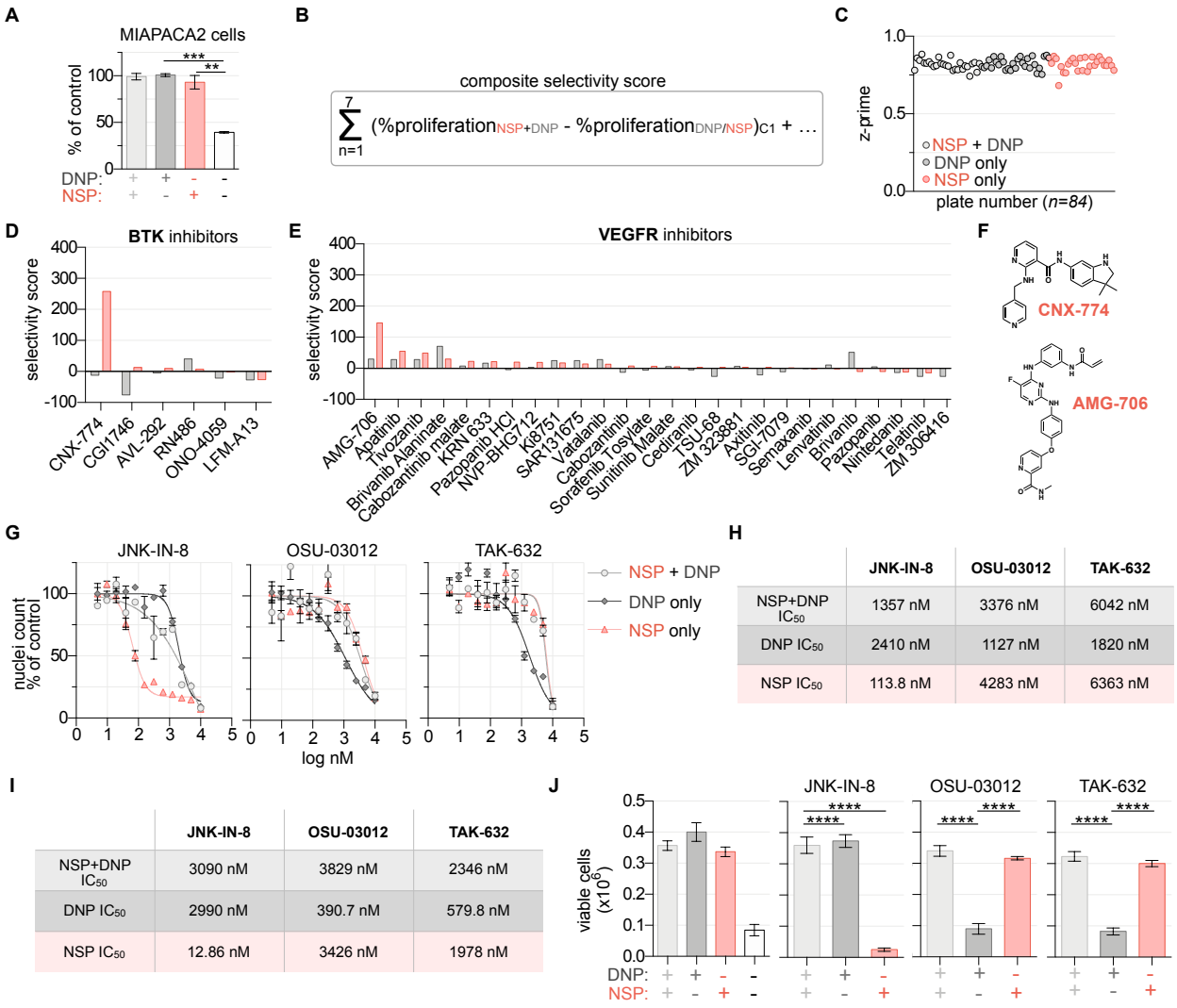

	JNK-IN-8	OSU-03012	TAK-632
NSP+DNP IC_{50}	1357 nM	3376 nM	6042 nM
DNP IC_{50}	2410 nM	1127 nM	1820 nM
NSP IC_{50}	113.8 nM	4283 nM	6363 nM

	JNK-IN-8	OSU-03012	TAK-632
NSP+DNP IC_{50}	3090 nM	3829 nM	2346 nM
DNP IC_{50}	2990 nM	390.7 nM	579.8 nM
NSP IC_{50}	12.86 nM	3426 nM	1978 nM

Figure S5.3 | Evaluation of UMP-NSP and -DNP inhibitor potency and selectivity. (**A**) Cell Titer Glo analysis of MIAPACA2 cells cultured in NSP+DNP (media +10 μM rU), DNP (media alone), NSP (media +10 μM rU +1 μM NITD-982) or starvation conditions (media + 1 μM NITD-982) for 72 h (mean±SD; n=4; one-way ANOVA corrected for multiple comparisons by Bonferroni adjustment, ** P < 0.01; *** P < 0.001) (**B**) Methodology applied to determine UMP-DNP and -NSP selectivity scores (n=2). (**C**) Z'-scores calculated for individual assay plates from experiment in **Figure 5.1**. (**D**) Selectivity scores for BTK inhibitors included in the screen. (**E**) Selectivity scores for VEGFR inhibitors included in the screen. (**F**) Structures of hit compounds. (**G**) Immuno-fluorescence microscopy nuclei counts of MIAPACA2 cells stained with Hoechst 33342 cultured in NSP+DNP (media +10 μM rU), DNP only (media alone) or NSP only (media

+10 μM rU +1 μM NITD-982) conditions for 72 h (mean±SD; n=4). (**H**) Calculation of IC_{50} values from experiment in **G**. (**I**) Calculation of JNK-IN-8, OSU-03012 and TAK-632 IC_{50} in JURKAT cells treated for 72 h determined using Cell Titer Glo. (**J**) JURKAT cell counts using trypan-blue exclusion following treatment ±100 nM JNK-IN-8 ±1 μM OSU-03012 ±1 μM TAK-632 for 72 h (mean±SD; n=4; one-way ANOVA corrected for multiple comparisons by Bonferroni adjustment,**** $P < 0.0001$).

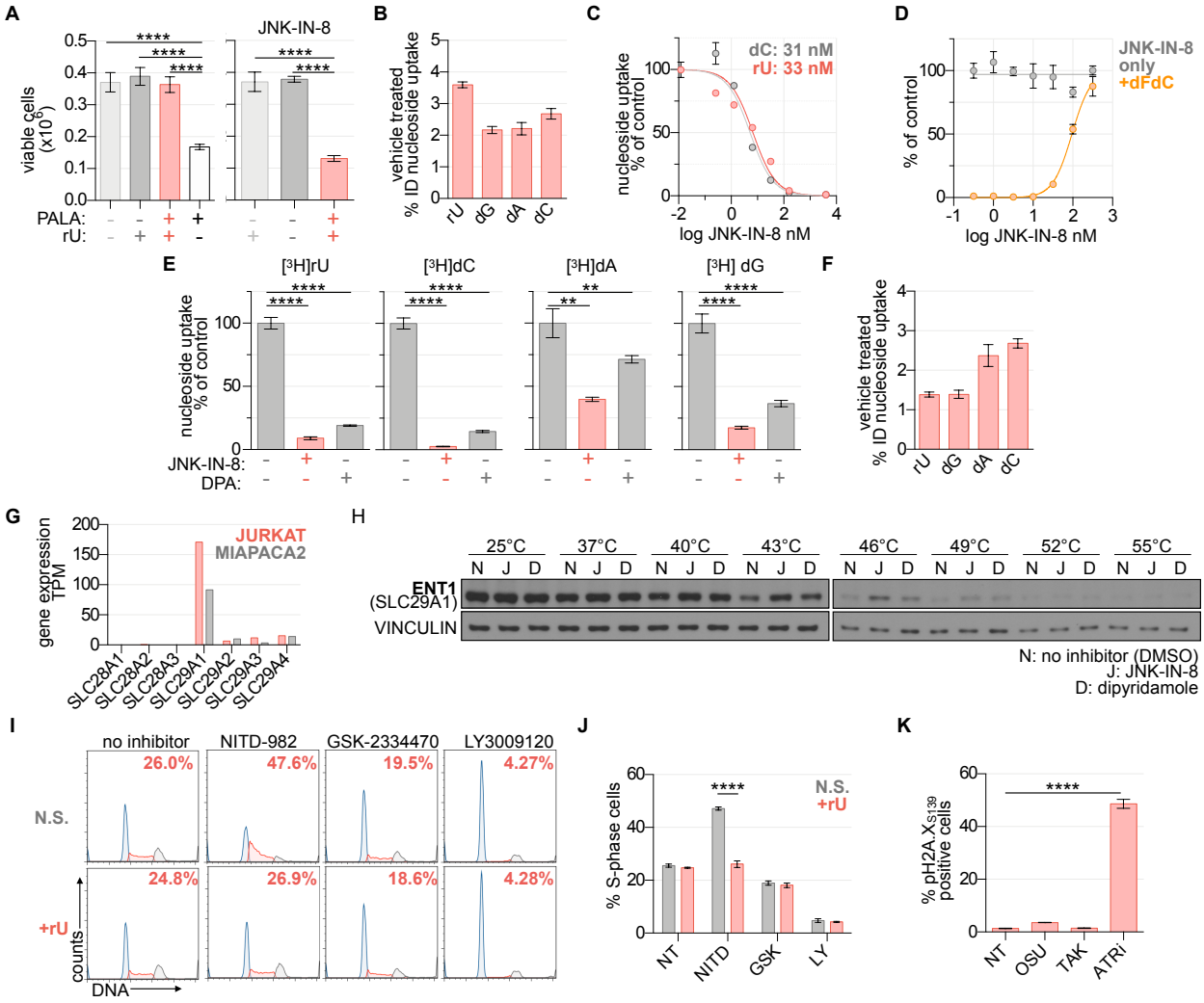

Figure S4.4 | Characterization of JNK-IN-8, OSU-03012 and TAK-632. (**A**) JURKAT cell counts using trypan-blue exclusion following treatment ±200 μM PALA ±10 μM rU ±100 nM JNK-IN-8 for 72 h (mean±SD; n=3; one-way ANOVA corrected for multiple comparisons by Bonferroni adjustment, **** P<0.0001). (**B**) Uptake of [^{3}H]labeled nucleosides in vehicle control condition from experiment in **Figure 5.2B**. Values represent % injected dose (%ID; n=3; 18.5 kBq). (**C**) Uptake of [^{3}H]rU or [^{3}H]dC in CCRF-CEM cells following 2 h incubation ± JNK-IN-8 (mean±SD; n=2; 18.5 kBq). IC_{50} values are indicated. (**D**) Cell Titer Glo analysis of JURKAT cells treated ±10 nM dFdC ± JNK-IN-8 for 72 h (mean±SD; n=4). (**E**) Uptake of [^{3}H]rU, [^{3}H]dC, [^{3}H]dA (+10 μM dCF), [^{3}H]dG (+1 μM BCX-1777) in MIAPACA2 cells following 2 h incubation ±1 μM JNK-IN-8 or 1 μM dipyridamole (DPA; 18.5 kBq; mean±SD; n=3; one-way ANOVA corrected

for multiple comparisons by Bonferroni adjustment; ns: not significant; ** P<0.01; *** P<0.001; **** P<0.0001). (**F**) Uptake of [^{3}H] labeled nucleosides in vehicle control condition from experiment in **E**. Values are expressed as % injected dose (%ID; n=3; 18.5 kBq). (**G**) Summary of nucleoside transporter expression (RNA-seq; *oasis-genomics.org*). (**H**) CETSA for ENT1 (SLC29A1) engagement in MIAPACA2 protein lysates. Lysates were incubated ±10 μM JNK-IN-8 or 10 μM DPA for 2 h, subsequently heat treated at the indicated temperatures and analyzed by immunoblot analysis. (**I**) Propidium iodide cell cycle analysis of MIAPACA2 PDAC cells treated ± 500 nM NITD-982 (NITD) ±5 μM GSK-2334470 (GSK) or ±10 μM LY3009120 (LY) supplement ±10 μM rU (N.S.: no supplement). Insert indicates % S-phase cells. (**J**) Summary of fold changes in S-phase cells from **I** (mean±SD; n=2; one-way ANOVA corrected for multiple comparisons by Bonferroni adjustment, ns: not significant; **** P<0.0001). (**K**) pH2A.X_{S139} flow cytometry analysis of MIAPACA2 cells treated ±5 μM OSU-03012 ±5 μM TAK-632 ±500 nM VE-822 (ATRi) for 48 h (mean±SD; n=2; one-way ANOVA corrected for multiple comparisons by Bonferroni adjustment, ns: not significant; **** P<0.0001).

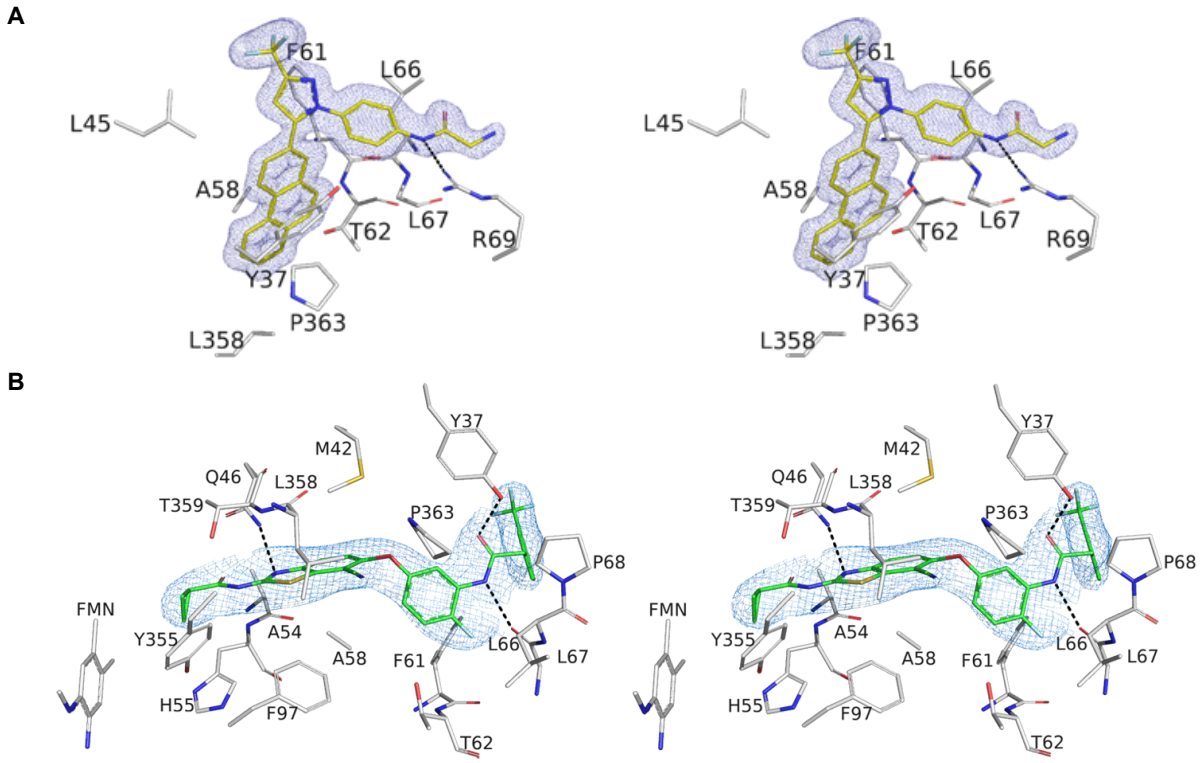

Figure S5.5 | Evaluation of DHODH and OSU-03012/TAK-632 molecular interactions. (**A**) Stereoscopic image of **Figure 5.4A** (OSU-03012). (**B**) Stereoscopic image of **Figure 5.4B** (TAK-632).

Structure	***DHODH + OSU-03012***	***DHODH + TAK-632***
PDB codes	6OC0	6OC1
Data collection statistics		
X-ray source and detector	LS-CAT 21-ID-D Dectris Eiger x 9M	LS-CAT 21-ID-G MARCCD 300
Wavelength (Å)	0.99987	0.97872
Temperature (K)	100	100
Resolution[a] (Å)	1.40 (1.48-1.40)	2.7 (2.85-2.7)
Number of Reflections		
Observed	1,090,019 (113,565)	306,440 (48,502)
Unique	114,363 (17,418)	13,751 (2,169)
Completeness (%)	99.0 (94.2)	99.9 (99.8)
R_{meas} (%)	7.0 (54.5)	17.0 (183.3)
$CC_{1/2}$ (%)	99.9 (87.8)	99.9 (71.1)
Average I/σ(I)	19.2 (2.8)	21.6 (2.1)
Space group	P 3_2 2 1	P 2_1 3
Unit cell: a, b, c (Å)	90.01, 90.01, 123.07	113.67, 113.67, 113.67
Unit cell: α, β, γ (°)	90, 90, 120	90, 90, 90
Wilson B-factors (Å^2)	13.9	66.4
Refinement statistics		
Refinement program	REFMAC5	REFMAC5
R_{work} (%)	15.7	23.4
R_{free} (%)	19.1	29.1
Resolution range (Å)	48.55-1.40	46.45-2.70
Protein molecules per a.u.	1	1
Number of atoms:		
Protein	2845	2769
Water molecules	232	36
ORO + FMN	42	42
Inhibitor	34	39
R.m.s. deviation from ideal:		
Bond length (Å)	0.009	0.0021
Bond angles (°)	1.7114	1.264
Average B-factors (Å^2)		
Protein	23.9	73.0
Water molecules	32.6	44.7
ORO + FMN	12.2	56.6
Inhibitor	29.3	73.0
Ramachandran plot statistics (%)		
Most favored regions	97	86
Additionally allowed regions	3	14
Outlier regions	0	1

[a]High resolution shell in parenthesis; r.m.s., root-mean-square; a.u., asymmetric unit

Figure S5.6 | DHODH crystallographic data collection and refinement statistics.

DISCUSSION

Our screening strategy expands on the concept of previously described “nutrient-sensitized” genetic and small molecule cell-based screens that leveraged the production of a proliferation-enabling metabolite by parallel and redundant metabolic networks to identify selective metabolism modifiers[31,32]. UMP biosynthesis (i.e. pyrimidine metabolism) proved to be compatible with this screening framework as UMP is produced by convergent (*de novo* and salvage) pathways, and UMP depletion triggers a quantifiable change in cellular proliferation.

JNK-IN-8, developed as an irreversible inhibitor of c-Jun N-terminal kinases 1, 2, and 3 with low-nanomolar affinity, was the most potent of three uridine salvage inhibitors identified[33]. Our data confirm that JNK-IN-8 also functions as a potent inhibitor of uridine and deoxycytidine transport both *in vitro* and *in vivo*. We conclude that JNK-IN-8 should not be used in conjunction with compounds which rely upon nucleoside transport, such as the anticancer agent gemcitabine, in research or therapy settings.

In addition to their role in pyrimidine salvage, equilibrative nucleoside transporters are well studied for their ability to regulate levels of the immuno-modulatory metabolite adenosine. ENT1 inhibitors increase extracellular adenosine levels which signal through the P1 purinergic receptor and are used clinically for the treatment of hypertension, among other disorders. Thus, the development of potent and selective inhibitors of ENT1 is an active area of investigation.

The recently reported co-crystal structure of ENT1 in complex with two small molecule inhibitors (NBMPR and dilazep) provided new insight into the molecular mechanism of nucleoside transport and suggested that structurally diverse ENT1 inhibitors possess unique modes of inhibition. ENT1 contains 10 cysteine residues and ENT1-mediated uridine transport can be inhibited by covalent modification of Cys416 by *N*-ethylmaleimide. Intriguingly, the two highest scoring NSP inhibitors in our screen, JNK-IN-8 and the BTK inhibitor CNX-774, both contain a reactive acrylamide group and are cysteine-targeting drugs. Future work will explore the

mechanism of ENT1 inhibition by JNK-IN-8 with a specific focus on the contribution of covalent interactions.

Positron emission tomography (PET) is a powerful approach to monitor cellular metabolism *in vivo,* and several nucleoside analog PET probes have been developed including both pyrimidine ([^{18}F]FAC, [^{18}F]FLT) and purine analogs ([^{18}F]CFA). Interestingly, ENT1 knockout mice exhibit significantly higher plasma thymidine but also paradoxically higher levels of thymidine analog [^{18}F]FLT uptake in the spleen and bone marrow compared to wild type controls. Discrepancies between *in vitro* and *in vivo* findings could result from shifts in nucleoside gradients or differential expression of nucleoside transporters mediated by cytokine signaling. Future work will focus on exploring the utility of nucleoside analog PET as a pharmacodynamic biomarker for ENT inhibitor activity *in vivo*.

The structurally and functionally unrelated OSU-03012 and TAK-632 were identified as inhibitors of the pyrimidine DNP. A recent report described the ability of OSU-03012 and analogs to inhibit virus propagation *via* pyrimidine nucleotide biosynthesis inhibition, specifically implicating modulation of DHODH activity[34]. Our work substantiates these findings, is the first to unambiguously confirm the affinity of OSU-03012 for DHODH through crystallography studies, and is the first to demonstrate the same for TAK-632. Notably, our studies show that OSU-03012 and TAK-632 bind in the same hydrophobic tunnel of DHODH as known inhibitors brequinar and teriflunomide (the active metabolite of leflunomide). This suggests that these two protein kinase inhibitors compete with ubiquinone, a redox partner of DHODH which traverses this hydrophobic tunnel to regenerate FMN from $FMNH_2$. By competitively inhibiting the binding of ubiquinone, these compounds prevent DHODH from completing its redox cycle and effectively abrogate its activity.

OSU-03012 has orphan drug designation in the European Union for treatment of tularaemia and cryptococcosis. We hypothesize that its effectiveness in these indications stems from its ability to inhibit DHODH, rather than from ‘on-target’ effects against PDK1. Indeed, DHODH inhibitors

have demonstrated efficacy against viruses such as dengue virus and respiratory syncytial virus[11,34,35]. In anticancer settings, OSU-03012 was recently demonstrated to synergize with CHK1 inhibitors in KRAS-mutant cancer[27], which was initially attributed to its ability to inhibit PDK1. However, our data show that GSK-2334470, a PDK1 inhibitor more potent than OSU-03012, displayed little synergy with ATR inhibition. In light of our crystallographic data we conclude that the synergy observed between OSU-03012 and ATR inhibition is likely a result of the DHODH-inhibitory ability of the former. Taken together, our data suggest that DHODH inhibitors may have utility in oncology, particularly if used in conjunction with ATR inhibitors or other DNA-damage response/replication stress response pathway inhibitors[2].

In summary, we designed and applied a metabolic modifier screen which identified multiple protein kinase inhibitors as having non-canonical targets within pyrimidine metabolism. Similarly constructed phenotypic screens designed against other metabolic networks containing convergent nodes may find use in drug discovery campaigns or in repurposing screens using existing compounds.

METHODS

Data Availability

The PDB accession numbers for the protein structure data reported in this chapter are **6OC0** (OSU-03012:DHODH) and **6OC1** (TAK-632:DHODH).

Experimental Model and Subject Details

Cell culture

All cell cultures were between passages 3 and 20 and maintained in antibiotic free DMEM or RPMI +10% dialyzed FBS, at 37ºC in 5% CO_2. We routinely monitored for mycoplasma contamination using the PCR-based Venor Mycoplasma kit. PDAC cell lines were acquired either from a commercial vendor (ATCC, DSMZ) or from collaborators (KP4662 from Dr. Vonderheide, UPenn). Cell line identity was independently authenticated by PCR.

Drugs

Drug stocks were prepared in DMSO or H_2O and diluted fresh in cell culture media for treatments. NITD-982 was synthesized as previously described[35]. N-phosphonacetyl-L-aspartate (PALA) was synthesized as previously described[36].

Method Details

Protein kinase inhibitor phenotypic screen

A library of 430 protein kinase inhibitors was arrayed in polypropylene 384-well plates at 200x concentrations covering a 7-point concentration range (corresponding to 1x concentrations: 5μM, 1.65μM, 550nM, 185nM, 61.5nM, 20.6nM, 6.85nM). 25μl per well of condition-specific growth media (DNP+NSP: media +10 μM rU; DNP: media alone; NSP: media +10 μM rU + 1 μM NITD-982) was plated in opaque-white 384-well plates using a BioTek multidrop liquid handler. Protein kinase inhibitors were added by 250 nL pin-tool transfer (BioMek FX, Beckman-

Coulter) and inhibitor/media mixtures were incubated at room temperature for 30 m. 25 µL of a 40,000 cells/mL MIAPACA2 suspension (for 1000 cells / well) was subsequently added to each well. After 72 h, 50 µL of Cell Titer Glo reagent diluted 1:4 in dH_2O was added to each well and luminescence was measured using a Wallac plate reader (Perkin Elmer). Each condition was assayed in duplicate (n=2) and % proliferation values were calculated by normalizing experimental wells to plate negative controls and averaging replicate values. Composite pathway selectivity synergy scores for each test compound were defined as the sum of the excess over additivity (% proliferation inhibition observed - % proliferation inhibition expected) between individual protein kinase inhibitor concentrations across the 7-point concentration range. Z factor scores for individual assay plates were calculated using eight positive and eight negative control wells on each plate as previously described[16]. All plates gave a Z factor > 0.5 (**Figure S5.3C**).

Cell Titer Glo viability analysis

Cells were plated at $1x10^3$ cells / well at 50 µl / well in white opaque 384-well plates and treated as described. Following incubation 50 µl of Cell Titer. Glo reagent (Diluted 1:5 in dH_2O) was added to each well, plates incubated at room temperature for 5 m and luminescence was measured using a BioTek microplate luminescence reader. Proliferation rate normalized growth inhibition was calculated using the previously described GR metric[13].

Trypan blue exclusion cell viability

Trypan blue exclusion cell viability analysis was performed using a ViCell analyzer following 72 h of treatment. Trypan blue-negative population counts are reported.

Microplate immunofluorescence microscopy cell scoring

MIAPACA2 cells were plated at 1000 cells/well in black-walled clear-bottom 384 well plates in 50 µL of media and treated as indicated with n=4 replicate wells per condition. After 72 h of drug exposure 50 µL of 10 µg/mL Hoechst 33342 dye diluted in culture media was added to

microplate wells. Following a 30 m incubation at 37C images were acquired using a ImageXpress Micro Confocal High-Content Imaging System at 10x magnification and 1 image/ well. Analysis was performed using the *Cell Scoring Application Module* in the MetaXpress analysis software. Nuclei counts for treatement groups were normalized to control wells.

Mass spectrometry

For analysis of stable isotope-labeled metabolite incorporation into newly replicated DNA, cells were cultured in glucose-free DMEM (for MIAPACA2 cells) or RPMI (for JURKAT cells) media supplemented with 10% dialyzed FBS, 4 mM glutamine, 1 g/L [$^{13}C_6$]glucose, 10 μM [$^{13}C_9$; $^{15}N_2$]rU and treated as indicated.

Genomic DNA was extracted using the Quick-gDNA MiniPrep kit and hydrolyzed to nucleosides using the DNA Degradase Plus kit, following manufacturer-supplied instructions. In the final step of DNA extraction, 50 μL of water was used to elute the DNA into 1.5 mL microcentrifuge tubes. A nuclease solution (5 μL; 10X buffer/DNA Degradase PlusTM/water, 2.5/1/1.5, v/v/v) was added to 20 μL of the eluted genomic DNA in an HPLC injector vial. The samples were incubated overnight at 37 ºC.

Hydrolyzed DNA was diluted 1/1 with solvent A (water/acetonitrile/formic acid, 95/5/0.1, v/v) aliquots of the solution (15 μL) were injected onto a porous graphitic carbon column (Thermo Hypercarb, 100 x 2.1 mm, 5 micron particle size) equilibrated in solvent A and eluted (300 μL/ min) with an increasing concentration of solvent B (acetonitrile/water/formic acid, 90/10/0.1). The HPLC timetable, in terms of min/%B, is the following: 0/0, 5/0, 12/20, 15/30, 17/50, 19/50, 20/0, 24/0. The effluent from the column was directed to Agilent Jet Stream connected Agilent 6460 QQQ operating in the positive ion MRM mode. After verification of retention times using authentic standards, the peak areas of the protonated nucleoside/protonated base fragment ion transitions for each of the nucleosides were recorded with instrument manufacturer-supplied software.

^{3}H-labeled metabolite uptake assays

Radioactive probe uptake assays were conducted as previously described[37]. Briefly, cells were pretreated with JNK-IN-8 or DPA for 2 h before incubation with 18.5 kBq of ^{3}H-labeled probe for 2 h. For purine uptake assays, cells were cultured in the presence of 10 μM dCF (for ^{3}H-dA) or 1 μM BCX-1777 (for ^{3}H-dG) to prevent nucleoside catabolism. Following incubation, cells were washed with PBS and lysed. Cell lysate radioactivity was measured using a beta-counter (Perkin-Elmer).

Flow cytometry

All flow cytometry data were acquired on five-laser BD LSRII, and analyzed using FlowJo software.

AnnexinV/PI: Treated PDAC cells were washed with PBS and incubated with AnnexinV and propidium iodide diluted in 1x Annexin binding buffer. 20,000 events were collected per sample.

Propidium iodide cell cycle analysis: Treated PDAC cells were washed with PBS and suspended in propidium iodide cell cycle staining solution (100 μg/ml propidium iodide; 20 μg/ml Ribonuclease A). 10,000 events were collected per sample.

pH2A.X$_{S139}$ flow cytometry: Treated cells were collected by trypsinization, incubated with Cytofix/Cytoperm reagent for 15 m at 4C, washed with PBS and incubated in 100 μL PermWash buffer for 15 m at 4C. Cells were washed with 1 mL Perm/Wash buffer, resuspended in 50 μL of staining solution (1:800 dilution of FITC-conjugated pH2AX$_{S139}$ antibody diluted in Perm/Wash buffer) and incubated for 20 m at 25C protected from light. Stained cells were washed and incubated in 500 μL of DAPI staining solution (1 μg/mL DAPI in PBS) before acquisition.

Gene cloning, protein expression, and purification of DHODH in E.coli cells

Primers were ordered to add NdeI (AGAGAACAGATTGGTGGTCATATGATGGCCACGGGAGATGAG) upstream of residue 29

(after the mitochondrial membrane associated loop) and BamHI (TCGGGCTTTGTTAGCAGCCGGATCCTTACCTCCGATGATCTGCTCC) after the stop codon to insert into N-terminal His-Sumo pET 14b vector. This clone, His-Sumo-DHODH 29-395 (subsequently referred to as DHODH) was successfully inserted into the vector in XL1-blue cells for vector propagation.

The vector was transformed into C41(DE3) cells for productions. Cells were grown at 37 °C in 2xYT medium supplemented with 100 µg/mL ampicillin (Amp), treated with 0.1 mM isopropyl β-D-1-thiogalactopyranoside (IPTG) at an OD600 nm of 0.6-0.8, and then cultured for an additional 18h at 18 °C. Cells were harvested by centrifugation, washed with 200 mM NaCl and 25 mM Tris pH 7.5, and pelleted at 5000 rpm for 20 minutes before storage at -20°C. 6.7g/L of cell pellet was obtained.

DHODH was purified according to known purification conditions[30]. The cell pellet was resuspended in lysis buffer (50 mM Tris pH 7.5; 600 mM NaCl; 0.33% w/v Thesit; 10% Glycerol; 1 mM PMSF) and lysed by sonication on ice. Lysed cells were centrifuged at 58,500 RCF for 45 minutes at 4°C, and the supernatant was filtered through a 0.45 µM filter and loaded onto a 5-mL His-Trap column pre-equilibrated with buffer A (50 mM Tris pH 7.4; 600 mM NaCl; 0.05% w/v Thesit; 10% Glycerol). The column was washed with buffer A for 70 mL, buffer A with 25 mM imidazole for 50 mL, and buffer A with 50 mM imidazole for 50 mL. The protein was eluted with buffer A with 250 mM imidazole. The eluted fraction was diluted 1:1 with Buffer A. Sumo protease was added and the protein was dialyzed overnight at 4°C against 1L of Buffer A. The dialyzed protein was loaded back onto the His-Trap column equilibrated with buffer A. The cut-DHODH was eluted with buffer A with 50 mM imidazole. The purified protein was concentrated to 5 mL and injected onto S-200 gel filtration column (GE Healthcare) equilibrated with: 50 mM HEPES pH 7.7, 400 mM NaCl, 10% Glycerol, 1mM EDTA, 0.05 % w/v Thesit. Eluted fractions consistent with monomer size were collected, concentrated, flash frozen, and stored at -80°C.

Recombinant DHODH enzyme assay

Evaluation of DHODH inhibition was performed as previously described[30]. The standard assay mixture contained 50 μM decyclo-ubiquinone, 100 μM dihydroorotate, and 60 μM 2,6-dichloroindophenol (DCIP). The amount of DHODH was 337.4 ng/mL. Measurements were conducted in 50 mM TrisHCl, 150 mM KCl, 0.1% Triton X-100, pH 8.0, at 30 °C in a final volume of 1 mL. The components were mixed, and the reaction was started by adding dihydroorotate. The reaction was followed spectrophotometrically by measuring the decrease in absorption at 600 nm for 2.5 min at 30 second intervals. The assay was linear in time and enzyme concentration. Inhibitory studies were conducted in a standard assay with additional variable amounts of inhibitor.

Crystallization of DHODH with OSU-03012 and TAK-632 compounds

For co-crystallizaion of DHODH and OSU-03012, crystals were obtained using the same conditions reported in previously published DHODH structures[30,39–48], namely 1.6 – 2.6 M ammonium sulfate and 5-30% glycerol in the well in pH 4.5, with 20 mg/mL DHODH with 2 mM dihydroorotate (DHO), 20.8 mM dodecyldimethyl-N-amineoxide (DDAO), and 400 μM inhibitor. Protein was mixed 1:1 with mother liquor and hanging drops were used at room temperature. Crystals appeared after 48 hours and reached maximal size within one week. Molecular replacement used 4OQV [49] as the starting model. Interestingly, DHODH-TAK-632 crystals grown in similar conditions to those used for the DHODH-OSU-03012 complex did not show TAK-632 density. As a result, novel DHODH crystallization conditions were identified using commercial screens. For co-crystallization of DHODH with TAK-632, crystals were obtained in conditions of 1.4-1.6 M sodium phosphate, pH 8.2. Protein solution (20 mg/mL DHODH with 2 mM DHO, 20.8 mM DDAO, and 400 μM inhibitor) was mixed 1:1 with mother liquor and hanging drops were used at room temperature. Crystals appeared after 48 hours and reached maximal size within one week. The lack of density of the TAK-632 structure in the initial crystallography condition is most likely due to the difference in pH between the conditions, pH 4.5 and pH 8.2

for the OSU-03012 and the TAK-632 structure, respectively. There are multiple hydrogen bonds and potentially labile hydrogens on the TAK-632 structure that at low pH could be protonated and charged, potentially preventing their insertion into the hydrophobic tunnel. Ligplot+ [50,51] was used to determine hydrophilic and hydrophobic interactions between inhibitors and DHODH molecules.

Immunoblot analysis

PBS-washed cell pellets were resuspended in cold RIPA buffer supplemented with protease and phosphatase inhibitors. Protein lysates were normalized using BCA assay, diluted using RIPA and 4x laemmli loading dye, resolved on 4-12% Bis-Tris gels and electro-transferred to nitrocellulose membranes. After blocking with 5% nonfat milk in TBS + 0.1% Tween-20 (TBS-T), membranes were incubated overnight in primary antibodies diluted (per manufacturers instructions) in 5% BSA in TBS-T. Membranes were washed with TBST-T and incubated with HRP-linked secondary antibodies prepared at a 1:2500 dilution in 5% nonfat dry milk / TBS-T. HRP was activated by incubating membranes with a mixture of SuperSignal Pico and SuperSignal Femto ECL reagents (100:1 ratio). Exposure of autoradiography film was used for detection.

Cellular thermal shift assay (CETSA)

MIAPACA2 cells were cultured in 10 cm plates, washed with PBS, and harvested by cell scraping following addition of 4 mL of lysis buffer (100 mM ammonium sulfate, 400 mM NaCl, 10% glycerol, 0.5% DDM and 1x protease inhibitor cocktail). The cell lysate was collected in a 15 mL conical tube, incubated on ice for 20 m, centrifuged at 5,000xg for 20 m at 4C and protein content of the supernatant was measured. 30 µL of protein lysate was aliquoted into 1.5 mL Eppendorf tubes and treated with either DMSO, JNK-IN-8 or dipyridamole for 30 m on ice. Lysates were subsequently heated at the indicated temperatures using an Eppendorf Thermomixer for 6 m, cooled to room temperature for 3 m and transferred to ice. Heated lysates

were centrifuged at 12,000xg for 40 m to pellet the insoluble protein fraction. Supernatants were processed for immunoblot analysis.

Statistical analyses

Data are presented as mean ± SD with number of biological replicates indicated. Comparisons of two groups were calculated using indicated unpaired two-tailed Student's t-test and P values less than 0.05 were considered significant. Comparisons of more than two groups were calculated using one-way ANOVA followed by Bonferroni's multiple comparison tests, and P values less than 0.05/m, where m is the total number of possible comparisons, were considered significant.

CHAPTER 5 Key Resource Table

Reagents	Source	Identifier
DMEM	Corning	10-107-CV
RPMI	Corning	10-040-CV
Glucose-Free DMEM	Corning	17-207-CV
Glucose-Free RPMI	Corning	10-043-CV
Dialyzed Fetal Bovine Serum	Gibco	26-400-044
Kinase Inhibitor Library	SelleckChem	L1200
JNK-IN-8	SelleckChem	S4901
TAK-632	Cayman Chemicals	16285
OSU-03012	SelleckChem	S1106
GSK2334470	Cayman Chemicals	18095
AMG-706	Cayman Chemicals	17671
CNX-774	Cayman Chemicals	21475
NITD-982	this study	N/A
PALA	this study	N/A
Dipyridamole	Sigma-Aldrich	D9766
Gemcitabine	SelleckChem	S1714
dCF (ADA inhibitor)	Sigma-Aldrich	SML0508
BCX-1777 (PNP inhibitor)	MedChemExpress	HY-16209
Uridine	Sigma-Aldrich	U3003
[^{3}H]dC	Moravek	MT673
[^{3}H]rU	PerkinElmer	NET367250UC
[^{3}H]dG	Moravek	MT507
[^{3}H]dA	Moravek	MT641
[$^{13}C_6$]glucose	Cambridge Isotope Laboratories	CLM-1396-1
[$^{13}C_9$; $^{15}N_2$]rU	Cambridge Isotope Laboratories	CNLM-3809-PK
Orotate	Sigma-Aldrich	O2750
VE-822	SelleckChem	S7102
Hoechst 33342	ThermoFisher Scientific	62249
BCA Assay	ThermoFisher Scientific	23225
RIPA Protein Lysis Buffer	Boston BioProducts	BP-115
Laemmli Loading Dye	Boston BioProducts	BP-110R
4-12% Bis-Tris Gels	ThermoFisher Scientific	NP0336
Nitrocellulose Membrane	ThermoFisher Scientific	88018
Nonfat Dry Milk	ThermoFisher Scientific	M-0841
Tris-Buffered Saline	ThermoFisher Scientific	50-751-7046
Tween-20	Sigma-Aldrich	P9416
SuperSignal West Pico	ThermoFisher Scientific	34580
SuperSignal West Femto	ThermoFisher Scientific	34095
Autoradiography Film	Denville	E3012
Halt Protease Inhibitor Cocktail	ThermoFisher Scientific	PI78430
Halt Phosphatase Inhibitor	ThermoFisher Scientific	PI78428
Matrigel	ThermoFisher Scientific	CB-40237
Cytofix/Cytoperm Buffer	BD Biosciences	554722
Perm/Wash Buffer	BD Biosciences	554723
White Opaque 384-well Plates	VWR	781080
Black Clear Bottom 384-well	VWR	781086
Zymo-Spin IC Columns	Zymo Research	C1004
DNA Degradase Plus	Zymo Research	E2021

Antibody	Source	Identifier
ACTIN	Cell Signaling Technology	3700
PHOSPHO CHEK1 S345	Cell Signaling Technology	2348
TOTAL CHEK1	Cell Signaling Technology	2360
PHOSPHO S6K T229	Novus Biologicals	MAB2964-SP
TOTAL S6K	Cell Signaling Technology	9202
PHOSPHO ERK1/2 T202/Y204	Cell Signaling Technology	9101
TOTAL ERK1/2	Cell Signaling Technology	9102
PHOSPHO H2A.X S139 - FITC	MilliporeSigma	16-202A
VINCULIN	Cell Signaling Technology	13901
ENT1	Novus Biologicals	NBP1-50508
ANTI-RABBIT IgG, HRP-LINKED	Cell Signaling Technology	7074
ANTI-MOUSE IgG, HRP-LINKED	Cell Signaling Technology	7076

DHODH assay reagents	Source	Identifier
Recombinant DHODH protein	this study	N/A
Dihydroorotate	Sigma-Aldrich	D1728
Coenzyme Q_{10}	Sigma-Aldrich	C9538
4-TFMBAO	Sigma-Aldrich	422231
$K_3[Fe(CN)_6]$	Sigma-Aldrich	244023
K_2CO_3	Sigma-Aldrich	P5833

Cell line	Source	Identifier
JURKAT	ATCC	TIB-152
MIAPACA2	ATCC	CRL-1420
CCRF-CEM	ATCC	CCL-119
KP4662	Gift from Dr. Vonderheide (UPenn)	N/A

Software	Developer	Identifier
Graphpad Prism	Graphpad Software	https://www.graphpad.com/scientific-software/prism/
FlowJo 7.6	TreeStar	https://www.flowio.com
OsiriX	Pixmeo	https://www.osirix-viewer.com/
MetaXpress	Molecular Devices	https://www.moleculardevices.com/products/cellular-imaging-systems/

Critical Commercial Assays	Source	Identifier
AnnexinV-FITC Apoptosis Detection Kit	BD Biosciences	556547
CellTiter-Glo	Promega	G7572
MycoPlasma Detection Kit	Sigma-Aldrich	MP0025

Equipment	Developer
ImageXpress Confocal Micro	Molecular Devices
ViCell Cell Viability Analyzer	Beckman Coulter
6460 Triple Quadruple Mass Spectrometer	Agilent

REFERENCES

1. Xu, S. et al. Hexokinase 2 is targetable for HK1 negative, HK2 positive tumors from a wide variety of tissues of origin. J Nucl Med (2018).
2. Le, T. M. et al. ATR inhibition facilitates targeting of leukemia dependence on convergent nucleotide biosynthetic pathways. Nat Commun 8, 241 (2017).
3. York, A. et al. Limiting Cholesterol Biosynthetic Flux Spontaneously Engages Type I IFN Signaling. Cell 163, 1716-1729 (2015).
4. Garcia-Bermudez, J. et al. Aspartate is a limiting metabolite for cancer cell proliferation under hypoxia and in tumours. Nat Cell Biol 20, 775-781 (2018).
5. Okesli, A., Khosla, C. & Bassik, M. C. Human pyrimidine nucleotide biosynthesis as a target for antiviral chemotherapy. Current Opinion in Biotechnology 48, 127-134 (2017).
6. An R. Van Rompay, A. N., Karin Linden, Magnus Johansson, Anna Karlsson. Phosphorylation of Uridine and Cytidine Nucleoside Analogs by Two Human Uridine-Cytidine Kinases. Molecular Pharmacology 59, 1181-1186 (2001).
7. Madak, J. T., Bankhead, A., Cuthbertson, C. R., Showalter, H. D. & Neamati, N. Revisiting the role of dihydroorotate dehydrogenase as a therapeutic target for cancer. Pharmacology & Therapeutics 195, 111-131 (2019).
8. Sykes, D. B. et al. Inhibition of Dihydroorotate Dehydrogenase Overcomes Differentiation Blockade in Acute Myeloid Leukemia. Cell 167, 171-186.e15 (2016).
9. Santana-Codina, N. et al. Oncogenic KRAS supports pancreatic cancer through regulation of nucleotide synthesis. Nat Commun 9, 4945 (2018).
10. Lolli, M. L. et al. Use of human Dihydroorotate Dehydrogenase (hDHODH) Inhibitors in Autoimmune Diseases and New Perspectives in Cancer Therapy. Recent Pat Anticancer Drug Discov 13, 86-105 (2018).
11. Wang, Q. Y. et al. Inhibition of dengue virus through suppression of host pyrimidine biosynthesis. J Virol 85, 6548-6556 (2011).

12. Evans, D. R. & Guy, H. I. Mammalian pyrimidine biosynthesis: fresh insights into an ancient pathway. J Biol Chem 279, 33035-33038 (2004).
13. Hafner, M., Niepel, M., Chung, M. & Sorger, P. K. Growth rate inhibition metrics correct for confounders in measuring sensitivity to cancer drugs. Nat Methods 13, 521-527 (2016).
14. Damaraju, V. L., Weber, D., Kuzma, M., Cass, C. E. & Sawyer, M. B. Selective Inhibition of Human Equilibrative and Concentrative Nucleoside Transporters by BCR-ABL Kinase Inhibitors. J Biol Chem 291, 18809-18817 (2016).
15. Huang, M. et al. Inhibition of Nucleoside Transport by p38 MAPK Inhibitors. J. Biol. Chem. 277, 28364-28367 (2002).
16. Ji-Hu Zhang, T. D. Y. C., Kevin R. Oldenburg. A simple statical parameter for use in evaluation and validation of high throughput screening assays. Journal of Biomolecular Screening 4, 67-73 (1999).
17. Zhu, J. et al. From the cyclooxygenase-2 inhibitor celecoxib to a novel class of 3-phosphoinositide-dependent protein kinase-1 inhibitors. Cancer Res 64, 4309-4318 (2004).
18. Okaniwa, M. et al. Discovery of a selective kinase inhibitor (TAK-632) targeting pan-RAF inhibition: design, synthesis, and biological evaluation of C-7-substituted 1,3-benzothiazole derivatives. J Med Chem 56, 6478-6494 (2013).
19. Fang, J. et al. Dihydro-orotate dehydrogenase is physically associated with the respiratory complex and its loss leads to mitochondrial dysfunction. Biosci Rep 33, e00021 (2013).
20. Collins, K. D. & Stark, G. R. Aspartate transcarbamylase. Interaction with the transition state analogue N-(phosphonacetyl)-L-aspartate. J Biol Chem 246, 6599-6605 (1971).
21. Peters, G. J. Antipyrimidine effects of five different pyrimidine de novo synthesis inhibitors in three head and neck cancer cell lines. Nucleosides Nucleotides Nucleic Acids 37, 329-339 (2018).

22. Byrne, K. T., Leisenring, N. H., Bajor, D. L. & Vonderheide, R. H. CSF-1R-Dependent Lethal Hepatotoxicity When Agonistic CD40 Antibody Is Given before but Not after Chemotherapy. J Immunol 197, 179-187 (2016).
23. Fernandez-Banet, J. et al. OASIS: web-based platform for exploring cancer multi-omics data. Nat Methods 13, 9-10 (2016).
24. Martinez Molina, D. & Nordlund, P. The Cellular Thermal Shift Assay: A Novel Biophysical Assay for In Situ Drug Target Engagement and Mechanistic Biomarker Studies. Annu Rev Pharmacol Toxicol 56, 141-161 (2016).
25. Radu, C. G. et al. Molecular imaging of lymphoid organs and immune activation by positron emission tomography with a new [18F]-labeled 2'-deoxycytidine analog. Nat Med 14, 783-788 (2008).
26. Bonomo, S., Tosco, P., Giorgis, M., Lolli, M. & Fruttero, R. The role of fluorine in stabilizing the bioactive conformation of dihydroorotate dehydrogenase inhibitors. J Mol Model 19, 1099-1107 (2013).
27. Yuan, T. L. et al. Differential Effector Engagement by Oncogenic KRAS. Cell Reports 22, 1889-1902 (2018).
28. Peng, S. B. et al. Inhibition of RAF Isoforms and Active Dimers by LY3009120 Leads to Anti-tumor Activities in RAS or BRAF Mutant Cancers. Cancer Cell 28, 384-398 (2015).
29. Zeman, M. K. & Cimprich, K. A. Causes and consequences of replication stress. Nat Cell Biol 16, 2-9 (2014).
30. Baumgartner, R. et al. Dual binding mode of a novel series of DHODH inhibitors. J Med Chem 49, 1239-1247 (2006).
31. Arroyo, J. D. et al. A Genome-wide CRISPR Death Screen Identifies Genes Essential for Oxidative Phosphorylation. Cell Metabolism 24, 875-885 (2016).
32. Gohil, V. M. et al. Nutrient-sensitized screening for drugs that shift energy metabolism from mitochondrial respiration to glycolysis. Nat Biotechnol 28, 249-255 (2010).

33. Zhang, T. et al. Discovery of potent and selective covalent inhibitors of JNK. Chem Biol 19, 140-154 (2012).
34. Yang, C. F. et al. Novel AR-12 derivatives, P12-23 and P12-34, inhibit flavivirus replication by blocking host de novo pyrimidine biosynthesis. Emerg Microbes Infect 7, 187 (2018).
35. Bonavia, A., et al.. Identification of broad-spectrum antiviral compoundsand assessment of the druggability of their target for efficacy against respiratory syncytial virus (RSV). Proc Natl Acad Sci USA 108, 6739-6744 (2011).
36. Morris, A. D. & Cordi, A. A. A New, Efficient, Two Step Procedure for the Preparation of the Antineoplastic Agent Sparfosic Acid. Synthetic Communications 27, 1259-1266 (1997).
37. Campbell, D. O. et al. Structure-guided Engineering of Human Thymidine Kinase 2 as a Positron Emission Tomography Reporter Gene for Enhanced Phosphorylation of Non-natural Thymidine Analog Reporter Probe. J. Biol. Chem. 287, 446-454 (2011).
38. Shu, C. J. et al. Novel PET probes specific for deoxycytidine kinase. J Nucl Med 51, 1092-1098 (2010).
39. Lewis, T. A. et al. Development of ML390: A Human DHODH Inhibitor That Induces Differentiation in Acute Myeloid Leukemia. ACS Med Chem Lett 7, 1112-1117 (2016).
40. Das, P. et al. SAR Based Optimization of a 4-Quinoline Carboxylic Acid Analog with Potent Anti-Viral Activity. ACS Med Chem Lett 4, 517-521 (2013).
41. Davies, M. et al. Structure-based design, synthesis, and characterization of inhibitors of human and Plasmodium falciparum dihydroorotate dehydrogenases. J Med Chem 52, 2683-2693 (2009).
42. Erra, M. et al. Biaryl analogues of teriflunomide as potent DHODH inhibitors. Bioorg Med Chem Lett 21, 7268-7272 (2011).
43. Hurt, D. E., Sutton, A. E. & Clardy, J. Brequinar derivatives and species-specific drug design for dihydroorotate dehydrogenase. Bioorg Med Chem Lett 16, 1610-1615 (2006).

44. Ladds, M. J. G. W. et al. Publisher Correction: A DHODH inhibitor increases p53 synthesis and enhances tumor cell killing by p53 degradation blockage. Nat Commun 9, 2071 (2018).
45. Liu, S., Neidhardt, E. A., Grossman, T. H., Ocain, T. & Clardy, J. Structures of human dihydroorotate dehydrogenase in complex with antiproliferative agents. Structure 8, 25-33 (2000).
46. McLean, L. R. et al. Discovery of novel inhibitors for DHODH via virtual screening and X-ray crystallographic structures. Bioorg Med Chem Lett 20, 1981-1984 (2010).
47. Sainas, S. et al. Targeting Myeloid Differentiation Using Potent 2-Hydroxypyrazolo[1,5-a]pyridine Scaffold-Based Human Dihydroorotate Dehydrogenase Inhibitors. J Med Chem 61, 6034-6055 (2018).
48. Walse, B. et al. The structures of human dihydroorotate dehydrogenase with and without inhibitor reveal conformational flexibility in the inhibitor and substrate binding sites. Biochemistry 47, 8929-8936 (2008).
49. Deng, X. et al. Fluorine modulates species selectivity in the triazolopyrimidine class of Plasmodium falciparum dihydroorotate dehydrogenase inhibitors. J Med Chem 57, 5381-5394 (2014).
50. Laskowski, R. A. & Swindells, M. B. LigPlot+: multiple ligand-protein interaction diagrams for drug discovery. J Chem Inf Model 51, 2778-2786 (2011).
51. Wallace, A. C., Laskowski, R. A. & Thornton, J. M. LIGPLOT: a program to generate schematic diagrams of protein-ligand interactions. Protein Eng 8, 127-134 (1995).